Characterization and qualification of damage-tolerant ceramic matrix composites for structural applications in hot gas turbines

Zur Erlangung des akademischen Grades eines

Doktors der Ingenieurwissenschaften (Dr.-Ing.)

von der KIT-Fakultät für Maschinenbau des

Karlsruher Instituts für Technologie (KIT)

genehmigte

Dissertation

von

M.Sc. Ingo Jürgen Markel

Tag der mündlichen Prüfung: 16.07.2021

Hauptreferent: Prof. Dr. Hans Jürgen Seifert

Korreferent: Prof. Dr.-Ing. Dietmar Koch

Acknowledgements

Contents

Contents

Abstract

Non-oxide ceramic matrix composites (CMC) posses excellent high-temperature resistance and tensile strength. Therefore, CMC have found increasing application in space industries and in the development of turbines for aviation and stationary power generation. Their use in turbines allows raising combustion temperature and thus an improvement in energy efficiency compared to conventional metallic materials. In addition, the potential weight saving due to a two-thirds lower density compared to conventional nickel-based alloys is attractive for aerospace applications. However, the extreme conditions in the hot gas path, such as high temperatures and the oxidizing and corrosive hot gas atmosphere, represent a challenge for the technical use of CMC.

In the present work, the phase formations and high-temperature stabilities of precursor derived Si-(B-)C-N ceramic matrix and interactions with ZrB_2 as a functional additive were investigated. Both ceramic materials can limit the maximum operating temperature of the CMC. Furthermore, the high-temperature oxidation behavior of the ZrB_2-additive as well as the ensemble of a ZrB_2-containing SiC-fiber reinforced Si-C-N ceramic was examined. To this end, thermodynamic equilibrium calculations were combined with experiments at high temperatures and under prototypic combustion atmospheres. The CALPHAD method allowed thermodynamic calculations of equilibrium states such as phase equilibria and their compositions. The results enabled the identification of reactions which occur during preparation or limit the high-temperature stability of the obtained CMC.

Si-C-N and Si-B-C-N ceramics were prepared by pyrolysis of the preceramic polysilazanes Ceraset® PSZ 10 and PSZ 20 as well as a polyborosilazane at 1273 K-1773 K in flowing Ar- and Ar/N_2-atmospheres, respectively. The pyrolysis behavior, high-temperature stability, decomposition reactions and crystallization of Si-(B-)C-N ceramics were investigated by a combination of STA, mass spectrometry, XRD and SEM/EDX. Furthermore the CALPHAD-method was used to predict gaseous pyrolysis- and decomposition reactions and phase stabilities as a function of temperature and nitrogen partial pressure. Thermodynamic calculations confirm and explain the experimental findings.

Based on the known chemical composition of the Ceraset® PSZ 10 and PSZ 20 precursor polymer, their transformation into a solid amorphous ceramic was modeled. The hydrogen, as a component of the functional groups in the polymer chain, is predominantly released in the form of H_2 and CH_4. Coupled STA and mass spectrometric analysis showed that pyrolysis is a two-step endothermic process. The actual composition of the obtained Si-C-N ceramics agreed well with the calculations. In thermodynamic equilibrium the composition is in the three-phase region $SiC+C+Si_3N_4$ for temperatures lower than 1757 K. The high-temperature stability of Si-C-N ceramics is determined by its composition. Calculated phase stability diagrams show that the

Abstract

carbothermic decomposition reaction ($Si_3N_4+3C=3SiC+2N_2$) at 1757 K is limiting the maximum application temperature under atmospheric pressure. This was confirmed qualitatively and quantitatively by combined mass spectrometry and thermogravimetry. The decomposition temperature decreases with decreasing nitrogen partial pressure.

Thermodynamic calculations and experimental investigations were also carried out based on the compositions of the *Si-B-C-N_2* polyborosilazane and the *Si-B-C-N_2* and *Si-B-C-N_1* ceramics. In addition to H_2 and CH_4, occurring N_2 (p_{N2}=0.06-0.12 bar) and NH_3 (p_{NH3}<4-10^{-4} bar) indicate a nitrogen excess of the *Si-B-C-N_2* preceramic polymer. As a result, the C and N contents decrease while the Si:B ratio remains constant during the pyrolysis of the polymer to the solid Si-B-C-N ceramic (($SiBC_3N_3H_{10})_n \rightarrow SiBC_{1.4}N_{2.3}$). The mass loss during crosslinking of the *Si-B-C-N_1* polyborosilazane is significantly higher than for Ceraset® PSZ 10 and PSZ 20 and associated with a pronounced release of H_2. As a result, bubbles are formed which are still present in the obtained Si-B-C-N ceramic. The ceramic yield of the *Si-B-C-N_1* polyborosilazane of about 50 wt.% is lower than that of the Ceraset® PSZ 10 (60 wt.%) and PSZ 20 (67 wt.%) Si-C-N precursor polymers. The composition of both obtained Si-B-C-N ceramics is in phase equilibrium Si_3N_4+SiC+BN+C (T<1757 K). For both Si-B-C-N ceramics, as well as the Si-C-N ceramics, the temperature-limiting reaction is the carbothermic decomposition reaction ($Si_3N_4+3C=3SiC+2N_2$) at 1757 K. Due to their different Si:B:C ratios, either Si_3N_4 or free carbon is completely consumed in this reaction. The ideal nitrogen content for maximum high-temperature stability, without formation of liquid or gaseous reaction products, was determined for the individual Si:B:C ratio from thermodynamic calculations. The *Si-B-C-N_1* ceramic exhibited a superior high-temperature resistance compared to Ceraset® PSZ 10- and PSZ 20-derived Si-C-N ceramics. Even above the carbothermic reaction temperature, mass loss is significantly lower.

A ZrB_2/Si-C-N composite was prepared by pyrolysis of a mixture of ZrB_2-powder and the polysilazane Ceraset® PSZ 20 at temperatures from 1473 K-1773 K. High-temperature reactions between the ZrB_2-additive and the equilibrium constituents of the ceramic Si-C-N matrix (Si_3N_4, SiC und C), limiting the high-temperature stability, were identified using the CALPHAD-method. The first reaction ($ZrB_2+Si_3N_4=ZrN+2BN+L(Si,Zr,B,N)$) occurs at 1870 K. Since this takes place 113 K above the carbothermal decomposition reaction of the Si-C-N matrix, the ZrB_2-additive does not represent a further limitation to the maximum application temperature. The formation mechanism for ZrC_xN_y was identified by a combination of CALPHAD-modeling and key experiments: First ZrN is formed from a nitriding reaction of ZrB_2 with the applied Ar/N_2 pyrolysis atmosphere (p_{N2}=0.5 bar). As soon as ZrN is present, free carbon dissolves from the Si-C-N matrix forming a ZrC_xN_y solid solution with a carbon content of C/(C+N) = 0.56. Therefore, formation of ZrC_xN_y can be prevented by suitable pyrolysis conditions, within the stability range of ZrB_2, during preparation of the ZrB_2/Si-C-N composite. This is the case at small nitrogen partial pressures and moderate temperatures below 1673 K.

2

The high-temperature oxidation behavior of compacted ZrB_2 powder pellets was investigated in flowing H_2O /Ar and O_2/Ar-atmospheres ($p_{H2O}=p_{O2}$=0.2 bar) at temperatures up to 1673 K. The onset of oxidation is at approximately the same temperature in both atmospheres. However, the higher mass gain was observed in steam-containing atmosphere. The measured mass change is a superimposition of two effects: mass gain by the oxidation of ZrB_2 and mass loss by volatilization of the liquid boria. Quantitative mass spectrometric analysis of H_2, as a side product of ZrB_2 oxidation in steam, allowed to separate the oxidation and volatilization reactions. Oxidation kinetics of ZrB_2 are complex and shows a strong temperature dependence changing from linear kinetics at 1073 K to sub-parabolic kinetics at 1673 K. Thermodynamic equilibrium calculations reveal the partial pressures of boron-containing gas species in O_2- and H_2O-containing atmospheres. The dominant gas species are $BO_2(g)$ (T<1493 K) and $B_2O_3(g)$ (T>1493 K) as well as orthoboric acid $H_3BO_3(g)$ (T<1179 K) and metaboric acid $HBO_2(g)$ (T>1179 K), respectively. Partial pressures are higher in H_2O-containing atmosphere. Mass spectrometric analysis of ZrB_2 oxidation in H_2O-containing atmosphere confirmed the formation of $H_3BO_3^+$, $H_2BO_3^+$, $H_2BO_2^+$, HBO_2^+ and BO_2^+ species.

The oxidation behavior of a ZrB_2-containing CMC (ZrB_2-SiC/Si-C-N) was investigated in flowing O_2- and H_2O-containing atmospheres at temperatures up to 1673 K. Similar to pure ZrB_2, the total mass change of the ZrB_2-SiC/Si-C-N CMC results from the superposition of mass gain by oxidation and mass loss by volatilization of boria. Quantitative mass spectrometric analysis of H_2, as a by-product of the oxidation reaction steam, allowed separation of the oxidation reaction from volatilization effects. From temperatures above about 1200 K, the volatilization becomes clearly noticeable. Thermodynamic calculations showed that boron-containing gas species are mainly responsible for volatilization in both O_2- and H_2O-containing atmospheres. Partial pressures of boron-containing gas species are several orders of magnitude higher than those of the silicon-containing gas species. The ZrB_2-SiC/Si-C-N CMC showed the intended formation of a liquid borosilicate melt and oxidation stopped in ZrB_2-rich cavities. This showed that the ZrB_2-additive might be able to improve the oxidation resistance of the CMC by sealing cracks upon oxidation and thereby slowing down the inward diffusion of oxidizing gas species, especially at lower temperatures where SiO_2 formation kinetics are slow.

In all sections, the combination of CALPHAD calculations and high-temperature experiments provided an excellent complementary method to elucidate the involved mechanisms.

1. Introduction

1.1. Ceramic matrix composites

Ceramic matrix composites (CMC) are a class of materials characterized by the application of long ceramic fibers embedded in a ceramic matrix. CMC are typically denominated by the utilized ceramic fiber and matrix material, respectively (e.g. C/SiC or C_f/SiC_m).

A basic distinction is made between oxide and non-oxide CMC. Typical oxide CMC are composed of Al_2O_3 fibers in an Al_2O_3 matrix. However, also matrices containing mullite ($x Al_2O_3 \cdot y SiO_2$) or Al_2O_3-YSZ (yttria stabilized zirconia) are technically applied [1]. Besides pure Al_2O_3 fibers, also mullite- or ZrO_2-containing fibers are available [2]. In addition, the synthesis of a number of other oxide fiber types such as mullite, spinel, YAG (yttrium aluminum garnet) and PZT (lead zirconate titanate) was demonstrated [3]. Non-oxide CMC are typically consisting of C or SiC fibers [4] embedded in a matrix consisting of Si [5], SiC [6] or Si-C-N [7]. Also boron-containing Si-(B-)C-N fibers [8][9] and matrix [10] are synthesized. In this context carbon is also considered as ceramic. The present work deals exclusively with non-oxide CMC. Due to covalent bonds, SiC fibers are mechanically more stable and less prone to creep than oxide fibers above 1273 K.

Figure 1.1 shows a SEM (scanning electron microscopy) micrograph of a cross-sectioned SiC/Si-C-N composite. The SiC-fibers are processed in a 2D fabric structure with a 0°/90° orientation of the individual fiber bundles and layers of this fabric stacked on top of each other. Fibers are surrounded by a ceramic Si-C-N matrix.
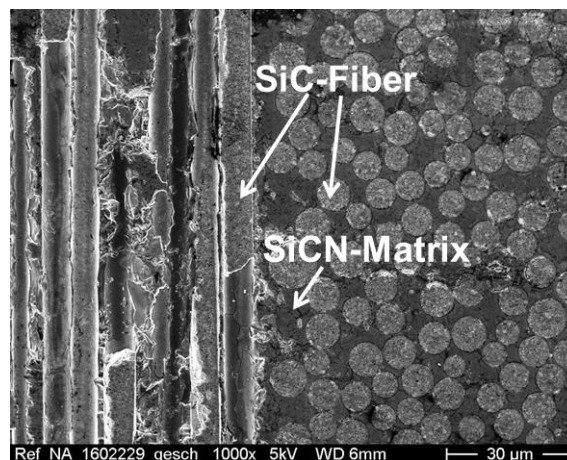
Figure 1.1: SEM micrograph of a cross section of a SiC-fiber reinforced Si-C-N composite.

Monolithic ceramics often show a brittle mode of failure. An improved fracture toughness is achieved by introducing ceramic fibers into the composite. CMC show an high crack propagation resistance resulting in a non-brittle failure mode, improved thermal shock resistance and dynamic cycling toughness.

Figure 1.2 shows the acting strengthening mechanisms in a CMC. These are all based on the consumption of energy, which is then no longer available for opening of the crack [11]:

- detachment of the fiber from the matrix and formation of a new interface
- crack deflection and branching along the fiber
- bridging of cracks by fibers preventing further opening of the crack
- crack shielding by load transfer to a fiber in front of crack tip
- consumption of energy by friction at fiber/matrix interface during fiber pull-out.
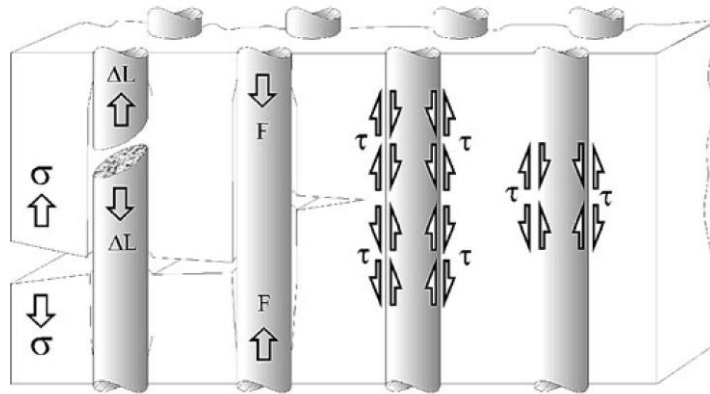
Figure 1.2: Scheme of reinforcement mechanisms acting in CMCs **[11]**.

These mechanisms are all based on a weak fiber-matrix interface which prevents a crack of cutting through the fiber. A Weak Matrix Composite (WMC), inherently has a weak connection due to a porous matrix. Therefore, a crack propagating through the matrix is deflected along the interface. A weak fiber-matrix interface can also be achieved by application of a fiber coating, also called *interphase*, which provides a weak interface in spite of the presence of a stiff matrix [12]. The coating is either conducted as single phase commonly consisting of pyrolytic carbon (PyC) or BN, or as a multilayered coating with SiC interlayers [13].

1.2.   Precursor-derived ceramic matrix

Different methods are used to produce the ceramic matrix of CMC. A fiber preform can be infiltrated either using gaseous precursor molecules (*chemical vapor infiltration*, CVI) or a melt (*liquid silicon infiltration*, LSI) [13]. Both LSI and CVI are suitable to produce CMC with a low residual porosity. However, CVI is very slow, and in LSI the melt can attack the ceramic fibers during infiltration at high temperatures ($T_{m,Si}$ = 1687 K).

The polymer infiltration and pyrolysis (PIP) process combines fast processing time and low processing temperatures compared to CVI and LSI, respectively. This makes the PIP process a comparably gentle processing technique preserving the fiber and fiber coatings, respectively.

The preparation of CMC by the PIP process is outlined in Figure 1.3. Ceramic fibers are processed by modern weaving technologies [14]. The obtained fiber preform can be coated by chemical vapor infiltration (CVI) or a wet-chemical process. The fiber preform is infiltrated with a liquid polymer which is transformed into a solid ceramic matrix by pyrolysis. Thereby hydrogen, as part of the polymers functional groups, is released into the atmosphere as hydrogen-containing gas species (H_2, CH_4, NH_3...) depending on the thermodynamic equilibrium conditions such as composition of the precursor polymer, temperature and nitrogen partial pressure of the atmosphere [15] (see Section 5). By release of the gaseous species and densification of the ceramic during pyrolysis, the ceramic matrix shrinks. To achieve the desired residual porosity < 10 %, the infiltration and subsequent pyrolysis is typically repeated 5 to 10 times.

```
                    ┌─────────────────────┐
                    │      SiC fiber      │
                    └─────────────────────┘
                              ↓
                    ┌─────────────────────┐
                    │   SiC fiber preform │
                    │  0/90° woven fabric │
                    └─────────────────────┘
                              ↓
                    ┌─────────────────────┐
                    │     fiber coating   │
                    │       C, BN,…       │
                    └─────────────────────┘
                              ↓
                    ┌─────────────────────┐
        ┌──────────→│   infiltration with │
        │           │ pre-ceramic polymer │
┌───────────────┐   └─────────────────────┘
│ 5-10 cycles   │             ↓
│ until aspired │   ┌─────────────────────┐
│ porosity      │   │       pyrolysis     │
│ is reached    │   │ pre-ceramic polymer │
└───────────────┘   │ → Si-(B-)C-N ceramic│
        │           └─────────────────────┘
        └──────────────────────┘
                              ↓
                    ┌─────────────────────┐
                    │    post processing  │
                    └─────────────────────┘
```
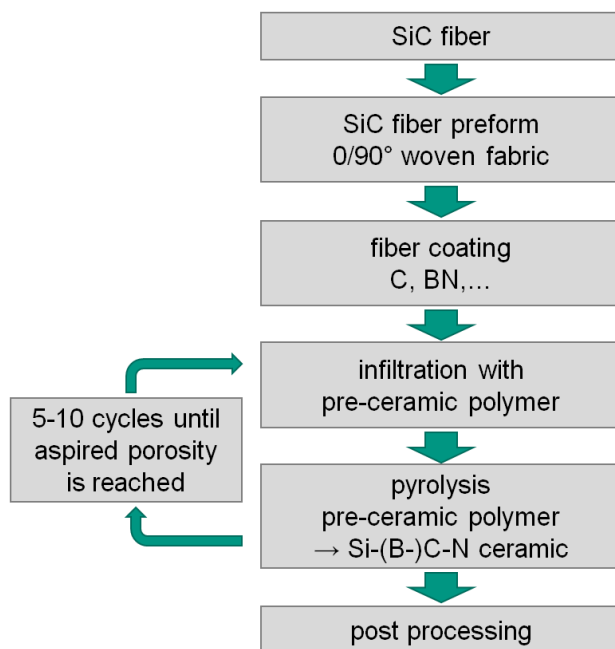
Figure 1.3: Schematic illustration of the PIP process.

Since the elemental constituents are incorporated on an atomic level in the preceramic polymer chain, the composition of the obtained ceramic matrix is extremely homogeneous. By selective synthesis of the polymer, the composition of the precursor-derived ceramic matrix and thereby its properties can be precisely adjusted (see Section 5). Also preceramic polymers containing B [16], Ti [17], Zr [18] or Hf [19] are synthesized. *Ultra high temperature ceramics* (UHTC) nano-composites can be obtained from Hf- or Zr-containing polymers. Polyborosilazanes give boron-containing Si-B-C-N ceramics with improved high-temperature stability [16] and oxidation tolerance [20].

Furthermore, the PIP process offers the opportunity to introduce additives into the matrix using particle-filled precursor polymers. Additives could be passive fillers, which are added to improve the degree of filling and reduce the total number of PIP cycles necessary to manufacture a

dense matrix. Moreover, active fillers with additional functions can be used. Reactive fillers, which undergo a volume expansion, can reduce the residual porosity and compensate the shrinkage or warping of the material [21][22][23]. Boron-containing filler can improve the oxidation resistance of conventional Si-C-N precursor-derived ceramics (see Section 8).

1.3.   High-temperature application of CMC in gas turbines

Due to their low weight, excellent high-temperature resistance and strength CMC are attractive materials for aerospace technology [4][12]. Therefore a number of studies deal with the application of SiC-based CMC in reentry vehicles [24], aircraft propulsion turbines [25][26] and gas turbines for stationary power generation [27][28].

Figure 1.4 shows the temperature stability of materials in aircraft turbines. The maximum allowable material temperature of nickel base superalloys is shown in black color. This is increasing with the development and introduction of directional solidified (DS) and single crystal (SX) alloys. The maximum operation temperature of metallic nickel-based superalloys is below 1000 °C. By using film cooling, thermal barrier coatings (TBC) and closed-loop cooling, the maximum allowable gas temperature can be increased accordingly. Compared to nickel-based superalloys, CMC inherently have a significantly higher temperature resistance. Therefore, the maximum gas temperature is above 1300 °C or 1500 °C with film cooling.
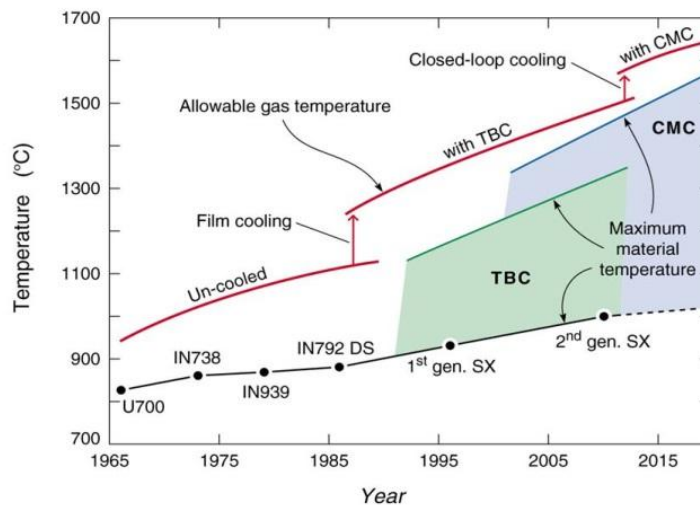
Figure 1.4: High-temperature stability of materials in aircraft turbines **[29]**.

Due to higher operating temperatures, the use of CMC in aircraft turbines can increase the fuel efficiency [30]. GE expects 10% better fuel efficiency and 25% more trust [31]. In addition to their superior high-temperature properties, CMC also have a 66 % lower density compared to nickel-based superalloys. This allows weight savings which are attractive in aviation [30][31].

Today CMC are already used in GE's LEAP engines as shrouds [32]. GE also demonstrated the function of CMC turbine blades [33].

Figure 1.5 shows a schematic illustration of the oxidation and volatilization processes acting on Si-based CMC in steam containing combustion atmosphere. Combustion atmosphere in conventional gas turbines and aero engines contains a number of oxidizing components such as O_2, CO_2, CO and H_2O [34]. These contribute to different degrees to the oxidation of Si-based CMC and the formation of SiO_2 under combustion conditions [25]. Water vapor plays a special role in this process. Besides its strong oxidizing effect [26], steam also causes the volatilization of SiO_2 by formation of gaseous silicon hydroxides such as $Si(OH)_4$ and $SiO(OH)_2$ [26][35][36]. Robinson and Smialek found SiC recession rates in the range of 0.2-2 μm/h under simulated gas turbine combustor conditions at 1200-1400 °C [25].
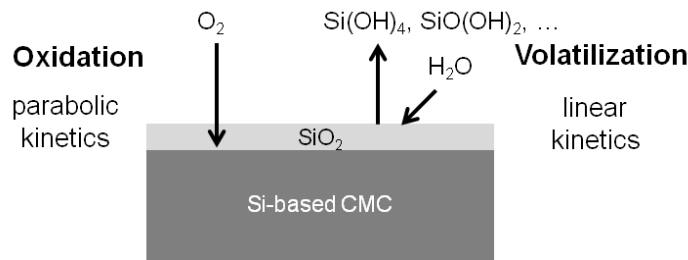
Figure 1.5: Schematic illustration of the oxidation and volatilization of Si-based CMC.

Various models have been published in literature to describe the oxidation and volatilization behavior of CMC. In general, the mass change per unit area $\Delta w/A$ can be described as:

$$\frac{\Delta w}{A} = k \cdot t^n \tag{1.1}$$

with the kinetic rate constant k, time t and the exponent n. Pure parabolic and linear kinetics result in $n=1/2$ and $n=1$, respectively.

Oxidation is controlled by the diffusion of oxidizing species through the growing oxide layer (e.g. SiO_2) to the oxide/CMC interface and therefore follows parabolic kinetics. Volatilization is controlled by the diffusion of gaseous volatilizations products from the oxide/gas interface into the combustion atmosphere and therefore shows linear kinetics. As a consequence, an overall paralinear behavior is observed [37]. Other authors consider oxidation and volatilization in two separate terms or include the partial pressures of the formed volatile gas species [36][37] [38].

Environmental barrier coatings (EBC) were developed to protect non-oxide CMC from oxidation and volatilization. The gas tight coating protects the underlying CMC and is not attacked by the steam-containing combustion gas due to its low SiO_2 activity. Various materials have been investigated as potential CMC [39][40][41]. Rare earth silicates, especially yttrium silicates (Y_2SiO_5, $Y_2Si_2O_7$) [42] and Ytterbium silicates (Yb_2SiO_5, $Yb_2Si_2O_7$) [43] have been of particular interest. In contrast to thermal barrier coatings, protection against high temperatures plays a

secondary role due to the inherent high temperature stability of CMC. However, chemical compatibility with the CMC and similar coefficient of thermal expansion (CTE) are important for good durability and thermal shock resistance [24]. Additional bond coatings are used to improve adhesion of the EBC on the CMC or gas tightness, respectively, see Figure 1.6.

Other concepts for improved oxidation protection of Si-based CMC use boron-containing components. By formation of a boro-silicate glass (T_E= 713 K [44]) cracks are closed and the inward-diffusion of oxidizing gas species is slowed down. The protective effect was demonstrated for BN fiber coatings [45], bulk ZrB_2-SiC and HfB_2-SiC ultra-high-temperature ceramics (UHTC) [46][47] and Si-B-C-N precursor-derived ceramics [20]. Figure 1.6 shows the use of a boron-containing filler in precursor-derived Si-C-N ceramics as alternative to polyborosilazanes containing boron in the precursor polymer chain [48][49]. Figure 1.6 shows schematically a CMC material system with combined oxidation protection consisting of EBC, fiber coating and functional additives.
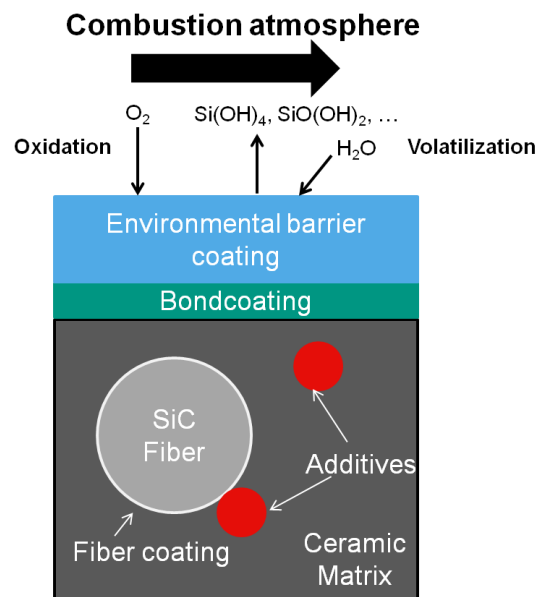
Figure 1.6: Scheme of combined oxidation protection of a Si-based CMC with EBC, fiber coating and functional additives.

The aim of this work is to investigate the behavior of the individual components of the Si-based CMC and their interaction under combustion conditions i.e. at high temperatures and in O_2- and H_2O-containing atmospheres.

Already during pyrolysis of preceramic polymers, reactions take place which influence the composition and microstructure of the obtained Si-(B-)C-N ceramic matrix. From the study and understanding of this process, suitable pyrolysis conditions for the preparation of precursor-derived Si-(B-)C-N ceramic are to be derived. Also reactions that intrinsically limit the high-temperature stability of the obtained Si-(B-)C-N ceramics must be identified. The dependence of these reactions on the composition of the ceramic as well as the atmosphere must be understood.

Additions of ZrB_2, as a boron-containing additive, might improve the oxidation resistance of the CMC. To obtain a ZrB_2-containing ceramic matrix, mixtures of liquid preceramic polymers and ZrB_2-powder can be pyrolyzed. This requires suitable pyrolysis conditions to avoid reactions of the ZrB_2-additive with the preceramic polymer, gaseous pyrolysis products or the applied pyrolysis atmosphere. In addition, the chemical compatibility of the ZrB_2-additive with the obtained ceramic matrix must be given. Possible high-temperature reactions that could limit the maximum operating temperature of the CMC must be identified.

Little is known about the high-temperature oxidation behavior of ZrB_2 in H_2O-containing atmospheres. In addition, also volatilization by formation of gaseous species plays an important role. The separation of both effects is not possible by thermogravimetry alone. Therefore, a combined approach using additional qualitative and quantitative mass spectrometric analysis is used in this work to separate oxidation and volatilization reactions.

Finally, samples of ZrB_2-containing SiC/Si-C-N CMC are exposed to prototypical combustion atmospheres. Their oxidation behavior is compared to ZrB_2-free SiC/Si-C-N CMC to evaluate the influence of the ZrB_2-additive on the oxidation behavior of Si-containing CMC.

An approach combining CALPHAD calculations and high-temperature experiments is used to investigate all these aspects concerning the HT-stability and oxidation resistance of the Si-based CMC.

2. Fundamentals of the CALPHAD-method

2.1. Introduction

The CALPHAD-method goes back to the idea of calculating phase equilibria from thermodynamics. Formerly, CALPHAD was the abbreviation of *CALculation of PHAse Diagrams*. Nowadays *Computer Coupling of Phase Diagrams and Thermochemistry* is used as a more accurate designation.

In 1908, van Laar demonstrated that the form of *T-x* phase diagrams can be derived from functions representing the temperature and composition dependence of the Gibbs energy of the particular phases [50]. Johanssons work in 1937, which derived thermodynamic properties by analyzing part of the Fe-C system [51], is considered today as "the *first modern CALPHAD assessment*" [52]. In the 1950s, calculation of phase equilibria was applied to systems of technological importance. Kaufman and Cohen investigated the martensitic transformation in the Fe-Ni system [53] and Meijering investigated the system Ni-Cr-Cu [54]. The actual coinage and distribution of the CALPHAD method was then made by Kaufman und Bernsteins book *Computer Calculation of Phase Diagrams* in 1970 [55].

The workflow of the CALPHAD-method is schematically depicted in Figure 2.1. The foundation of the CALPHAD method is the analytical description of the Gibbs free energy of all phases, species and elements in the considered system with thermodynamic models. Thereby, the dependence on temperature, composition and pressure is considered. Models are based on physical, chemical and crystallographic properties of the phases such as crystal structure, chemical bond type, order/disorder or phase transitions. However, also purely mathematical approximations by polynomial functions, of grade *i*, are used, which are able to describe the correct course of the thermodynamic data. However, these parameters do not possess a physical meaning. In both cases, the models contain adjustable parameters, which are determined using thermodynamic data from experiments, ab-initio calculations and, if no other satisfactory data are available, estimates. This process of adjusting parameters by least squares method is called thermodynamic optimization. The obtained functions, representing the analytical description of the Gibbs free energy, are stored in databases. Using appropriate software like Thermo-Calc [56] phase equilibria are calculated for prescribed boundary conditions. From this, phase and property diagrams are drawn and thermodynamic quantities are calculated even for multicomponent systems. These data can also be used as input for kinetic models.
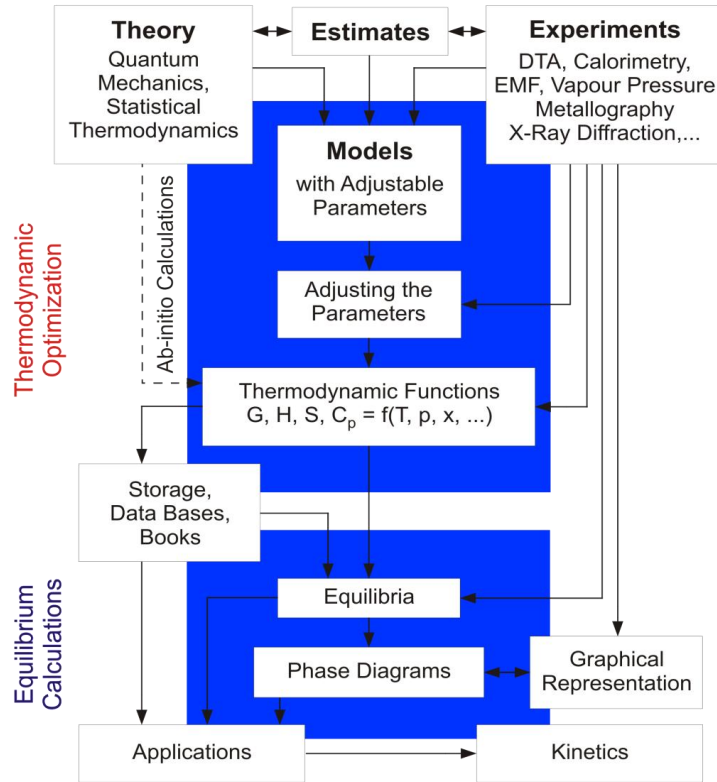
Figure 2.1: Schematic description of the CALPHAD method **[57]**.

The evaluation of these data gives important information for the materials application:

- Design of new materials
- Limitations for applicability
- Identification of underlying heterogeneous reactions between the components and with the atmosphere.

A great advantage of the CALPHAD method is that with the obtained Gibbs free energy descriptions, extrapolations into experimentally unexplored (*T, p, x*) or metastable regions are possible. Not the whole system has to be assessed experimentally, but few key experiments are sufficient to validate the calculations.

In this chapter, an introduction into the CALPHAD method and into the underlying models for description of the phases is given.

2.2.   Analytical description of the Gibbs free energy

It is essential for the CALPHAD-method that the Gibbs free energy (G) functions for all stable and metastable phases of the regarded system are known. This function must be able to describe the dependence of G on the temperature, pressure, and for solution phases also on the composition. In general, the Gibbs free energy function of a phase Φ is given by:

$$G_\Phi(T) - H^{\mathrm{SER}} = \left(G_\Phi^{\mathrm{ref}} - H^{\mathrm{SER}}\right) + G_\Phi^{\mathrm{id}} + G_\Phi^{\mathrm{ex}}$$

(2.1)

consisting of three terms: the reference state G_Φ^{ref}, the ideal mixing entropy G_Φ^{id} and the excess enthalpy G_Φ^{ex}. The first term describes a "mechanical" mixture of the components. As G can't be calculated as an absolute value, it is given as the difference to a reference state H^{SER}, which is defined as the sum of the enthalpies of the pure chemical elements $i = A$, B in its stable state under standard conditions (**S**tandard **E**lement **R**eference; SER). The second term, the ideal mixing- or configurational entropy S^{id}, describes an ideal mixture without interactions between the components (or species) of the system. Only the entropic contribution is considered, which can be calculated as an absolute value and does therefore not require an reference state. The third term is the excess free enthalpy and describes additionally the interactions between the components.

Concentration dependence

For solution phases, the concentration dependence of the free energy function needs to be considered. The Gibbs free energy of the reference state is given by the sum of the individual element contributions G_i^0 according to their mole fractions x_i:

$$G_\Phi^{\mathrm{ref}} = \sum_{i=1} x_i \cdot G_i^0(T)$$

(2.2)

The concentration dependence of the ideal mixture is defined as:

$$G_\Phi^{\mathrm{id}} = -TS^{\mathrm{id}} = RT \sum_{i=1} x_i \ln x_i$$

(2.3)

The excess term describes the interactions of the components. For ideal solutions this term is zero. For real solutions the contribution of the interatomic interactions needs to be considered. Mixing and demixing tendencies can thereby be expressed by an interaction parameter Ω:

$$G_\Phi^{\mathrm{ex}} = H_{\mathrm{mix}} = \Omega x_A x_B$$

(2.4)

For binary non-symmetrical solutions the mixing enthalpy can be expressed as:

$$G_\Phi^{ex} = x_i x_j \sum_{v=0} {}^v L_{ij}(T) \cdot \left(x_i - x_j\right)^v \tag{2.5}$$

with the Redlich-Kister parameter ${}^v L_{ij}$ [58].

Temperature dependence

The temperature dependence of the Gibbs free energy description of a phase Φ is usually described by a power series above the Debye temperature:

$$G_\Phi(T) - \sum_i b_i H_i^{SER} = a_0 + a_1 T + a_2 T \ln T + a_3 T^2 + a_4 T^{-1} + a_5 T^3 + \cdots \tag{2.6}$$

with $\sum_i b_i H_i^{SER}$ the sum of the enthalpies of the elements i in their reference state weighted by their fraction b_i in Φ. Typically such equations are derived for certain temperature ranges to improve the accuracy of the Gibbs free energy description. The coefficients a_0 and a_1 are expressions for $H(T_0)$ and $S(T_0)$. a_2 and higher terms describe the heat capacity $C_p = -T \left(\frac{\partial^2 G}{\partial T^2}\right)$.

Pressure dependence and the gas phase

At moderate pressures which apply under synthesis and application conditions, the pressure dependence of the Gibbs Free energy is usually negligible for condensed phases. Only for very high pressures models considering the pressure dependence need to be applied [59][60][61][62]. However, for the gas phase, which is usually modeled as an ideal gas, the pressure gives an important contribution to the Gibbs free energy description which is considered by adding the term $RT\ln(p/p_0)$, with the total pressure p_0.

Hence, for every individual constituent i (e.g. N_2, O_2, Ar,…) of the gas phase an equation can be formulated:

$$^0 G_i^{gas}(p,T) = G_i(T) + RT \ln \frac{p}{p_0} \tag{2.7}$$

The descriptions of the constituents are summed up according to their fraction y_i, resulting in an overall description of the gas phase:

$$G_m^{gas} = \sum_i y_i \left[{}^0 G_i^{gas} - \sum_j b_{ij} H_j^{SER} + RT \ln(y_i) \right] + RT \ln \left(\frac{p}{p_0}\right) \tag{2.8}$$

with the constituent's fraction y_i being the partial pressure referred to the total pressure.

Only at very high pressures, the pressure is replaced by the fugacity f to describe non-ideal behavior of the gas phase [63].

2.3. Model description of the melt

The thermodynamic description of the melt is of special interest in high temperature applications. In multicomponent materials, eutectic reactions can drastically lower the application temperatures.

In literature, different authors prefer different models for the thermodynamic description of their systems. Therefore, upon building up a multicomponent database from literature data the compatibility of these data is of great importance. In general, melt constituents can be converted into each other [63]. However, problems can occur in systems containing neutral components (see further: Zr-C and Zr-N in Section 4.1.2.1).

The two mostly used models, for thermodynamic description of the melt, are described below.

2.3.1. Substitutional-solution model

The substitutional-solution model describes melts in form of substitutional solution of the elements $i = A$, B and C. This model is widely applied to describe metallic melts and is written as:

$$(A, B, C) \tag{2.9}$$

and can be described by the Redlich-Kister formalism (eqn. (2.5)). Commonly, the temperature dependence of the interaction parameter $^{v}L_{ij}$ for a binary system i-j is described by a linear relation:

$$^{v}L_{ij} = {}^{v}a_{ij} + {}^{v}b_{ij}T \tag{2.10}$$

with $^{v}a_{ij}$ describing the compositional dependence of the excess enthalpy and the excess entropy $^{v}b_{ij}$.

In cases where liquids show a tendency for short-range ordering in form of molecular-like associates or salt melts consisting of charged liquid constituents more sophisticated models like the *associate solution model* [64] and the *partially ionic liquid model* are applied, respectively.

2.3.2. Partially ionic two-sublattice liquid model

This model was originally developed to describe salts which possess highly ordered structures with cations and anions occupying particular lattice sites forming an own sublattice each. Temkin [65] developed a model for the configurational entropy of salt mixtures by assuming that ionic substances have a large tendency for chemical ordering even in the melt. Therefore, ions are practically only surrounded by the counter-ion. This short-range order is considered as two sublattices in the liquid. Based on this work, Hillert and Staffansson formulated a regular solution model for ionic melts and introduced vacancies as an additional component in one sublattice [66][67]. By introducing hypothetically vacancies with an induced charge and neutral species the model was extended to be able to describe also multicomponent melts with different valences of the components [68]. To maintain electro-neutrality, the hypothetical vacancies carry an induced charge equal to the average charge of the species occupying the cation sublattice.

For liquids this model does not possess a physical meaning. Because there is no long-range ordering in liquids, there are also no separate anion and cation lattice sites. However mathematically, this model describes well the thermodynamic properties of liquids, even for purely metallic liquids, partly ionic character and solution of non-metals. Also associates, which can form in the melt by short-range ordering (e.g. SiO_4^{4-}), can be described by assigning them to one of the sublattices according to their charge.

The model is described as:

$$\left(C_i^{v_i+}\right)_P \left(A_j^{v_j-}, Va^{-Q}, B_k^0\right)_Q \tag{2.11}$$

where two sublattices are either occupied by positively charged cations $C_i^{v_i+}$ or by negatively charged anions $A_j^{v_j-}$, vacancies Va^{-Q}, with a hypothetically induced negative charge, and neutral species B_k^0; v_j and v_i are the (different) charges of the ions. P and Q are stoichiometric numbers describing the number of sites on the particular sublattice. Illustratively P and Q are derived from the average charge of the other sublattice:

$$P = \sum_j \left(-v_j y_{A_j}\right) + Q y_{Va} \tag{2.12}$$

$$Q = \sum_i \left(-v_i y_{C_i}\right) \tag{2.13}$$

with y_i denoting the fraction of constituent i. Therefore, P and Q are composition-dependent. To maintain electro-neutrality, vacancies have the induced charge Q. For obvious reasons, neutral species B_k^0 are not contributing to P and Q.

2.4. Thermodynamic equilibrium

The general equilibrium condition is fulfilled if the chemical potential of a component i is equal in all phases $\Phi = ', '', '''$.

$$\mu_i' = \mu_i'' = \mu_i''' = \cdots \tag{2.14}$$

The thermodynamic description of a total system requires the analytical descriptions of the molar Gibbs energy of all relevant phases Φ. These are summed up weighted by their amounts n^Φ or fractions:

$$G = \sum_\Phi n^\Phi G_m^\Phi = \text{minimum} \tag{2.15}$$

The thermodynamic equilibrium state of a total system is defined by its energetic minimum at constant T, p and x_i^0:

$$\left(\frac{\partial G}{\partial x_i}\right)_{x_i^0, T, p} = 0 \tag{2.16}$$

A constant x_i^0 ensures mass conservation, i.e. no mass is transported into or out of the system. Equilibrium calculation can be performed by an iteration algorithm using appropriate software. If several minima fulfill this equilibrium condition, the most negative or global minimum is called stable equilibrium. Other local minima are metastable equilibria.

From the calculated equilibrium state, thermodynamic properties and compositions are obtained for all components, species or phases.

2.5. Thermodynamic optimization

The thermodynamic optimization is the process of adjusting the unknown coefficients (a_0, a_1, ...) of the analytical description of the Gibbs free energy function (eqn. (2.6)) to all available data. These can originate from experimental determination of thermodynamic properties, ab-initio calculations or estimates. The resulting thermodynamic description should reproduce the input data as good as possible.

The least-square method by Gauss is used to determine the best fit of parameters in a way that the error between the result of the optimization and the measured value is as small as possible [63].

A set of g measured (or calculated) values W_i is expressed by functions F_i by a set of h unknown coefficients C_j with x_{ki} independent variables (measurement i with variable k: T, p, concentration,…):

$$W_i = F_i(C_j, x_{ki})$$

(2.17)

with $i = 1, ..., g$ and $j = 1, ..., h$.

The error E_i is defined as difference between the calculated F_i and the measured value L_i, weighted by w_i:

$$\left(F_i(C_j, x_{ki}) - L_i\right) \cdot w_i = E_i$$

(2.18)

In case that $g > h$ it is not possible to find a set of coefficients C_j for which the calculated value W_i is equal to the measured value L_i. Then the best set of coefficients C_j is the one with the smallest sum of the squared error:

$$\sum_{i=1}^{g} E_i^2 = \text{minimum}$$

(2.19)

From this condition, h equations are found with respect to the C_j coefficients:

$$\frac{\partial}{\partial C_j} \sum_{i=1}^{g} E_i^2 = 0$$

(2.20)

To solve this set of equations a Taylor series expansion of E_i according to Gauss is used, which is terminated after the linear term with the correction term ΔC_l for C_l.

$$E_i(C_j, x_{ki}) \approx E_i^0(C_j^0, x_{ki}) + \sum_{l=1}^{h} \frac{\partial E_i}{\partial C_l} \cdot \Delta C_l$$

(2.21)

This system of equations is solved iteratively by calculating ΔC_l for a start value C_j^0. The start value is then corrected by ΔC_l and the procedure is repeated until the deviation is below a predefined value. The mean square error thereby determines the statistical deviation between the measured values and the determined values calculated from the set of coefficients C_j:

$$\text{mean square error} = \sum_{i=1}^{g} \frac{E_i^2}{g - h}$$

(2.22)

The weighting factor w_i in eq. (2.18) can be taken as reciprocal of the estimated accuracy ΔL_i of the measured values and may also include the limited accuracy of the independent variables x_{ki} to take into account differences of the errors in different experimental methods [69].

2.6.   Graphical representation of heterogeneous reactions

For graphical representation of the equilibrium state of materials phase and property diagrams are drawn under consideration of a number of variables. Pelton and Schmalzried developed a classification of phase diagrams according to extensive and intensive variables [70]. Extensive variables are depending on the size of the system (x, m, n, S, G, H, V). In contrast to that, intensive variables are independent of the size of the system (μ, T, p, c). Thereof three types of phase diagrams are distinguishable:

- First order diagrams are plots with axes of two intensive variables (p-T, μ-T and μ_i-μ_j diagrams).
- Second order diagrams are plots with axes of an intensive and an extensive variable (T-x, p_{O2}- or p_{N2}-x diagrams).
- Third order diagrams are plots with axes of two extensive variables (isothermal sections x_i-x_j plots of ternary systems, G-x plots).

Property diagrams express a quantity as a function of another for example the phase fraction or the composition of a phase as a function of the temperature. In contrast, phase diagrams have independent quantities on the axes. The phase diagram shows therefore the equilibrium state of the system, i.e. phases which are in equilibrium.

In this work different types of phase and property diagrams were drawn. These are utilized as roadmaps for materials development and enable to identify and understand reactions which are critical for the production process of the ceramic matrix composites or are determining the application limits. For example, the pyrolysis of preceramic polymers, maximum application temperatures or oxidation and corrosion processes were determined by application of the CALPHAD-method.

3. Experimental methods

This chapter covers the types of samples investigated in this work and also the applied characterization techniques.

3.1.   Sample preparation

Various types of samples were used in this work depending on the case of investigation.

Si-(B-)C-N were obtained by pyrolysis of liquid preceramic polymers in flowing Ar- or Ar/N$_2$-atmospheres (p$_{N2}$ = 0.5 bar), respectively, using a Netzsch STA 449 F3 Jupiter. To ensure crosslinking and outgassing of the polymer, samples were first subsequently heated to 573 K. Samples were then heated with 5 K/min from 573 K to the final pyrolysis temperature (1273 K-1773 K), which was held for 5 h, and cooled down to room temperature with 20 K/min.

Interactions and phase equilibria of ZrB$_2$ with Si-C-N and nitrogen-containing atmosphere (Section 6) were investigated with mixtures of ZrB$_2$ powder (average grain size 3.2 µm, H.C. Starck) and Ceraset$^®$ PSZ 20. Both, ZrB$_2$-powder and preceramic polymers were provided by Clariant SE in the framework of the BMBF project NewAccess. Homogenization of the ZrB$_2$-PSZ 20 mixture was performed by thorough stirring. Subsequently the mixture was pyrolysed in an STA in flowing Ar- or Ar/N$_2$-atmospheres (p$_{N2}$ = 0.5 bar) using alumina crucibles.

The high temperature oxidation behavior of ZrB$_2$ was investigated using cylindrical samples (Ø = 5 mm, approx. height = 2 mm) obtained by uniaxial pressing of powders with a pressure of 130 MPa for 5 min. Subsequently, samples were sealed in a plastic foil and further compacted by cold isostatic pressing at a pressure of 497 MPa for 3 min. The obtained samples were not sintered because of the high oxidation susceptibility of ZrN and ZrB$_2$. Isothermal nitriding experiments were performed using uncompacted ZrB$_2$ powder in flowing Ar/N$_2$-atmospheres (p$_{N2}$ = 0.5 bar).

The high temperature oxidation behavior was investigated using fully prepared CMC samples with a dimension of 3x10x10 mm^3 manufactured and provided by the German Aerospace Center (DLR), Institute of Structures and Design in the framework of the BMBF-project NewAccess. A SiC-fiber reinforced Si-C-N CMC (SiC/Si-C-N) was obtained by a PIP process infiltrating a Tyranno SA3 SiC fiber preform with Ceraset$^®$ PSZ 20. Details are described in [7]. A second batch of CMC samples containing a ZrB$_2$-additive (ZrB$_2$-SiC/Si-C-N) was also provided by the DLR. The ZrB$_2$-additive was introduced into the CMC by using a mixture of Ceraset$^®$ PSZ 20 and ZrB$_2$-powder in a first laminating step of the SiC fiber-preform. All following PIP cycles were performed with pure Ceraset$^®$ PSZ 20.

3.2. Simultaneous Thermal Analysis (STA)

Simultaneous thermal analysis is a combination of thermogravimetric analysis (TGA) and differential thermal analysis (DTA). The combination of both methods offers the possibility to analyze temperature-dependent effects like decomposition or phase transformations. In this work, STA was mostly applied in the TGA-mode to investigate the pyrolysis of preceramic polymers (Section 5), high-temperature reactions (Section 6) and the oxidation behavior of ceramic composites in O_2- and H_2O-containing atmospheres (Section 8). DTA-mode was used in addition to investigate heat-effects resulting from pyrolysis and high-temperature reactions.

To this end different STA-systems were used:

The Netzsch STA 449 F3 Jupiter, equipped with two furnaces, was used in combination with the mass-spectrometer Netzsch QMS 403C Aeolos (see Section 3.4). The setup with the "SiC-furnace", equipped with SiC-heating elements, allowed experiments in dry atmosphere up to maximum temperatures 1873 K. Therein gas is introduced at the bottom of the cylindrical furnace, passing the sample upwards (see Figure 3.1a). The "steam-furnace", equipped with Kanthal-heating elements, allowed experiments in steam-containing atmosphere up to maximum temperatures of 1523 K. To avoid damage of the balance by condensation of steam, the steam-furnace obeys a more complex geometry (see Figure 3.1b). Pure steam, or mixtures with other gases, is introduced into the outer mantle of the furnace, passing the sample from the top. A counter-flow of Ar through an alumina attachment at the outlet of the balance case prevents ingress of steam-containing atmosphere into the balance case. However, the protective Ar-gas flow does not reach the sample. Therefore, experiments in pure steam are possible. After passing the sample, the steam-containing atmosphere is leaving the furnace, together with the protective Ar gas, at the bottom of the inner tube. The steam generator by *aDROP* produced a continuous steam-flow in the range of 0.4-20 g/h without application of a carrier gas. All gas transfer lines and valves were heated to temperatures above 373 K to avoid condensation. Steam-flow was first allowed to equilibrate before starting the experiment by redirecting the gas to the STA with a manual valve. Both furnaces were controlled by Type-S thermocouples. Temperature calibration was performed measuring the melting point of Al, Ag, Au and Ni.
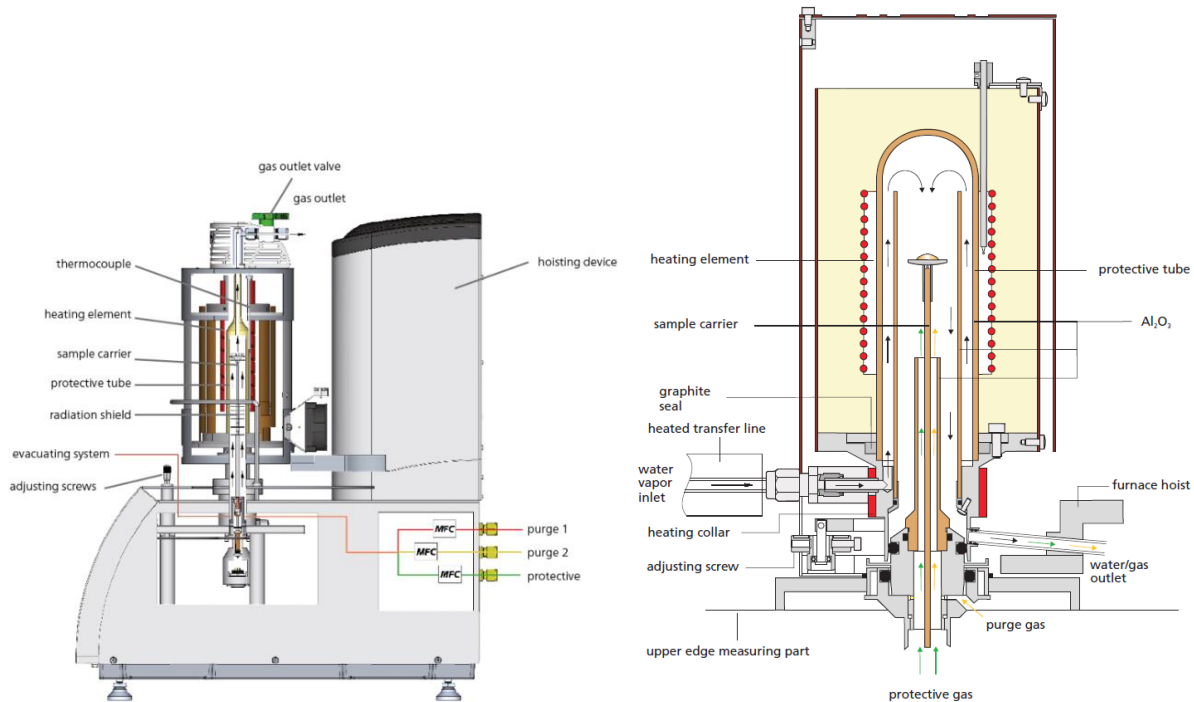
Figure 3.1: Experimental setup of the a) Netzsch STA 449 F3 Jupiter equipped with the SiC-furnace and b) detail view of the steam-furnace **[71]**.

In addition a Netzsch STA 409, equipped with a steam-furnace and an *aDROP* steam generator, was used for oxidation experiments in steam. This STA was coupled with a *Balzers GAM 300* mass spectrometer (see Section 3.4), which allowed quantitative analysis of gaseous reaction and oxidation products.

3.3.   Oxidation tests at very high temperatures

Oxidation tests in steam at temperatures above the capability of the STA 449 and STA 409 (1523 K, see Section 3.2) were conducted in the BOX-furnace. This furnace consists of a horizontal alumina tube equipped with molybdenum-heaters allowing maximum temperatures of 1873 K in steam. Steam-generation was controlled by a *LIQUI-FLOW* and a *controlled evaporator-mixer* by Bronkhorst. Detailed description of the BOX-facility can be found in Steinbrück et al. [72].

In this work, the BOX-furnace was used for oxidation experiments of ZrB_2 in steam. Mass-change upon oxidation and volatilization was determined by weighting the samples before and after the experiment with a laboratory balance. For quantitative analysis of gaseous oxidation- and volatilization products, the BOX was coupled with a *Balzers GAM 300* mass spectrometer (see Section 3.4).

3.4. Mass Spectrometry (MS)

Mass spectrometry was applied for on-line analysis of gaseous pyrolysis-, reaction-, oxidation- and volatilization products during high-temperature experiments.

A *Netzsch QMS 403C Aëolos* was used for semi-quantitative analysis, coupled with the off-gas line of a Netzsch STA 449 F3 Jupiter (see Section 3.2). With this setup, gaseous pyrolysis and decomposition products of precursor-derived ceramics were measured during thermal curing, pyrolysis and high-temperature annealing. Additionally, a *Balzers GAM 300* quadrupole mass spectrometer coupled to the off-gas of the BOX-furnace (Section 3.3) and the *Netzsch STA 409* (Section 3.2) was used for quantitative analysis. With this device, the H_2-release rate during oxidation of ZrB_2 and CMCs in steam was measured to quantify the oxidation process. Furthermore, volatilization products of B_2O_3-containing oxide scales, such as boron-hydroxides, were monitored. Both mass spectrometers were calibrated using certified calibration gases and steam/Ar-mixtures of defined composition, respectively.

This set-up allowed the investigation of high-temperature reactions and oxidation processes simultaneously by a combination of TGA, DTA and mass spectrometry.

Volumetric flow rates $\dot{V}$ of gas species like H_2 were calculated using the known flow rates of Ar as reference:

$$\dot{V}_{H_2} = \frac{c_{H_2}}{c_{Ar}} \cdot \dot{V}_{Ar}$$

(3.1)

with the volumetric flowrates $\dot{V}_{H_2}$ and $\dot{V}_{Ar}$ of H_2 and Ar, respectively. c_{H_2} and c_{Ar} are the measured concentrations of H_2 and Ar.

3.5. X-Ray Diffraction (XRD)

X-ray diffraction is one of the most important non-destructive characterization techniques in materials science providing information about phase constitution, texture and stresses [73].

X-rays are high-energy electromagnetic waves with a wavelength in the range of 10^{-3}-10 nm. These interact with the electrons of the sample atoms and are scattered at the periodic atomic lattice. For constructive interference, Bragg's law relates the lattice plane spacing d^{hkl} and the diffraction angle Θ^{hkl} with the wavelength λ and the diffraction order n.

$$n\lambda = 2d^{hkl} \sin \Theta^{hkl}$$

(3.2)

XRD measurements were carried out on massive samples (CMCs) or powders obtained by grinding the Si-(B-)C-N ceramics in an agate mortar. A Seifert PAD II powder diffractometer was used in Bragg-Brentano geometry using monochromatic Cu-Kα radiation (λ = 0.15418 nm).

Diffraction patterns were recorded in the diffraction-angle range 10° < 2Θ < 90° with a step size of 0.01° and a holding time of 360s per step.

3.6.   Scanning Electron Microscopy (SEM)

Scanning electron microscopy allows to investigate the microstructure of a sample surface beyond the resolution of an optical microscope. In addition, information about the elemental composition of the sample can be obtained.

A focused electron beam is scanned over the sample surface. The incident primary electron beam interacts in various ways with electrons of the sample. Secondary electrons (SE) are generated in the sample and have a low energy compared to the primary electron beam. Therefore, SE are emitted from a surface-near sample volume and allow to image the surface topology with a high resolution. Back-scattered electrons (BSE) of the primary beam underwent elastic scattering in the sample. Since elastic scattering depends on the atomic mass of an element, BSE provides a material contrast. Both SE and BSE are commonly used for imaging.

In addition, the high-energetic primary electron beam is capable to knock-out electrons from the inner electron shells of sample atoms. These vacant shell is filled with electrons from an outer low-energetic shell. The energy difference is emitted as X-rays which are characteristic for the energy difference between the involved electron shells. Energy-dispersive (EDX) or wavelength-dispersive (WDX) X-ray spectroscopy provides information about the elemental composition of the sample.

In this work, a *Philips XL 30 S FEG* was used to image the microstructure of CMCs and polymer-derived ceramics. Images were recorded with an acceleration voltage of 7 kV. To this end samples were embedded in a two-component epoxy. After curing at room temperature, samples were ground, polished and sputter-coated with a thin gold layer to enhance electrical conductivity. The instrument was equipped with an energy-dispersive x-ray detector (*EDX, E2V Scientific Instruments Ltd.*) for quantitative elemental analysis. EDX was used to analyze the elemental composition of high-temperature reaction and oxidation products.

3.7. Chemical Analysis

The chemical composition of precursor-derived Si-(B-)C-N ceramics was analyzed by the group for chemical analytics at the IAM-AWP headed by Dr. T. Bergfeldt. To this end, preceramic polymers were pyrolyzed in flowing Ar or N_2-containing atmosphere at 1473 K and ground in an agate mortar.

Samples were triple determined in the acid-pressure extraction system *DAB2* from Berghof. The elements silicon and boron were then analyzed by ICP-OES in an *OPTIMA 4300DV* from Perkin-Elmer. Carbon was quantified with the C/S-analyzer *CS600* from LECO. Nitrogen and oxygen, as common impurity in Si-(B-)C-N ceramics, were analyzed by carrier gas hot extraction in an *TC600* from LECO.

3.8. Neutron Tomography

The neutron tomography investigations were performed at POLDI facility [74] at the Swiss neutron source SINQ (Paul Scherrer Institute Villigen, Switzerland) using the neutron microscopy setup. The pixel size of 2.7 µm results in a spatial resolution of about 5 µm. The field of view was about 2.5 mm (horizontal) x 5.5 mm (vertical). Two samples with cross sections of about 1 mm^2 were clued on each other to investigate both in one tomography run including 375 projections. The illumination time per frame was 98.6 s. Together with the read-out time a frame repetition time of 100 s was selected. The 3D reconstruction was performed using the *muhrec* software package.

Table 3.1 gives the total microscopic neutron cross section σ_{total} for thermal neutrons. Boron has an about two orders of magnitude higher cross section compared to the other elements in the system. Boron containing parts of the sample attenuate the neutron beam much stronger than boron free parts resulting in strong contrasts of the boron containing locations and the boron free matrix. Therefore, neutron tomography is very powerful to detect the boron distribution.

Table 3.1: Total microscopic neutron cross sections σtotal of zirconium, boron, silicon, carbon and nitrogen **[75]**.

Element (nat. isotope mixing)	Zr	B	Si	C	N
σ_{total} in barn	6.64	772.24	2.34	5.55	13.41

4. Thermodynamic modeling

In this work, computation of phase equilibria was performed using the CALPHAD (CALculation of PHAse Diagram) method [63]; see Section 2 for details. To this end, a multicomponent thermodynamic database was compiled in the system Zr-Si-B-C-N-O-H. Additionally, Ar was added as an inert gas species to establish a stable gas phase under all conditions. Thermodynamic descriptions of the pure elements were taken from the SGTE Unary database PURE v5.1 [76]. The liquid phase was modeled by a partially ionic sublattice model (see Section 2.3.2). Besides thermodynamic descriptions of condensed phases, 178 gas species were considered in the database. Thermodynamic data of the gas species were added from the SGTE substance database SSUB v4.1 [76], unless otherwise stated.

In the following section, thermodynamic descriptions selected from literature and derived by reoptimization are described for the underlying subsystems.

4.1.   The multicomponent system Zr-Si-B-C-N-O-H and subsystems

4.1.1. The system Si-B-C-N

The quaternary system Si-B-C-N is essential to perform thermodynamic equilibrium calculations in non-oxide SiC-based ceramics. Reactions limiting the high-temperature stability of precursor-derived Si-(B-)C-N ceramics are described in Section 5.

The quaternary system Si-B-C-N was thoroughly investigated by Kasper [44]. Thermodynamic data of the binary systems Si-N, Si-B, B-C, B-N and ternary systems B-C-N, B-C-Si, B-N-Si were accepted from Kasper. The binary system Si-C was taken from Gröbner et al. [77]. Gröbner only considers the cubic modification β-SiC since hexagonal α-SiC is considered metastable [77][78]. In this work, the Si-B-C-N system was updated using thermodynamic data for the pure elements and gas species from the SGTE databases PURE v5.1 and SSUB v4.1, respectively.

Figure 4.1 shows the binary phase diagrams in the quaternary system Si-B-C-N.
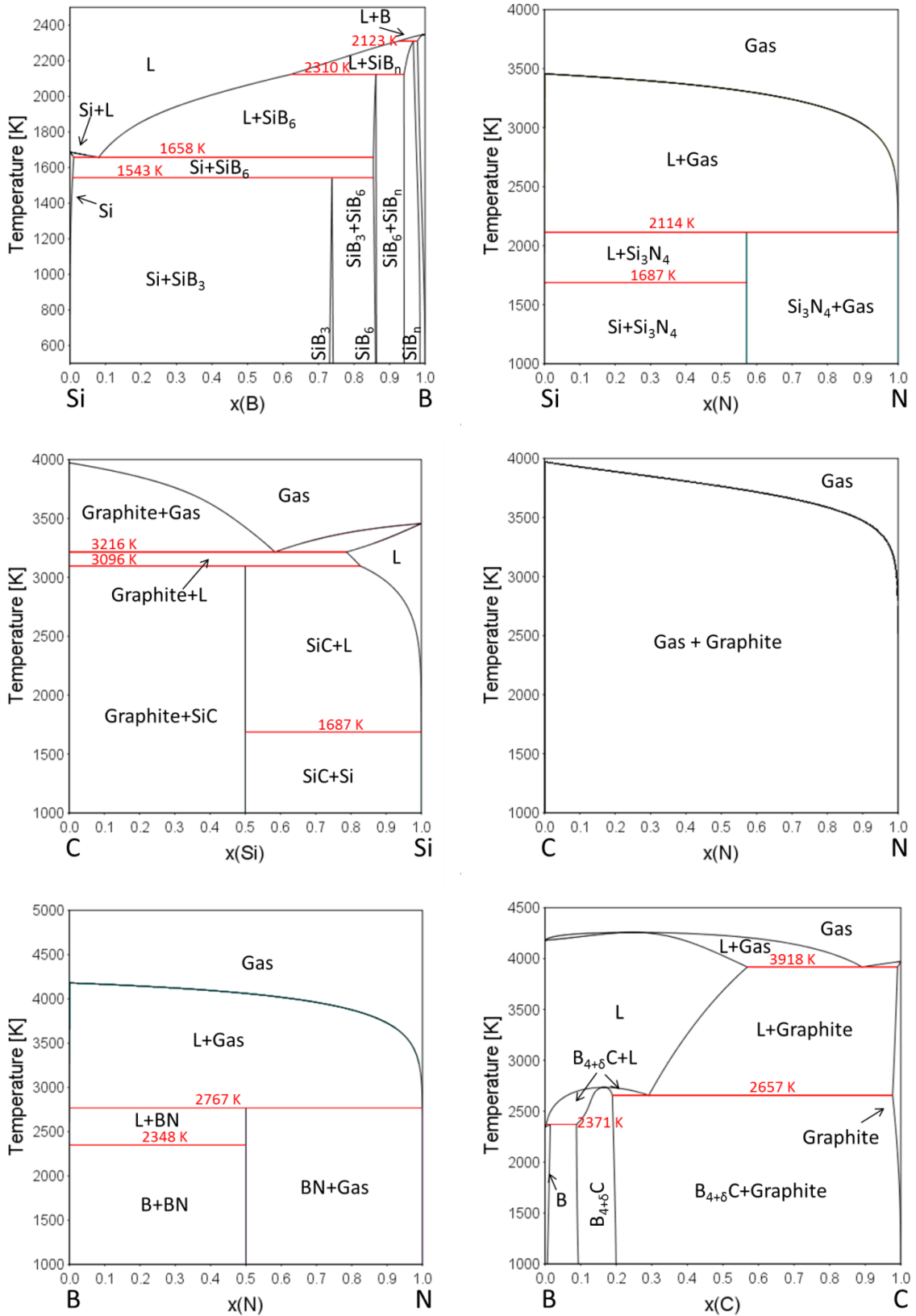
Figure 4.1: Calculated binary phase diagrams in the Si-B-C-N system.

4.1.2. The system Zr-Si-B-C-N

To enable thermodynamic equilibrium calculations involving the ZrB$_2$-additive in SiC/Si-C-N CMCs (see Section 6), the quaternary Si-B-C-N database was extended by zirconium. Therefore, thermodynamic data of Zr-containing binary and ternary sub-systems were added to the Si-B-C-N database. The binary systems Zr-B [79], Zr-Si [79] and the ternary systems Zr-Si-C [80] and Zr-B-C [81] were accepted unmodified from literature. The calculated binary phase diagrams and ternary isothermal sections are shown in Figure 4.2 and Figure 4.3, respectively.

Figure 4.2: Calculated binary phase diagrams a) Zr-B and b) Zr-Si.

Figure 4.3: Calculated isothermal section in the systems a) Zr-B-C and b) Zr-Si-C at 1473 K.

4.1.2.1. Reoptimization of the interaction parameters of the liquid phase in the systems Zr-C and Zr-N

Figure 4.4 shows calculated binary phase diagrams for the systems Zr-C [82] and Zr-N [83]. The phase diagrams obtained by Guillermet and Ma et al., respectively using a substitutional solution model for the liquid phase are plotted in solid lines. Phase diagrams obtained by transferring the liquid phase descriptions into the partially ionic liquid model are plotted with dashed lines. The resulting phase diagrams are deviating considerably in the composition and temperature of the invariant reactions. To obtain compatibility of the liquid phase descriptions, a reoptimization of the interaction parameters of the liquid phase was carried out for the binary systems Zr-C and Zr-N. The obtained interaction parameters are given in Table 4.1. The resulting binary phase diagrams are depicted in Figure 4.5.
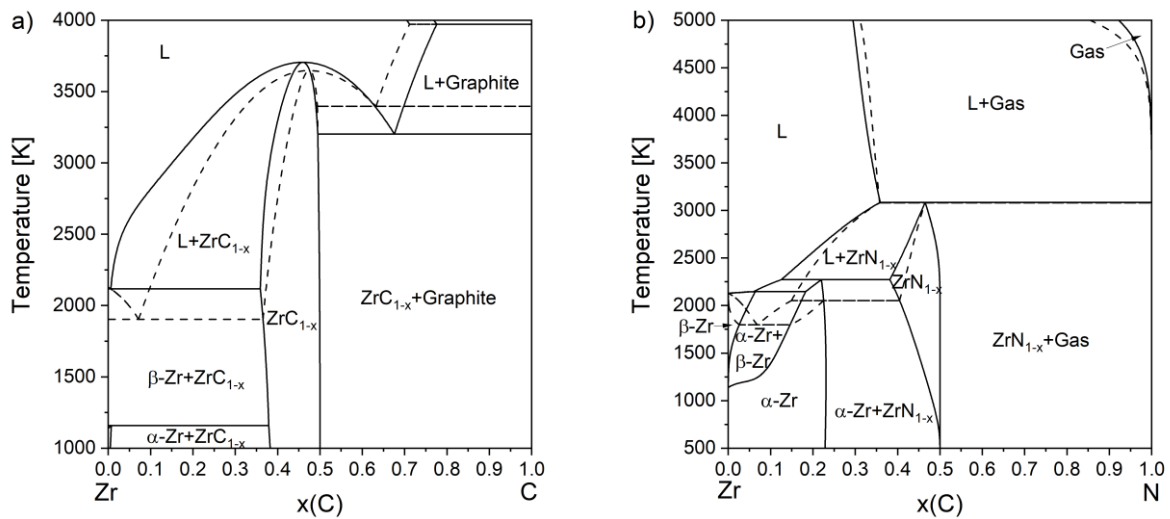
Figure 4.4: Calculated binary phase diagrams for the systems a) Zr-C and b) Zr-N. Diagrams obtained from data by Guillermet **[82]** and Ma et al. **[83]**, respectively using a substitutional solution model are plotted as solid lines. Diagrams obtained by transferring the liquid phase interaction parameters into the partially ionic sublattice model are plotted as dashed lines.

Table 4.1: Reoptimized interaction parameters of the liquid phase for the binary systems Zr-C and Zr-N.

Ionic Liquid
$(B^{+3}, Si^{+4}, Zr^{+4})_P(C, N, SiN_{4/3}, Va)_Q$
$L_0(\text{Ionic Liquid}, Zr^{+4} : C, Va) = -310825.555 + 17.8033498 \cdot T$
$L_1(\text{Ionic Liquid}, Zr^{+4} : C, Va) = +39539.7481$
$L_2(\text{Ionic Liquid}, Zr^{+4} : C, Va) = +50000$
$L_0(\text{Ionic Liquid}, Zr^{+4} : N, Va) = -249605.669 - 65.2089004 \cdot T$
$L_1(\text{Ionic Liquid}, Zr^{+4} : N, Va) = +152559.417 - 48.3959946 \cdot T$
298.15 K - 6000 K
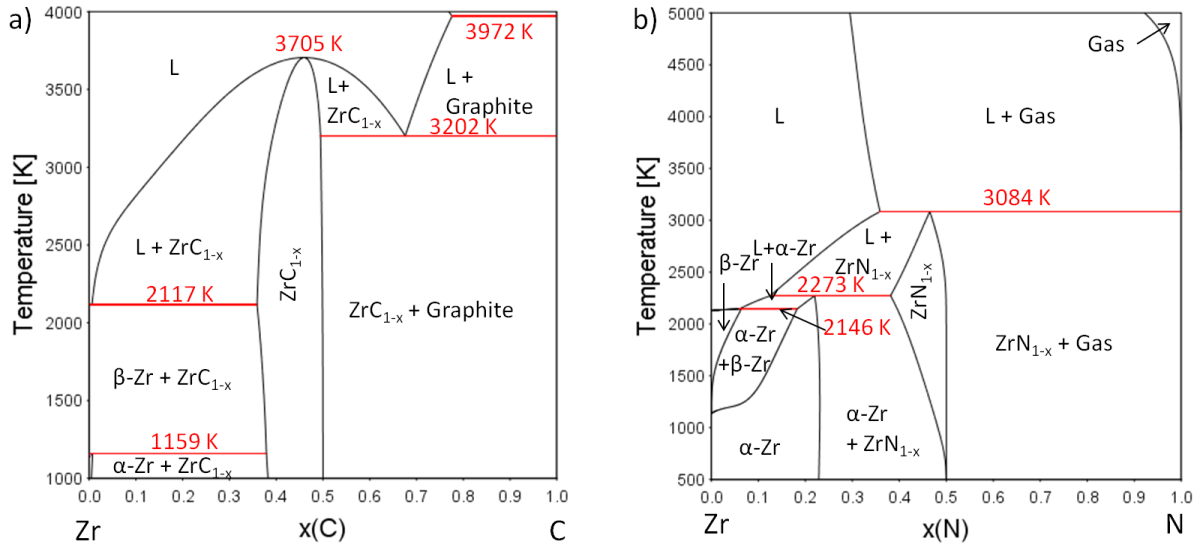
Figure 4.5: Calculated binary phase diagrams for the systems a) Zr-C and b) Zr-N with the reoptimized melt description.

Figure 4.6 shows the composition of the liquid phase calculated at 2773 K. In the partially ionic liquid model, the melt is modeled with two sublattices, which are either occupied by positively charged cations or by negatively charged anions, vacancies and neutral species. To compensate for neutral species and ensure overall charge neutrality, vacancies carry a hypothetically induced negative charge (see Section 2.3.2). In the systems Zr-C and Zr-N, the first sublattice is only occupied by Zr^{+4} cations. Therefore, the fraction of Zr^{+4} ions on this sublattice is equal to one over the whole composition range. On the second sublattice, the fraction of the neutral species (C or N) and vacancies are developing counteractive.
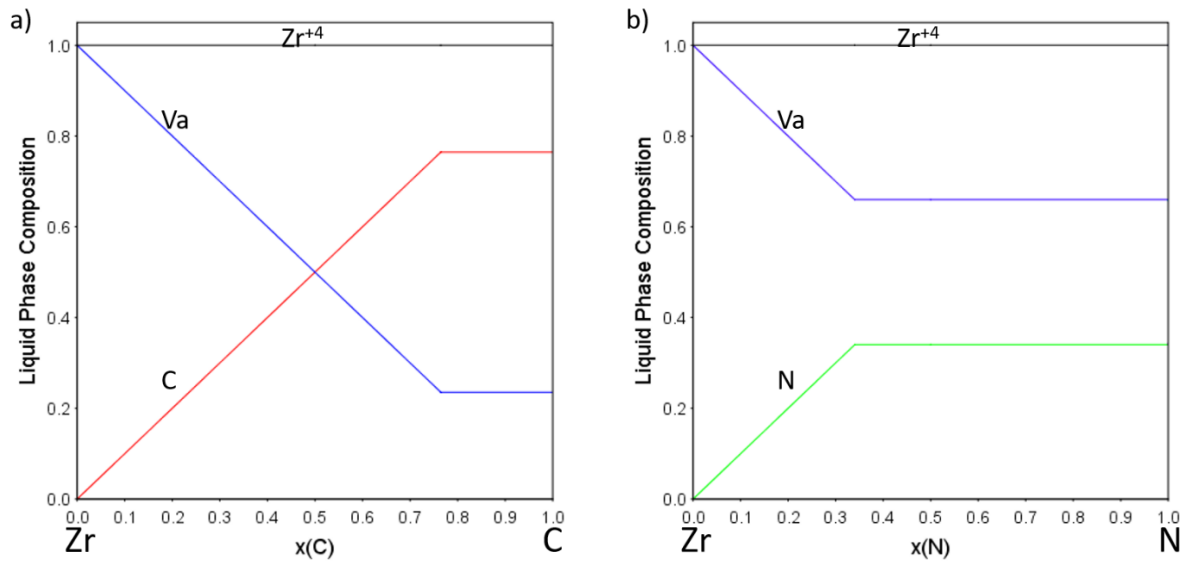
Figure 4.6: Composition of the liquid phase in the binary systems a) Zr-C and b) ZrN at 2773 K according to the partially ionic sublattice model $(Zr^{+4})_P(C, N, Va)_Q$.

4.1.3. Zr-Si-B-C-N-O

The dataset Zr-Si-B-C-N was extended by oxygen to enable thermodynamic equilibrium calculations in oxidizing environments. A variety of different sublattice models were chosen by different authors in literature to model solid solution phases. Therefore, compatibility was an important criterion for selection of the oxide systems. The binary systems Zr-O [84], Si-O [85] and B-O [44] were accepted from literature (see Figure 4.7). The binary systems C-O and N-O do not contain condensed oxide species or homogeneity ranges, but only oxygen-containing gas species.
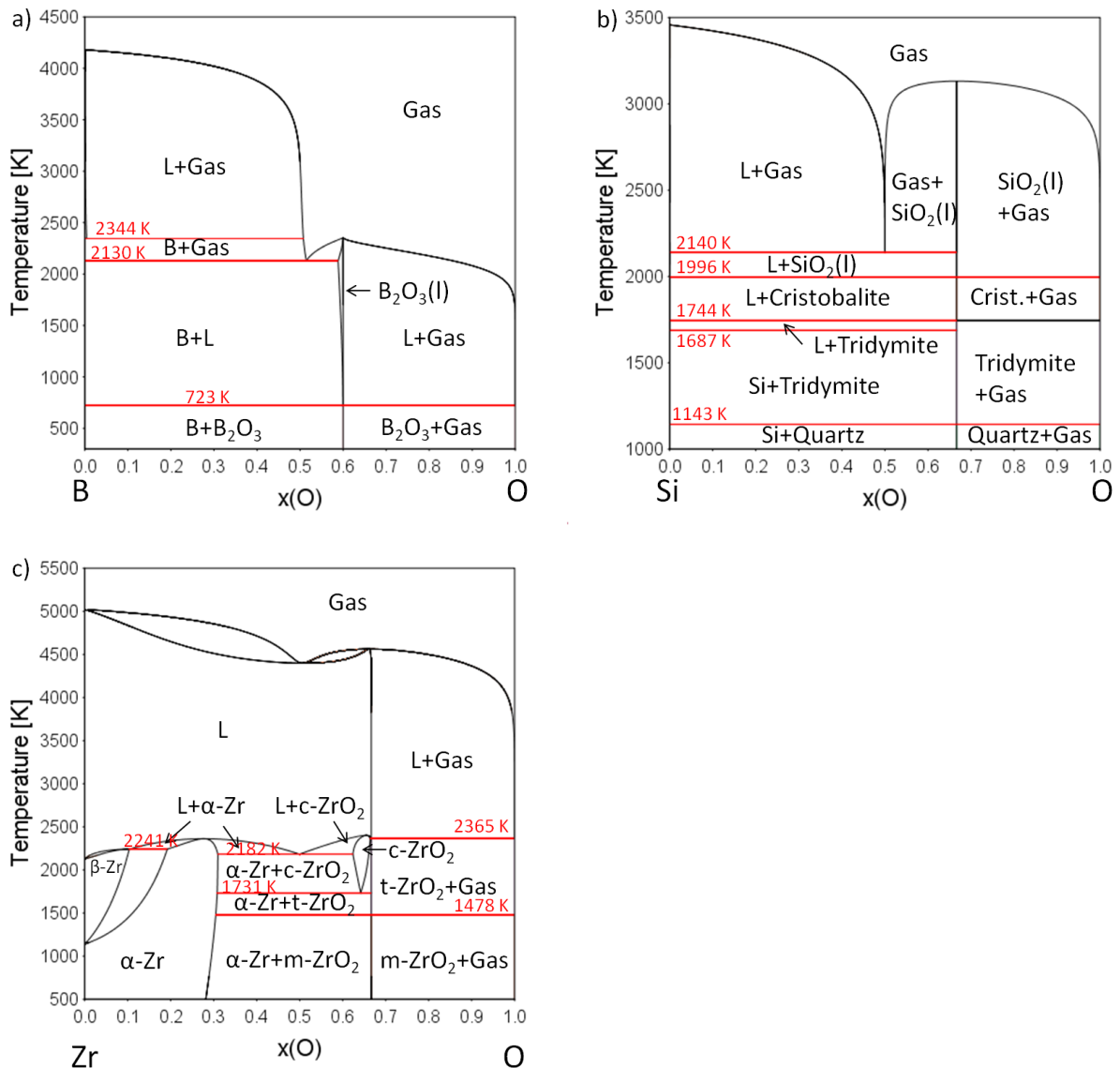
Figure 4.7: Calculated binary phase diagrams of a) B-O, b) Si-O and c) Zr-O systems.

The ternary system Si-B-O was accepted from Kasper [44]. Figure 4.8a shows the calculated isothermal section in the system Si-B-O at 1073 K. This system contains no ternary phases but a low-temperature eutectic at 713 K in the system B_2O_3-SiO_2 (see Figure 4.8b). The formation of a liquid phase is very important for the durability of the ceramic but also for wetting of the surface and cracks and the volatilization of oxides by formation of B- and Si-containing gas species (see Section 8).
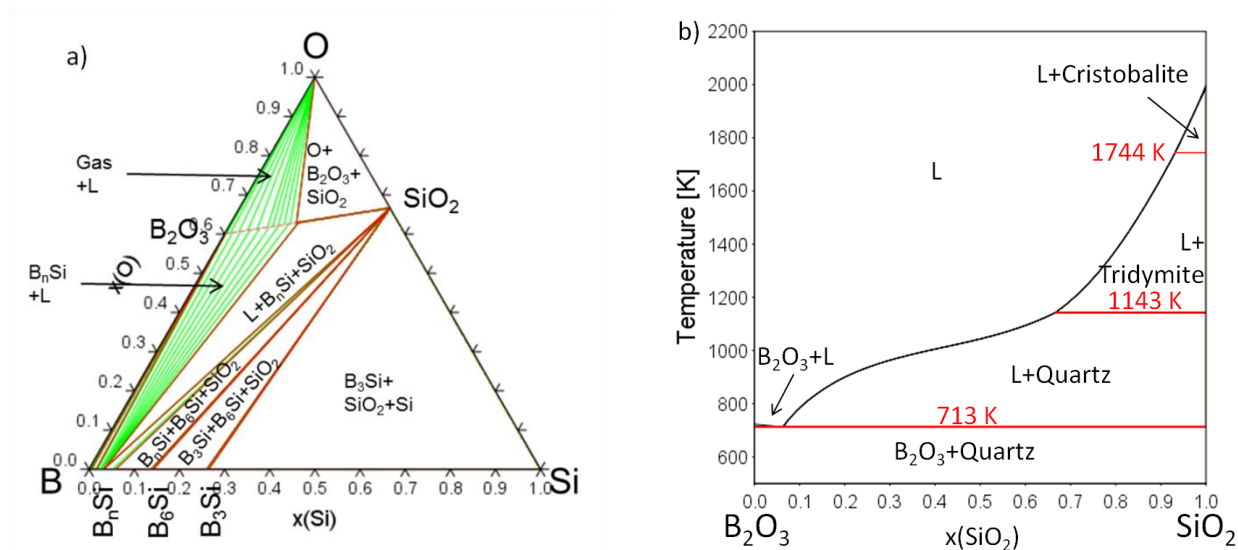
Figure 4.8: The ternary system Si-B-O according to Kasper **[44]**: Calculated a) isothermal section at 1073 K and b) isopleth B_2O_3-SiO_2.

The system Zr-Si-O contains the ternary zircon phase ($ZrSiO_4$) in the quasibinary system ZrO_2-SiO_2. This subsystem is well investigated [86][87][88][89]; it contains an eutectic point and a miscibility gap in the liquid phase.

In this work a thermodynamic dataset for the system ZrO_2-SiO_2 was accepted from Franke [90]. This data set describes the subsystem very well. However, interactions with other constituents of the multicomponent database result in incomplete description of the liquid phase in this work. The obtained ZrO_2-SiO_2 phase diagram is shown in Figure 4.9. The calculated dissociation temperature of $ZrSiO_4$ is 23 K lower compared to Franke or Kaiser et al. [91] but acceptable. However the eutectic temperature is too low and the miscibility gap in the liquid phase is not reproduced with the present database. Karlsdottir et al. [92] also optimized the system ZrO_2-SiO_2 but no dataset was published. Since no experiments were performed above the decomposition temperature of $ZrSiO_4$, no reoptimization of the system ZrO_2-SiO_2 was carried out in the framework of this work.
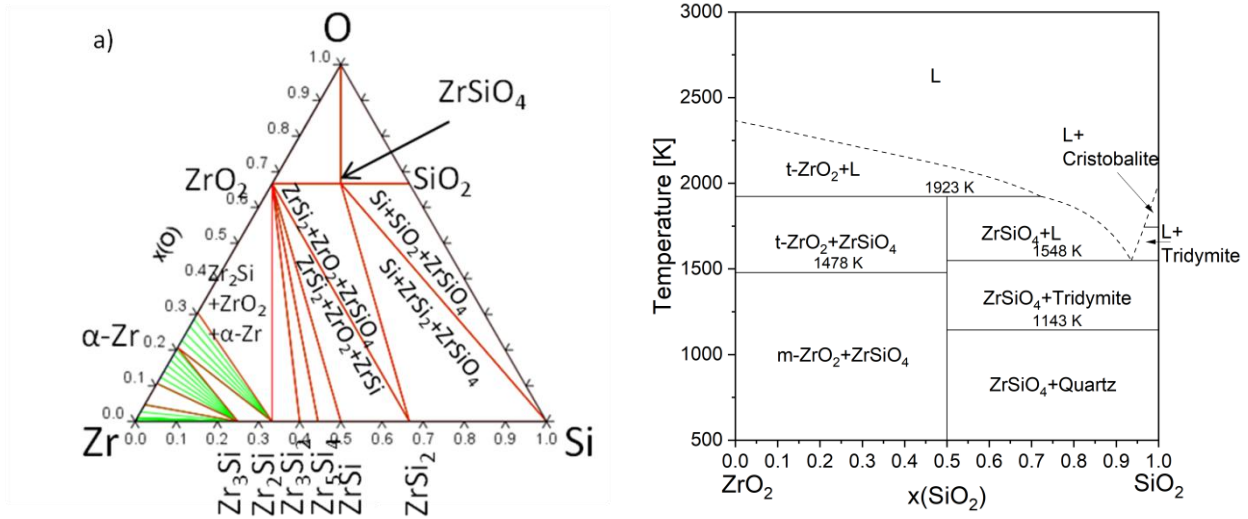
Figure 4.9: Calculated a) isothermal section in the system Zr-Si-O at 1473 K and b) isopleth ZrO_2-SiO_2.

No ternary phases exist in the system Zr-B-O. Karlsdottir et al. [92] optimized the ZrO_2-B_2O_3 phase diagram according to experimental data by Beard et al. [93]. The obtained B_2O_3-ZrO_2 phase diagram shows a ZrO_2 solubility of 0.9 mol-% in the liquid phase at 1473 K and a metastable liquid miscibility gap with T_c = 1335 K. In the same work, Karlsdottir et al. also extrapolate a tentative isothermal section in the system ZrO_2-SiO_2-B_2O_3 at 1773 K. However, due to scarce experimental data, no published thermodynamic dataset and the absence of ternary and quaternary phases, the systems ZrO_2-B_2O_3 and ZrO_2-SiO_2-B_2O_3 by Karlsdottir et al. were not included in this work.

4.1.4. Zr-Si-B-C-N-O-H

For thermodynamic modeling of composites in steam-containing atmosphere, hydrogen was added to the Zr-Si-B-C-N-O database. This allows thermodynamic equilibrium calculations not only for oxidation of CMC, but also volatilization under extreme conditions.

Only the binary system Zr-H contains, besides pronounced solubility of hydrogen in metallic zirconium, solid hydrides δ-ZrH_2, ε-ZrH_2 and metastable γ-ZrH [94]. These play an important role for the application of metallic Zr-based alloys in nuclear fuel applications [95][96]. Since no metallic zirconium was investigated in this work, only gaseous zirconium hydrides were considered. Overall, the Zr-Si-B-C-N-O-H database includes 111 hydrogen-containing gas species. Thermodynamic data for gaseous $SiO(OH)_2$ and $Si(OH)_4$ were taken from a recent reevaluation by Avincola et al. [36]. All other gas species were accepted from the SGTE substance database SSUB v4.1 [76].

5. Phase equilibria in precursor-derived Si-(B-)C-N ceramics

Precursor-derived ceramics are obtained by pyrolysis of preceramic polymers. By selective synthesis of the polymer the composition of the obtained ceramic can be adjusted precisely. Furthermore, the distribution of the elements in the obtained ceramic is extremely homogeneous. Infiltration of fiber preforms with liquid precursor polymers and pyrolysis (PIP-process) is an attractive way to produce CMC combining short processing times and low processing temperatures compared to chemical vapor infiltration (CVI) and liquid silicon infiltration (LSI), respectively. This reduces, for example, the attack of fibers and fiber coatings. Moreover, the PIP process allows to introduce passive or active fillers which improve the degree of filling or add additional functionalization (see also Section 8). Although amorphous Si-(B-)C-N ceramics are not in thermodynamic equilibrium, phase formation, crystallization, and high-temperature reactions can be understood by considering thermodynamic equilibrium calculations [97][98][99].

In this Section, Si-C-N and Si-B-C-N ceramics were prepared by pyrolysis of preceramic polysilazanes as well as a polyborosilazane in flowing Ar- and Ar/N_2-atmospheres, respectively. The polysilazanes Ceraset$^{®}$ PSZ 10 and PSZ 20 were provided by Clariant SE Germany, within the framework of the BMBF-project NewAccess. PSZ 10 and PSZ 20 are different molecular fractions of the Ceraset$^{®}$ polysilazane. Therefore, both polysilazanes and the obtained Si-C-N ceramics have the same composition, given in Table 5.1 and Table 5.2, respectively. A Si-B-C-N ceramic (hereafter *Si-B-C-N_1*) was obtained by pyrolysis a polyborosilazane precursor-polymer. The composition of the obtained *Si-B-C-N_1* ceramic was determined by the chemical analysis group at KIT, IAM-AWP (Dr. Bergfeldt) and is given in Table 5.2. Additionally, a $SiBC_{1.4}N_{2.3}$ ceramic (hereafter *Si-B-C-N_2*) obtained by pyrolysis of a precursor-polymer with a nominal composition of $[SiBC_3N_3H_{10}]_n$ was considered from literature. No experiments were conducted with the *Si-B-C-N_2* precursor-polymer or ceramic. Only the composition was considered for thermodynamic modeling of the pyrolysis process of the preceramic-polymer and the high-temperature stability of the resulting Si-B-C-N ceramic. The oxygen content of the obtained solid Si-C-N and *Si-B-C-N_1* ceramics was below 1 wt.% and 1.5 wt.%, respectively. Oxygen was therefore not considered in the calculations.

Thermodynamic calculations were used to predict gaseous pyrolysis- and decomposition reactions and phase stabilities as a function of temperature and nitrogen partial pressure based on the compositions of the preceramic polymers and the obtained ceramics. Combined TG/MS analysis and post-test examinations were used to investigate the pyrolysis behavior, high-temperature stability, decomposition reactions and crystallization of the obtained Si-(B-)C-N ceramics. Thermodynamic calculations confirm and explain the experimental findings.

Parts of this Chapter were published in [100], but more details and further results are presented here.

Table 5.1: Composition of the preceramic-polymers.

		Nominal composition	Si	B	C	N	H
Ceraset$^\circledR$ PSZ 10 / PSZ 20	at.%	$[SiC_{1.4}NH_{5.4}]_n$	11.4	-	15.8	11.4	61.4
SiBCN_2	at.%	$[SiBC_3N_3H_{10}]_n$	5.56	5.56	16.67	16.67	55.56

Table 5.2: Composition of the investigated precursor-derived Si-(B-)C-N ceramics.

		Nominal composition	Si	B	C	N
Ceraset$^\circledR$ PSZ 10 / PSZ 20	at.%	$Si_{1.3}CN$	40.03	-	30.12	29.85
SiBCN_1	at.%	$Si_6BC_5N_7$	32.47	5.25	26.42	35.86
SiBCN_2	at.%	$SiBC_{1.4}N_{2.3}$	17.54	17.54	24.56	40.35

5.1. Ceraset PSZ 10 and PSZ 20-derived Si-C-N ceramics

5.1.1. Thermodynamic analysis of pyrolysis and high-temperature stability

Figure 5.1 shows the phase fraction diagram and composition of the gas phase calculated as a function of the temperature for the Si-C-N-H composition of the Ceraset$^\circledR$ PSZ 10 and PSZ 20 polymer.
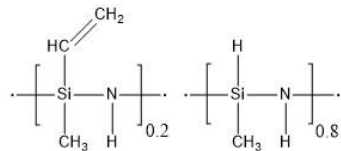
Calculations were performed as a closed system with a constant amount of substances (1 mol) and constant pressure of $p = 1$ bar. At temperatures below approximately 700 K the system consists of three phases: gas, Si_3N_4 and SiC. The gas phase consists of predominantly CH_4 (0.26 bar) and H_2 (0.74 bar). Above 700 K, the material shows a four-phase region: Gas, SiC, Si_3N_4 and graphite are in thermodynamic equilibrium. The amount of CH_4 is decreasing while H_2 is increasing with a point of intersection at 777 K. At this and higher temperatures also other H-containing gas species are formed, however, with relatively low partial pressures ($< 10^{-3}$ bar). The nitrogen partial pressure evolving in equilibrium with the condensed phases is discussed below. Therefore, primarily the formation of H_2 and CH_4 is influencing the composition of the condensed phases.
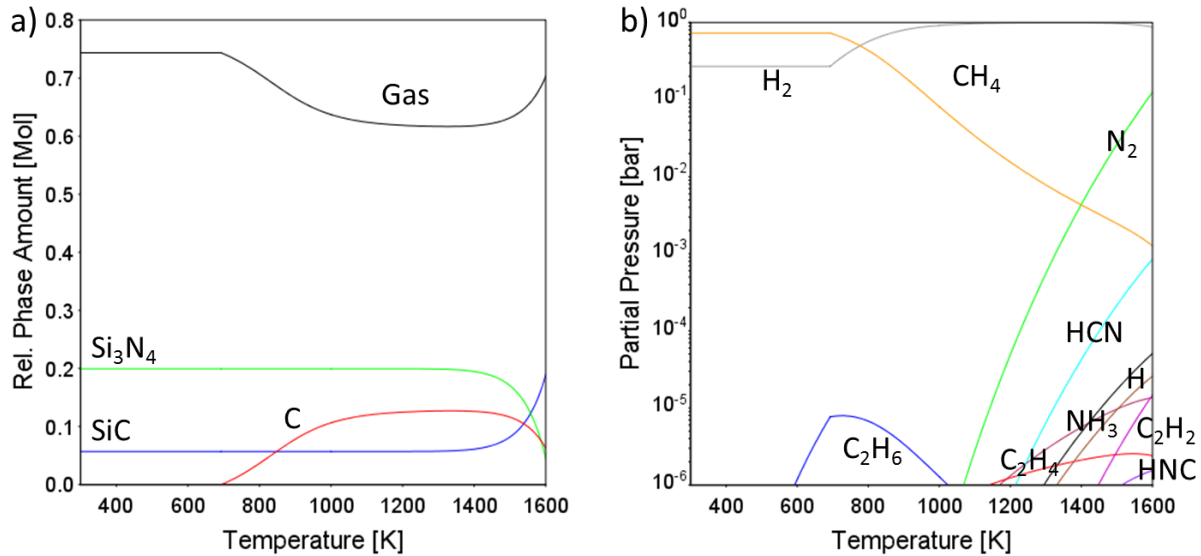
Figure 5.1: Calculated a) phase fraction and b) composition of the gas phase for the composition of the Ceraset® PSZ 10 and PSZ 20 polymer.

The overall composition of the condensed phases in Figure 5.1a is plotted into the isothermal section of the Si-C-N system at 1200 K Figure 5.2. At the lowest temperatures, the composition of the condensed phase is on the tie-line SiC-Si$_3$N$_4$. With increasing temperature, CH$_4$ dissociates according to reaction (5.1) into condensed graphite and molecular hydrogen. This is resulting in a shift of the composition of the condensed phases to higher carbon content along a line of constant Si/N-ratio with Si/N=1:

$$CH_4 = C_{graphite} + 2H_2 \tag{5.1}$$
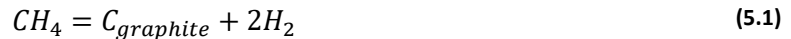
At temperatures higher than approx. 1400 K, the composition of the condensed phases is shifting to lower nitrogen content along a line of constant Si/C-ratio with Si/C=0.73. This temperature corresponds to the point of intersection between the partial pressures of CH$_4$ and N$_2$ in Figure 5.1b at 1399 K. The actual composition of the precursor-derived Si-C-N ceramic is plotted additionally. It is close (within approx. 5 %) to the calculated composition of the condensed phases at 850 K-900 K, however, shifted to a lower nitrogen content.
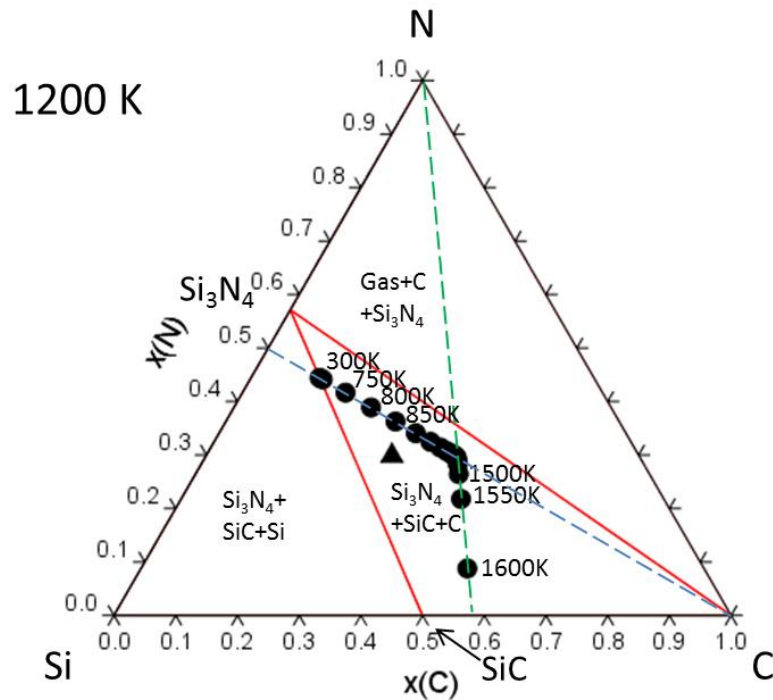
Figure 5.2: Calculated isothermal section in the system Si-C-N. The composition of the condensed phase in Figure 5.1a (●) and the composition of the Ceraset® PSZ 10 and PSZ 20 precursor-derived Si-C-N ceramic (▲) are inserted.

Figure 5.3 shows isothermal sections in the quaternary system Si-C-N-H at constant x(H) = 0.64, which is corresponding to the hydrogen content of the PSZ 10 and PSZ 20 precursor polymers. Depending on the composition, five different phase stability fields exist: Gas+Si$_3$N$_4$, Gas+C+Si$_3$N$_4$, Gas+C+SiC+Si$_3$N$_4$, Gas+SiC+Si$_3$N$_4$ and Gas+Si+SiC+Si$_3$N$_4$. With increasing temperature, the phase fields Gas+C+Si$_3$N$_4$ and Gas+C+SiC+Si$_3$N$_4$ are growing at the expense of the phase fields Gas+Si$_3$N$_4$ and Gas+SiC+Si$_3$N$_4$, which are decreasing in size until they disappear. The phase stability field Gas+Si+SiC+Si$_3$N$_4$ does not change in size with temperature. The composition of the PSZ 10- and PSZ 20-derived Si-C-N ceramics is indicated. At the lowest temperature, the composition is in the three phase field Gas+SiC+Si$_3$N$_4$. Above approx. 700 K the composition of the ceramic is in the four phase field Gas+C+SiC+Si$_3$N$_4$.
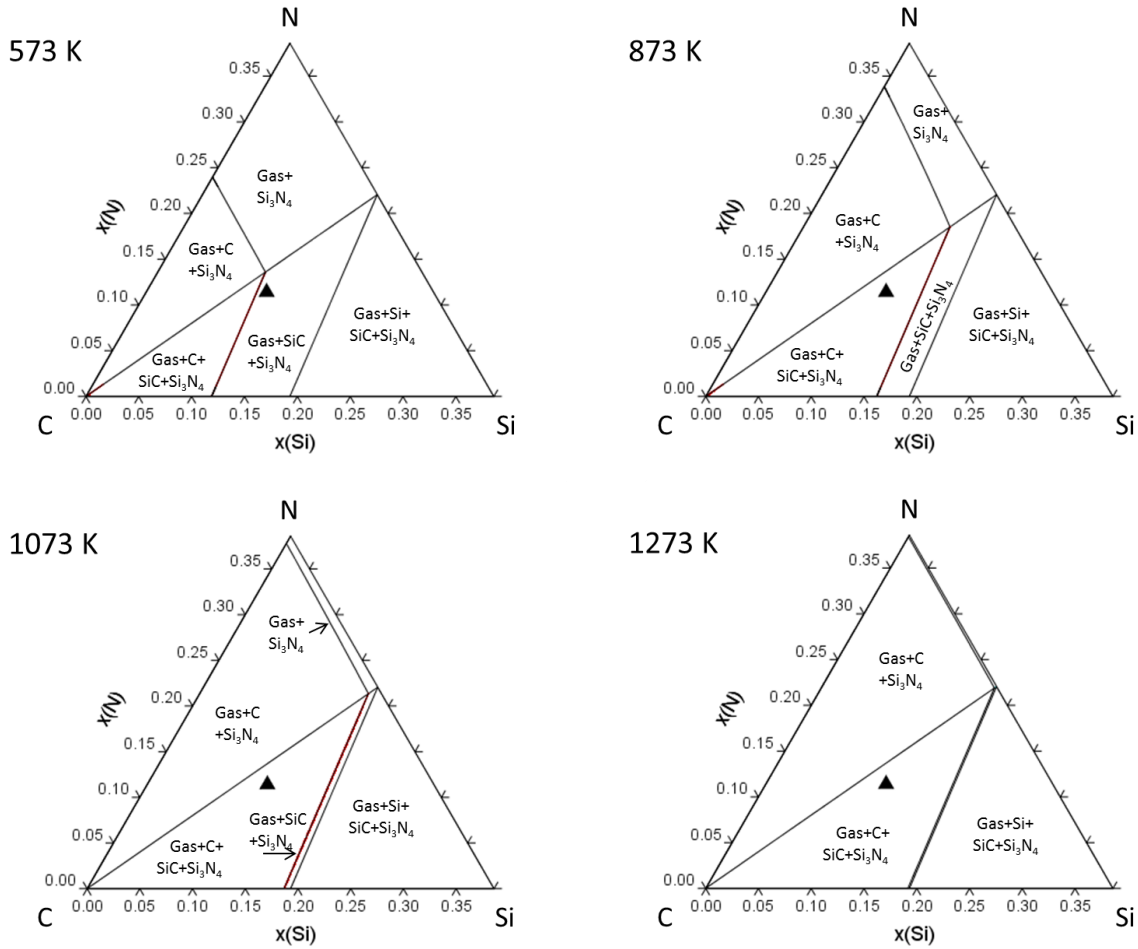
Figure 5.3: Calculated isothermal sections of the Si-C-N-H system at constant x(H) = 0.614.

Figure 5.4 shows isothermal sections in the system Si-C-N. The composition of the PSZ 10- and PSZ 20-derived Si-C-N ceramics is indicated. At temperatures below 1757 K the composition of the Si-C-N ceramic, if crystallization would occur, is located in the three-phase field Si$_3$N$_4$+SiC+C. At 1757 K, Si$_3$N$_4$ and excess carbon are reacting under formation of SiC and N$_2$ according to:

$$Si_3N_4 + 3C = 3SiC + 2N_2 \uparrow \tag{5.2}$$

Thus the Si-C-N ceramic is located in the three-phase field Gas+Si$_3$N$_4$+SiC at 1757 K < T < 2114 K. The gas phase is consisting only of N$_2$, which is released to the gas phase. Thereby the composition of the Si-C-N ceramic is shifting along the reaction path, which is indicated by the arrow, to the tie-line SiC-Si$_3$N$_4$. At 2114 K, the remaining Si$_3$N$_4$ is thermally decomposed into silicon, which is liquid at this temperature, and N$_2$, which is released into the atmosphere.

$$Si_3N_4 = 3Si_l + 2N_2 \uparrow \tag{5.3}$$

Thus, above 2114 K the composition of the Si-C-N ceramic is located in the three-phase field Gas+SiC+Si$_l$. By release of N$_2$, the composition of the remaining ceramic is shifting along the

reaction path from the N-corner of the isothermal section beyond the previous composition to the tie-line SiC-Si$_l$. The isothermal section at 3000 K shows that at very high temperatures the gas phase possesses a spatial expansion in the Si-C-N isothermal section, meaning that also C- and N-containing gas species are formed. At lower temperatures, the gas phase has only a punctual expansion in the N-corner consisting only of N$_2$.
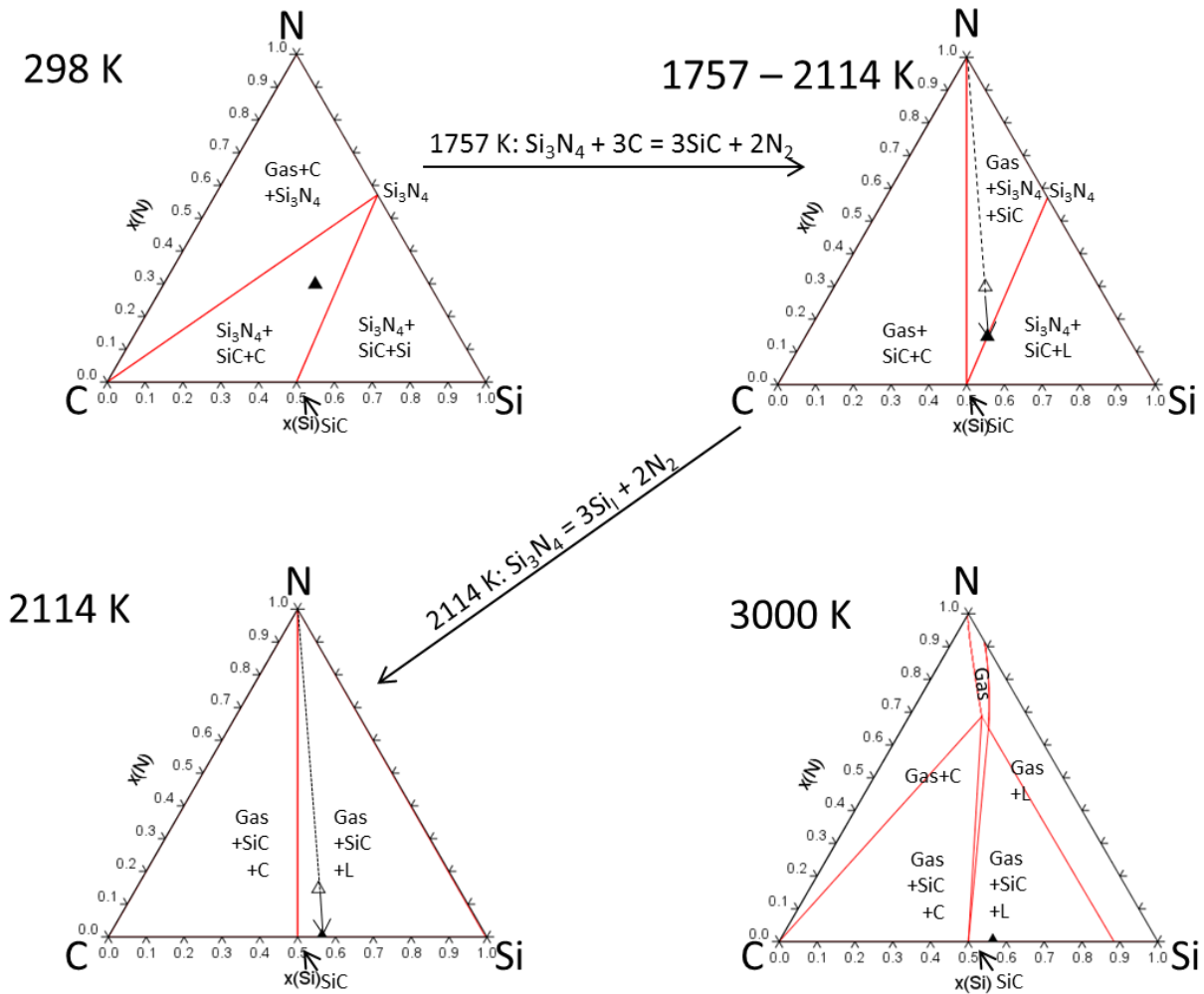
Figure 5.4: Isothermal sections of the Si-C-N system at temperatures of 298 K, 1757 < T < 2114 K, 2114 K and 3000 K. The composition of the PSZ 10- and PSZ 20-derived Si-C-N ceramic and the associated reaction paths are indicated.

Figure 5.5 shows the phase fraction diagram and the composition of the associated gas phase for the PSZ 10- and PSZ 20-derived ceramics. Calculations were performed for a closed system with a constant amount of substance of 1 mol. A small amount of Ar (x_{Ar}=0.01) was added to establish a stable gas phase at all temperatures. The evolution of the phase composition, which is discussed before, is depicted in a quantitative manner. Figure 5.5a shows the decreasing amount of Si$_3$N$_4$ at 1757 K and at 2114 K due to reaction (5.2) and reaction (5.3), respectively. Graphite is totally consumed by the reaction at 1757 K, while SiC and Si$_l$ are formed as product phases at 1757 K and 2114 K, respectively. In Figure 5.5b the release of N$_2$ during both reactions

at 1757 K and 2114 K is depicted relative to the constant amount of inert Ar. Other, Si- and C-containing gas species (Si, C_2Si, CSi_2,...), are formed only at temperatures above 2500 K. At lower temperatures, N_2 is the only gas species in equilibrium with the condensed phases. The curvature of the phase fraction curves towards the reaction temperatures are a direct result of the application of Ar as an inert gas. The volume of the gas phase in equilibrium with the condensed phases is depending on the amount of Ar, which is used. Therefore, the larger the amount of Ar, the larger the amount of nitrogen (molecules), which is required to establish the equilibrium partial pressure under the given conditions. As a result, the phase amount of Si_3N_4 is decreasing to provide the nitrogen. The remaining Si is reacting with C to form SiC. Without using Ar in the calculation, the phase fraction diagram would yield a distinct step-profile at the individual reaction temperatures. However, it would not be possible to display the release of N_2 relative to the constant amount of Ar.
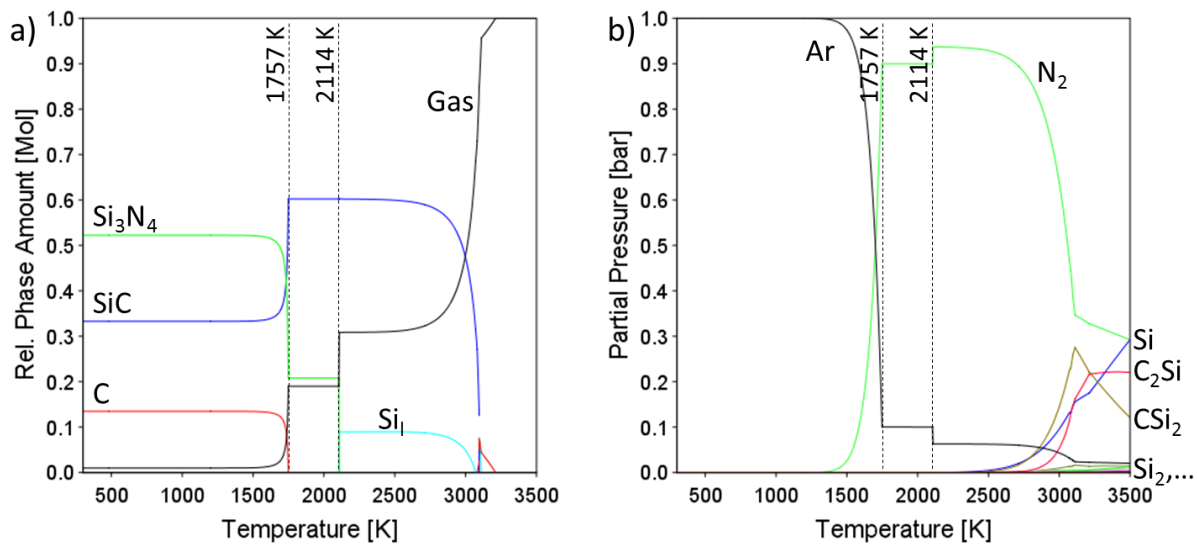
Figure 5.5: Phase fraction diagram and composition of the associated gas phase for the PSZ 10 and PSZ 20-derived Si-C-N ceramic.

Figure 5.6 shows a theoretical mass change curve calculated from the phase fraction of the condensed phases in Figure 5.5a. Thereby 100 % is referring to the solid Si-C-N ceramic. Reaction (5.2) at 1757 K is resulting in a mass change of approximately -40 % of the solid phases. The thermal decomposition of Si_3N_4 (reaction (5.3) at 2114 K) is resulting in another mass change of -30 %. The thermal decomposition of SiC and vaporization of liquid Si leads to the mass loss of the last 30 % at temperatures above 3000 K.
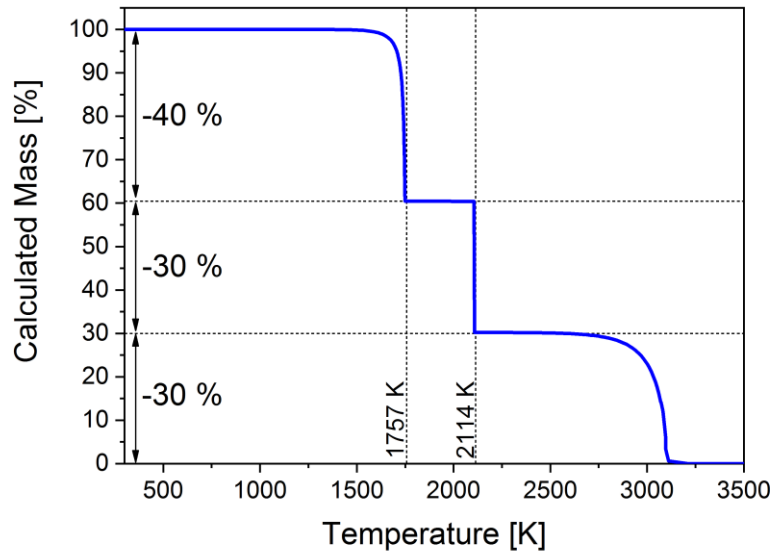
Figure 5.6: Theoretically calculated mass change curve for PSZ 10- and PSZ 20-derived Si-C-N ceramics.

The phase stability diagram for the PSZ 10- and PSZ 20-derived Si-C-N ceramics is plotted in Figure 5.7 as a function of the nitrogen partial pressure and temperature. Only condensed phases are indicated although the gas phase is in thermodynamic equilibrium with these at every point of the diagram. The partial pressure of other gas species is negligible at these temperatures. Therefore, the gas phase consists only of N_2 and p_{N2} corresponds to the total pressure. Lines correspond to univariant three phase equilibria i.e. p_{N2} and temperature cannot be changed independently without leaving the respective phase equilibrium. Areas correspond to bivariant two-phase equilibria, which means that p_{N2} and temperature can be varied independently without leaving the particular phase stability field. At relatively low temperatures and high p_{N2}, carbon (graphite) and Si_3N_4 are coexisting in thermodynamic equilibrium. Upon crossing the line, indicated by the phase equilibrium $Si_3N_4+3C=3SiC+2N_2$, by increasing the temperature or decreasing p_{N2}, graphite and Si_3N_4 are reacting under formation of SiC and N_2. For Si-C-N ceramics with Si/C > 1, the free carbon is consumed completely by the reaction with Si_3N_4 [97]. The remaining Si_3N_4 is in equilibrium with SiC for 1757 < T < 2114 K at p_{N2} = 1 bar. The calculated phase stability diagram shows clearly how the reaction temperatures in the PSZ 10- and PSZ 20-derived Si-C-N ceramics depend on the nitrogen partial pressure. With decreasing p_{N2}, reaction temperatures are shifted to lower values. For example the temperature of reaction (5.2) is 1757 K and 1858 K at p_{N2} = 1 bar and p_{N2} = 0.1 bar, respectively. In accordance with that, reaction temperatures are shifted to higher values for p_{N2} > 1 bar.
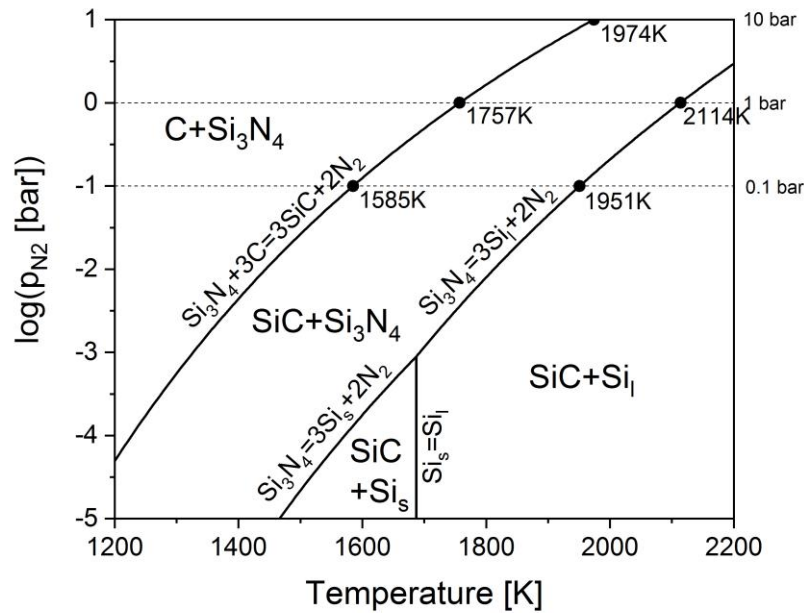
Figure 5.7: Phase stability diagram for Si-C-N with Si/C > 1.

Figure 5.8 shows the isopleth calculated for C-Si$_{39.0}$N$_{29.1}$ with the composition of the PSZ 10- and PSZ 20-derived Si-C-N ceramic indicated with a dashed line. For x(N) < 0.27, no Si$_3$N$_4$, but free carbon remains at temperatures above 1757 K. Thus, reaction (5.3), the thermal decomposition of remaining Si$_3$N$_4$, cannot take place with increasing temperature. For x(N) > 0.34 free Si is present, which transforms into a melt at 1687 K.
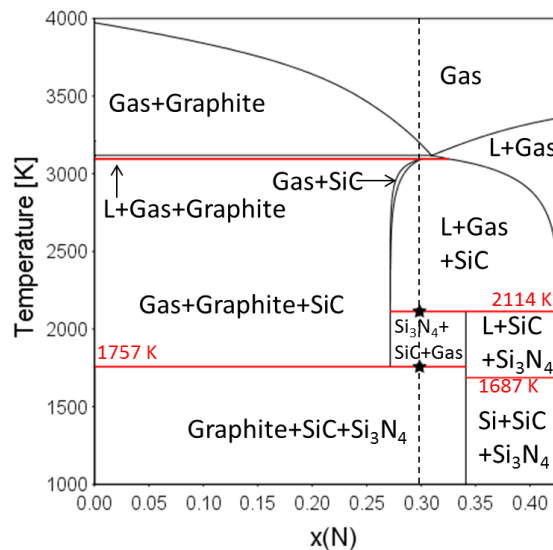
Figure 5.8: Calculated isopleth in the Si-C-N system for C-Si$_{39.0}$N$_{29.1}$. The composition of the PSZ 10- and PSZ 20-derived Si-C-N ceramic is indicated. Reactions (5.2) and (5.3) are marked (★).

5.1.2. Experimental investigations

Combined thermogravimetric and mass spectrometric analysis of the pyrolysis and heat treatment of PSZ 10- and PSZ 20-derived Si-C-N ceramic were conducted in order to validate the thermodynamic calculations. Figure 5.9 shows results of a test series with both precursor polymers in flowing Ar. The experiment was divided into three stages. In stage 1 (T < 573 K) the liquid preceramic polymer is crosslinked. The heating procedure was performed stepwise with holding times of 1 h at 473 K, 523 K and 573 K to allow outgassing of the polymer without bubble formation. In this stage, PSZ 10 samples show a higher mass loss compared to PSZ 20 samples. During stage 2 (573 K < T < 1273 K) a mass loss is observed connected with the actual pyrolysis of the polymer. Thereby, the formation of the Si-C-N network is accompanied by the release of hydrogen and hydrogen-containing gas species from Si-H, N-H and C-H groups of the polymer. The release of H_2 and CH_4 during this stage was detected by mass spectrometric analysis of the STA offgas (Figure 5.10 and Figure 5.11) and occurs in accordance with the observed mass loss. In stage 3 (T > 1273 K) the final pyrolysis temperature was held for 5 h to allow a complete conversion of the polymer into the Si-C-N ceramic. Heat treatment up to final temperatures of 1273 K – 1573 K does not result in further mass changes of the samples. This is indicating that no further reactions are taking place at these temperatures. However, samples heat treated up to 1673 K and 1773 K show an additional mass loss during stage 3. The observed mass loss is taking place gradually at 1673 K and abruptly at 1773 K and is accompanied by the release of N_2 (see Figure 5.10 and Figure 5.11). In total, the pyrolysis of PSZ 10 is resulting in a higher mass loss compared to PSZ 20, but the difference is caused completely by the cross-linking process in stage 1. Once the cross-linking is completed, both preceramic polymers show the same mass evolution.
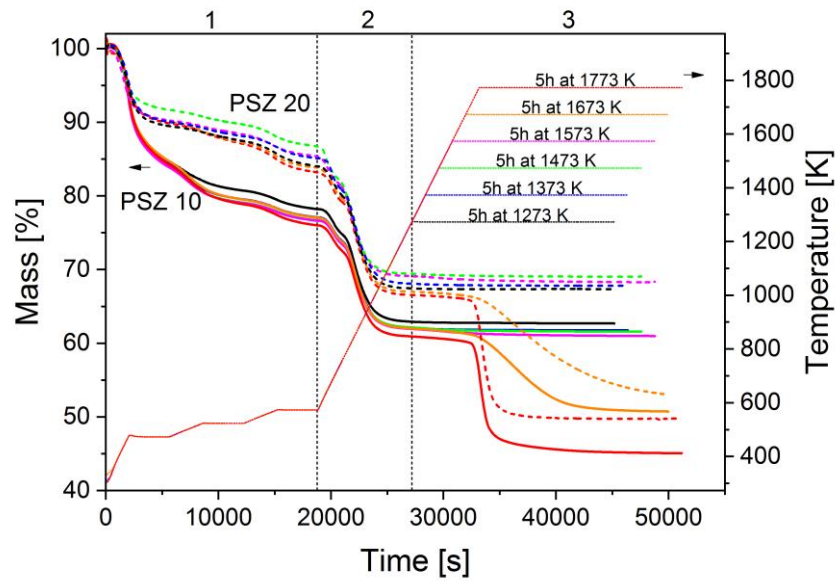
Figure 5.9: Thermogravimetric analysis of PSZ 10 and PSZ 20 pyrolysis up to maximum temperatures of 1273 K – 1773 K in flowing Ar-atmosphere.
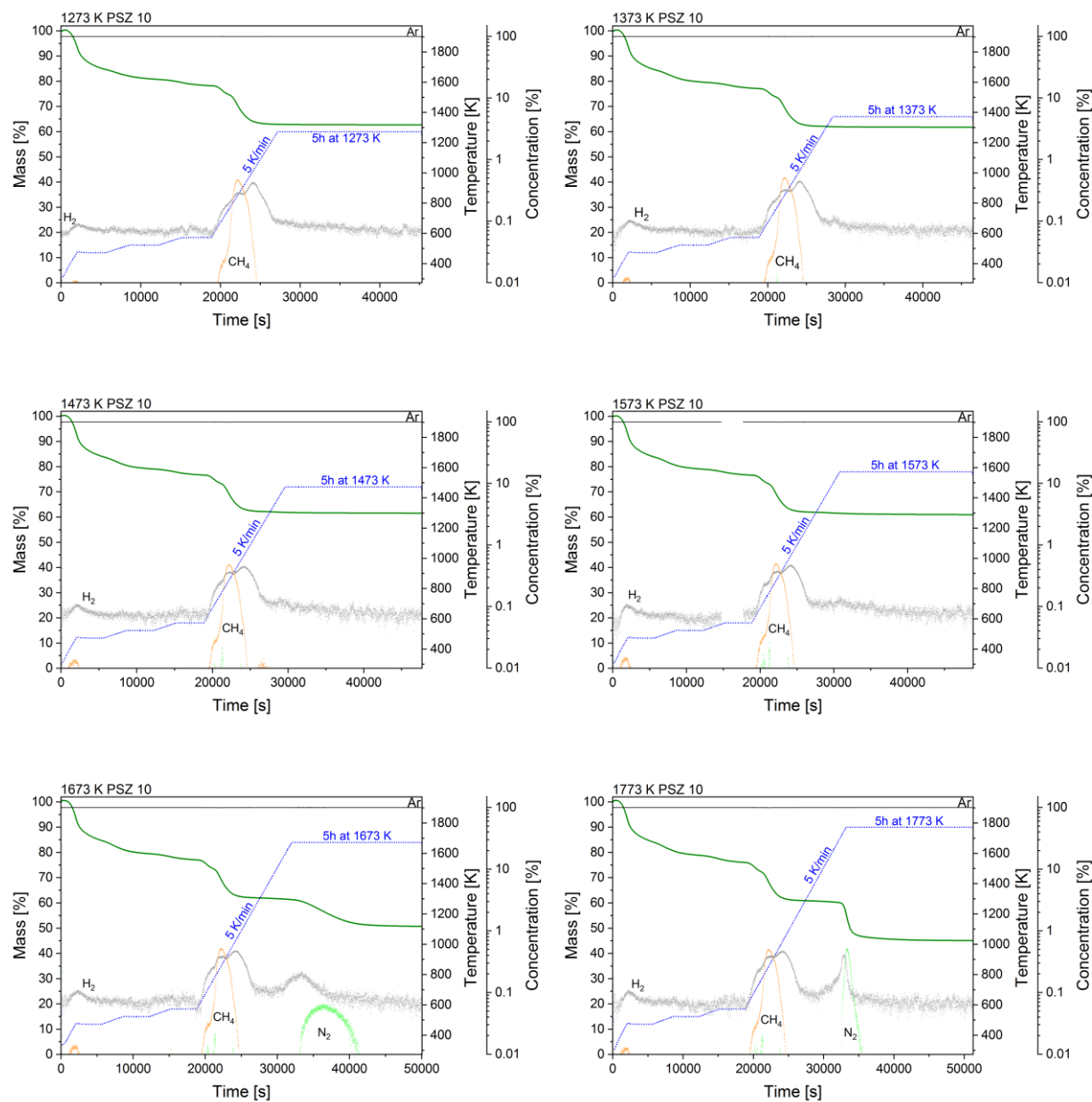
Figure 5.10: Combined thermogravimetric and mass spectroscopic analysis during pyrolysis of Ceraset® PSZ 10-derived Si-C-N ceramics in flowing Ar-atmosphere.
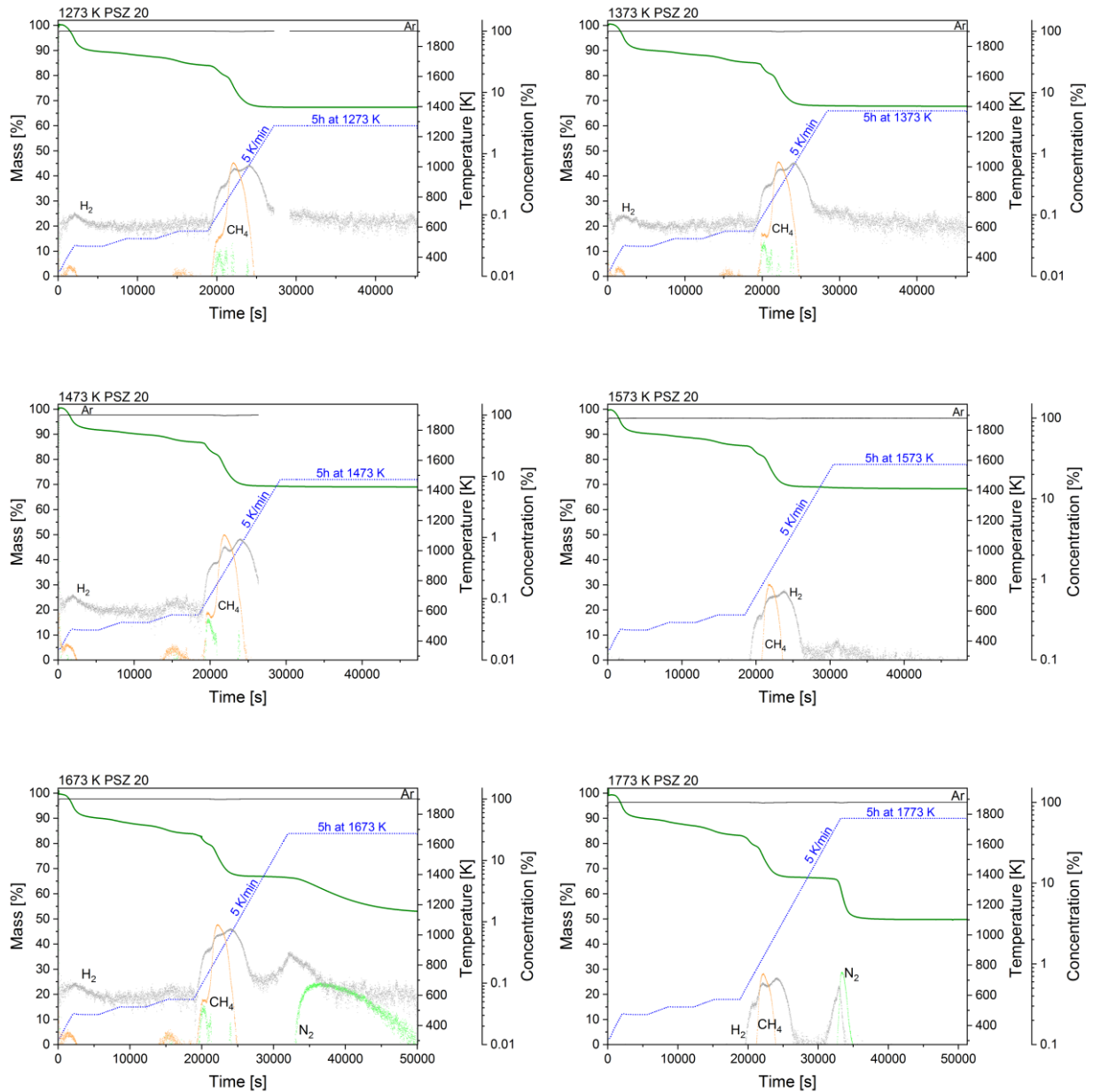
Figure 5.11: Combined thermogravimetric and mass spectroscopic analysis during pyrolysis of Ceraset® PSZ 20-derived Si-C-N ceramics in flowing Ar-atmosphere.

Figure 5.12 shows a combined DTA, thermogravimetric and mass spectroscopic analysis of the pyrolysis of Ceraset® PSZ 20 in flowing pure Ar and Ar/N$_2$ (p$_{N2}$=0.5 bar), respectively. Note that only semi-quantitative analysis is possible with the used *Netzsch QMS 403C Aëolos* mass spectrometer (see also Section 3.4). Two endothermic peaks are observed in the temperature range from 800 K to 1250 K. The first peak, with an onset temperature of 800 K, corresponds to the release of H$_2$ and CH$_4$ at the same time while the second peak is only accompanied by the release of H$_2$. In both atmospheres, the H$_2$-release spreads from approx. 650 K to 1200 K, which is giving the pyrolysis apparently a triple character. However, no DTA signal is observed in the initial state below 800 K. The mass loss of the preceramic polymer also shows a two-step character at temperatures between 573 K and 1250 K. This highest mass loss is slightly shifted to lower temperatures compared to the DTA signal. Additionally, the endothermic reaction (Si$_3$N$_4$+3C=3SiC+2N$_2$) is observed in Ar atmosphere with a maximum around 1850 K together with the release of N$_2$. The onset temperature according to the mass loss and the N$_2$-release is approx. 1750 K. No DTA signal is detected in Ar/N$_2$ at these temperatures. Furthermore, the mass loss above approx. 1750 K is significantly smaller compared to the experiment in pure Ar. It's obvious that the release of N$_2$ cannot be detected in N$_2$-containing atmosphere.
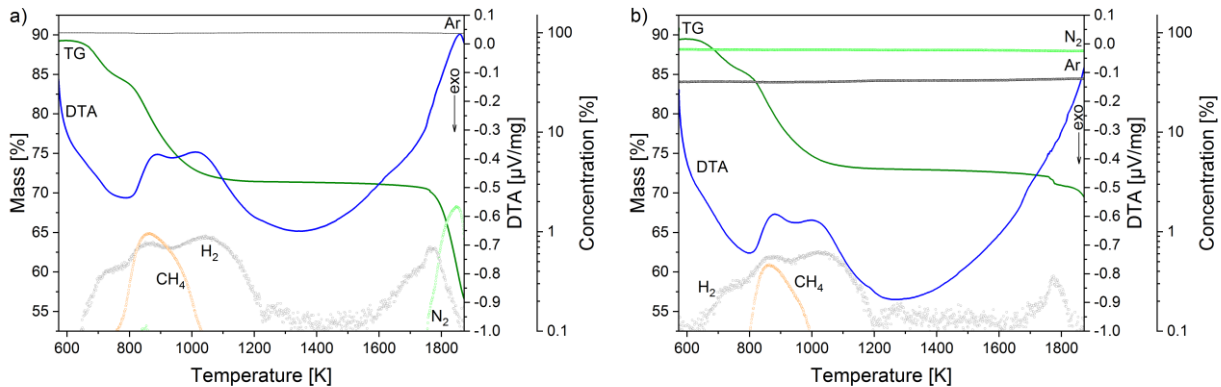
Figure 5.12: Combined thermogravimetric, mass spectroscopic and DTA analysis of PSZ 20 during heat-up with 10 K/min in flowing a) Ar and b) Ar/N$_2$ (p$_{N2}$ = 0.5 bar) atmosphere. Note that only semi-quantitative analysis is possible with the used mass spectrometer.

Micrographs of the PSZ 10 und PSZ 20-derived Si-C-N ceramics obtained in Ar atmosphere are depicted in Figure 5.13 and Figure 5.14, respectively. All samples exhibit extensive crack formation as a result of the shrinkage associated with release of hydrogen-containing gas species during the pyrolysis process. Si-C-N ceramics, pyrolyzed at maximum temperatures up to 1573 K, show a very smooth and homogeneous microstructure. In contrast to that, microstructures appear partly and completely porous after pyrolysis at 1673 and 1773 K, respectively. The Si-C-N ceramic pyrolyzed at 1673 K shows both characteristics: smooth and homogeneous areas, which seem not (yet) transformed and porous areas where the

transformation of the Si-C-N ceramic by reaction (5.2) took place. Thereby, the edges the Si-C-N ceramic adjacent to cracks, which are accessible for the atmosphere, are always transformed.
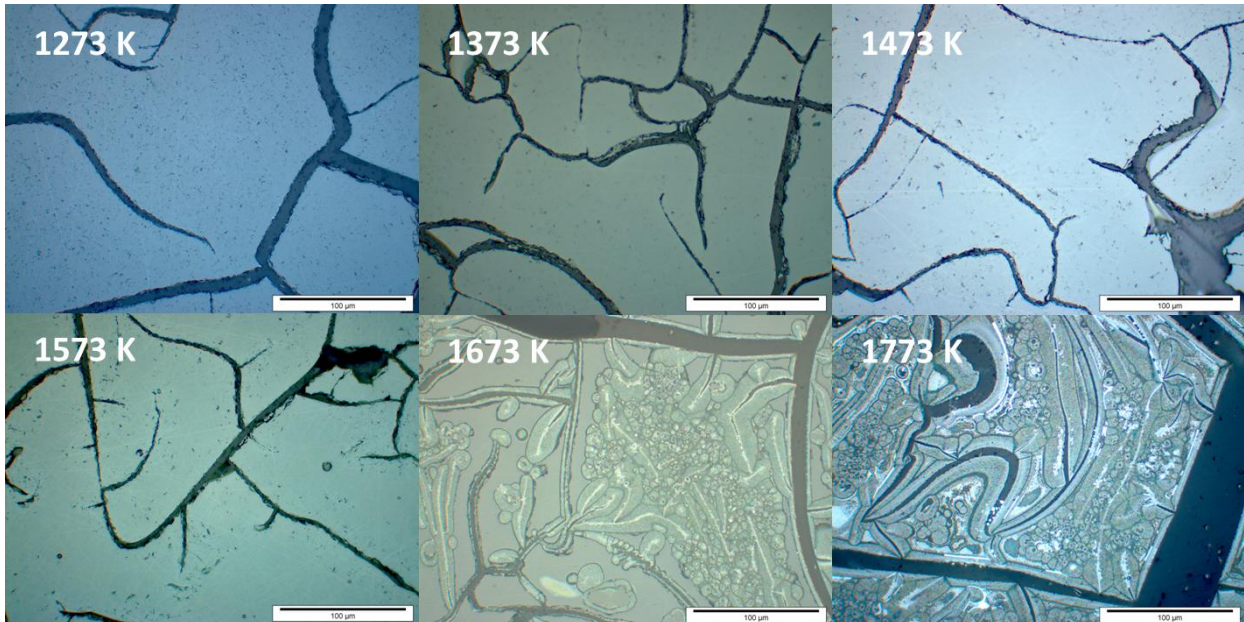
Figure 5.13: Micrographs of PSZ 10-derived Si-C-N ceramics pyrolyzed at 1273 K – 1773 K in flowing Ar. Scale bars correspond to 100 μm.
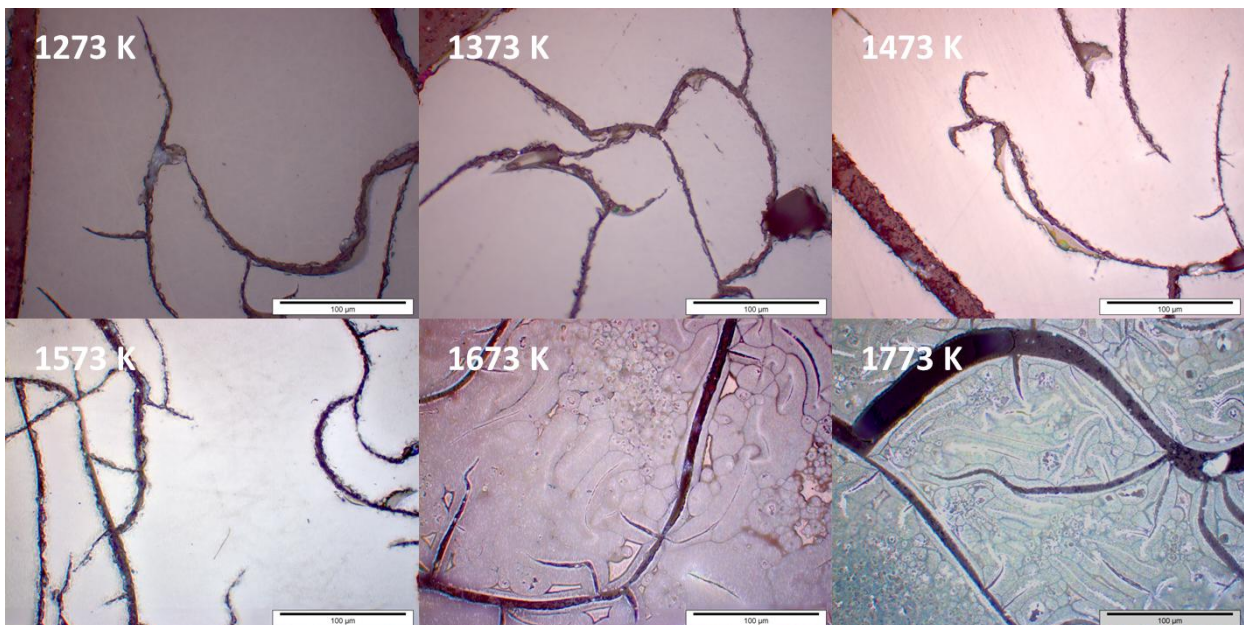
Figure 5.14: Micrographs of PSZ 20-derived Si-C-N ceramics pyrolyzed at 1273 K – 1773 K in flowing Ar. Scale bars correspond to 100 μm.

Figure 5.15a shows a SEM micrograph of the Si-C-N ceramic obtained from pyrolysis of PSZ 20 at 1673 K in flowing Ar. EDX analysis (Figure 5.15b and c) shows, that the smooth and homogeneous areas which correspond to microstructures obtained at T < 1673 K have a significantly higher nitrogen content compared to the porous areas. This is indicating that the reaction $Si_3N_4+3C=3SiC+2N_2$ already took place in the porous areas.
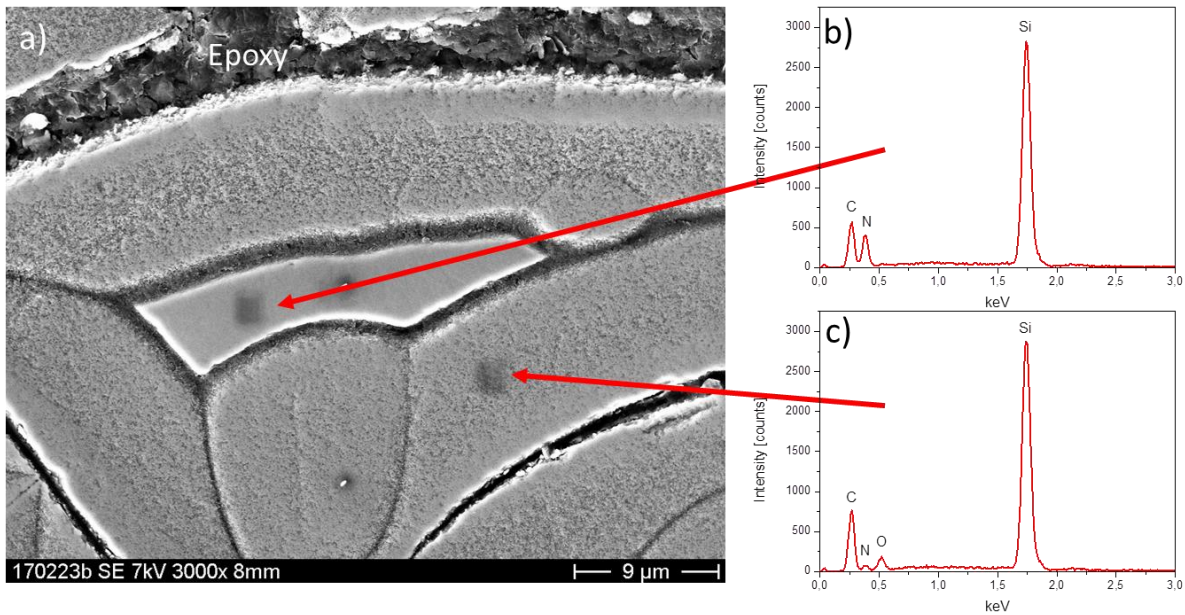
Figure 5.15: SEM micrograph and EDX analysis of PSZ 20-derived Si-C-N ceramic pyrolysed at 1673 K in flowing Ar.

XRD patterns show that the PSZ 10 and PSZ 20-derived Si-C-N ceramics (Figure 5.16) are X-ray amorphous up to pyrolysis temperatures of 1573 K. Pyrolysis at 1673 K and 1773 K results in the crystallization of β-SiC. Additionally, weak Si reflections are observed after pyrolysis of PSZ 10 at 1773 K in flowing Ar.
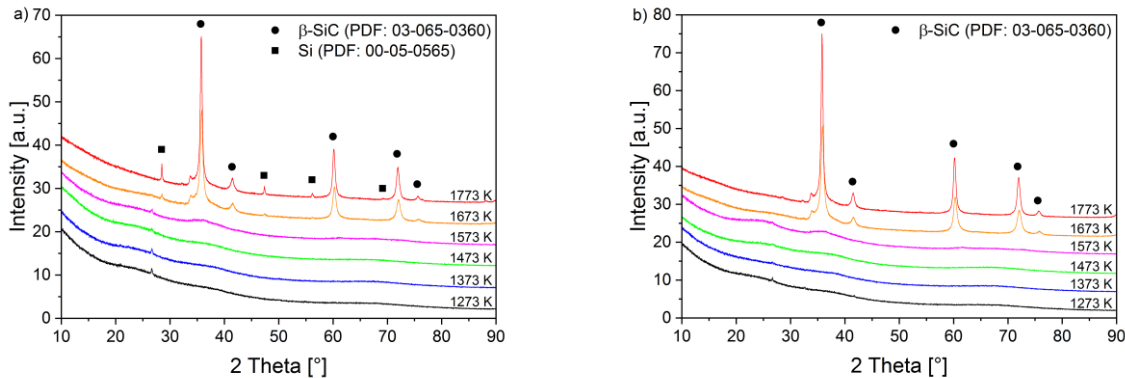
Figure 5.16: XRD patterns of a) PSZ 10- and b) PSZ 20-derived Si-C-N ceramics obtained by pyrolysis in flowing Ar atmosphere.

To investigate the p_{N2}-dependence of the phase evolution in Si-C-N (see Figure 5.7) PSZ 10 and PSZ 20 was pyrolyzed in flowing Ar/N$_2$ with p_{N2} = 0.5 bar. Figure 5.17 shows thermogravimetric experiments during pyrolysis of PSZ 10 and PSZ 20 in Ar/N$_2$ together with the corresponding experiments in Ar. The mass loss of PSZ 10 is generally lower in Ar/N$_2$ atmosphere compared to pure Ar. This is resulting from the lower mass loss during crosslinking of the liquid polymer below 573 K in stage 1 (see also Figure 5.18). The mass loss of PSZ 20 in stage 1 is slightly steeper in Ar compared to Ar/N$_2$ but the total mass change is the same. No dependence of the

mass loss on the p_{N2} is observed in stage 2 (573 K < T < 1273 K). The main effect of the different p_{N2} is observed in stage 3 (T > 1273 K). Samples, which were pyrolyzed at maximum temperatures of 1273 K – 1573 K show a constant mass during stage 3 in both, Ar/N$_2$ and pure Ar atmospheres. However, heat-treatment up to maximum temperatures of 1673 K and 1773 K in Ar/N$_2$ results in much lower and less pronounced mass losses compared to pure Ar (see also Figure 5.18). As predicted by the calculation in Figure 5.7, an increase of the p_{N2} is resulting in an increased temperature of reaction (5.2).
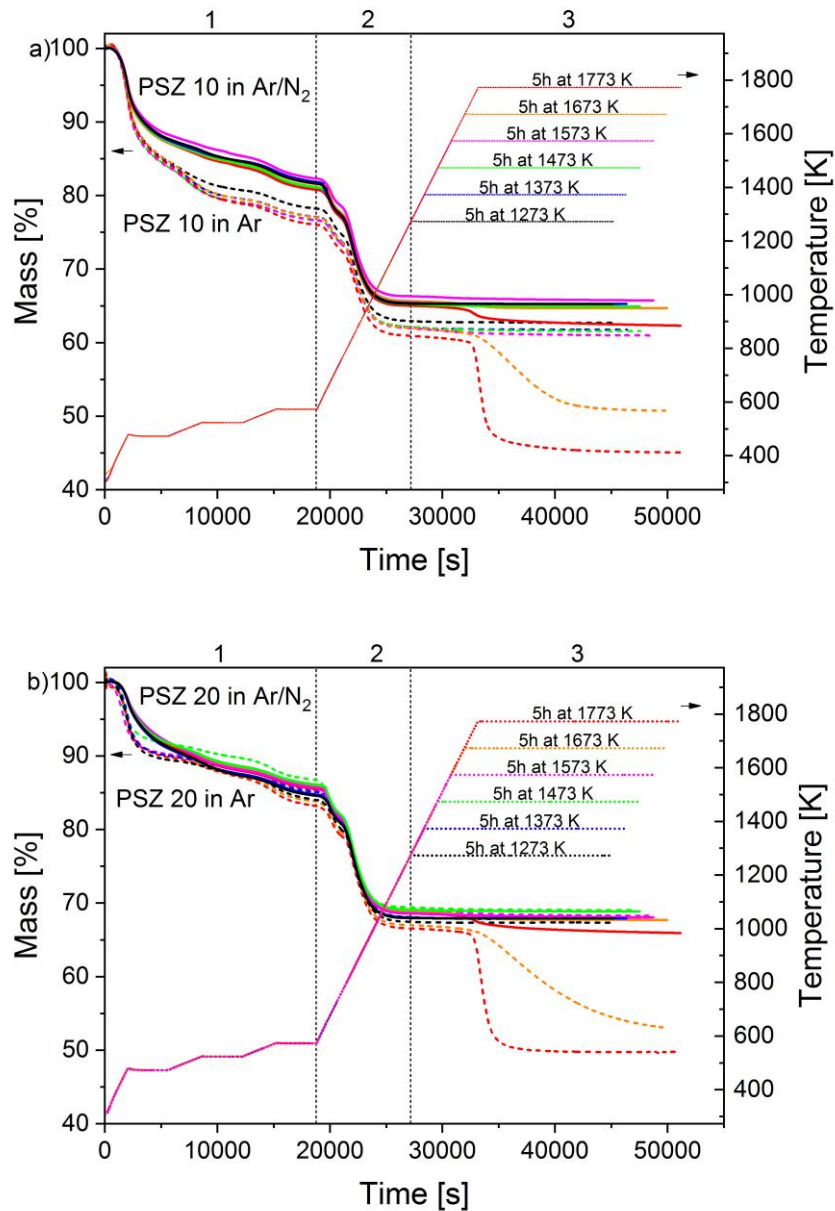
Figure 5.17: Thermogravimetric analysis of a) PSZ 10 and b) PSZ 20 pyrolysis up to maximum temperatures of 1273 K – 1773 K in flowing Ar/N$_2$ (p_{N2} = 0.5 bar). Results for pyrolysis in flowing Ar are shown for comparison.
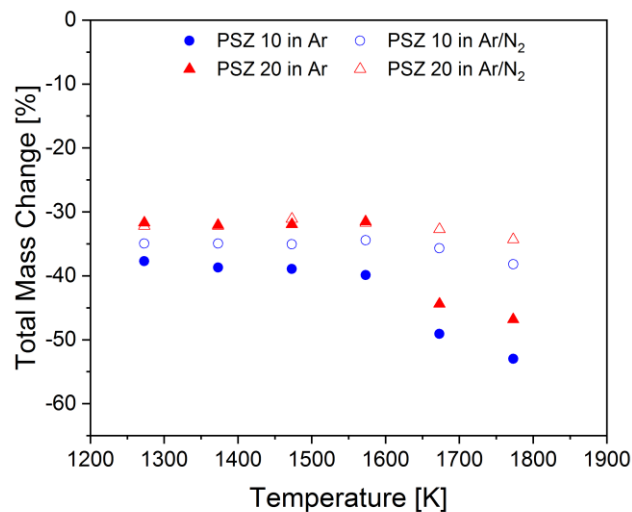
Figure 5.18: Total mass change of PSZ 10- and PSZ 20-derived Si-C-N ceramics after pyrolysis in flowing Ar- and Ar/N$_2$-atmosphere.

Microstructures of PSZ 10 and PSZ 20-derived Si-C-N ceramics, which were prepared in Ar/N$_2$ (p$_{N2}$ = 0.5 bar), are depicted in Figure 5.19 and Figure 5.20, respectively. Pyrolysis at maximum temperatures of 1273 K to 1573 K resulted in very homogeneous microstructures. These samples were X-ray amorphous (see Figure 5.21). Si-C-N ceramics, which were pyrolyzed at maximum temperatures of 1673 K and 1773 K, show precipitation of particles and partly transformed domains corresponding to crystallization of Si$_3$N$_4$ in Figure 5.21.
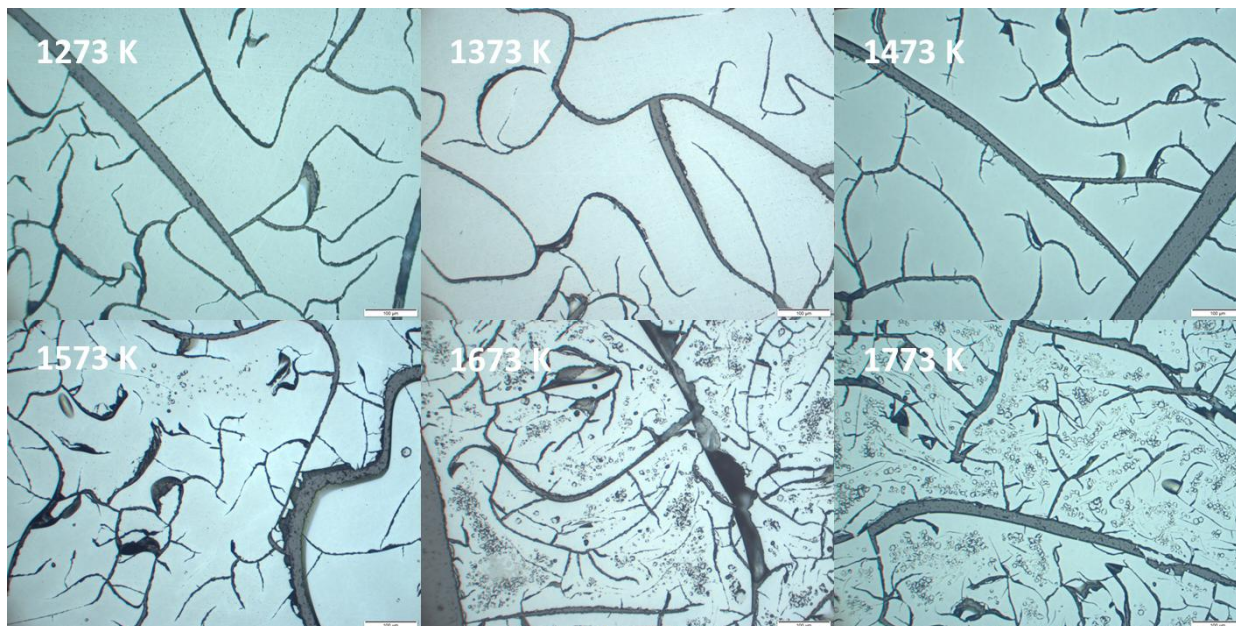
Figure 5.19: Micrographs of PSZ 10-derived Si-C-N ceramics pyrolyzed at 1273 K – 1773 K in flowing Ar/N$_2$ (p$_{N2}$ = 0.5 bar). Scale bars correspond to 100 µm.
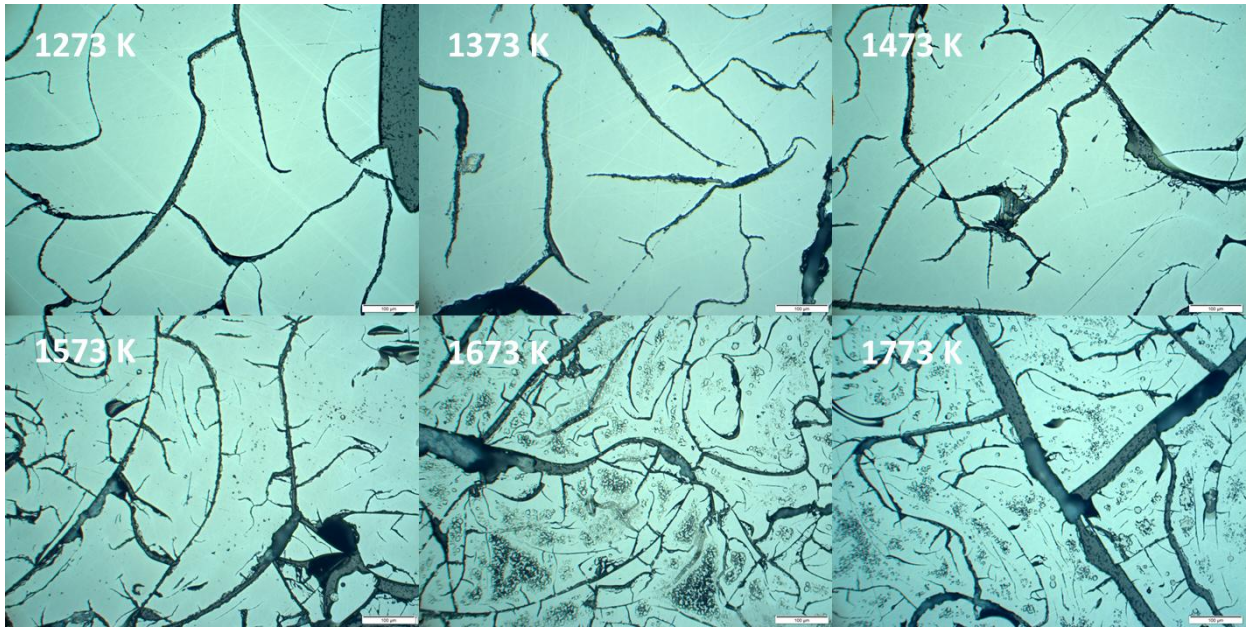
Figure 5.20: Micrographs of PSZ 20-derived Si-C-N ceramics pyrolyzed at 1273 K – 1773 K in flowing Ar/N$_2$ (p$_{N2}$ = 0.5 bar). Scale bars correspond to 100 µm.
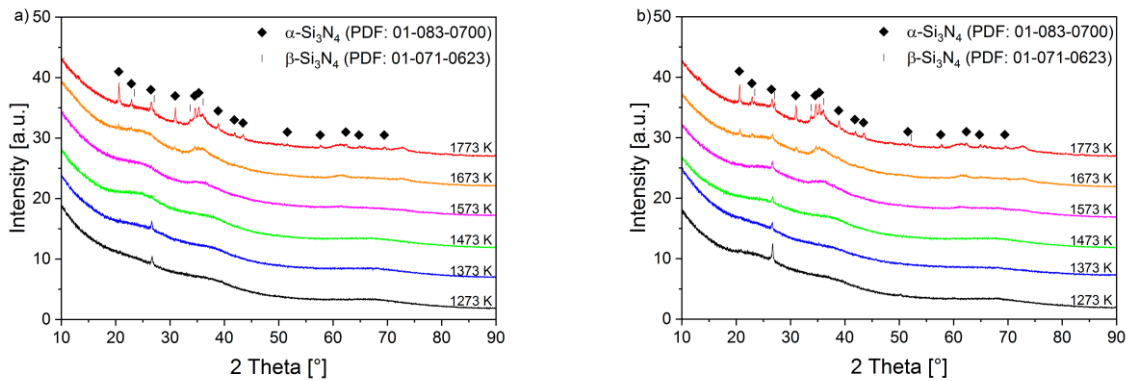
Figure 5.21: XRD patterns of a) PSZ 10- and b) PSZ 20-derived Si-C-N ceramics obtained by pyrolysis in flowing Ar/N$_2$ atmosphere.

5.1.3. Discussion and Conclusion

Although amorphous Si-(B-)C-N ceramics are not in thermodynamic equilibrium, the observed phase formation, crystallization, and high-temperature reactions can be understood by considering thermodynamic equilibrium calculations based on their composition [16][97][98][99][101] [102][103][104].

Thermodynamic modeling of the phase evolution, based on the Si:C:N:H-composition of the preceramic polymer (Figure 5.1) displays the pyrolysis i.e. the transformation of the liquid preceramic polymer into an amorphous solid Si-C-N ceramic in a closed system. Hydrogen, which is an inherent part of the polymers functional groups, is forming hydrogen-containing gas species. According to Figure 5.1b, CH_4 and H_2 are the major gaseous pyrolysis products. Other hydrogen-containing gas species are only present with a very low partial pressure. At high temperatures, additionally N_2 plays a key role. Pyrolysis products, predicted by the calculation, were confirmed experimentally by mass spectroscopic analysis of the STA off-gas (see Figure 5.10 and Figure 5.11). Combined DTA, thermogravimetric and mass spectroscopic analysis (see Figure 5.12) show that pyrolysis is an endothermic process with a two-step character. The first peak at about 900 K is associated with the release of CH_4 and H_2 and the second peak at around 1050 K only with the release of H_2. However, the release of H_2 is observed over a temperature range from 600 K to 1250 K. The observed temperature ranges of CH_4 and H_2 evolution is in good accordance with the work by Garcia-Garrido et al. [105]. Additionally, also the mass change during pyrolysis coincides with the two-step process.

The precursor polymers Ceraset® PSZ 10 and PSZ 20 possess a hybrid-structure consisting of units of polyhydridomethylsilazane (PHMS) and polymethylvinylsilazane (PMVS). For PHMS Bill et al. [16] [102] has shown, that around 800 K crosslinking of $Si-CH_3$ and $Si-CH_3$ or Si-H groups leads to the release of CH_4 and H_2, respectively. Above 800 K crosslinking of $Si-CH_3$ and Si-H with N-H groups leads to the formation of Si-N bonds and the release of CH_4 and H_2, respectively. For PMVS it was shown by Bill et al. [16][101], that crosslinking of the vinyl groups takes place up to temperatures of 600 K. At higher temperatures sp²-hybridized carbon (C=C) and Si-H are formed. Around 800 K, Si-H and N-H groups react and form Si-N bonds under release of H_2. Thus, the sum of all these effects contributing to the release of CH_4 and H_2, is observed in the conducted experiments. Additionally, the release of NH_3 was observed by Bill et al. [101] during pyrolysis of PMVS in the temperature range from 500 K to 800 K. The release of NH_3 was not observed in our experiments. Due to the small amount of PMVS-like units (x=0.2) in the preceramic polymer Ceraset® PSZ 10 and PSZ 20, NH_3 is only expected to a very low amount (see Figure 5.1b) which was not detectable. Furthermore, experiments were conducted in pure Ar atmosphere, in contrast to experiments in nitrogen by Bill et al. [101].

The mass loss during crosslinking of PSZ 10 is larger compared to PSZ 20 indicated by the pre-pyrolysis step (stage 1) in Figure 5.9. PSZ 10 is a low-molecular fraction of the Ceraset®

polysilazane. Therefore, the evaporation of oligomers could be more pronounced and thus lead to the larger mass loss during this stage compared to PSZ 20. Long holding times, which were applied to prevent the formation of bubbles during stage 1, probably spread the release of H_2 over a time-period, which is too long and prevents the detection by mass spectrometry. Only a small H_2-peak, which is visible at the end of the first heating period to 573 K in Figure 5.10 and Figure 5.11 could account for crosslinking process during this stage. In addition PSZ 10 shows a lower mass loss during the crosslinking process in stage 1 in Ar/N_2 compared to pure Ar (Figure 5.17a). In contrast to that, the mass loss of PSZ 20 is just initially steeper in Ar/N_2 and approaches the same value as in pure Ar. This is indicating, that the evaporation of polysilazane oligomers, which are present in the low-molecular PSZ 10 in a higher amount compared to PSZ 20 is strongly depending on the nitrogen partial pressure. With higher p_{N2}, the evaporation of oligomers during crosslinking in stage 1 is slowed down.

Conclusively, the composition of the gas phase has a direct influence on the composition of the condensed phase. Since calculations have been performed in a closed system, the gas phase, consisting of hydrogen-containing gas species, is in equilibrium with the condensed phase at every point (Figure 5.1). Therefore, the thermal dissociation of methane ($CH_4=C+2H_2$) above 693 K is influencing the composition of the Si-C-N ceramic, by increasing its carbon content. According to the calculations, depicted in Figure 5.3, the thermodynamic equilibrium composition of the PSZ 10- and PSZ 20-derived Si-C-N-H system is in the three-phase field Gas+SiC+Si_3N_4 below 693 K. Therefore, the composition of the condensed phases is on the tie-line SiC-Si_3N_4 in the isothermal section of the system Si-C-N (see Figure 5.2). Thus, all carbon is bound either as SiC or as methane in the gas phase. Above 693 K, the equilibrium composition of the PSZ 10- and PSZ 20-derived Si-C-N-H system is in the four-phase field Gas+SiC+Si_3N_4+C (see Figure 5.3).

Contrary to the thermodynamic calculations, experiments were performed in an open system. Therefore, hydrogen-containing gas species, which are formed upon pyrolysis of the preceramic polymer, are carried away in the experiment by the flowing gas atmosphere and are removed from the considered system. Consequently, effects like the thermal dissociation of methane will not affect the composition of the condensed phase in the same way. Both, the actual composition of the PSZ 10- and PSZ 20-derived amorphous Si-C-N ceramic and the overall composition of the condensed phases calculated from the Si-C-N-H-ratio of the preceramic polymer in a closed system are inserted into the isothermal section of the Si-C-N system at 1757 K in Figure 5.2. The isothermal section as well as the concentration of the condensed phases calculated from the Si-C-N-H ratio are valid for the fully crystalline constituents of the Si-C-N ceramic in thermodynamic equilibrium. However, the actual PSZ 10- and PSZ 20-derived Si-C-N ceramic is amorphous and requires temperatures above 1573 K (see Figure 5.16 and Figure 5.21). Seifert et al. even give temperatures of about 1700 K for crystallization [104]. Nevertheless, the overall composition of the amorphous PSZ 10- and PSZ 20-derived Si-C-N

ceramic and the composition of the condensed phases calculated from the Si-C-N-H ratio of the preceramic polymer are both located in the three-phase field SiC+Si_3N_4+C or on the tie-line SiC-Si_3N_4.

The actual composition of the PSZ 10- and PSZ 20-derived amorphous Si-C-N ceramic and the composition of the condensed phases calculated from the Si-C-N-H-ratio of the preceramic polymer in a closed system are in fairly good agreement (see Figure 5.2). The closest agreement exists with the calculated composition at 850 K. However, with a shift to a higher Si content of less than 5 %. This temperature is in good agreement with the start of the endothermic reaction at 800 K observed in DTA investigations (see Figure 5.12). However, the experimentally observed temperature range of the pyrolysis process ends at 1250 K. In comparison to the calculated composition at 1250 K, the actual composition of the PSZ 10- and PSZ 20-derived Si-C-N ceramic is shifted to lower carbon content. This is consistent with the discussion above. Contrary to the calculation in a closed system, CH_4 is carried away in the experimental setup by the flowing atmosphere. Therefore, the thermal dissociation of CH_4 above 693 K does not contribute to the carbon content of the obtained ceramic. Seifert et al. [104] already discussed this depletion in carbon compared to thermodynamic modeling for PNVS-, PHMC-, PMVC-, PHMS- and PMVS-derived Si-C-N ceramics.

The composition of the condensed phases calculated from the Si-C-N-H composition at 300 K to 700 K is located on the tie-line SiC-Si_3N_4 i.e. shifted to even lower carbon content compared to the measured composition of the PSZ 10- and PSZ 20-derived Si-C-N ceramic. Since the pyrolysis of the preceramic polymer does not take place at these temperatures, the calculated values do not have an actual physical meaning. The activation energy for the endothermic transformation of the polysilazane into the solid amorphous Si-C-N ceramic is not available at these temperatures.

At about 1400 K, the composition of the condensed phases, calculated from the composition of the Si-C-N-H polymer, changes from constant Si/N-ratio to a constant Si/C-ratio. This means, the overall composition of the condensed phases is depleted in its nitrogen content. This temperature corresponds to the point of intersection of the equilibrium partial pressures of CH_4 and N_2 in the gas phase at 1399 K, which is established as a result of the Si-C-N-H composition of the preceramic polymer (see Figure 5.1).

High-temperature stability

The high-temperature stability of the PSZ 10- and PSZ 20-derived Si-C-N ceramic is determined by its composition. Figure 5.4 shows the composition of the obtained Si-C-N ceramic in isothermal sections of the Si-C-N system. At temperatures below 1757 K, the composition of the PSZ 10- and PSZ 20-derived Si-C-N ceramic is in the three-phase field SiC+Si_3N_4+C if crystallization would occur. At temperatures above 1757 K, reaction (5.2) takes place. The

calculated phase fraction diagram in Figure 5.5 shows that C and Si_3N_4 are reacting under formation of SiC and N_2, which is released into the atmosphere. Therefore, the composition of the Si-C-N ceramic is located in the three-phase field Gas+SiC+Si_3N_4 for 1757 K < T < 2114 K. Reaction (5.2) was validated by detecting the N_2-release by mass spectroscopy (see Figure 5.10 and Figure 5.11). Due to the release of N_2, the composition of the Si-C-N ceramic is depleted in nitrogen. The composition of the remaining Si-C-N ceramic is shifting along the marked reaction path to the tie-line SiC-Si_3N_4.

The release of N_2 in reaction (5.2) results additionally in a mass loss, which was detected by thermogravimetry (see Figure 5.9). The experimentally observed mass loss is thereby in very good agreement with the mass change calculated from the phase fraction diagram (see Figure 5.6). Due to their identical composition, PSZ 10 and PSZ 20 yield the same mass loss due to the high-temperature reaction (5.2).

Microstructure and crystallization

The observed microstructural changes of PSZ 10- and PSZ 20-derived Si-C-N ceramics above 1573 K are also resulting from the release of N_2 by reaction (5.2). After heat treatment at maximum temperatures of 1673 K and 1773 K, the otherwise homogeneous microstructure (Figure 5.13 and Figure 5.14) of the obtained Si-C-N ceramics transforms and becomes porous as a result of the mass loss by release of N_2. Additionally, EDX analysis (Figure 5.15) revealed that the composition of the Si-C-N ceramic becomes nitrogen-poor. XRD analysis (Figure 5.16) showed, that crystallization of β-SiC occurs under these conditions. This is in good accordance with literature data, reporting crystallization of Si-C-N ceramics at about 1700 K in Ar [106]. Since the crystallization of β-SiC coincides with the occurrence of reaction (5.2), it must be concluded, that β-SiC which is newly formed during this process is detected. This is in accordance with Janakiraman et al. [107] who observed the rapid crystallization of SiC as a result of the carbothermal reaction in precursor-derived Si-B-C-N ceramics. Golczewski [108][109] derived an approach to describe the structural transformation during crystallization of short-range ordered SiC_iN_{4-i} (i = 1-3) ceramics by thermodynamic equilibrium calculations. According to that, mixed tetrahedra in the Si-C-N structure have a particularly higher resistance against crystallization [109]. After crystallization of one of the components, depending on the specific composition of the amorphous Si-C-N ceramic, the remaining material is decomposing in an eutectoid-like transformation (amorph.-Si-C-N = nano-SiC + nano-SiN) [108]. Since homogeneous and X-ray amorphous Si-C-N ceramics were obtained by pyrolysis up to a maximum temperature of 1573 K in Ar and Ar/N_2 atmosphere, this is considered as the maximum applicable pyrolysis temperature.

pN$_2$-dependent reactions

The influence of the nitrogen partial pressure on the high-temperature stability of the PSZ 10- and PSZ 20-derived Si-C-N ceramic was predicted by thermodynamic equilibrium calculations. With increasing p_{N2}, the reaction temperatures in the Si-C-N system are shifted to higher temperatures (see Figure 5.7). For the experimentally applied conditions p_{N2} = 0.5 bar, reaction temperatures of 1701 K and 2062 K are expected for reaction (5.2) and (5.3), respectively. This is confirmed by experimental investigations. Si-C-N ceramics obtained by pyrolysis of PSZ 10- and PSZ 20 in flowing Ar/N$_2$ (p_{N2} = 0.5 bar) at a maximum temperature of 1673 K do not show an additional mass loss by reaction (5.2). Only heat-treatment at a maximum temperature of 1773 K in flowing Ar/N$_2$ (p_{N2} = 0.5 bar) resulted in a pronounced mass loss by reaction (5.2). However, the mass loss at 1773 K in Ar/N$_2$ is lower compared to pure Ar atmosphere. Therefore, reaction kinetics seem to be slower in Ar/N$_2$ compared to pure Ar and the reaction seems to be not completed after the applied holding time of 5 h. Due to the less pronounced transformation by reaction (5.2) in Ar/N$_2$, the obtained Si-C-N ceramics show a more homogeneous microstructure (see Figure 5.19 and Figure 5.20). However, precipitations are visible in after heat-treatment up to 1673 K and 1773 K, which correspond to the crystallization of α- and β-Si$_3$N$_4$ (see Figure 5.21). This is in good accordance with work by Riedel et al. [106] who observed crystallization of the NCP 200-derived Si-C-N ceramic at up to 200 K higher temperatures in N$_2$ compared to Ar atmospheres. Furthermore, crystallization started with β-SiC in Ar and Si$_3$N$_4$ in N$_2$ as a result of the carbothermal reaction shifted to lower temperatures in Ar.

The influence of the nitrogen partial pressure on the high-temperature stability can also be observed very locally. Si-C-N ceramics, which were obtained by pyrolysis at maximum temperatures of 1673 K in Ar exhibit a microstructure being partly transformed by the carbothermal reaction and partly (yet) unaffected (see Figure 5.13-Figure 5.15). Areas, which are at the surface or adjacent to cracks and thus accessible for the pure Ar atmosphere, are always transformed. In contrast, untransformed areas are never located directly adjacent to cracks. These "survive" in the bulk of the Si-C-N ceramic because of locally higher nitrogen partial pressures compared to the flowing Ar atmosphere.

As the temperature of reaction (5.3) was not reached, the related mass loss was not observed in the conducted thermogravimetric experiments.

Conclusively, thermodynamic calculations were well suitable to predict the pyrolysis behavior of the precursor-polymers Ceraset® PSZ 10 and PSZ 20 as well as the high-temperature stability and the underlying reactions of the obtained Si-C-N ceramic.

5.2. Si-B-C-N ceramics

In this section, phase equilibria of precursor-derived Si-B-C-N ceramics were investigated by thermodynamic calculations and high-temperature experiments. To this end, pyrolysis of the *Si-B-C-N_2* preceramic-polymer was modeled by thermodynamic calculations using the polymer composition (see Table 5.1). The high temperature stability of the precursor-derived *Si-B-C-N_2* and *Si-B-C-N_1* ceramics was modeled using the composition of the obtained ceramic (see Table 5.2). Additionally, combined thermogravimetric, DTA and mass spectrometric investigations were conducted with the *Si-B-C-N_1* preceramic-polymer at temperatures from 1473 K to 1773 K in flowing gas atmospheres of different nitrogen partial pressure (pure Ar and Ar/N_2 with p_{N2} = 0.5 bar).

5.2.1. Thermodynamic analysis of pyrolysis and high-temperature stability

Figure 5.22 shows the phase fraction diagram and the composition of the associated gas phase calculated for the composition of the *Si-B-C-N_2* precursor-polymer ($SiBC_3N_3H_{10}$)$_n$. The calculations were performed for a closed system under the boundary conditions of a total amount of substances of 1 mol and at a constant ambient pressure of $1 \cdot 10^5$ Pa with a self-developing gas volume. In thermodynamic equilibrium, the composition of the *Si-B-C-N_2* precursor is located in the four-phase field Gas+Si_3N_4+BN+Graphite over the whole temperature range. While the relative amounts of Si_3N_4 and BN are constant at 0.13 mol and 0.11 mol, respectively, the relative amount of graphite is increasing from approx. 0.03 mol to approx. 0.17 mol in the temperature range 500 K – 1200 K. The gas phase (Figure 5.22b), which is in thermodynamic equilibrium with the condensed phases, is mainly consisting of CH_4, H_2, N_2 and NH_3. Thereby, the decreasing amount of CH_4 by thermal dissociation (CH_4=C+$2H_2$) is corresponding to the increasing amount of H_2, with a point of inversion at 771 K and 0.45 bar, and graphite. The partial pressures of N_2 and NH_3 are predominantly decreasing with increasing temperature. In general, mainly C- and N-containing gas species are formed while B- and Si-containing gas species are only present in very small fractions (< 10^{-8} bar) and at the highest temperatures (> 1250 K). As a consequence, upon pyrolysis of the polymer, with permanent exchange of the atmosphere, the composition is shifted to lower C- and N-content while both the Si- and B-content remains constant (($SiBC_3N_3H_{10}$)$_n$ $\rightarrow$ $SiBC_{1.4}N_{2.3}$).
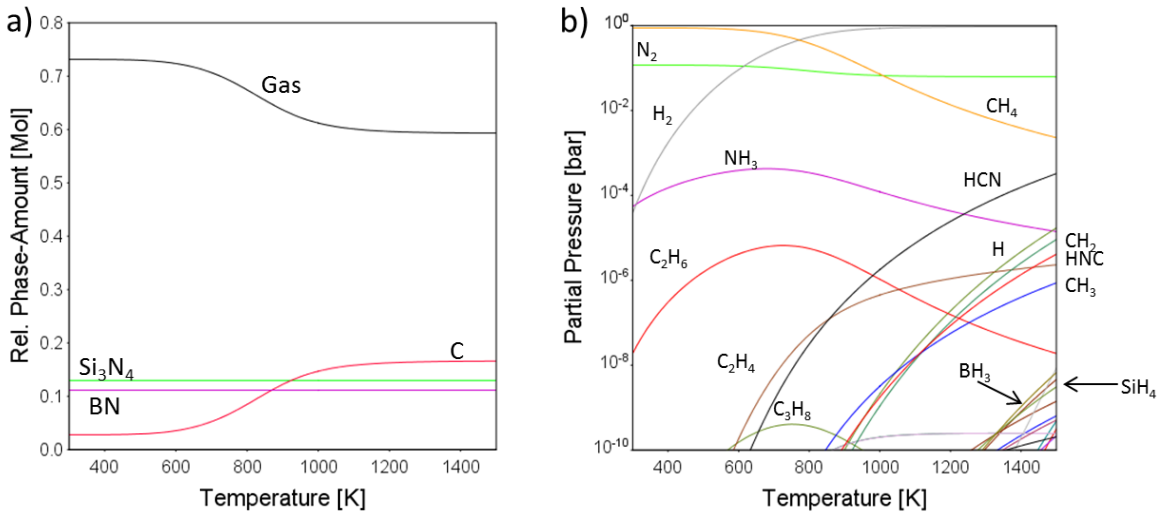
Figure 5.22: Calculated a) phase fraction diagram and b) composition of the gas phase for the *Si-B-C-N_2* precursor polymer [SiBC$_3$N$_3$H$_{10}$]$_n$.

Figure 5.23 shows the isothermal section in the Si-B-C-N system at constant x(B) = 0.1754. In contrast to the isothermal sections in the ternary Si-C-N system (Figure 5.4), in the isothermal sections of the quaternary Si-B-C-N system, the corners of the diagram do not only represent the pure element, but the element plus a constant amount of boron (e.g. x(B) = 0.1754). Equally, the ends of the tie-lines do not represent a single phase but two phases, for example Si$_3$N$_4$+BN.

If crystallization would occur, the composition of the *Si-B-C-N_2* precursor-derived ceramic, indicated in Figure 5.23, is located in the four-phase field BN+C+Si$_3$N$_4$+SiC at temperatures below 1773 K. The corresponding phase amounts are depicted in Figure 5.24. In contrast to the equilibrium calculation of the Si-B-C-N-H polymer (Figure 5.22), were the condensed phase is consisting of Si$_3$N$_4$+BN+C, the calculation with the composition of the resulting Si-B-C-N ceramic is resulting in BN+C+Si$_3$N$_4$+SiC (Figure 5.23) with a small amount of SiC (Figure 5.24).

At 1757 K, Si$_3$N$_4$ is reacting with the excess graphite under formation of SiC and N$_2$ (reaction (5.2)). While Si$_3$N$_4$ is consumed completely, the amount of BN remains constant (see Figure 5.24a). Figure 5.24b shows the release of N$_2$ into the atmosphere relative to the constant amount of Ar. As a result, the Si-B-C-N ceramic is in the four-phase field Gas+C+BN+SiC at temperatures between 1757 K and 2586 K. Figure 5.24a shows that a melt is at 2586 K by quaternary transition reaction:

$$BN + SiC + C = L\left(\underline{B}, Si, C\right) + 1/2 N_2 \qquad (5.4)$$

under release of N$_2$ (Figure 5.24b). Molecular nitrogen is the only gas species which is formed up to the highest temperatures above 2586 K were also Si- and C-containing gas species (Si, SiC$_2$, Si$_2$C, B) are formed.

Figure 5.25 shows the isothermal section in the system Si-B-C-N at constant x(B) = 0.0525. The composition of the *Si-B-C-N_1* precursor-derived ceramic is indicated. At temperatures below 1757 K, the composition of the *Si-B-C-N_1* ceramic is located in the four-phase field BN+C+Si_3N_4+SiC. Therefore, the transition reaction of Si_3N_4 with the excess graphite under formation of SiC and release of N_2 takes place at 1757 K (Figure 5.26). However, the carbon content is lower compared to the *Si-B-C-N_2* ceramic, (*Si-B-C-N_1*: C/Si_3N_4 < 1/3; *Si-B-C-N_2*: C/Si_3N_4 > 1/3) resulting in left over Si_3N_4 after the reaction (Figure 5.26a). Therefore, the composition of the Clariant Si-B-C-N ceramic is located in the four-phase field Gas+Si_3N_4+SiC+BN between 1757 K and 2114 K (Figure 5.25c). As a result, the thermal decomposition of the surplus Si_3N_4 into Si, which is liquid at this temperature, and N_2 is taking place at 2114 K (Figure 5.26a). At 2114 K < T < 2564 K the composition of the Clariant Si-B-C-N ceramic is in the four phase field Gas+SiC+BN+L (Abb. 5.24d). At 2564 K the reaction of BN with SiC is taking place:

$$BN + SiC = L(\underline{B}, Si, C) + 1/2 N_2 \qquad (5.5)$$
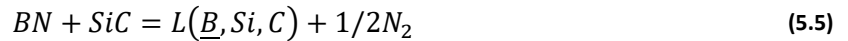
All reactions in the *Si-B-C-N_1* ceramic are taking place under release of N_2 (Figure 5.26). Other, Si- and C-containing gas species are only formed at the highest temperatures above 2564 K.
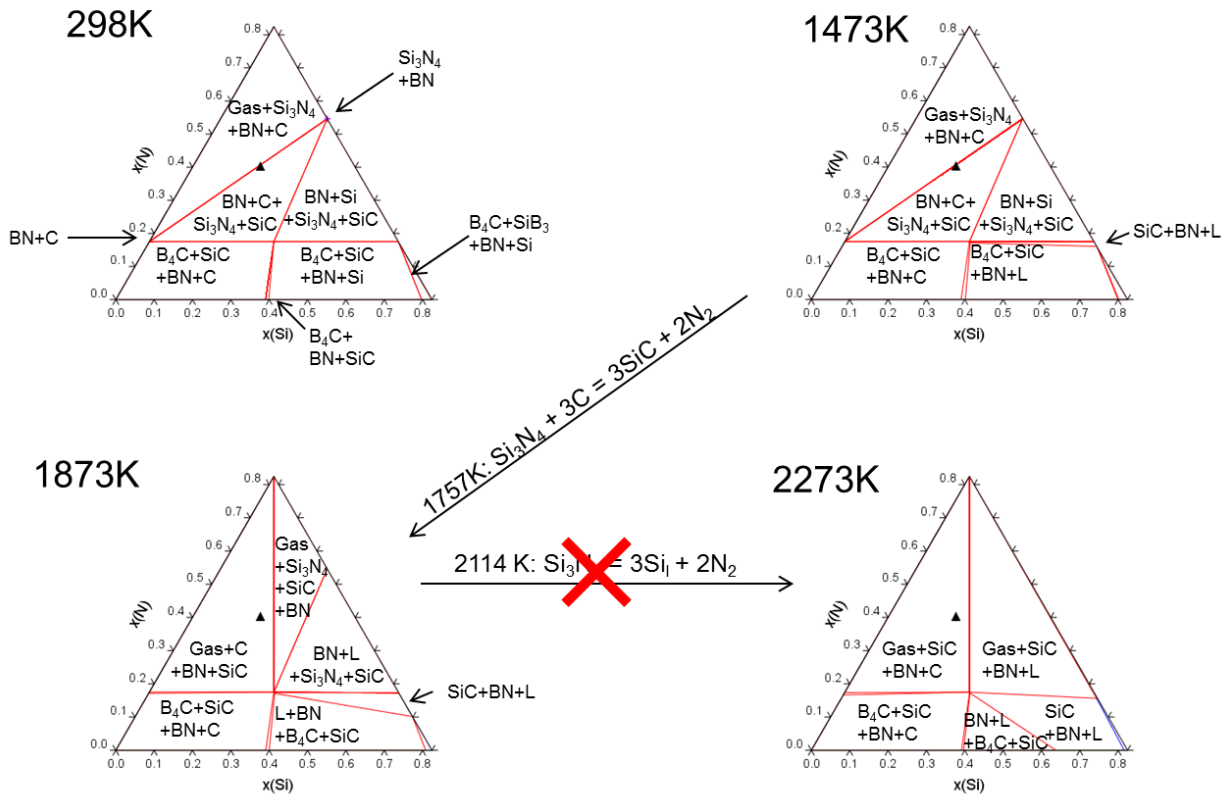
Figure 5.23: Calculated isothermal sections for constant x(B) = 0.1754. The composition of the *Si-B-C-N_2* precursor-derived ceramic is indicated.
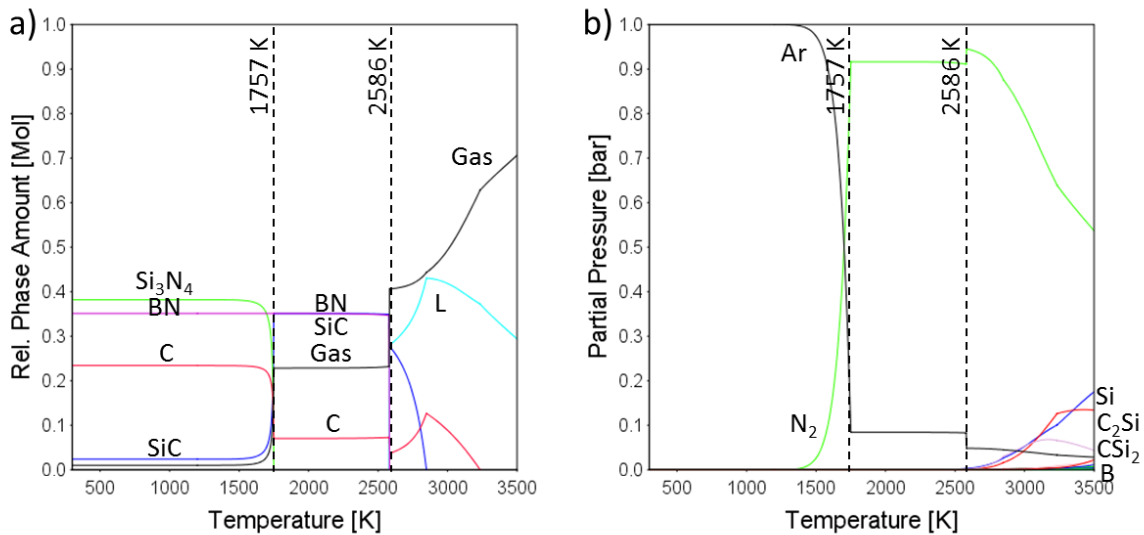
Figure 5.24: Calculated a) phase fraction diagram and b) composition of the gas phase for the *Si-B-C-N_2* precursor-derived ceramic.
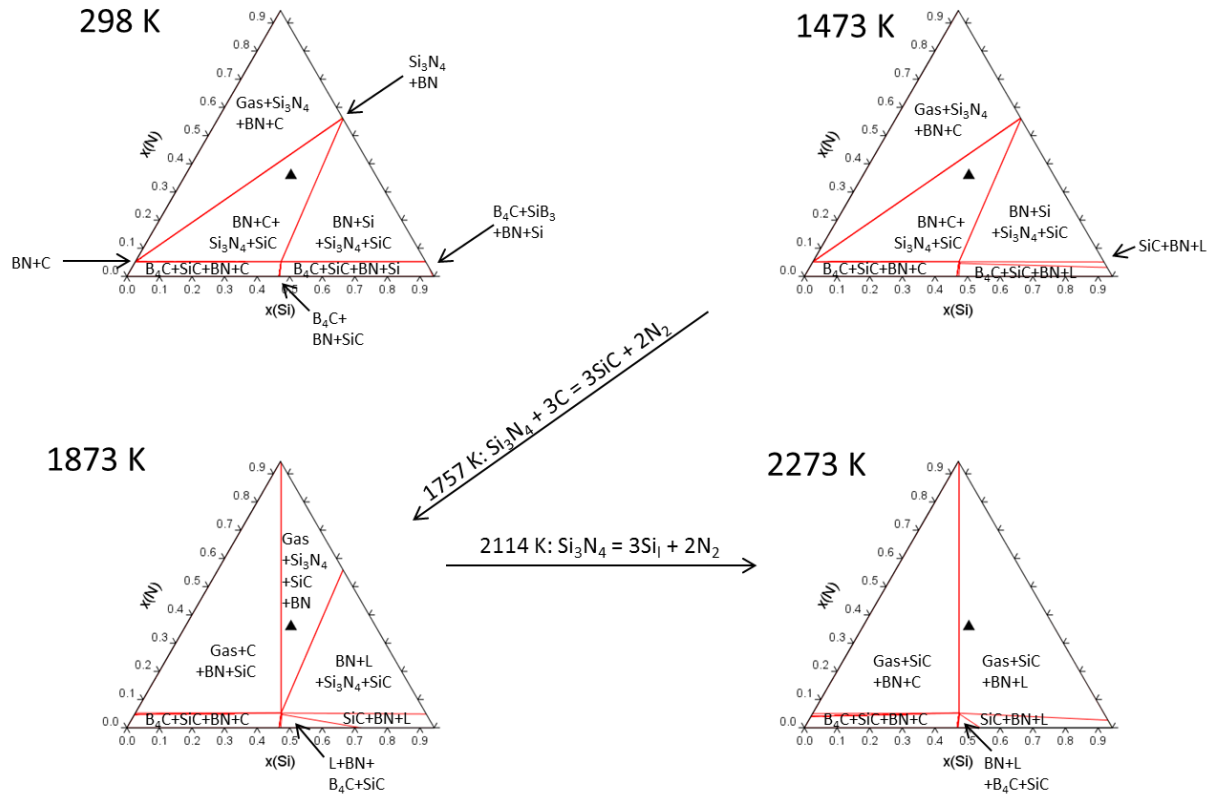
Figure 5.25: Calculated isothermal sections for constant x(B)= 0.0525. The composition of the *Si-B-C-N_1* precursor-derived Si-B-C-N ceramic is indicated.
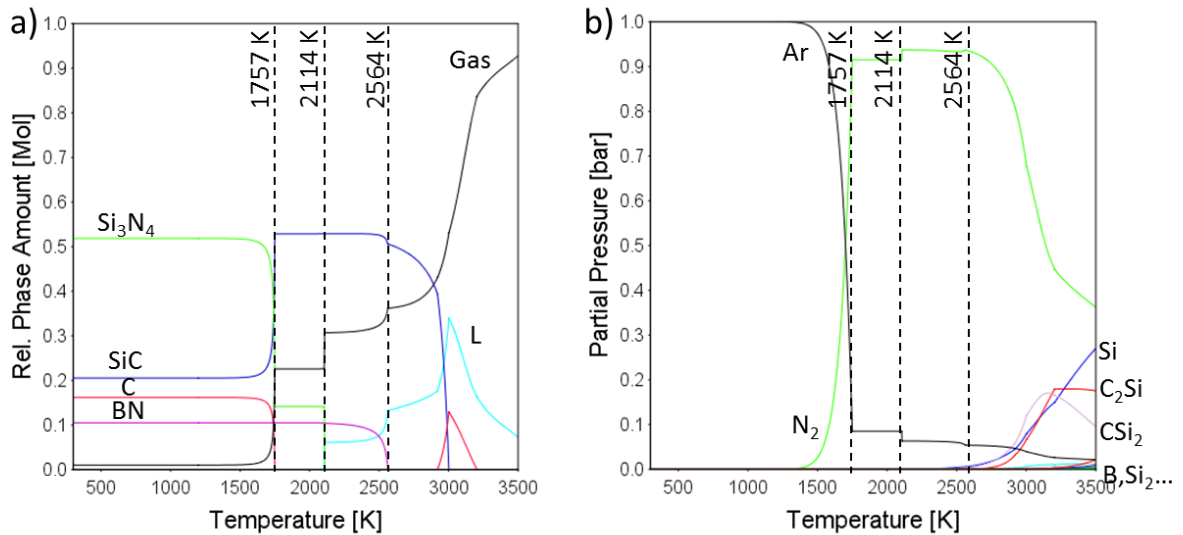
Figure 5.26: Calculated a) phase fraction diagram and b) composition of the gas phase for the *Si-B-C-N_1* precursor-derived Si-B-C-N ceramic.

Figure 5.27 shows isothermal sections of the ternary Si-B-C system. The Si:B:C ratios of the *Si-B-C-N_2* ($Si_1B_1C_{1.4}$) and *Si-B-C-N_1* ($Si_6B_1C_5$) ceramics are located in the three-phase fields $B_4C+C+SiC$ and $B_4C+Si+SiC$, respectively. In the latter case, a melt is formed at 1657 K in the ternary system, which is 30 K lower compared to pure Si.

1473 K   **1673 K**
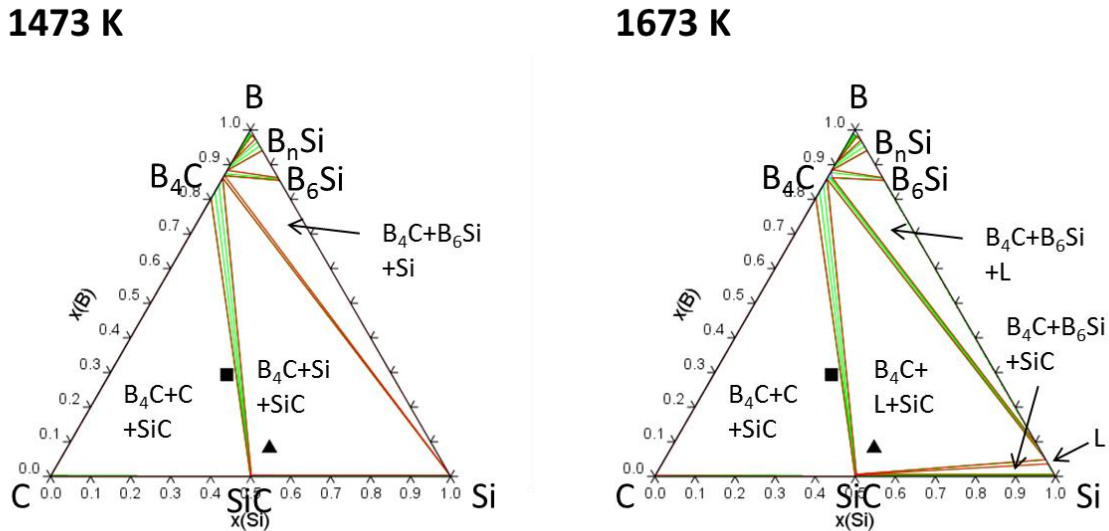
Figure 5.27: Calculated isothermal sections of the Si-B-C system at 1473 K and 1673 K. The compositions of ▲ *Si-B-C-N_1* and ■ *Si-B-C-N_2* ceramics are indicated.

The nitrogen content is decisive for the high-temperature stability of Si-B-C-N-ceramics. To discuss the ideal nitrogen-content, isopleths from the Si:B:C-ratio of the *Si-B-C-N_2* ($Si_1B_1C_{1.4}$) and *Si-B-C-N_1* ($Si_6B_1C_5$) ceramic to the N-corner of the Si-B-C-N tetrahedron were calculated. These are depicted in Figure 5.28. The isopleth $Si_1B_1C_{1.4}$-N including the *Si-B-C-N_2* ceramic (Figure 5.28a) is divided into three parts. For x(N) < 0.23 the ceramic is in the four-phase field $B_4C+C+SiC+BN$. Melt and gas phase are formed at 2568 K and 2586 K, respectively. A nitrogen content of 0.23 < x(N) < 0.41 is resulting in the four-phase field $Si_3N_4+C+SiC+BN$ at temperatures below 1757 K and Gas+C+SiC+BN at 1757 K – 2586 K. The composition of the *Si-B-C-N_2* ceramic is located in this area. For x(N) > 0.41, the composition is resulting in the four-phase field $Si_3N_4+Gas+C+BN$ up to 1757 K, containing free (molecular) nitrogen gas. The isopleth $Si_6B_1C_5$-N including the *Si-B-C-N_1* ceramic is more complex at low nitrogen fractions (Figure 5.28b). For x(N) < 0.07 and x(N) < 0.16 the ceramic contains free Si in form of $B_4C+Si+SiC+BN$ and $Si_3N_4+Si+SiC+BN$, respectively. Therefore, melt formation is observed in the multi-component system at 1669 K and 1686 K, respectively. The composition of the *Si-B-C-N_1* ceramic is located in the range 0.16 < x(N) < 0.43. Therefore, the phase evolution discussed in Figure 5.26 is found: $Si_3N_4+C+SiC+BN$ up to 1757 K, $Si_3N_4+Gas+SiC+BN$ up to 2114 K, L+Gas+SiC+BN up to 2564 K and L+Gas+SiC above 2564 K. The latter transition is concentration-dependent. The highest application temperatures, i.e. without formation of a gas or liquid phase, for the *Si-B-C-N_2* ceramic would be for x(N) < 0.41 and < 0.23 at 1757 K and 2568 K, respectively. For the *Si-B-C-*

N_1 ceramic the highest application temperature is found for a nitrogen content of 0.16 < x(N) < 0.43 at 1757 K.
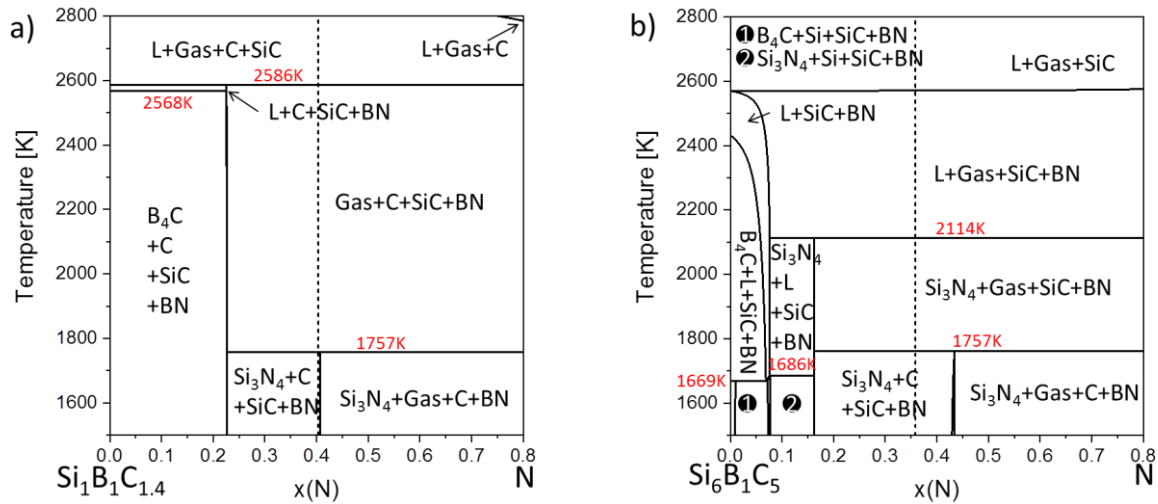
Figure 5.28: Calculated isopleths in the Si-B-C-N system for a) $Si_1B_1C_{1.4}$-N and b) $Si_6B_1C_5$-N. Compositions of the a) *Si-B-C-N_2* and b) *Si-B-C-N_1* ceramics are indicated as dashed lines.

Phase stability diagrams for the Si:B:C-ratios of the *Si-B-C-N_2* ($Si_1B_1C_{1.4}$) and *Si-B-C-N_1* ($Si_6B_1C_5$) ceramic are shown in Figure 5.29. These diagrams show the dependence of the phase equilibria on the temperature and nitrogen partial pressure. Si_3N_4+C+BN are in thermodynamic equilibrium with the gas phase below 1757 K at ambient pressure. Along the line Si_3N_4, graphite and SiC are in equilibrium with the gas phase. Upon crossing the line, Si_3N_4 and graphite are reacting according to reaction (5.2). Depending on the composition, either Si_3N_4 or graphite is thereby consumed completely. For the composition of the *Si-B-C-N_2* ceramic, Si_3N_4 is consumed completely, while for the *Si-B-C-N_1* ceramic Si_3N_4 is left after the reaction. With increasing p_{N2}, reaction temperatures are shifting to higher values while decreasing p_{N2} lower the reaction temperatures.
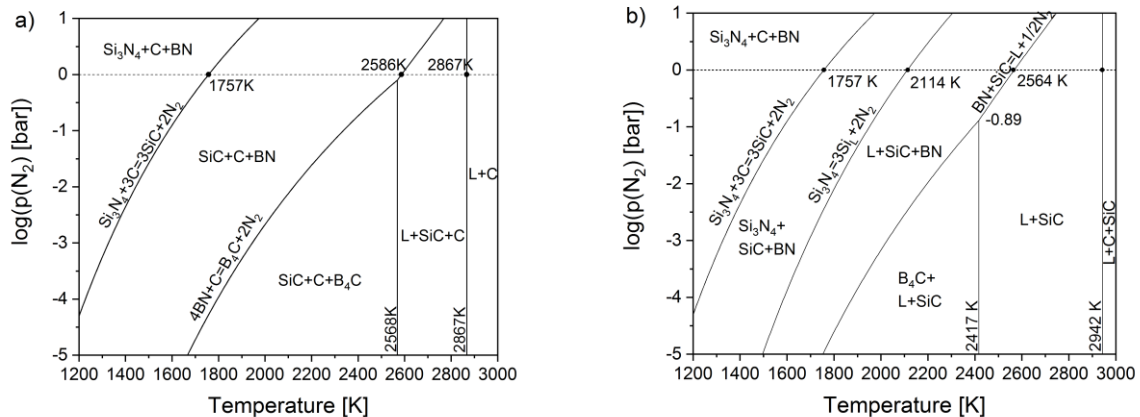
Figure 5.29: Calculated phase stability diagrams for the composition of the a) $Si_1B_1C_{1.4}$ (*Si-B-C-N_2*) and b) $Si_6B_1C_5$ (*Si-B-C-N_1*) precursor-derived Si-B-C-N ceramics.

5.2.2. Experimental investigations

Si-B-C-N ceramics were prepared from the *Si-B-C-N_1* precursor polymer in flowing Ar and Ar/N$_2$ atmospheres, respectively. Figure 5.30 shows the corresponding thermogravimetric curves for pyrolysis of the *Si-B-C-N_1* precursor polymer in flowing Ar. Results for pyrolysis of PSZ 10 and PSZ 20 in Ar are shown for comparison (see Section 5.1.2).

In stage 1 (T < 573 K), the crosslinking of the preceramic polymer takes place. During this stage, the *Si-B-C-N_1* polymer undergoes a much higher mass loss compared to PSZ 10 and PSZ 20. Figure 5.31 shows the mass spectrometric analysis of the pyrolysis atmosphere. A strong release of H$_2$ is observed during stage 1, which is much more pronounced compared to the crosslinking of PSZ 10 and PSZ 20. Since the crosslinking of the preceramic polymer takes places by split of and release of low molecular species, bubble formation is corresponding to the observed strong H$_2$-release
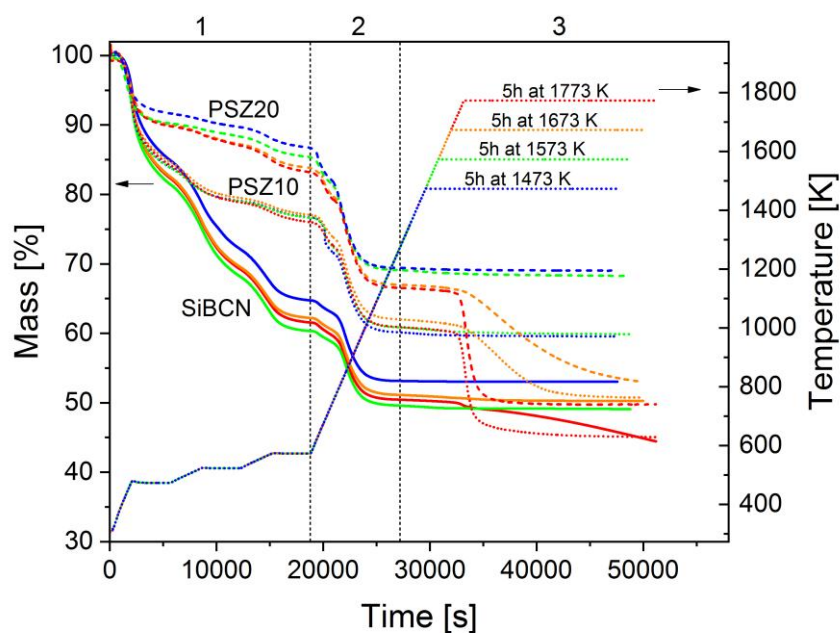
Figure 5.30: Thermogravimetric curves for pyrolysis of the *Si-B-C-N_1* precursor-polymer at 1473 K – 1773 K in flowing Ar. Results for PSZ 10 and PSZ 20 are shown for comparison.

During stage 2 (573 K < T < 1273 K) the actual pyrolysis takes place. The mass loss of the *Si-B-C-N_1* precursor during stage 2 is comparable with PSZ 10 and PSZ 20 and shows the same two-step characteristics. The crosslinked precursor polymer is transformed into a solid ceramic during this stage. Hydrogen, which is bound in the polymers functional groups (Si-H, C-H, N-H) is released in form of hydrogen-containing gas species. Figure 5.31 shows, that predominantly H$_2$ and CH$_4$ are released during this stage. However, also small amounts of N$_2$ are observed.
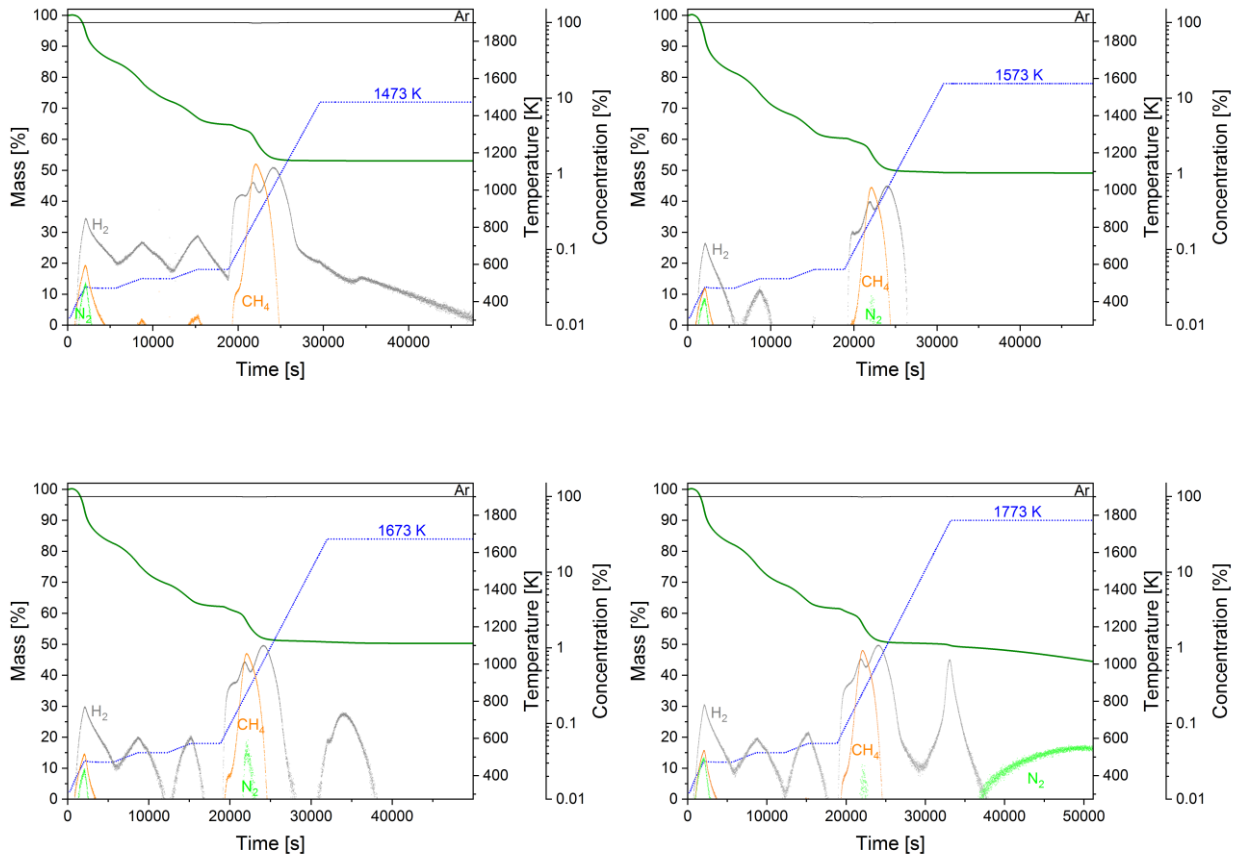
Figure 5.31: Combined thermogravimetric and mass spectroscopic analysis during pyrolysis of *Si-B-C-N_1* ceramics. In flowing Ar atmosphere.
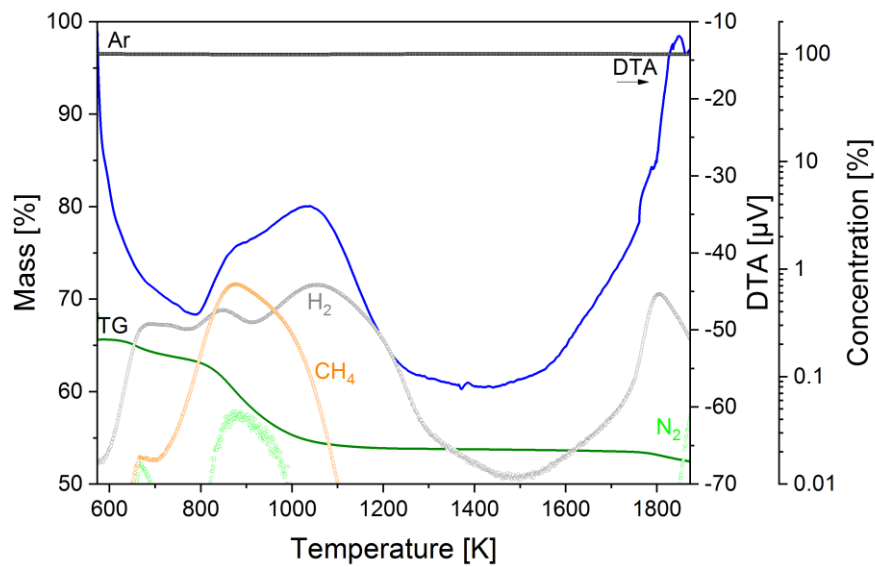
Figure 5.32: DTA/TG analysis of *Si-B-C-N_1* precursor-polymer combined with mass spectrometry in flowing Ar.

The combined DTA/TG and mass spectroscopic analysis during heat-up of the crosslinked *Si-B-C-N_1* precursor-polymer from 573 K with 10 K/min (Figure 5.32) shows that pyrolysis in stage 2 is an endothermic process. The DTA signal exhibits two endothermic reaction peaks in the temperature range from 800 K to 1100 K, corresponding to the two-step mass loss detected by thermogravimetric analysis. From the mass spectroscopic signal, even three maxima can be distinguished. The first and the third maxima are mainly characterized by the release of H_2 while the second maximum predominantly shows CH_4 release. In stage 3 (T > 1273 K) the final temperature is kept constant for 5 h to ensure complete transformation of the ceramic. Samples, which were pyrolyzed at maximum temperatures of 1473 K, 1573 K and 1673 K in Ar, showed a constant mass during this stage indicating that the pyrolysis process was completed and no additional reactions take place. However, the sample pyrolyzed at a maximum temperature of 1773 K shows an additional gradual mass loss, which is accompanied by the release of N_2 (Figure 5.31) and another endothermic peak in the DTA signal (Figure 5.32). In total, the precursor-derived *Si-B-C-N_1* ceramic shows a higher mass loss and therefore a lower ceramic yield compared to the PSZ 10 and PSZ 20-derived Si-C-N ceramics.

Figure 5.33 shows thermogravimetric curves for the pyrolysis of the *Si-B-C-N_1* precursor-polymer in flowing Ar/N_2 (p_{N2} = 0.5 bar). The mass loss observed in Ar/N_2 does not differ from the experiments in Ar during stage 1 (crosslinking) and stage 2 (pyrolysis). Also in stage 3, samples do not show an additional mass loss at maximum temperatures of 1473 K, 1573 K and 1673 K in Ar/N_2. However, pyrolysis at a maximum temperature of 1773 K in Ar/N_2 shows a significantly lower mass loss compared to experiments in Ar atmosphere in stage 3.
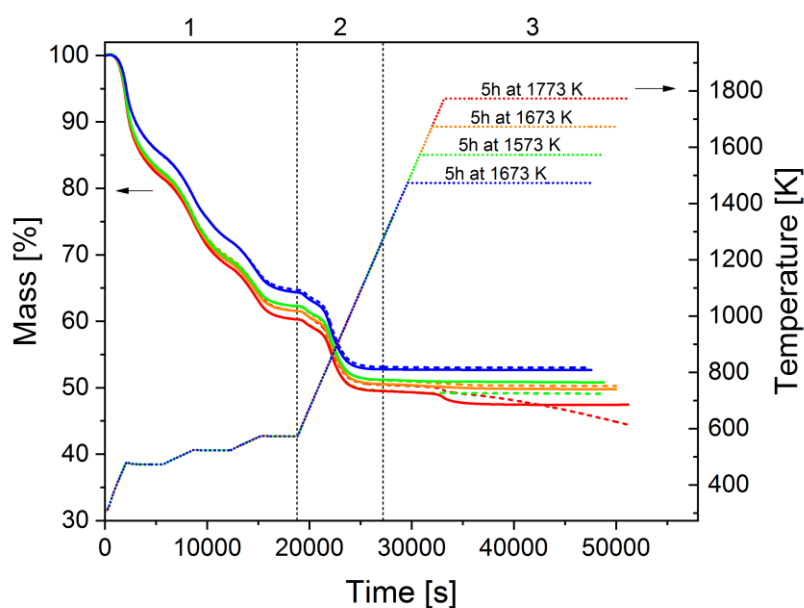
Figure 5.33: Thermogravimetric experiments for pyrolysis of the *Si-B-C-N_1* precursor-polymer in flowing Ar/N_2 (p_{N2} = 0.5 bar). Results for pyrolysis in Ar (dotted line) are shown for comparison.

The Si-B-C-N-ceramics obtained by pyrolysis of the *Si-B-C-N_1* precursor-polymer in flowing Ar and Ar/N$_2$ atmospheres are shown in Figure 5.34. All samples show macroscopically an extensive bubble formation. Bubbles have been formed before crosslinking is completed since the viscosity of the preceramic polymer is only low enough during stage 1 (< 573 K). After complete pyrolysis, the material is too hard and rigid to allow formation of bubbles.
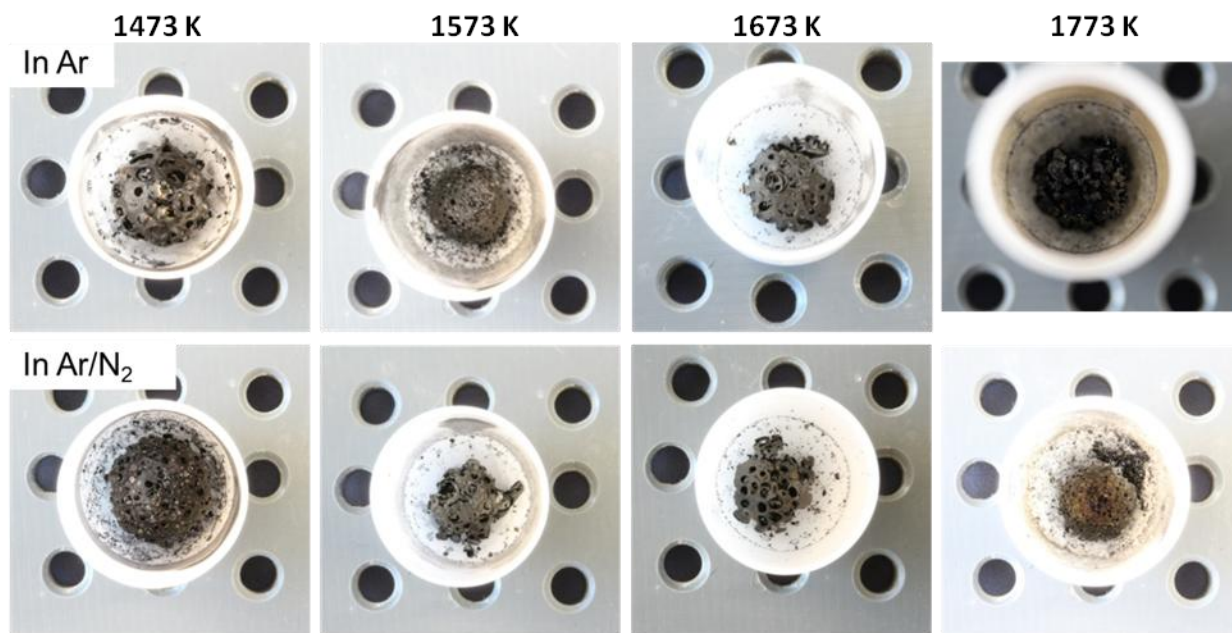
Figure 5.34: Si-B-C-N ceramics obtained by pyrolysis of the *Si-B-C-N_1* precursor-polymer in flowing Ar and Ar/N$_2$ (p_{N2} = 0.5 bar), respectively. The outer diameter of the Al$_2$O$_3$ crucibles is 17.3 mm.

Figure 5.35 shows SEM micrographs of the obtained Si-B-C-N ceramics. Samples, which were pyrolyzed up to maximum temperatures of 1473 K, 1573 K and 1673 K in both flowing Ar and Ar/N$_2$, show very homogeneous microstructures. Pyrolysis up to 1773 K in flowing Ar resulted in a partly porous and rough microstructure. However, also untransformed regions remain which correspond to the smooth microstructures at lower temperatures. EDX analysis (Figure 5.36) reveals a significantly lower nitrogen content of the porous regions compared to the smooth areas.
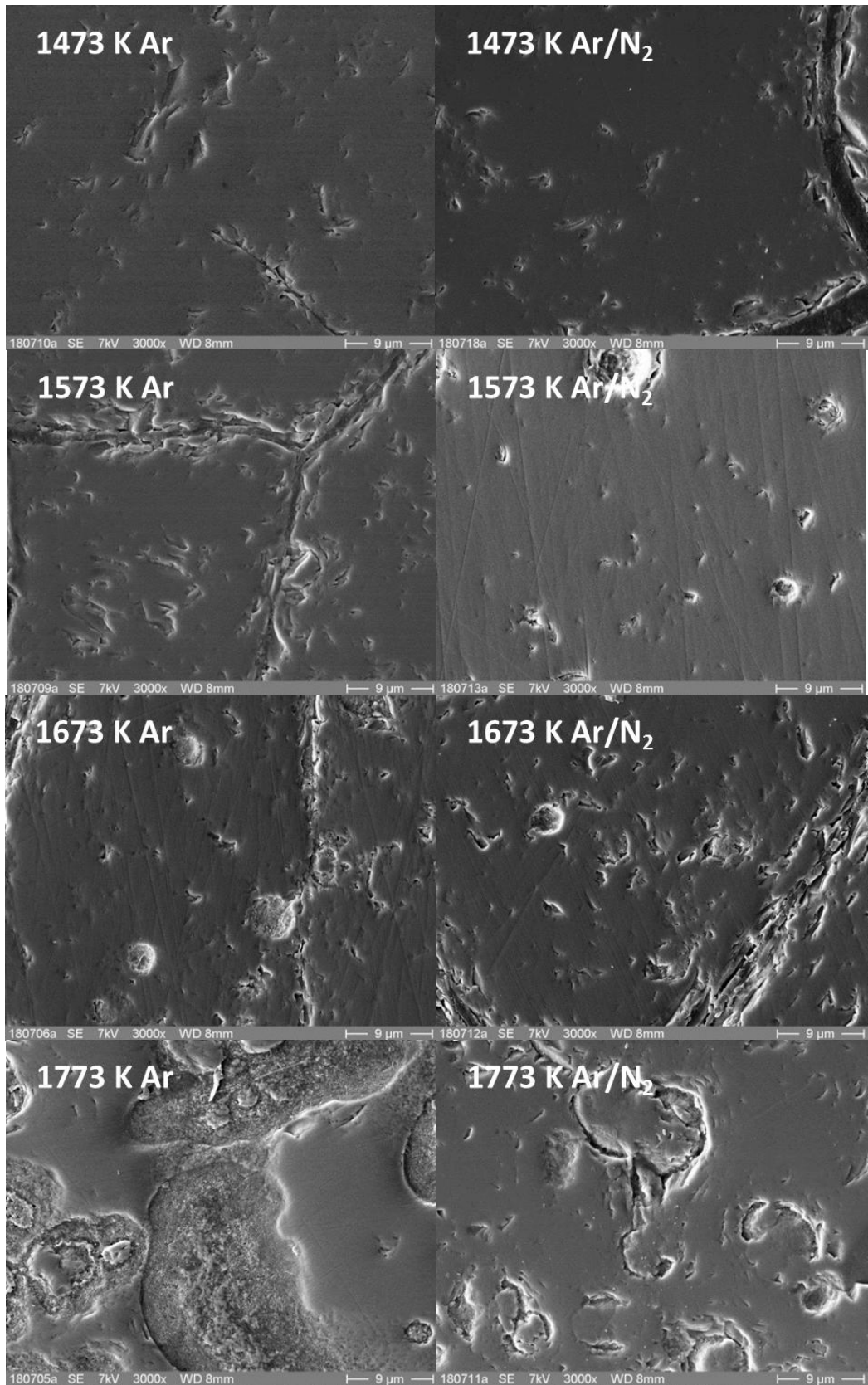
Figure 5.35: Micrographs of Si-B-C-N ceramic obtained by pyrolysis of *Si-B-C-N_1* precursor-polymer in flowing Ar and Ar/N$_2$ (p$_{N2}$ = 0.5 bar).
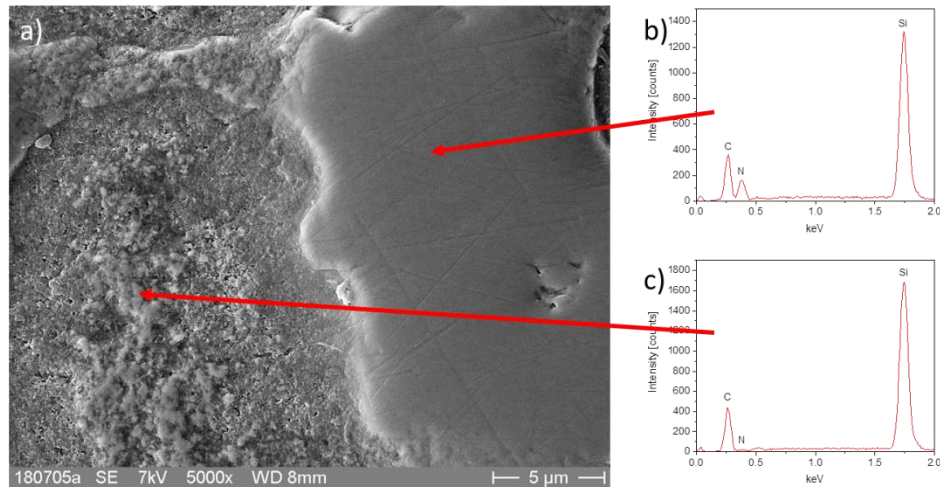
Figure 5.36: SEM micrograph and EDX analysis of Si-B-C-N ceramic obtained by pyrolysis of the *Si-B-C-N_1* precursor-polymer at 1773 K in flowing Ar.

XRD patterns depicted in Figure 5.37 show, that the obtained Si-B-C-N ceramics are X-ray amorphous after pyrolysis at 1473 K, 1573 K and 1673 K in Ar and at all temperatures in Ar/N_2. Pyrolysis at maximum 1773 K in Ar resulted in crystallization of β-SiC and Si.
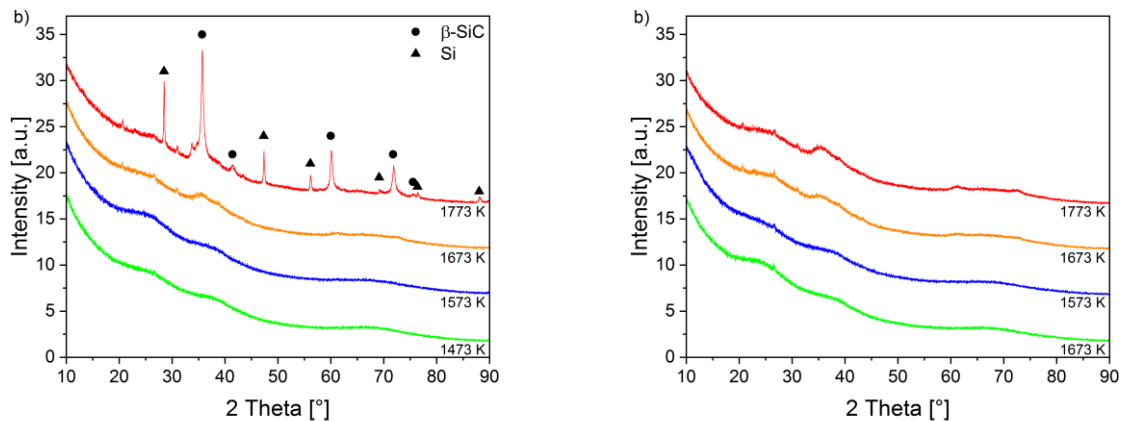
Figure 5.37: XRD patterns of Si-B-C-N ceramic obtained by pyrolysis of the *Si-B-C-N_1* precursor-polymer at 1473 K-1773 K in flowing a) Ar and b) Ar/N_2 (p_{N2} = 0.5 bar).

5.2.3. Discussion and Conclusion

Pyrolysis of the preceramic-polymer

Thermodynamic modeling of the pyrolysis process of the *Si-B-C-N_2* precursor-polymer was conducted using the composition of the polymer chain $(SiBC_3N_3H_{10})_n$. The calculations (Figure 5.22) reveal the thermodynamic equilibrium phases resulting from the specific composition of the *Si-B-C-N_2* precursor-polymer. Besides the condensed phases Si_3N_4, BN and C (graphite) also a gas phase is formed. The gas phase contains in particular the hydrogen from the polymer chain in form of hydrogen-containing gas species. Similar to the polysilazane precursor-polymers Ceraset® PSZ 10 and PSZ 20 (see Section 5.1.1), the major gas species which are formed are H_2 and CH_4. By thermal dissociation of methane ($CH_4=C+2H_2$) the partial pressure of CH_4 is decreasing with temperature while the partial pressure of H_2 is increasing with a point of inversion at 771 K. However, unlike the Ceraset® PSZ 10 and PSZ 20 precursor-polymers, no temperature range of constant H_2 and CH_4 pressure is observed for the *Si-B-C-N_2* precursor-polymer.

Contrary to Ceraset® PSZ 10 and PSZ 20, N_2 is present with a constant partial pressure (0.06-0.12 bar) in the considered temperature range. Additionally, NH_3 is formed with a partial pressure up to $4 \cdot 10^{-4}$ bar from the composition of the *Si-B-C-N_2* precursor-polymer. Both is indicating, that the nitrogen content of the *Si-B-C-N_2* precursor-polymer is slightly too high to be bound chemically in the Si-B-C-N ceramic. In contrast to the calculation of phase equilibria from the composition of the obtained Si-B-C-N ceramic (Si_3N_4+BN+C+SiC; see Figure 5.24), no SiC is found upon using the composition of the precursor-polymer (Gas+Si_3N_4+BN+C; see Figure 5.22). An explanation for this observation can be derived from the isothermal section $Si_1B_1C_{1.4}$-N in Figure 5.28. The composition of the *Si-B-C-N_2* ceramic (x(N) = 0.4035) is located very close to the phase boundary between the phase equilibria BN+C+Si_3N_4+SiC (0.23 < x(N) < 0.41) and Gas+Si_3N_4+BN+C (x(N) > 0.41). Therefore, a slight deviation in the nitrogen content of the Si-B-C-N precursor-polymer can result in either one or the other phase equilibrium. Experimental investigation by Wilfert [110] showed, that the *Si-B-C-N_2* ceramic remains X-ray amorphous after heat-treatment at a maximum temperature of 1838 K and below. While predominantly C- and N-containing gas species are formed, Si- and B-containing species exhibit only very low partial pressures below 10^{-8} bar in the considered temperature range up to 1500 K. Hence, the decreasing carbon and nitrogen content and constant Si:B-ratio upon pyrolysis of the precursor-polymer and formation of the amorphous Si-B-C-N ceramic $((SiBC_3N_3H_{10})_n \rightarrow SiBC_{1.4}N_{2.3})$ is a direct consequence of the equilibrium partial pressures of the gas species which are forming during pyrolysis.

Experimental investigations were performed with the *Si-B-C-N_1* precursor-polymer. Mass loss during the initial cross-linking process (stage 1) is much higher compared to Ceraset® PSZ 10 and

PSZ 20 (see Figure 5.30). Up to the 523 K isothermal, the mass change is similar to PSZ 10 but sinks to lower values upon further heat-treatment.

The high mass loss during crosslinking is accompanied by a very pronounced release of H_2 (see Figure 5.31), which is higher compared to heat-treatment of Ceraset® PSZ 10 (Figure 5.10) and PSZ 20 (Figure 5.11), respectively. This is in good accordance with the observed porosity resulting from the formation of bubbles (Figure 5.34). As the crosslinked and pyrolyzed polymer is too rigid, bubbles must be formed as long as the polymer is still viscous, i.e. before crosslinking is complete. This is supported by the observed H_2 signal and mass loss during this stage. In contrast to the porous *Si-B-C-N_1* ceramics, Si-C-N ceramics derived from Ceraset® PSZ 10 and PSZ 20, which were obtained by the same heat-treatment, exhibit a dense lens-like appearance. The higher mass loss of Ceraset® PSZ 10 compared to PSZ 20 was accountable to the evaporation of oligomers, which are presumably present in a higher number in the low-molecular PSZ 10 (see Section 5.1.3). Such a statement for the *Si-B-C-N_1* precursor-polymer would necessitate further investigations.

The endothermic pyrolysis process is accompanied by the release of H_2 and CH_4 (see Figure 5.32). DTA measurements and mass change clearly show a two-step character of the pyrolysis process. The release of H_2 and CH_4 in the temperature range of 600-1300 K and 700-1100 K, respectively, even suggest a three-step character. This observation is consistent with experimental thermogravimetric data on the pyrolysis of other polyborosilazanes [111][112]. Mass loss during the actual pyrolysis (stage 2) is similar to Ceraset® PSZ 10 and PSZ 20. The resulting overall ceramic yield of approx. 50 % for *Si-B-C-N_1* precursor-polymer is lower compared to Ceraset® PSZ 10 (60 %) and PSZ 20 (67 %) Si-C-N precursor-polymer (see Figure 5.30). However, this is only resulting from the higher mass loss during crosslinking and outgassing (stage 1) of the precursor-polymer.

High-temperature stability

In-depth analysis of the high-temperature stability and the underlying high-temperature reactions was performed by thermodynamic calculations based on the composition of the *Si-B-C-N_2* ($Si_1B_1C_{1.4}N_{2.3}$) and *Si-B-C-N_1* ($Si_6B_1C_5N_7$) precursor-derived Si-B-C-N ceramics. The boron content of these ceramics corresponds to 17.54 at.% and 5.25 at.%, respectively. According to the isothermal sections in the quaternary Si-B-C-N system at constant B-content, the composition of the *Si-B-C-N_2* (Figure 5.23) and *Si-B-C-N_1* (Figure 5.25) precursor-derived ceramics are in the same four-phase equilibrium Si_3N_4+SiC+BN+C, at temperatures up to 1757 K and assuming complete crystallization. However, the fractions of these four phases is quite different as can be seen from the phase fraction diagrams in Figure 5.24 and Figure 5.26, respectively. For example, the *Si-B-C-N_2* ceramic is poor in SiC, while the *Si-B-C-N_1* ceramic is rich in SiC.

At 1757 K, the carbothermal reaction of Si_3N_4 and C as equilibrium constituents of the Si-B-C-N ceramic is taking place under formation of SiC and N_2, which is released to the atmosphere. Due to the partly transition of the Si-B-C-N ceramic into gaseous N_2 and the associated degradation, this reaction is limiting for the application temperature. Due to their different Si:B:C-ratios (see Figure 5.27), the obtained compositions of the Si-B-C-N ceramics are located in different phase fields above 1757 K. The composition of the *Si-B-C-N_2* and *Si-B-C-N_1* ceramics are located in the phase equilibria Gas+C+BN+SiC and Gas+Si_3N_4+SiC+BN, respectively. Hence, Si_3N_4 is consumed completely in the carbothermal reaction of the *Si-B-C-N_2* ceramic and carbon is consumed completely for the *Si-B-C-N_1* ceramic. Due to the residual Si_3N_4, the *Si-B-C-N_1* ceramic additionally shows the thermal dissociation of Si_3N_4 at 2114 K.

The different Si:B:C-ratio (see Figure 5.27) of the *Si-B-C-N_2* and *Si-B-C-N_1* precursor-derived ceramics also predefines the nitrogen content, which is delimiting the maximum high-temperature stability. Ideally, compositions of Si-B-C-N ceramics should be chosen in a composition range were no gas or liquid phase are formed in the aspired application temperature range. For the *Si-B-C-N_2* ceramic this would be $x(N) < 0.41$ and < 0.23 for a maximum application temperature of 1757 K and 2568 K, respectively (see Figure 5.28). The *Si-B-C-N_1* ceramic possesses the highest application temperature of 1757 K for $0.16 < x(N) < 0.43$.

Therefore, the same reaction (5.2) is limiting for the high-temperature stability of the Ceraset PSZ 10 and PSZ 20-derived Si-C-N ceramics (see Section 5.1) as well as the *Si-B-C-N_2* and *Si-B-C-N_1* precursor-derived ceramics. However, the *Si-B-C-N_1* precursor-derived ceramic shows a considerably much lower mass loss in thermogravimetric experiments above the reaction temperature of 1757 K in Ar as well as Ar/N_2 atmosphere. In Ar-atmosphere, a shift of the reaction temperatures to lower values is expected from the phase stability diagram in Figure 5.29. However, the *Si-B-C-N_1* precursor-derived ceramic does not show a mass loss or a related N_2 signal, contrary to PSZ 10 and PSZ 20-derived Si-C-N ceramics under the same conditions. In addition, the microstructural analysis of the obtained Si-B-C-N ceramics in Figure 5.35 does not show signs of the carbothermal decomposition reaction at 1673 K. This is clearly demonstrating the superior high-temperature stability of the *Si-B-C-N_2* precursor-derived ceramic.

An outstanding high-temperature stability of Si-B-C-N ceramics is known from literature. Resistance against carbothermal reaction is reported up to 2273 K [113]. Jalowiecki et al. [114] found in HRTEM investigations a so-called turbostratic BNC_x-structure surrounding SiC and Si_3N_4 grains. Seifert et al. [104][115] demonstrated, that two effects contribute to the high-temperature stabilization: (1) an increase in pressure inside the encapsulated regions would shift the carbothermal decomposition of Si_3N_4 to higher temperatures; and (2) a lower carbon activity inside the turbostratic BNC_x-structure would also shift the carbothermal decomposition temperature to higher values. However, the high-temperature stability of Si-B-C-N ceramics is depending on the composition. While some do not show significant decomposition up to

2273 K [113][116], others already decompose at temperatures below 2073 K [116][117]. Müller et al. [118][119] investigated the effect of the boron content on the high-temperature stability of Si-B-C-N ceramics. It was shown, that with increasing boron content, the persistence against crystallization and degradation increases. The authors find a minimum boron content of 5.7 at.% [118] and 9 at.% [119], respectively, sufficient to protect the material against thermal degradation and crystallization. Different values were attributed to differences in microstructure upon using different precursors.

Crystallization

XRD analysis, depicted in Figure 5.37, revealed, that the obtained *Si-B-C-N_1* precursor-derived ceramics are X-ray amorphous after heat-treatment at 1473 K-1773 K in Ar/N_2 and 1473 K-1673 K in Ar. Only heat treatment at 1773 K in flowing Ar resulted in the crystallization of β-SiC and Si. The occurrence of β-SiC is coincident with the carbothermal reaction observed in REM/EDX (Figure 5.36) and STA/MS (Figure 5.32). Therefore, crystalline β-SiC must be formed as a result of the carbothermal reaction instead of crystallizing from the amorphous matrix. The N_2-starvation conditions in flowing Ar might be resulting in the observation of Si reflections. According to the phase stability diagram, shown in Figure 5.29, reaction temperatures are decreasing with decreasing p_{N2}. A nitrogen partial pressure below $10^{-2.5}$ bar would be sufficient at 1773 K to form Si from the thermal decomposition of Si_3N_4. Although Si_3N_4 is an equilibrium phase for the composition of *Si-B-C-N_1* precursor-derived ceramic, crystallization of α-/β-Si_3N_4 is not observed contrary to Ceraset® PSZ 10- and PSZ 20-derived Si-C-N ceramics. Tavakoli et al. investigated the effect of boron on the crystallization of Si-B-C-N ceramics extensively [120][121]. Gao et al. [122] identified processes as (1) demixing of SiC_xN_{4-x} mixed domains into SiC_4 and SiN_4 tetrahedra, (2) cleavage of the mixed bonds at interdomain regions and (3) coarsening of the domains. Tavakoli et al. [120][123] found, that the stabilizing effect of boron on the crystallization of α-/β-Si_3N_4 is rather a kinetic, than a thermodynamic effect. With increasing boron content, the thermodynamic stability of the crystalline components SiC, Si_3N_4, BN and C (graphite) actually increases [123][124]. However, the turbostratic BNC_x-layers lead to a delay in coarsening of the nanodomains [123].

6. Phase equilibria and constitution in ZrB₂-filled SiC/Si-C-N-ceramics

During cyclic operation of turbines, crack formation might occur, which would lead to an ingress of the oxidizing combustion atmosphere through the cracks into the material. This could lead to an increased degradation of the material and its mechanical properties. The addition of boron-containing additives into the matrix could improve the oxidation resistance of the material inherently. In the presence of a crack, the additive would form a borosilicate melt (eutectic temperature 713 K [44]), which is filling the crack and thereby slowing down the inward diffusion of the oxidizing gas species from the combustion atmosphere. This could promote self-healing of the matrix during operation to a certain extend. The oxidation protective effect of boron-containing components on SiC-based ceramics by formation of a boro-silicate is already known for ceramic fibers with BN coatings [45], ultra-high-temperature ceramics (UHTC) ZrB₂-SiC (and HfB₂-SiC) [46][47] and boron containing precursor-derived Si-B-C-N ceramics [20]. Apart from polyborosilazanes, where boron is chemically bond in functional groups of the precursor polymer chain [48][49], ZrB₂-filler containing precursor-derived Si-C-N ceramics could be a cost-effective alternative to introduce boron to the ceramic matrix. Furthermore, She et al. [125] showed, that the volume increase induced by the nitriding reaction of ZrB₂ forming ZrN induces the healing of surface defects and reduces the amount of surface connected pores. Thus, a systematic conditioning of ZrB₂/Si-C-N composites in N_2 after manufacturing could promote self-healing. Reactive active fillers, which undergo a volume expansion, are also used to improve porosity and dimensional change of the ceramic matrix [21][22][23].

Parts of this Chapter were published in [126], but more details and further results are presented here.

6.1. Preselection of the boron-containing filler

BN is a possible candidate as boron-containing filler for the Si-C-N matrix in composites/CMCs. Due to its chemical inertness with Si-C-N ceramics it was used as crucible material for earlier work on precursor-derived ceramics by Wagner [127]. Figure 6.1 shows the phase fraction diagram and the composition of the gas phase for BN in equilibrium with Si-C-N, according to the composition of PSZ 10 and PSZ 20-derived ceramics, if crystallization would occur. Only reactions of the Si-C-N ceramic itself are found (1757 K: $Si_3N_4+3C=3SiC+2N_2$; 2114 K: $Si_3N_4=Si_l+N_2$ see also Section 5.1). No additional interactions of BN and the constituents of the Si-C-N ceramic are visible in this temperature range. Only at 2588 K, BN and SiC are consumed by the formation of a liquid phase and gas. Therefore, BN is fully compatible with the PSZ 10 and PSZ 20-derived Si-C-N ceramic within its application-relevant temperature range.
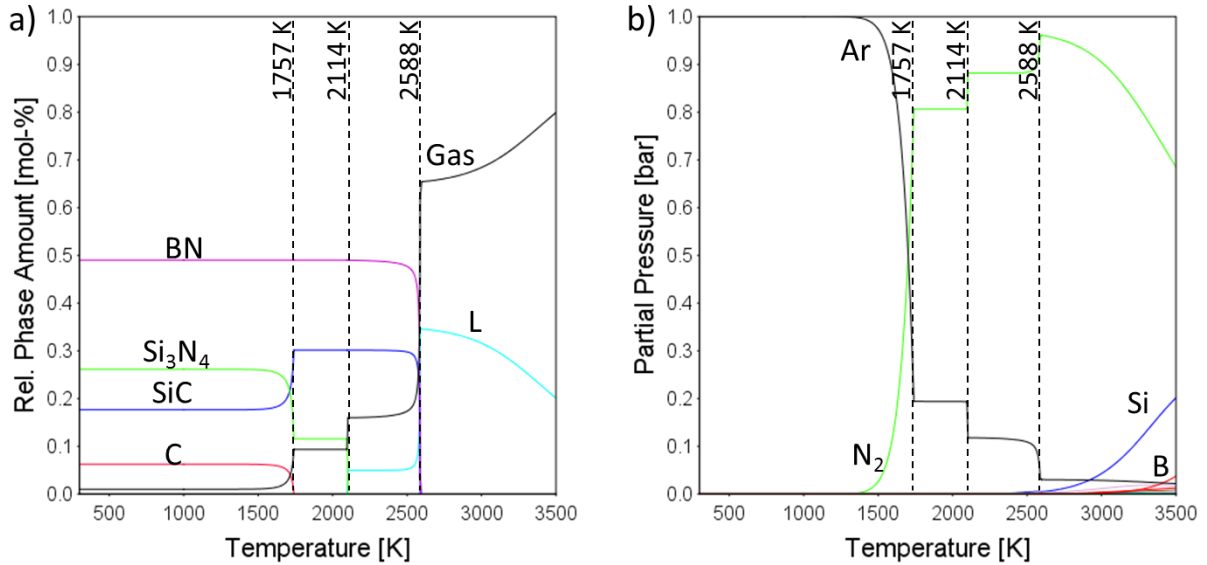
Figure 6.1: Calculated a) phase fraction diagram and b) composition of the gas phase for BN/Si-C-N composite.

Figure 6.2 shows results of the thermogravimetric analysis of the pyrolysis of BN powder containing PSZ 20 in flowing Ar. Results of the BN-containing samples were normalized to their PSZ 20 content for better comparability. The mass loss in stage 1, resulting from the evaporation of oligomers and crosslinking of the polymer, shows a very low scattering and is very similar to pure PSZ 20. In addition, the actual pyrolysis process in stage 2 leads to identical mass losses. Pyrolysis up to maximum temperatures of 1473 K and 1573 K results in a constant mass in stage 3. BN/Si-C-N ceramics, which were obtained by pyrolysis at maximum temperatures of 1673 K and 1773 K, show an additional mass loss which is comparable to pure PSZ 20-derived Si-C-N ceramics. The mass loss in stage 3 is resulting from the matrix internal reaction of Si$_3$N$_4$ with graphite forming SiC and N$_2$ (see Section 5, reaction (5.2). Summarizing, the addition of BN powder does not influence the pyrolysis behavior of PSZ 20. Furthermore no difference in the high-temperature stability was observed between the obtained BN/Si-C-N ceramic and the pure PSZ 20-derived Si-C-N ceramic matrix.
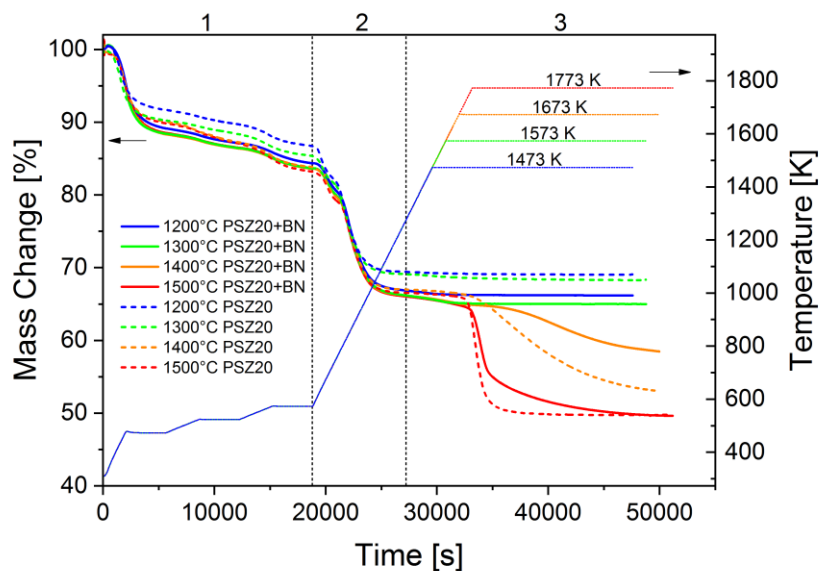
Figure 6.2: Thermogravimetric experiments with PSZ 20-derived BN/Si-C-N composites in flowing Ar. Results for pure PSZ 20 are shown for comparison.

The microstructure of the obtained BN/Si-C-N ceramics is shown in Figure 6.3. BN particles are homogeneously distributed throughout the Si-C-N matrix. The matrix itself is homogeneous and smooth after pyrolysis at maximum temperatures of 1473 K and 1573 K. Only samples which were pyrolyzed at 1673 K and 1773 K show a rough and porous microstructure, indicating a partly transformation of the Si-C-N matrix according to reaction (5.2).
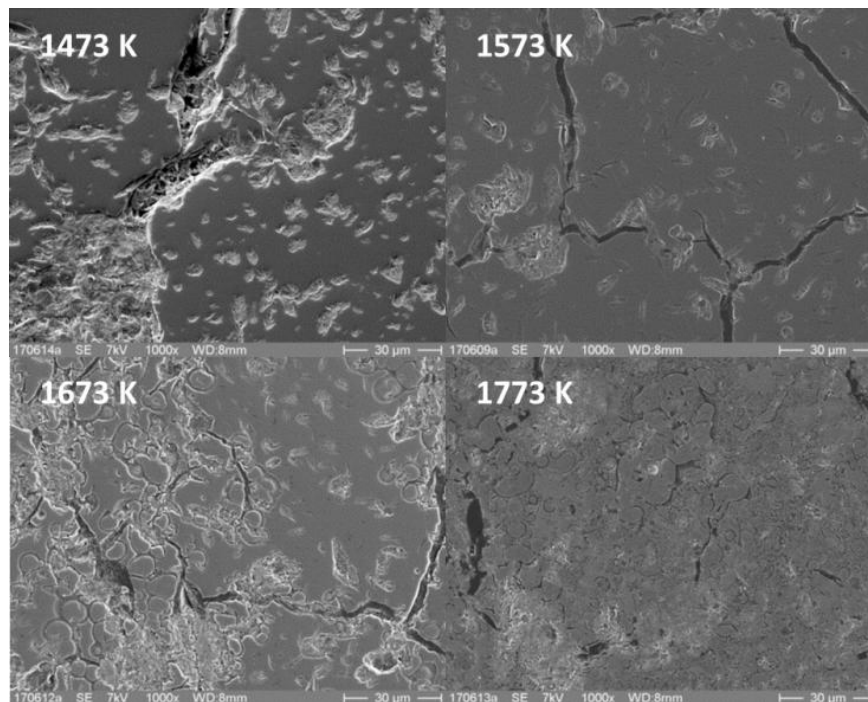
Figure 6.3: Micrographs of BN/Si-C-N composites obtained from pyrolysis in flowing Ar.

The XRD patterns, shown in Figure 6.4, reveal that after pyrolysis at maximum temperatures of 1473 K and 1573 K, only reflections of the hexagonal BN-filler are observed. The Si-C-N matrix itself is X-ray amorphous at these temperatures. Pyrolysis at 1673 K and 1773 K additionally resulted in crystallization of β-SiC. This is analogous to the observations on pure PSZ 20-derived ceramics (see Section 5.1).
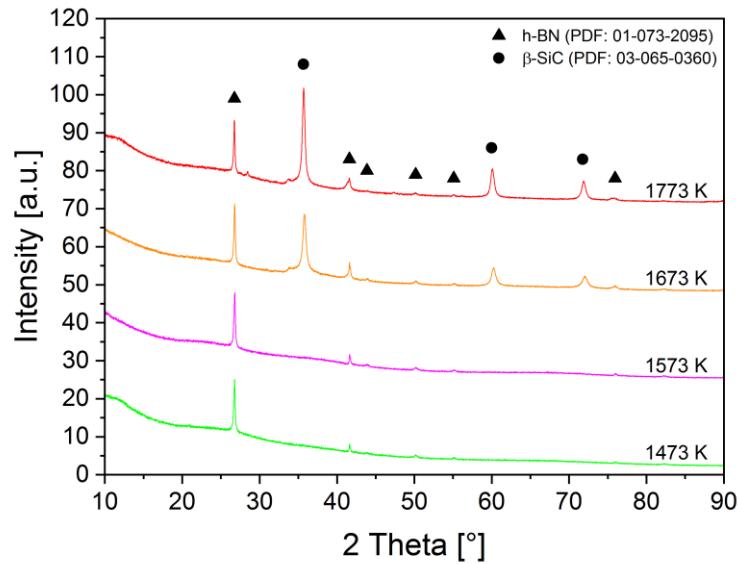
Figure 6.4: XRD pattern of PSZ 20-derived BN/Si-C-N composites.

Figure 6.5 shows phase fraction diagrams for the oxidation of the potential filler materials B$_4$C, BN und ZrB$_2$. Calculations were performed as a closed system consisting of a constant amount of substance (1 mol) at ambient pressure of p = 1·10^5 Pa with a self-developing gas volume. Phase fraction diagrams were calculated with a small amount of Ar (x(Ar) = 0.01) to establish a stable gas phase under all conditions. These are oxidizing according to reactions:

$$ZrB_2 + 5/2 O_2 = ZrO_2 + B_2O_3 \qquad \text{(6.1)}$$

$$2BN + 3/2 O_2 = B_2O_3 + N_2 \uparrow \qquad \text{(6.2)}$$

$$B_4C + 7/2 O_2 = 2B_2O_3 + CO \uparrow \qquad \text{(6.3)}$$

$$B_4C + 4O_2 = 2B_2O_3 + CO_2 \uparrow \qquad \text{(6.4)}$$
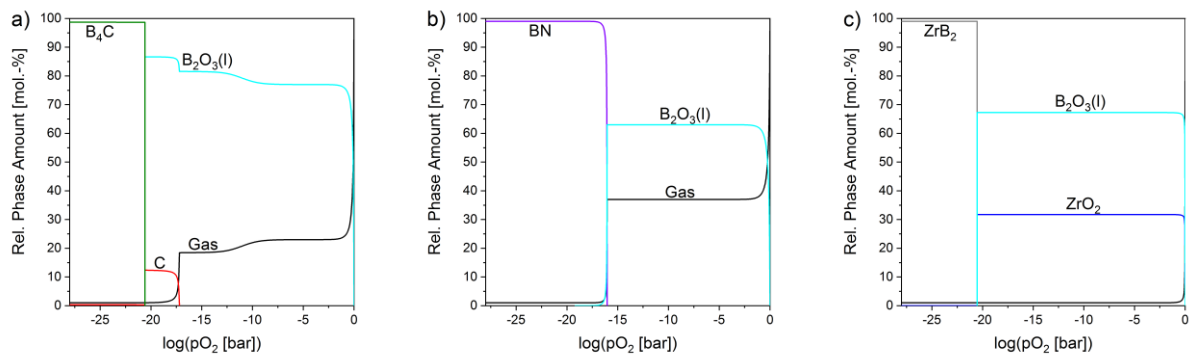
Figure 6.5: Calculated phase fraction diagrams for a) B₄C, b) BN and c) ZrB₂ as a function of p$_{O2}$ at 1473 K.

B₄C and BN are oxidizing under release of gaseous CO, CO₂ and N₂, respectively. Although BN is compatible with the Si-C-N matrix as filler, as has been shown by CALPHAD calculations and investigation of the BN/Si-C-N composites, gas formation upon oxidation could be problematic. The B₂O₃-melt, which is intended to fill cracks upon oxidation, could be pushed out of the material by the gas. The same holds for B₄C. In contrast to that, ZrB₂ is forming only condensed phases, ZrO₂ and B₂O₃-melt, upon oxidation. This makes ZrB₂ the favorable and promising boron-containing filler for improving the oxidation tolerance of Si-C-N ceramics.

In the following, phase stabilities and intrinsic high-temperature reactions between the ZrB₂-additive and the components (Si₃N₄, SiC and C) of the PSZ 20-derived Si-C-N ceramic matrix were investigated. The CALPHAD method was used to identify reactions, which are limiting the maximum application temperature. ZrB₂/Si-C-N composites were prepared from ZrB₂-powder/PSZ 20-mixtures by pyrolysis and heat-treatment up to maximum temperatures of 1473 K, 1573 K, 1673 K, and 1773 K in flowing pure Ar- and a Ar/N₂-mixture. The pyrolysis process was monitored by a combination of thermogravimetric and mass spectrometric investigation. Post-test examinations of the obtained ZrB₂/Si-C-N composite were performed by XRD and SEM. A mechanism for the formation of a zirconium carbonitride (ZrC$_x$N$_y$) was proposed and conditions for the avoidance of ZrC$_x$N$_y$ were delimited with respect to temperature and nitrogen partial pressure of the atmosphere. It is shown that observed experimental findings are confirmed and explained by CALPHAD-modeling.

6.2. Thermodynamic calculations on the compatibility of ZrB$_2$ and Si-C-N

Thermodynamic equilibrium calculations were performed to investigate the compatibility between the ZrB$_2$ additive and the Si-C-N matrix. Phase stabilities and high temperature reactions between ZrB$_2$ and the individual equilibrium components (C, SiC and Si$_3$N$_4$, if crystallization would occur), were identified using the CALPHAD method. To this end, the dataset Zr-Si-B-C-N, which was derived in Section 4.1 was utilized. Calculations were performed as a closed system consisting of a constant amount of substance (1 mol) at ambient pressure of $p = 1\cdot10^5$ Pa with a self-developing gas volume. Phase fraction diagrams were calculated with a small amount of Ar (x(Ar) = 0.01) to establish a stable gas phase under all conditions. Reaction pairs were considered as mechanical powder mixtures.

Figure 6.6 and Figure 6.7 show the phase fraction diagrams and isopleths for the reaction pairs C-ZrB$_2$ and SiC-ZrB$_2$, respectively. Phase fractions are constant up to temperatures above 2500 K, indicating that no reactions take place. Above 2500 K melt formation occurs in both reaction pairs C-ZrB$_2$ and SiC-ZrB$_2$. The phases, which are shown in brackets, are present in thermodynamic equilibrium, however to a negligible amount.
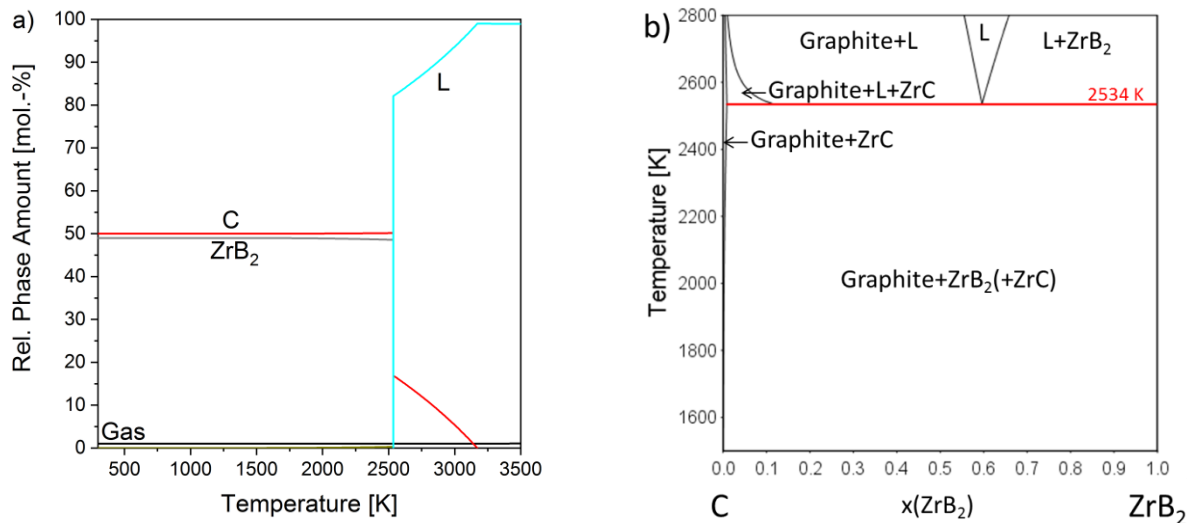
Figure 6.6: Calculated a) phase fraction diagram and b) isopleth for the couple C-ZrB$_2$.
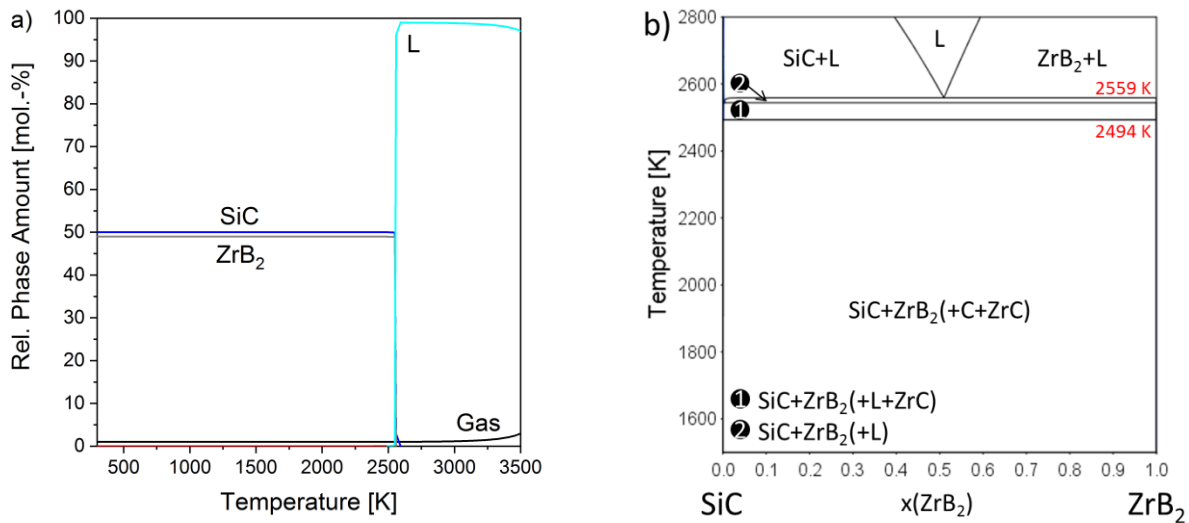
Figure 6.7: Calculated a) phase fraction diagram and b) isopleth for the couple SiC-ZrB₂.

The phase fraction diagram and the composition of the gas and liquid phase of the mechanical powder mixture ZrB₂-Si₃N₄, depicted in Figure 6.8, reveal more reactions:

1870 K
$$ZrB_2 + Si_3N_4 = ZrN + 2BN + L\left(\underline{Si}, B, Zr, N\right) \tag{6.5}$$

2191 K
$$ZrN + 2BN = ZrB_2 + 3/2N_2 \uparrow \tag{6.6}$$
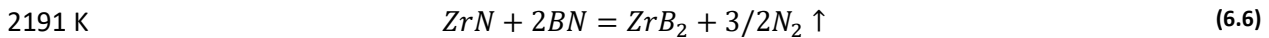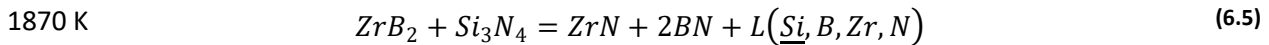
At 1870 K the first reaction occurs between ZrB₂ and Si₃N₄ under formation of ZrN, BN and a melt, which is mainly consisting of Si with minor amounts of B, Zr and N (see Figure 6.8c). Since the melt is described by a partially ionic liquid model, the constituents are ions, vacancies (Va) and neutral species (see also Section 2.3.2). Due to the formation of a melt, the maximum application temperature of a ZrB₂/Si-C-N-composite is limited to 1870 K by reaction (6.5). At 2191 K a further reaction takes place: The recombination of ZrN and BN forming ZrB₂ and N₂, which is released into the atmosphere (see Figure 6.8b).

The small portion of Ar (x(Ar)=0.01) used to establish a stable gas phase under all conditions allows to depict the N₂-release relative to the fixed amount of Ar. However, the use of Ar also results in artifacts in the calculation. The use of a, even small amount, of Ar defines the volume of the gas phase which is in equilibrium with the condensed phases in the closed system which is considered in the calculation. To establish the corresponding equilibrium partial pressure of N₂ in the gas phase, an amount of nitrogen is required which depends on the gas volume and is provided by the dissociation of Si₃N₄ into free Si and N₂. Therefore, reactions involving N₂ show rounded phase fraction transitions instead of sharp edges at the reaction temperatures. Furthermore, the free Si, which is present in the considered closed system, causes apparently a stable liquid phase consisting of Si, Zr and B at 1658 K although no reactions between the constituents take place at this temperature. Therefore, both the round edges of the phase

fractions and the liquid phase below 1870 K are an artifact resulting from the use of Ar in the calculation.
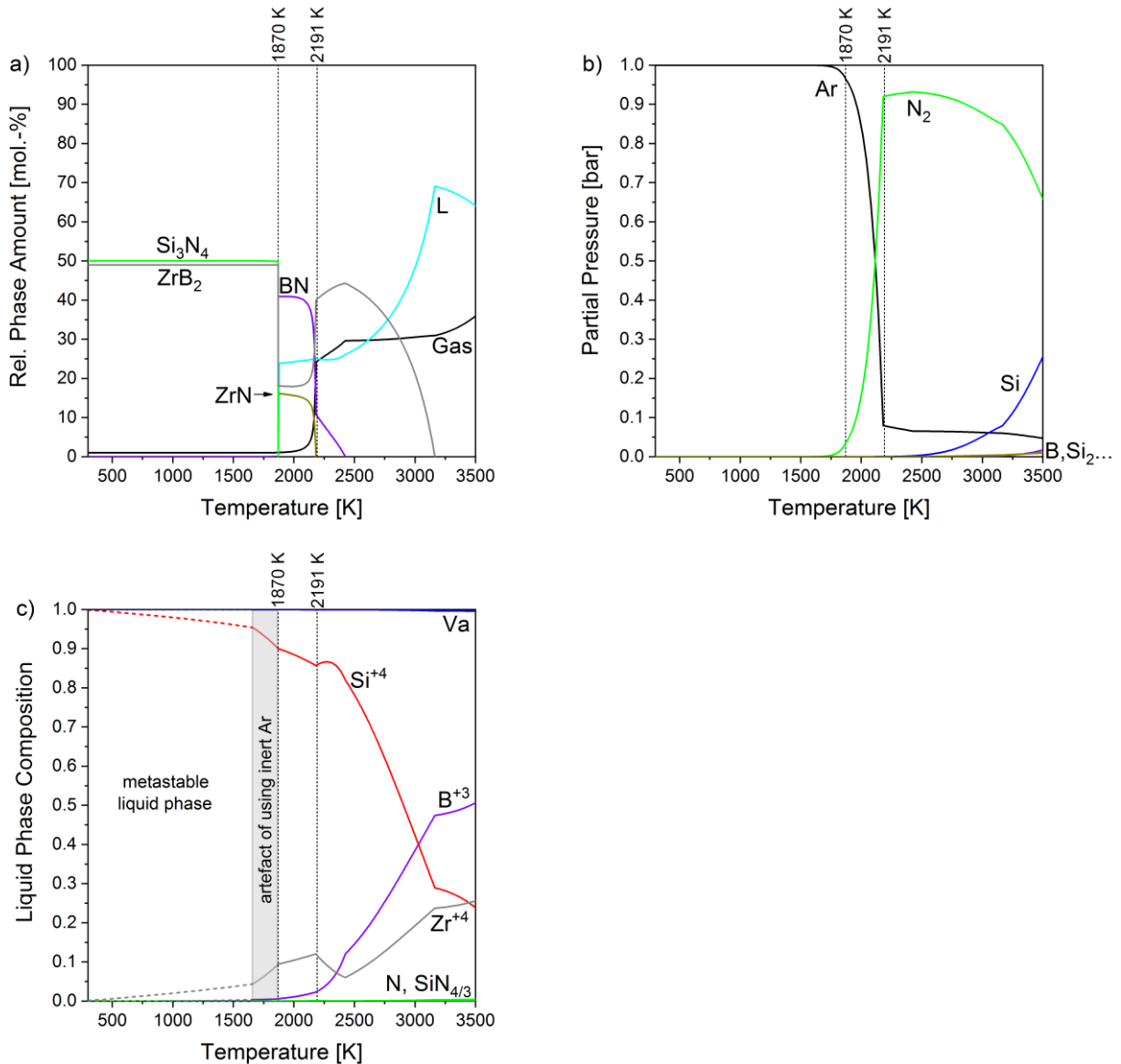
Figure 6.8: Calculated temperature dependence of the a) phase fractions, b) associated gas phase composition and c) composition of the liquid phase for the couple ZrB₂-Si₃N₄.

Phase equilibria for variable Si₃N₄-ZrB₂ composition are depicted in Figure 6.9. An excess amount of Si₃N₄, i.e. more than is consumed by reaction (6.5), results additionally in the thermal decomposition of the remaining Si₃N₄ at 2096 K. The thermal decomposition reaction occurs 18 K lower compared to pure Si₃N₄ due to presence of the melt, which is containing Si, Zr, B and N.
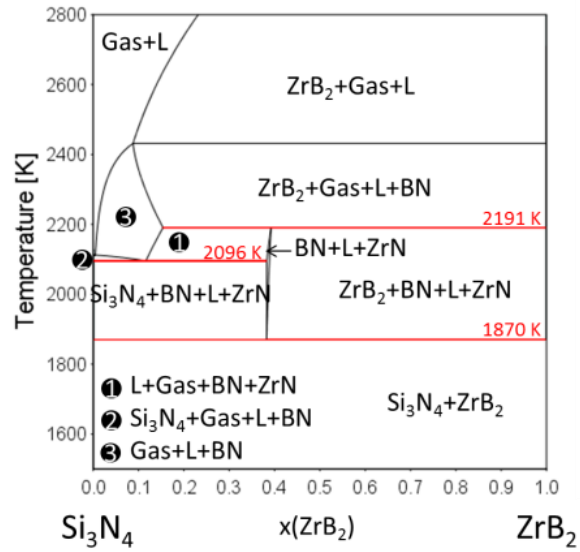
Figure 6.9: Calculated isopleth Si₃N₄-ZrB₂ in the system Zr-Si-B-N.

The Zr-B-N system

The phase stability diagram in the system Zr-B-N is shown in Figure 6.10. Phase equilibria of solid phases, in equilibrium with the gas phase, are depicted as a function of nitrogen partial pressure and temperature. Areas correspond to the bivariant single-phase equilibrium ZrB$_2$ and the two-phase equilibrium ZrN+BN while the line corresponds to the univariant three-phase equilibrium ZrB$_2$+ZrN+BN. At all conditions, condensed phases are in equilibrium with N$_2$, as only constituent of the gas phase. ZrB$_2$ is stable at high temperatures and low p$_{N2}$ while at higher p$_{N2}$ and lower temperatures ZrN and BN are the equilibrium phases. Upon crossing the line, reaction (**6.7**) takes place.

$$ZrB_2 + 3/2N_2 = ZrN + 2BN \qquad \textbf{(6.7)}$$

The reaction temperature and therefore the stability of ZrB$_2$ is strongly depending on the nitrogen partial pressure of the atmosphere. As the formation of other gas species than N$_2$ is negligible, p$_{N2}$ is equal to the total pressure. At p$_{N2}$ = 1 bar, i.e. in pure nitrogen at ambient pressure, reaction (**6.7**) proceeds at 2191 K. A reduction of the nitrogen partial pressure to 0.5 bar or 0.1 bar reduces the reaction temperature to 2115 K and 1959 K, respectively.
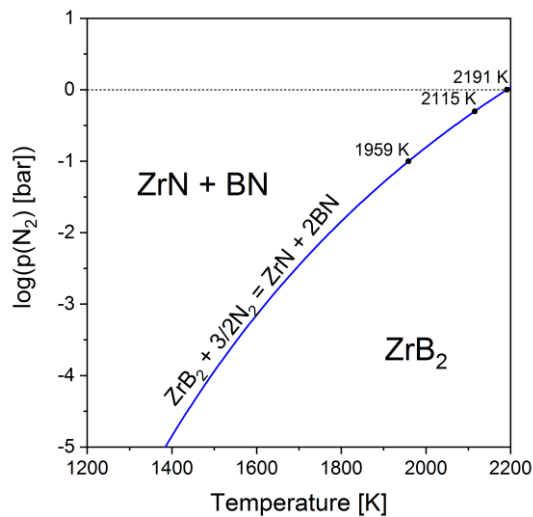
Figure 6.10: Calculated phase stability diagram for the Zr-B-N system.

The Zr-C-N system

The interaction between ZrN and carbon as constituent of the Si-C-N ceramic is depending on the carbon activity. Figure 6.11 shows the phase fraction, site occupancies and composition of the gas phase calculated for ZrC$_x$N$_y$ at 1473 K. With increasing carbon activity, carbon is incorporated into the ZrC$_x$N$_y$ crystal structure and nitrogen is released as N$_2$ into the atmosphere.
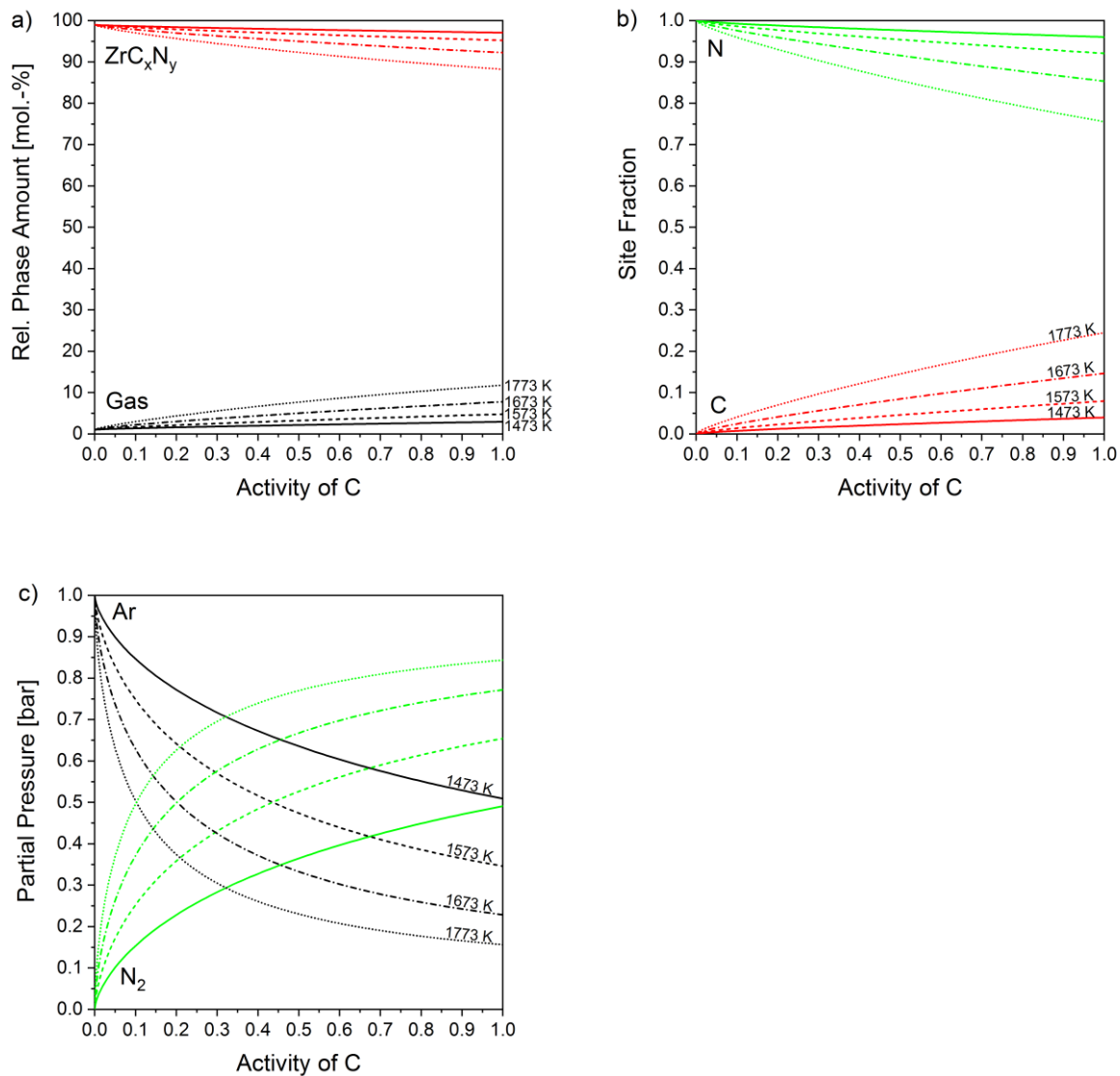
Figure 6.11: Calculated a) phase fraction, b) site fraction and c) composition of the gas phase for ZrC$_x$N$_y$ as a function of the carbon activity.

Figure 6.12 shows different aspects of the interaction between ZrN and graphite as a function of the temperature. The phase fractions of ZrN and graphite (C) are constant up to about 1200 K (Figure 6.12a), indicating that no reaction occurs. At higher temperatures, carbon is dissolved in

the ZrN crystal structure forming ZrC$_x$N$_y$. Figure 6.12b shows how the fraction of carbon decreases in the ZrC$_x$N$_y$ lattice at the expense of nitrogen, which is therefore released as molecular N$_2$ into the atmosphere (Figure 6.12c). At the highest temperatures also vacancies are formed.
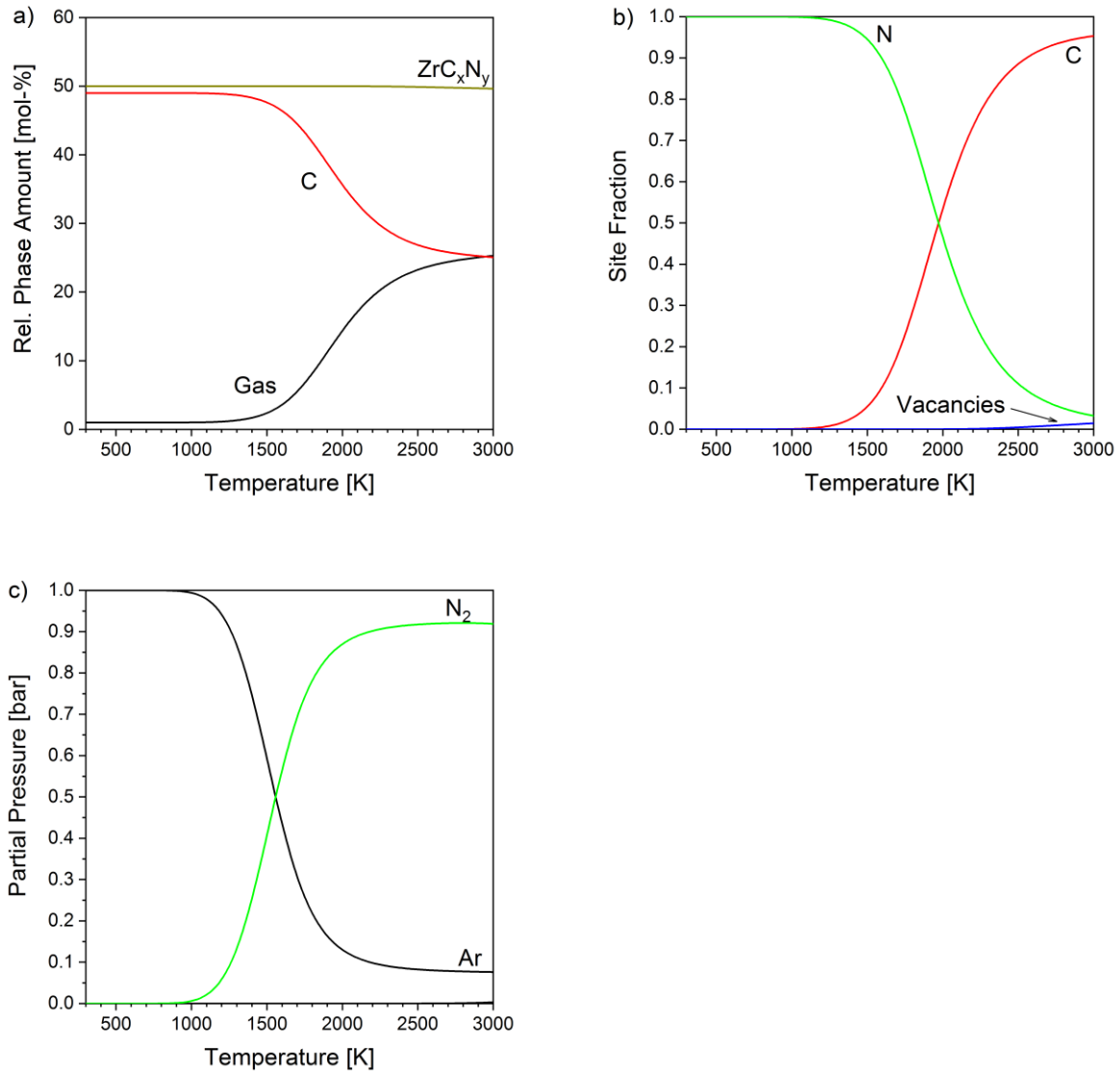
Figure 6.12: Calculated temperature dependence of the a) phase fraction, b) site fraction and c) gas composition for ZrC$_x$N$_y$ and graphite.

6.3. Experimental investigations

ZrB_2/Si-C-N-composites were prepared by pyrolysis of a mixture of ZrB_2 powder with the liquid precursor polymer PSZ 20 (see also Section 3.1). Figure 6.13 shows thermogravimetric experiments during heat-treatment of the ZrB_2/PSZ 20-mixture in flowing Ar and Ar/N_2 atmosphere (p_{N2} = 0.5 bar). Thermogravimetric experiments for the pyrolysis of pure PSZ 20 under identical conditions are shown for comparison (see Section 5.1.2). The mass-changes obtained with the ZrB_2/PSZ 20-mixtures are normalized to their PSZ 20 content for better comparability.

In the first stage, the liquid polysilazane PSZ 20 is cross-linked by stepwise heating from room temperature to 573 K. During this stage a mass-loss is obtained by evaporation of oligomers and by the release of gaseous hydrogen-containing molecules (H_2, CH_4,...) upon formation of new bonds between individual polymer chains (see also Section 5.1). The mass change during stage 1 does not differ between the ZrB_2-containing and the pure PSZ 20.

In the second stage, the actual pyrolysis process is initiated by heating the crosslinked polymer with 5 K/min. An additional mass loss is observed during this stage upon transformation of the cross-linked polymer into a solid, amorphous Si-C-N ceramic. This process is accompanied by the release of hydrogen, which is an integral part of the polymers functional groups (Si-H, N-H, C-H), in form of hydrogen-containing gas species (H_2, CH_4, NH_3,...). The mass change during stage 2 shows a higher scattering for ZrB_2-containing samples compared to pure PSZ 20.

In stage 3 a final holding time of 5 hours is applied at the maximum temperature of 1473 K, 1573 K, 1673 K and 1773 K, respectively. This is intended to ensure that the pyrolysis process is completed and possible reactions within the Si-C-N ceramic or with the ZrB_2-additive can take place. Maximum temperatures of 1673 K and 1773 K result in an additional mass loss during this stage.

The mass changes in stage 1 and stage 2 do not differ whether experiments were conducted in Ar/N_2 or pure Ar. However, in stage 3, samples show higher mass-losses in Ar/N_2 compared to pure Ar.
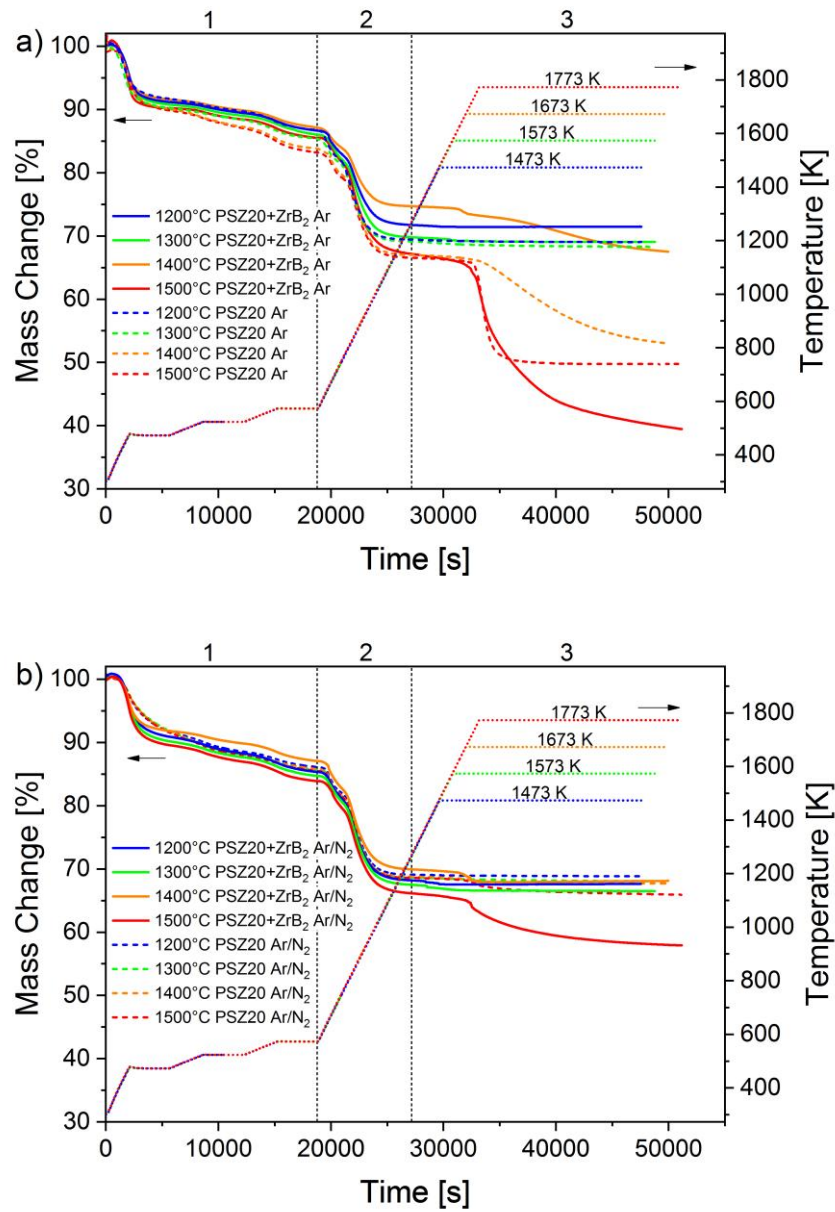
Figure 6.13: Thermogravimetric analysis of the pyrolysis of ZrB$_2$-filled PSZ 20 in flowing a) Ar and b) Ar/N$_2$ (p_{N2} = 0.5 bar). Results for pure PSZ 20 are shown for comparison.

The micrographs of the ZrB$_2$/Si-C-N-composites, depicted in Figure 6.14, reveal a homogeneous distribution of ZrB$_2$-particles in the Si-C-N matrix. Cracks are resulting from shrinkage during pyrolysis upon transformation of the liquid preceramic polymer into the solid Si-C-N matrix. Samples, which were heat-treated at maximum temperatures of 1473 K - 1573 K in Ar and 1473 K - 1673 K in Ar/N$_2$, show a very homogeneous Si-C-N matrix surrounding the ZrB$_2$ particles. After pyrolysis and heat-treatment at 1673 K and 1773 K in Ar and 1773 K in Ar/N$_2$ the Si-C-N matrix possesses a porous microstructure resulting from the decomposition reaction corresponding to the behavior of pure PSZ 10 and PSZ 20 during pyrolysis and heat-treatment under the same conditions (see also Section 5.1.2).

Figure 6.15 shows a higher magnification of a ZrB$_2$/Si-C-N composite obtained by pyrolysis at a maximum temperature of 1773 K in flowing Ar. EDX-analysis was performed at three individual regions of the sample: a ZrB$_2$ particle, the surrounding Si-C-N matrix and a smooth area adjacent to a ZrB$_2$ particle, which is silicon-rich and low in carbon content. The Si-C-N matrix mainly consists of Si and C after heat treatment at 1773 K in Ar, indicating the depletion of nitrogen during the decomposition reaction of the matrix (see also Section 5.1). The porous microstructure is probably prone to wet sample preparation, resulting in a small oxygen signal only in this region.
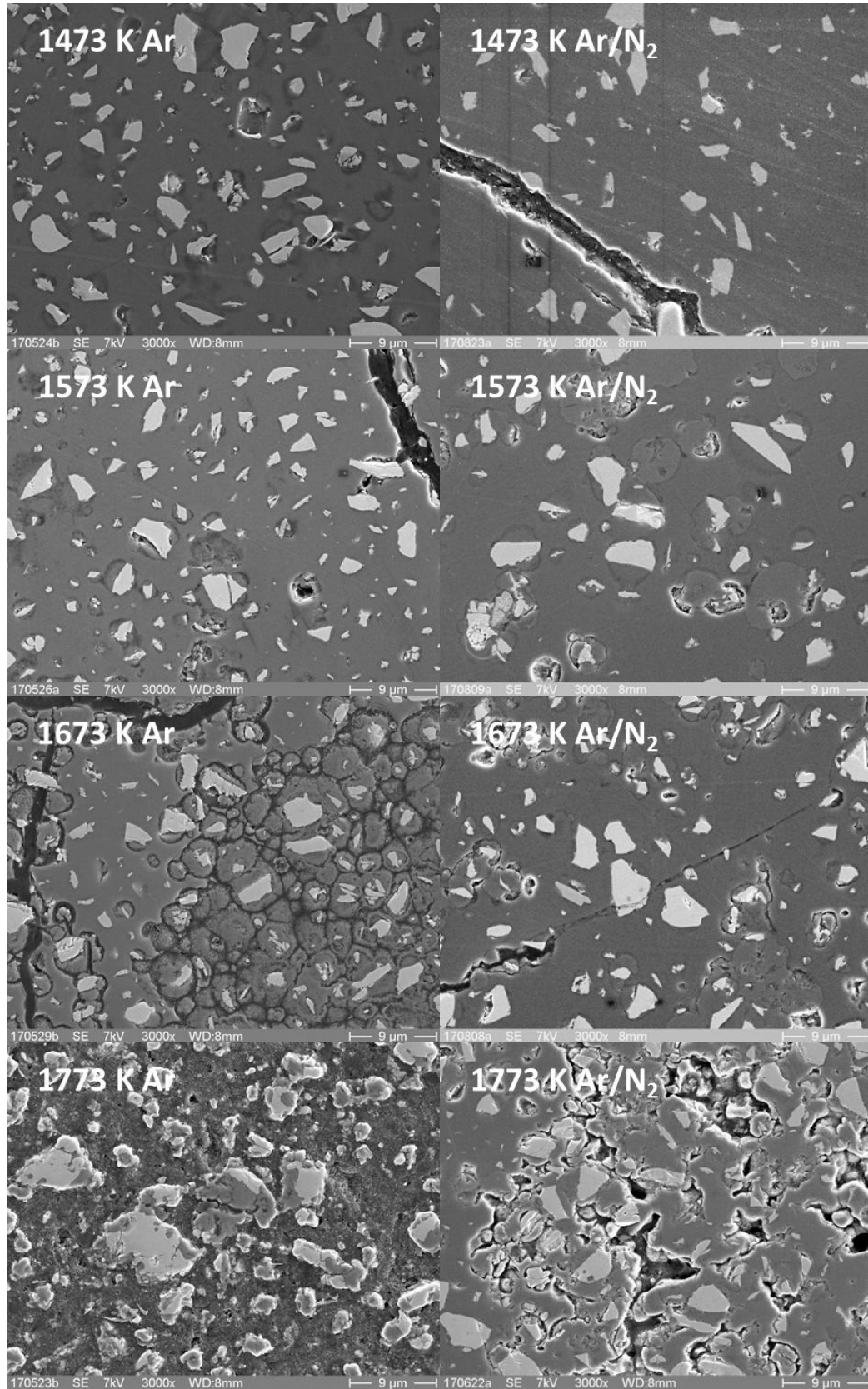
Figure 6.14: Micrographs of ZrB$_2$/Si-C-N composites obtained from pyrolysis in flowing Ar and Ar/N$_2$.
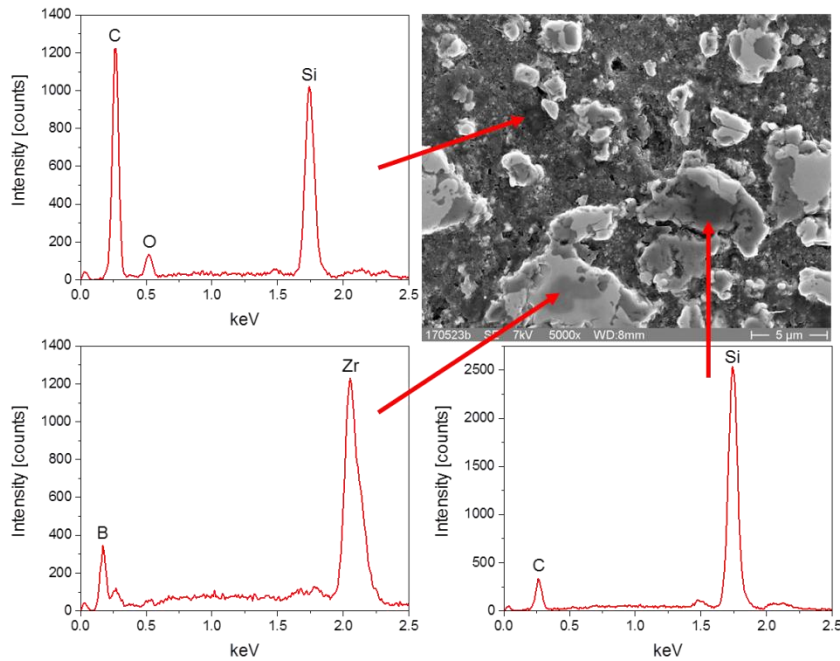
Figure 6.15: SEM micrograph and EDX analysis of a ZrB₂/Si-C-N composite obtained from pyrolysis at 1773 K in flowing Ar.

Figure 6.16 clearly shows that the distribution of the transformed and untransformed regions depends on the distribution of the cracks. The Si-C-N matrix possesses a smoother and more homogeneous microstructure along the cracks compared to the bulk. This is indicating, that the cracks provide locally a higher nitrogen partial pressure, which is retarding the decomposition reaction.
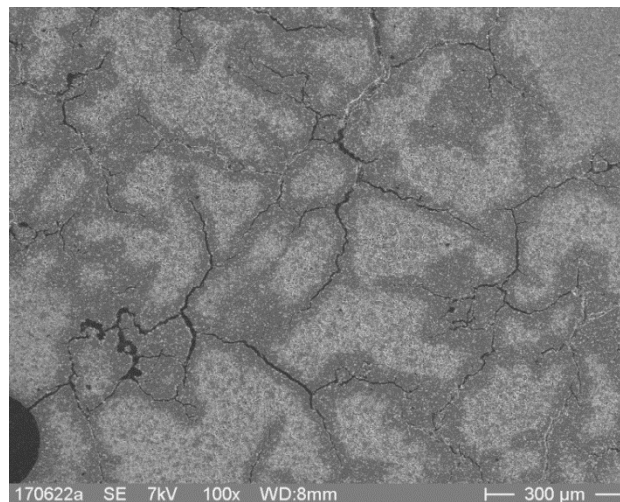
Figure 6.16: Micrograph of a ZrB₂/Si-C-N composite obtained from pyrolysis at 1773 K in flowing Ar/N₂ (p_{N2} = 0.5 bar).

XRD patterns of the obtained ZrB₂/Si-C-N composites, depicted in Figure 6.17, reveal the formation of ZrC$_x$N$_y$ at 1673 K in Ar and at 1573 K, 1673 K and 1773 K in Ar/N₂. The reflex position is between pure ZrC and ZrN. However, reflections of the ZrB₂ additive are predominant under all conditions. The Si-C-N matrix is X-ray amorphous after heat-treatment up to maximum

temperatures of 1573 K in Ar and up to 1773 K in Ar/N$_2$. Heat-treatment up to maximum temperatures of 1673 K and 1773 K in Ar results in crystallization of β-SiC. At the highest temperature of 1773 K in Ar, also reflections with very low intensity for Si are present. Preparation in Ar/N$_2$ at 1773 K resulted in rudimentary reflections of α-Si$_3$N$_4$ and ZrO$_2$ in cubic and monoclinic modification.
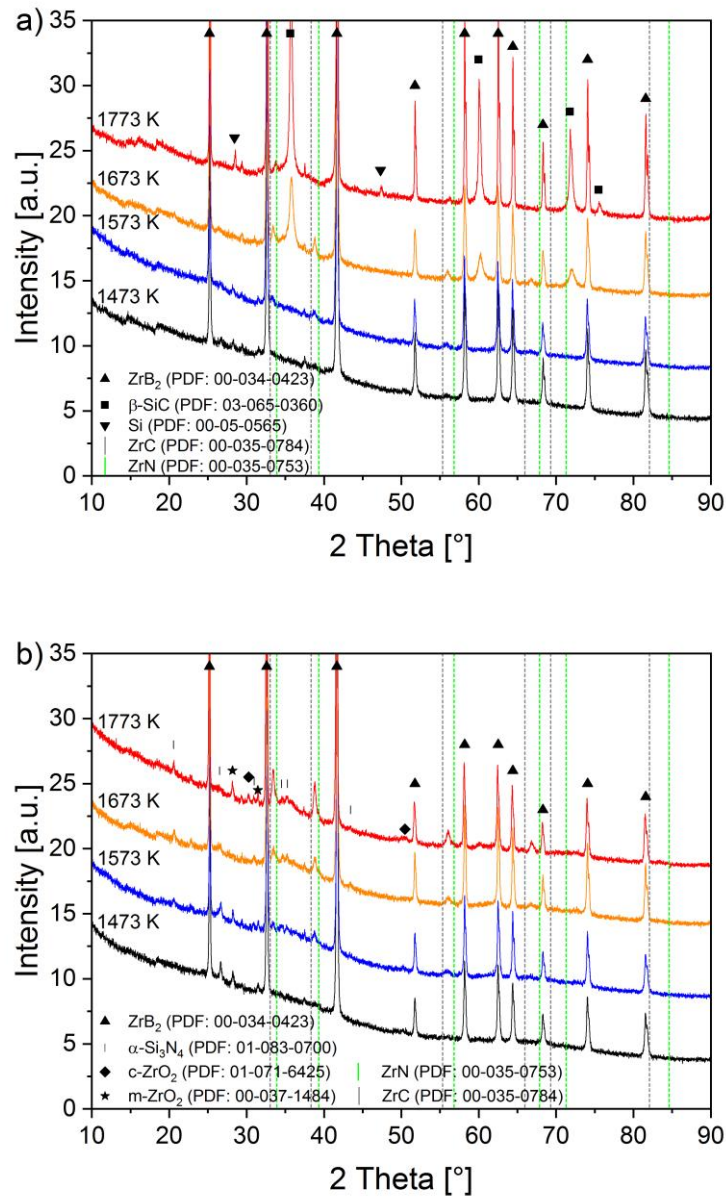
Figure 6.17: XRD patterns of ZrB$_2$/Si-C-N composites obtained from pyrolysis of ZrB$_2$-filled PSZ 20 in flowing Ar and Ar/N$_2$ at various maximum temperatures.

Isothermal nitriding of pure ZrB_2 powder

For further investigation of the ZrC_xN_y formation, isothermal nitriding experiments were performed with pure ZrB_2 powder at 1473 K, 1573 K, 1673 K and 1773 K. XRD patterns obtained after isothermal nitriding of ZrB_2 for 25 h in flowing Ar/N_2 (p_{N2} = 0.5 bar) are shown in Figure 6.18. Reflections of ZrB_2, show the highest intensities at all temperatures. In addition, reflections of ZrN are present with very low intensities already after nitriding at 1473 K. Increasing intensities of ZrN reflections are indicating an increasing phase fraction of ZrN after nitriding at higher temperatures. After preparation at all temperatures, samples showed rudimentary reflections of ZrO_2 in cubic modification. Intensities of c-ZrO_2 reflections are not increasing with temperature. Therefore, ZrO_2 is probably not formed during the experiments by oxygen impurities in the applied atmosphere but already present in the ZrB_2-powder.
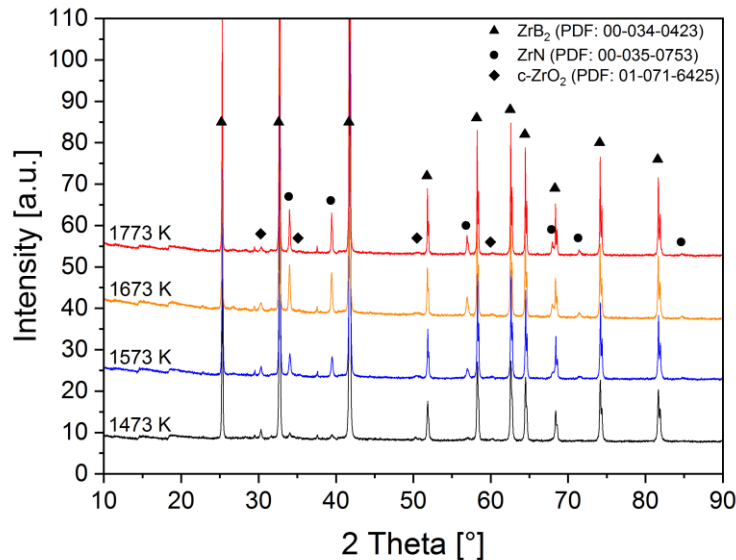
Figure 6.18: XRD patterns obtained from isothermal nitriding of ZrB_2 powder for 25h at 1473 K, 1573 K, 1673 K and 1773 K in flowing Ar/N_2 atmosphere (p_{N2} = 0.5 bar).

The mass conversion degree α was calculated according to:

$$\alpha = \frac{w_i - w_0}{w_f - w_0}$$

(6.8)

with the initial w_0, intermediate w_i and final w_f mass for complete nitriding reaction of ZrB_2 according to reaction (6.7).

The linear reaction constant k_l and the Avrami exponent n of the nitriding reaction were determined using the Johnson-Mehl-Avrami-Kolmogorow (LMAK) equation [128][129][130]:

$$\alpha(t) = 1 - \exp\left(-k_l \cdot t^n\right)$$

(6.9)

The evolution of the mass conversion degree during isothermal nitriding (Figure 6.19a) shows linear nitriding kinetics at 1473 K, 1573 K and 1673 K. The obtained kinetic parameters are summarized in Table 6.1. The Arrhenius plot of the linear reaction constant k_l (Figure 6.19b) yields an apparent activation energy of 154 kJ/mol. Isothermal nitriding at 1773 K results in more complex non-linear behavior and is therefore not considered for kinetic evaluation.
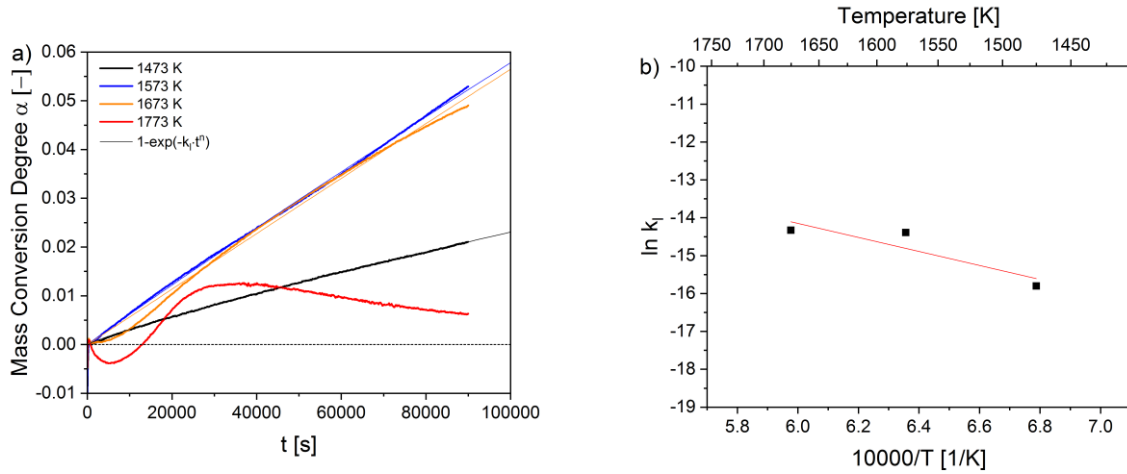
Figure 6.19: a) Mass conversion degree α and b) Arrhenius plot of the linear reaction constants obtained from isothermal nitriding of ZrB₂ powder at 1473 K, 1573 K, 1673 K and 1773 K in flowing Ar/N₂ (p_{N2} = 0.5 bar).

Table 6.1: Fitting parameters obtained from isothermal nitriding data of ZrB₂ powder.

Temperature [K]	n	k_l	R^2
1473	0.88	$1.37 \cdot 10^{-7}$	0.996
1573	0.98	$5.63 \cdot 10^{-7}$	0.999
1673	1.01	$5.99 \cdot 10^{-7}$	0.994

6.4. Discussion and Conclusion

Thermodynamic modeling revealed no interactions of the ZrB_2-additve with SiC and C, as constituents of the Si-C-N ceramic matrix, up to liquid phase formation at 2559 K and 2535 K, respectively. These finding are supported by the work of Kaufman [131] who found eutectic temperatures of 2480 K and 2663-2700 K for the systems ZrB_2-SiC and ZrB_2-C, respectively. Nasiri et al. [132] investigated the high-temperature stability of carbon fiber-reinforced ZrB_2-SiC (ZrB_2-SiC-C_{sf}) nanocomposites. No interactions of the constituents were observed up to the highest investigated temperature of 2423 K. ZrB_2 and Si_3N_4 show the first reaction, under formation of a liquid phase (reaction (6.5)), at 1870 K. This is confirmed by experimental work by Guo et al. [133][134] who observe the reaction of ZrB_2 and Si_3N_4 at temperatures from 1873 K in Ar. $ZrSi_2$ as found by Guo et al. was probably crystallizing from the Si- and Zr-containing liquid phase. Additionally, the Si- and Zr-containing melt is reducing the thermal decomposition temperature of the remaining Si_3N_4 by 23 K compared to pure Si_3N_4. Fortunately, the reaction of ZrB_2 and Si_3N_4 occurs 113 K above the internal carbothermic reaction of the PSZ 20-derived Si-C-N matrix (see Section 5.1, reaction (5.2). Therefore, the ZrB_2-additive does not represent an additional limitation for the maximum application temperature of the ZrB_2/Si-C-N-composite.

In the following, the formation mechanism of ZrC_xN_y is discussed. A direct reaction of the ZrB_2-additive and C from the Si-C-N matrix is excluded by the CALPHAD-modeling (Figure 6.6a). Brewer et al. [135] also confirmed the non-reactivity experimentally. Furthermore, a reaction of ZrB_2 and Si_3N_4 in the Si-C-N matrix is excluded at the experimentally considered temperatures ($\leq$ 1773 K) according to the CALPHAD-modeling (Figure 6.8). Instead, a solid/gas reaction of ZrB_2 and N_2 from the atmosphere is indicated by the more pronounced ZrC_xN_y-formation in ZrB_2/Si-C-N composites in Ar/N_2 compared to pure Ar (Figure 6.17) as well as ZrN-formation during isothermal nitriding experiments of ZrB_2-powder (Figure 6.18), respectively.

The phase stability diagram, depicted in Figure 6.10, shows that ZrB_2 is only stable at the highest temperatures und low nitrogen partial pressures. At lower temperatures and high p_{N2} ZrN and BN are stable equilibrium phases. With increasing p_{N2}, the transition according to reaction $ZrB_2 + 3/2 N_2 = ZrN + 2BN$ is shifted to lower temperatures. These findings are in good accordance with experimental work by Brewer et al. [135] (Ti, Zr, W, Cr-borides in N_2) and Kiessling et al. [136] (Cr, Fe, W-borides in ammonia). They observed that borides are only stable at the highest temperatures, and nitrides are formed at lower temperatures. Brewer et al. [135] found ZrB_2 being stable at 1820 K in 0.5 atm N_2. This is in contrast to the calculated phase stability diagram in Figure 6.10, which predicts the reaction $ZrB_2 + 3/2 N_2 = ZrN + 2BN$ below 2115 K under these conditions. This shows that local conditions at solid/gas interfaces can differ from overall equilibrium conditions. Reactions can be defined by the local boundary conditions like diffusion of gaseous products or educts in boundary layers.

XRD measurements (Figure 6.17) revealed that ZrC_xN_y-formation is much more pronounced in Ar/N_2-atmosphere. This is especially evident at 1773 K, where still no ZrC_xN_y-formation is observed in pure Ar-atmosphere. Only for the ZrB_2/Si-C-N-composite obtained by pyrolysis and heat-treatment up to a maximum temperature of 1673 K in Ar, ZrC_xN_y-formation is observed. An indication for this observation can be found in the combined thermogravimetric and mass spectroscopic analysis of the pyrolysis and high-temperature stability of PSZ 20 in Ar (see Section 5.1.2, Figure 5.11). In Ar, the carbothermic reaction according to reaction (5.2) already occurs at 1673 K, which is indicated by the observed mass loss and N_2-release. However, at 1673 K the mass loss and N_2-release are spread over a period of 5 hours, while at 1773 K a sudden mass loss and N_2-release is observed. Therefore, the extended N_2-release range at 1673 K is likely to account for the observed nitriding reaction of ZrB_2. An estimation of the N_2-amount, which is released by the carbothermic reaction of the PSZ 20-derived Si-C-N matrix, gives 0.01 mol per gramm of liquid PSZ 20 precursor polymer. This amount of nitrogen is enough to nitride the whole ZrB_2 in the ZrB_2/Si-C-N composite according to reaction (6.6).

Isothermal nitriding experiments using ZrB_2-powder where performed to investigate the solid/gas-reaction reaction between ZrB_2 and nitrogen in the Ar/N_2-atmosphere. XRD patterns of the obtained material (Figure 6.18) show the temperature-dependence of the ZrN-formation. Linear nitriding kinetics (Figure 6.19) are obtained at 1473 K, 1573 K and 1673 K with an apparent activation energy of 154 kJ/mol. Due to the limited number of experiments and the rather high uncertainty of the fit, this value should be considered as an indicative value. However, the activation energy is in the same range as obtained for nitriding powders of Si (114 kJ/mol [137]), Ti (202 kJ/mol [138]) and $TiSi_2$ (245-594 kJ/mol [139]). At 1773 K, a high deviation from the linear nitriding behavior is observed, which is probably resulting from the superimposition with other effects. However, no other phases are formed according to the XRD analysis depicted in Figure 6.18. A possible process could be an oxidizing reaction between the ZrB_2-powder and the Al_2O_3-crucible. The obtained boron-oxide species would have a high volatility at this temperature (see also Section 7), which would result in an overall mass loss.

A complete solubility is existing in the system ZrC-ZrN [140][141][142][143] due to the same crystal structure and similar lattice constants. Therefore, ZrN possesses a solubility for carbon. Hence, ZrC_xN_y is formed by dissolution of carbon from the Si-C-N matrix as soon as ZrN is present.

The state of the carbon in Si-C-N ceramic is essential for its solubility in ZrN. Bill et al. [16][101][102] found carbon in form of CSi_4- as well as mixed SiN_xC_y-units (with x=2.3, x+y=4) and sp^2-hybridized carbon in similar amorphous Si-C-N precursor-derived ceramics. However, the actual activity of carbon in the Si-C-N matrix is not known. Figure 6.11 shows that with increasing carbon activity, the solubility of carbon in ZrN is increasing. Furthermore, the solubility of carbon is increasing with temperature (Figure 6.12). Up to about 1200 K, ZrN and carbon are

coexisting chemically stable next to each other. At higher temperatures ZrC$_x$N$_y$ is formed, which for example contains 1 at.% of carbon at 1273 K (see Figure 6.12b).

The XRD measurements of the ZrB$_2$/Si-C-N composites (Figure 6.17) yield a lattice parameter of 4.64 Å for ZrC$_x$N$_y$. The system ZrC-ZrN obeys Vegard's law [141][144][145]. Therefore, according to the work by Lengauer et al. [145] (see Figure 6.20), the lattice parameter corresponds to a composition of C/(C+N) = 0.56. This conclusion is valid despite a possible under-stoichiometry of ZrC$_x$N$_y$ because an under-stoichiometry of ZrC and ZrN [146] has a minor effect on the lattice parameter compared to the C/(C+N) ratio in ZrC$_x$N$_y$ [145]. The obtained composition is in very good agreement with the work by Sun et al. [147] who observed ZrC$_x$N$_y$ with a composition of x = y = 0.5, or C/(C+N) = 0.5, after annealing a ZrB$_2$/Si-C-N composite at 1773 K in Ar, i.e. above the carbothermal reaction temperature of the Si-C-N matrix. Sun et al. [147] did not specify the annealing duration.
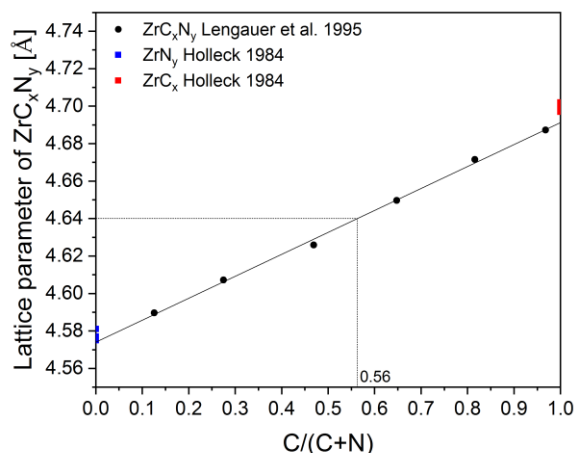
Figure 6.20: Compositional dependence of the lattice parameter in ZrC$_x$N$_y$ **[145][146]**. The lattice parameter, which was determined in this work, is indicated.

Additionally, Sun et al. [147] attribute a stabilizing effect of the ZrB$_2$-additive on the carbothermal decomposition reaction of the Si-C-N matrix. This observation was not confirmed in this work. Thermogravimetric curves obtained from pyrolysis of ZrB$_2$/PSZ 20 and BN/PSZ 20 mixtures, which were normalized to their PSZ 20-content, did not show a systematic difference compared to pure PSZ 20 samples (see Figure 6.13).

Microscopically, the ZrB$_2$/Si-C-N composites show cracks (Figure 6.14), similar to behavior of pure Si-C-N composites (Figure 5.20). These are resulting from the shrinkage upon transformation of the liquid polymer into the solid Si-C-N ceramic. However, ZrB$_2$-filled PSZ 20 show additionally spallation of small parts of the sample upon pyrolysis of the samples and thus also a higher scattering in the thermogravimetric measurements (Figure 6.13). This scattering is much more pronounced in the pyrolysis of ZrB$_2$-containing samples compared to pure PSZ 20 or BN/PSZ 20 mixtures (Figure 6.2). This is most likely a result of the significant mismatch in the

thermal expansion coefficients (CTE) between the ZrB$_2$-additive (α = 6.6-8.4·10^{-6} K^{-1} [148][149]) and the surrounding ceramic Si-C-N Matrix 3.1-3.5·10^{-6} K^{-1} [150]. The CTE of ZrC$_x$N$_y$, with the composition derived in this work (C/(C+N) = 0.56) is α = 7.8·10^{-6} K^{-1} according to the work by Aigner et al. [151] and thus very similar to ZrB$_2$.

The decomposition reaction of the Si-C-N matrix in the ZrB$_2$/Si-C-N composite at 1773 K in Ar/N$_2$ (see Figure 6.16) is retarded along cracks compared to the bulk of the sample. Cracks make part of the sample accessible to the flowing Ar/N$_2$ atmosphere with p_{N2}=0.5 bar. In contrast to that, the bulk of the sample is cut off from the atmosphere and additionally depleted in p_{N2} by the solid/gas nitriding reaction (6.6) of the ZrB$_2$-additive (see Figure 6.10). Therefore, the strongly p_{N2}-dependent carbothermic reaction (5.2) of the Si-C-N matrix causes a much more pronounced microstructural change within the sample compared to areas, which are accessible by cracks.

Silicon-rich regions adjacent to ZrB$_2$ particles in the ZrB$_2$/Si-C-N composites after heat-treatment up to 1773 K in Ar (Figure 6.15) are possibly solidified Si-rich melt. Pure PSZ 10 derived Si-C-N ceramics already show weak Si reflections in XRD measurements (Figure 5.16) under these conditions. Additionally, Si possesses a solubility for carbon according to the binary Si-C phase diagram [77].

BN/PSZ 20 mixtures do not show spallation upon pyrolysis and therefore exhibit no scattering in thermogravimetric experiments (see Figure 6.2). Both, the obtained ZrB$_2$/Si-C-N and BN/Si-C-N ceramics show a homogeneous distribution of the additive. However, ZrB$_2$ is present in the Si-C-N matrix as discrete solid particles, whereas BN appears agglomerate-like (see Figure 6.3). BN/PSZ 20 and ZrB$_2$/PSZ 20 mixtures were prepared equimolar with regard to their boron content. Therefore, the molar fraction of BN is twice the molar fraction of ZrB$_2$ to obtain the same boron content. However, the resulting molar volume fraction of BN (23.6 cm³ per two mole) and ZrB$_2$ (18.6 cm³ per one mole) are very similar and should therefore not account for the observed spallation of ZrB$_2$-containing samples. Hexagonal BN has a highly anisotropic CTE of -2.7·10^{-6} K^{-1} perpendicular to the c-axis and 38·10^{-6} K^{-1} parallel to the c-axis [152]. Therefore, most likely the layered, agglomerate-like structure of the BN additive should account for the improved resistance against spallation of the BN/Si-C-N composites compared to ZrB$_2$/Si-C-N composites.

7. High-temperature oxidation behavior of ZrB₂

ZrB_2 is considered as an ultra high temperature ceramic (UHTC) and one of the most oxidation resistant transition metal diborides [153][154] with potential application in extreme environments like aerospace reentry vehicles and hypersonic vehicles [155]. Therefore, the focus of most studies is on the oxidation of ZrB_2 in oxygen [153][156][157][158]. Only few studies are available on the oxidation behavior in steam at high temperatures. Therefore, the oxidation and volatilization behavior of ZrB_2 in atmospheres O_2- and H_2O-containing was investigated in the present chapter. For this purpose, a combination of thermodynamic calculations and high-temperature oxidation tests was used.

7.1.   Thermodynamic analysis of ZrB₂ oxidation

Figure 7.1 shows phase stability diagrams for Zr and B as a function of the nitrogen and oxygen partial pressures. For the depiction of the Zr phase stability diagram, solubilities were neglected, which would result in curved phase boundaries. Metallic Zr (Figure 7.1a) is only stable at the lowest p_{N2} and p_{O2}. With increasing p_{O2} and p_{N2}, ZrO_2 and ZrN is formed, respectively. For boron (Figure 7.1b), equilibrium partial pressures are higher for both oxidizing and nitriding reactions by a factor of 10^8. Generally, equilibrium partial pressures for oxidizing and nitriding are increasing with temperature.
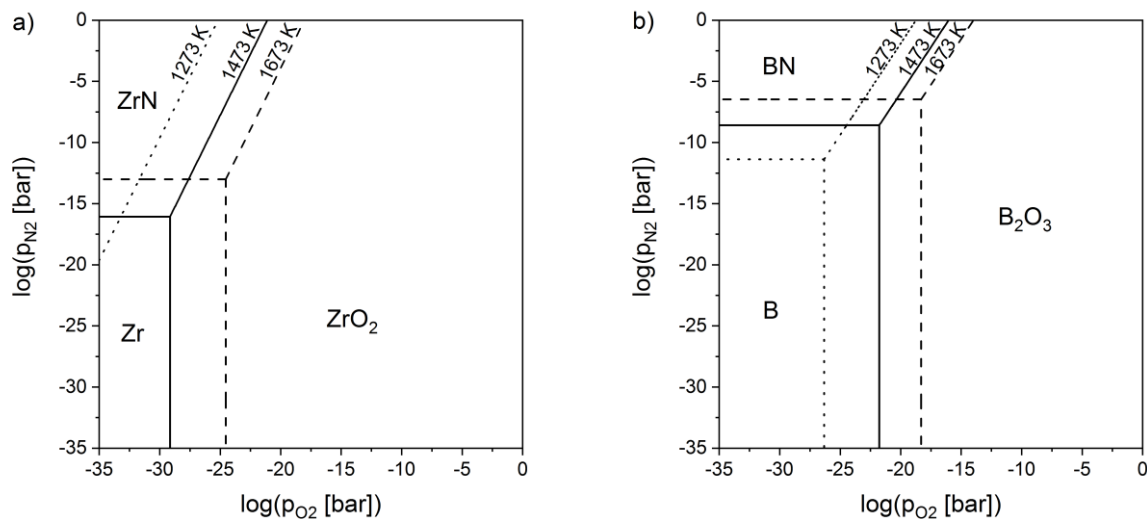
Figure 7.1: Calculated phase stability diagrams for a) Zr and b) B at 1273 K, 1473 K and 1673 K.

Figure 7.2 shows calculated partial pressures of the volatile species BO$_x$ and ZrO$_x$ as a function of p$_{O2}$ at 1473 K. Additionally, the corresponding volatility diagrams calculated, following the approach of Lou and Heuer [159], at 1273 K, 1473 K and 1673 K are shown. The dashed line marks the equilibrium oxygen partial pressure for the oxidation reaction (e.g. 2B+3/2O$_2$=B$_2$O$_3$; log p$_{O2}$ = -21.77). This means, below the dashed line, B- and Zr-containing gas species are in equilibrium with solid B and Zr, respectively. The formation of condensed oxide B$_2$O$_3$ or ZrO$_2$, at p$_{O2}$ higher than indicated by the dashed line, has potentially a passivating effect on the oxidation behavior of the underlying material.

The equilibrium oxygen partial pressure for the oxidation of boron is log p$_{O2}$ = -21.77. In equilibrium with solid boron, mainly the gas species B(g), BO(g) and B$_2$O$_2$(g) are formed with increasing p$_{O2}$. In equilibrium with the solid oxide B$_2$O$_3$, B$_2$O$_2$(g), B$_2$O$_3$(g) and BO$_2$(g) are formed with the highest partial pressures. In addition, minority gas species B$_2$O(g) and B$_2$(g) are present at lower partial pressures outside the depicted pressure range.

Gaseous Zr-species yield much lower partial pressures compared to B. Therefore, diagrams in Figure 7.2c and d are depicted over a larger scale. The majority gas species in equilibrium with solid Zr is Zr(g) almost up to the equilibrium p$_{O2}$ for the oxidation (log p$_{O2}$ = -33.56). In equilibrium with solid oxide ZrO$_2$, mainly gaseous ZrO(g) and ZrO$_2$(g) are formed. Additionally, the minority gas species Zr$_2$(g) is formed.
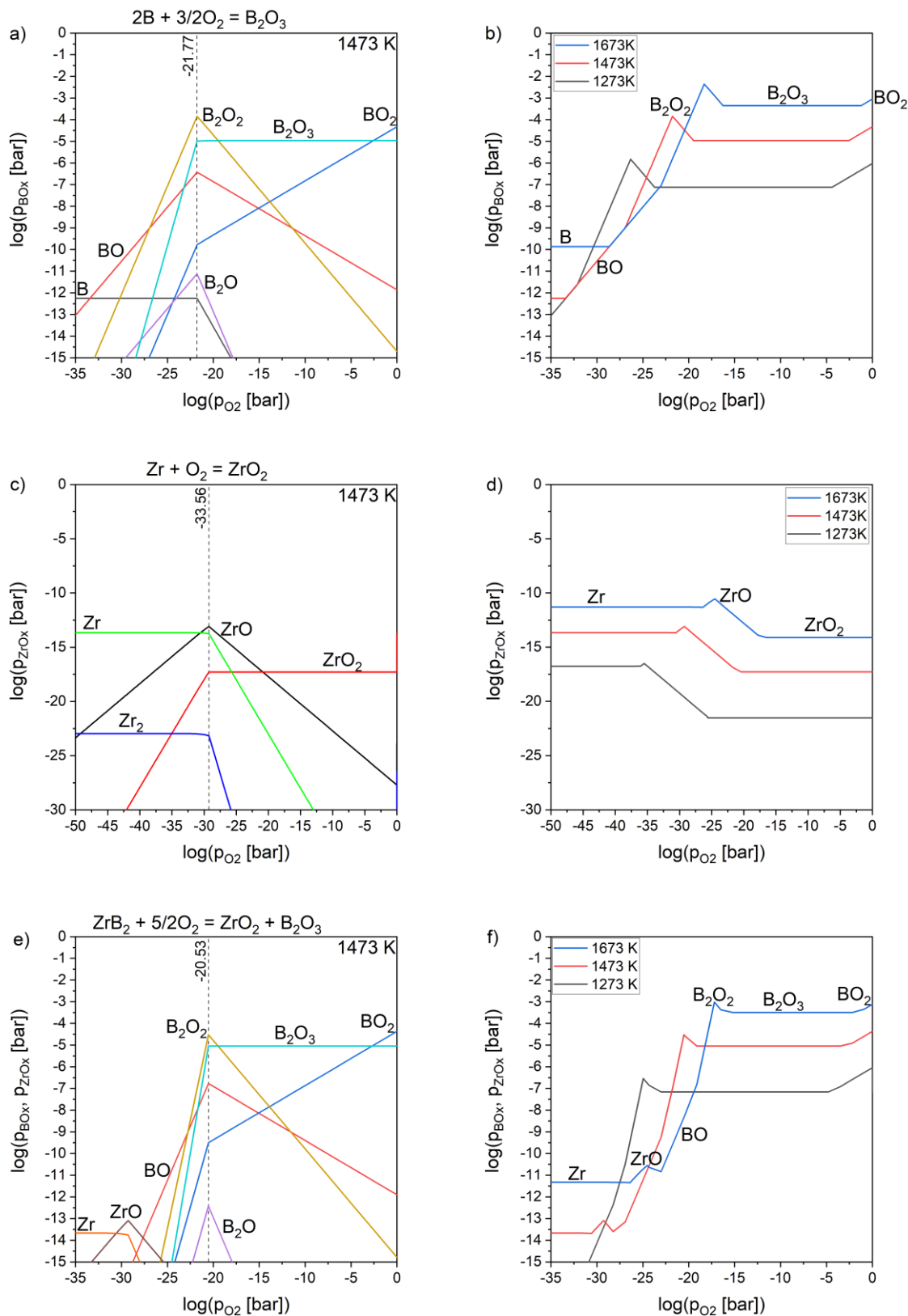
Figure 7.2: Calculated partial pressures as a function of the oxygen partial pressure for a) B, c) Zr and e) ZrB$_2$ at 1473 K. The respective volatility diagrams at 1273 K, 1473 K and 1673 K are depicted in b), d) and f).

The composition of the self-developing gas phase for B$_2$O$_3$ in a) oxygen and b) steam at p_{O2} = 0.2 bar and p_{H2O} = 0.2 bar, respectively, is shown in Figure 7.3. The gas species O$_2$ and H$_2$O and their dissociation products are considered in the equilibrium calculations but not depicted in Figure 7.3. The same holds for the constant amount of Ar (x(Ar)=0.01) which was added as an inert gas to establish a stable gas phase at every temperature. In the employed SGTE dataset (see also Section 4) the gas species H$_3$B$_3$O$_6$(g) is included. This species is formed in a polymerization reaction from the metaboric acid HBO$_2$(g). However, this reaction is very slow and H$_3$B$_3$O$_6$(g) is considered to be stable only at low temperatures according to Miyahara et al. [160]. Therefore, H$_3$B$_3$O$_6$(g) was not considered in the equilibrium calculation. In oxygen (Figure 7.3a), oxygen-containing gas species B$_2$O$_3$(g) and BO$_2$(g) are formed with the highest partial pressures as well as BO(g) and B$_2$O$_2$(g) with intermediate partial pressures (p < 10^{-4} bar). Atomic gaseous boron is formed with the lowest partial pressure at the highest temperatures. In steam (Figure 7.3b), primarily hydroxides are formed. Below 1179 K the main gas species formed is orthoboric acid H$_3$BO$_3$(g) and above 1179 K metaboric acid HBO$_2$(g). Due to the formation of gaseous hydroxides, partial pressures are higher in steam compared to oxygen atmosphere. At all considered temperatures, partial pressures of boron hydroxides are higher than 3·10^{-4} bar.
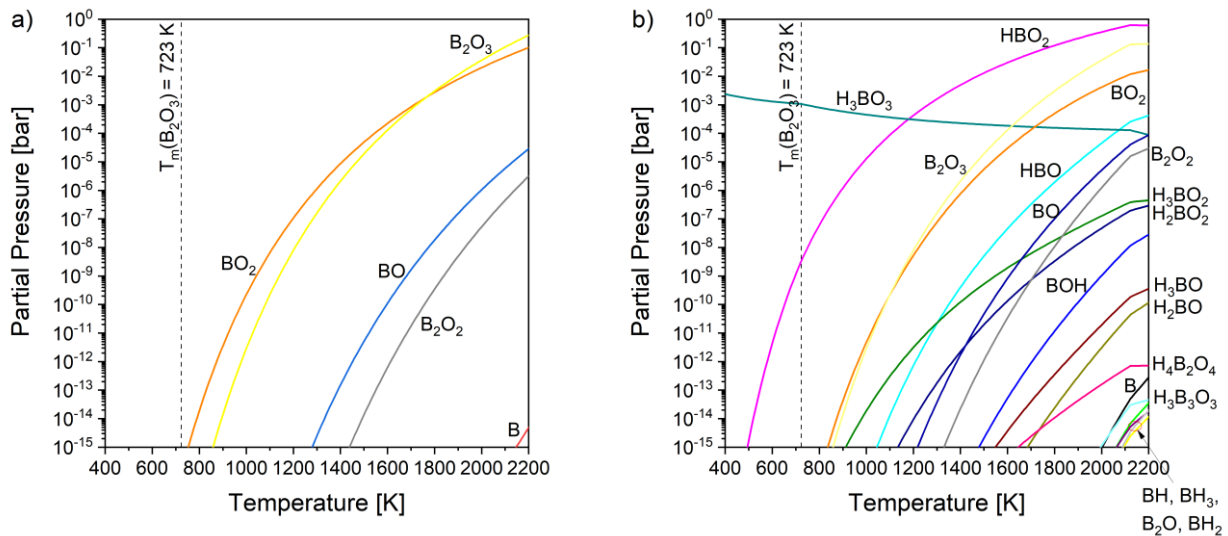
Figure 7.3: Calculated partial pressures of the boron-containing gas species as a function of temperature for B$_2$O$_3$ at a) p_{O2} = 0.2 bar and b) p_{H2O} = 0.2 bar.

Figure 7.4 shows the phase stability diagram of ZrB$_2$, ZrC and ZrN as a function of temperature, p_{O2}. The lines correspond to the following equilibrium reactions with oxygen:

$$ZrB_2 + 5/2 O_2 = ZrO_2 + B_2O_3 \qquad (7.1)$$

$$ZrC + 3/2 O_2 = ZrO_2 + CO \qquad (7.2)$$

$$ZrC + 2O_2 = ZrO_2 + CO_2 \tag{7.3}$$

$$ZrN + O_2 = ZrO_2 + 1/2N_2 \tag{7.4}$$
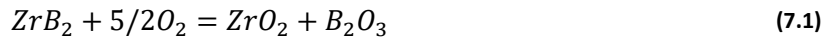
In oxygen, the equilibrium oxidation reaction occurs at about the same oxygen partial pressure for ZrB₂, ZrC and ZrN. Although ZrC possesses the lowest oxidation partial pressure, only a minor difference is observed compared to ZrN and ZrB₂.
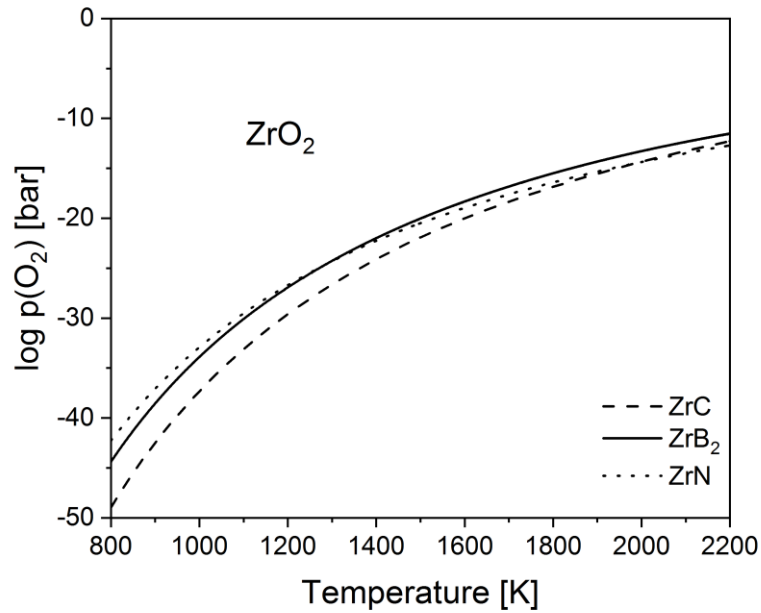
Figure 7.4: Phase stability diagram of ZrB₂, ZrC and ZrN as a function of temperature and p_{O2}.

7.2. ZrB$_2$ oxidation protection and passivation in oxygen

Figure 7.5 and Figure 7.6 are showing results from dynamic oxidation experiments of ZrN and ZrB$_2$ during heating up with 5 K/min to a maximum temperature of 1473 K in O$_2$/Ar-atmosphere (p$_{O2}$=0.2 bar). ZrN is forming ZrO$_2$ under release of N$_2$ upon oxidation in oxygen-containing atmosphere according to equation (7.4). Therefore, the progress of the oxidation reaction can be followed not only by the mass change but also by the accompanied N$_2$-signal in the off-gas of the instrument. The onset of the oxidation reaction is above about 700 K with a maximum oxidation rate at about 900 K. At higher temperatures the mass change shows a discontinuity, followed by a second maximum in the oxidation rate above 1000 K. This behavior is probably a result of the breakup of the oxide formed during the first part of the experiment, and the related exposure of underlying 'fresh' material to the oxidizing atmosphere. This is supported by the appearance of the sample after the oxidation experiment (Figure 7.5c), which is completely disintegrated to a fine powder. It is well known that ZrN is undergoing a large increase in the molar volume of 48 % upon oxidation, which is leading to so-called breakaway oxidation [161]. This means that the resulting ZrO$_2$-scale is not mechanically stable or dense and does therefore not protect the underlying material from oxidation. At about 1100 K the maximum mass of the sample is reached indicating that the sample was oxidized completely. At higher temperatures, the slight mass loss is accompanied by an exponentially temperature dependent N$_2$-release. This corresponds to a wide homogeneity range in the Zr-O-N system [162]. Released nitrogen was probably solved in the material at lower temperatures.
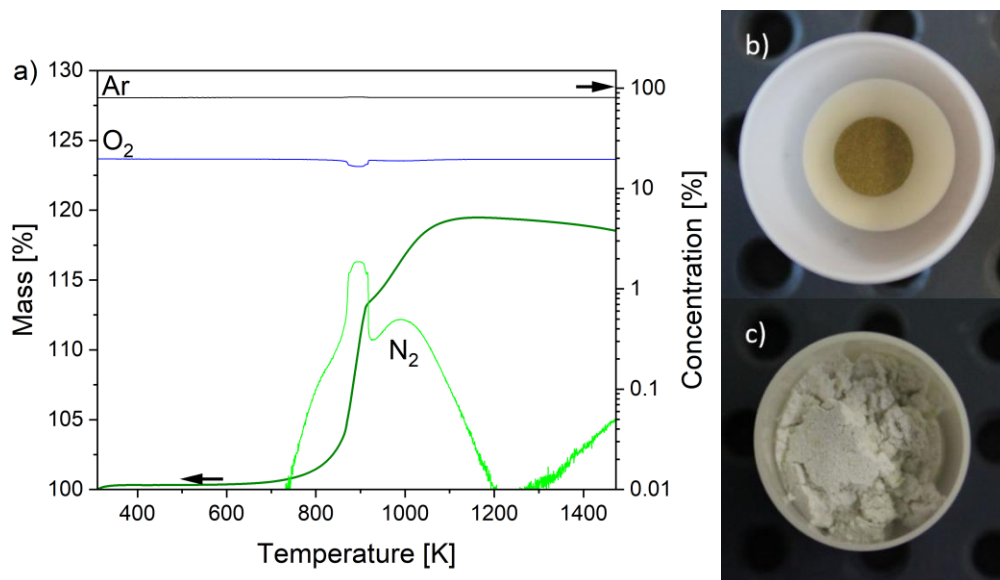
Figure 7.5: Dynamic oxidation experiment of compacted ZrN powder in O$_2$/Ar (p$_{O2}$=0.2 bar); a) thermogravimetric and mass spectrometric analysis, b) ZrN sample before and c) after oxidation in O$_2$/Ar-atmosphere heated with 5 K/min to 1473 K. The diameters of the specimen and the alumina crucible correspond to 5 mm and 17.3 mm, respectively.

A dynamic oxidation experiment of ZrB$_2$ in oxygen-containing atmosphere is shown in Figure 7.6. The onset of oxidation at about 700 K indicated by the gradual increase of the mass change curve. The highest oxidation rate is at about 950 K, which is 50 K higher than for oxidation of ZrN. However, the ZrB$_2$ sample does not oxidize completely. Instead, the mass increase is declining strongly above 1000 K and almost stops completely at higher temperatures. Only at the highest temperatures above 1400 K, a slight mass increase is observed again.

The improved oxidation resistance of ZrB$_2$ compared to ZrN is due to the formation of B$_2$O$_3$ besides ZrO$_2$ analogous to equation (7.1). B$_2$O$_3$ is liquid at temperatures above 748 K. As a result, a protective layer is formed on the sample protecting the underlying sample material. Figure 7.7 shows the dense oxide layer enclosing the ZrB$_2$ sample including a crack, which is providing access for the oxidizing atmosphere. ZrB$_2$ starts oxidizing at lower temperatures compared to ZrN. At these temperatures the oxidation kinetics of ZrB$_2$ are too slow to form enough B$_2$O$_3$ to protect the sample. In addition, the slight increase in sample mass at temperatures above 1400 K is indicating a declining oxidation resistance at temperatures above 1500 K. This is most likely a result of first the increasing diffusivity of oxygen with increasing temperature and second the protective oxide layer is deteriorated by volatilization of boron-containing gas species (see also Section 7.1).
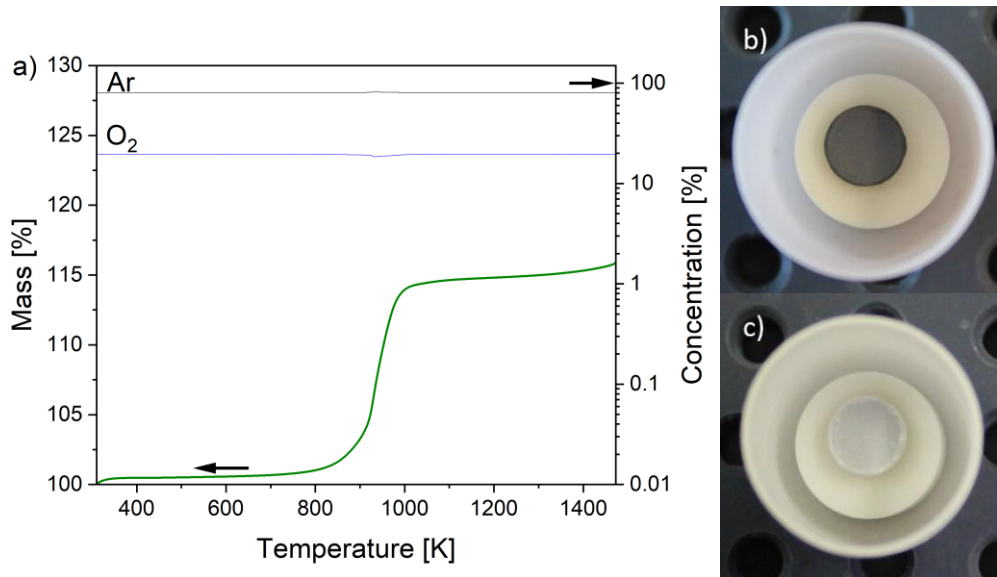
Figure 7.6: Dynamic oxidation experiment of compacted ZrB$_2$ powder in O$_2$/Ar (p_{O2}=0.2 bar); a) thermogravimetric and mass spectrometric analysis, b) ZrB$_2$ sample before and c) after oxidation in O$_2$/Ar-atmosphere heated with 5 K/min to 1473 K. The diameters of the specimen and the alumina crucible correspond to 5 mm and 17.3 mm, respectively.
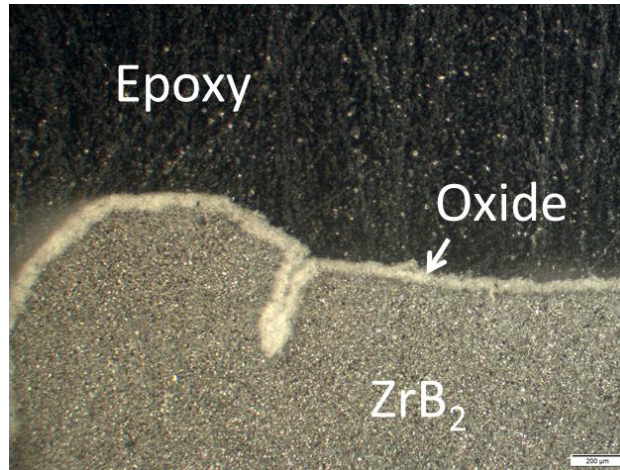
Figure 7.7: Micrograph of a ZrB$_2$ sample after heat-up with 5 K/min in O$_2$/Ar-atmosphere (p$_{O2}$=0.2 bar) to 1473 K. The scale bar corresponds to 200 µm.

7.3. ZrB₂ oxidation tests in steam and mass spectroscopic investigation

Figure 7.8 shows results from a dynamic oxidation experiment of ZrB$_2$ in steam-containing atmosphere. The sample was heated up with 10 K/min to 673 K in Ar and then equilibrated for 20 min. Subsequently, the sample was heated up with 5 K/min from 673 K to 1473 K in H$_2$O/Ar (p$_{H2O}$=0.2 bar). The composition of the STA off-gas, measured by mass spectrometry, is depicted in addition to the thermogravimetric data. The measured steam content is lower than 20 % since the protective Ar gas, flowing through the balance casing, is detected also. However, the protective Ar gas flow (5L/h) does not reach the sample. Therefore, the partial pressure of steam at the sample is still p$_{H2O}$=0.2 bar. With the introduction of steam (see dashed line in Figure 7.8), H$_2$ is released, which is a measure for the oxidation according to reaction:

$$ZrB_2 + 5H_2O = ZrO_2 + B_2O_3 + 5H_2 \qquad \textbf{(7.5)}$$
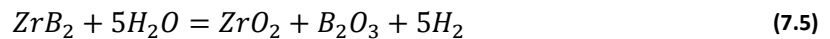
For each mole of ZrB$_2$, which is oxidized in steam, five moles of H$_2$ are released into the atmosphere.
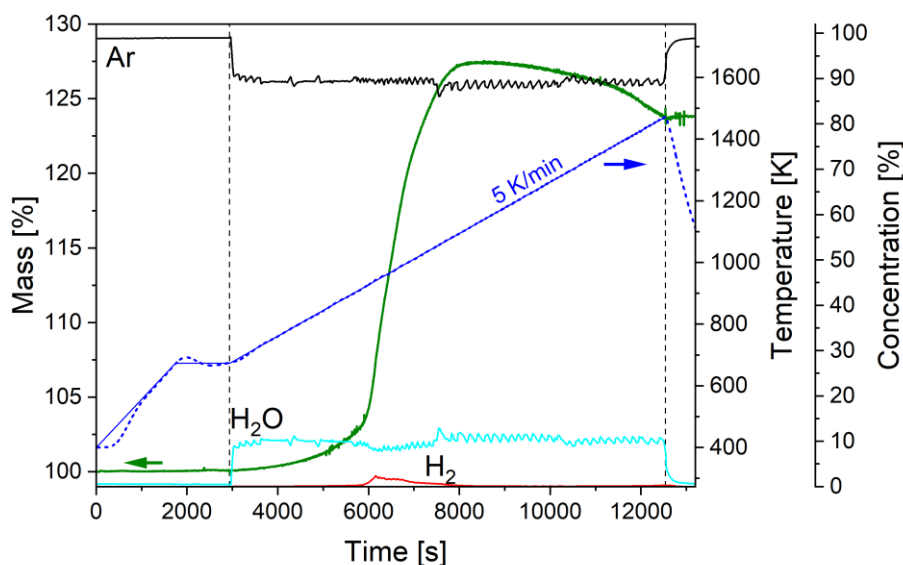
Figure 7.8: Thermogravimetric and mass spectrometric analysis of ZrB_2 oxidation in steam. After heat-up and equilibration in Ar, the sample was heated from 673 K to 1473 K with 5 K/min in H_2O/Ar-atmosphere (in between vertical dashed lines; p_{H_2O}=0.2 bar). The set temperature program is indicated by a solid blue line.

Therefore, the H_2 release rate is a valuable indicator for the progress of the oxidation. Especially, when the mass signal is the result of the superimposition of several processes taking place at the same time. By normalizing the measured H_2-concentration to the known amount of Ar as reference gas and the sample surface area, the H_2-release rate was calculated using equation (3.1) and plotted together with the mass change in Figure 7.9.

After start of steam injection during the heat-up phase starting at 673 K, at first, a gradual increase of the sample mass and the H_2 release rate is observed. From 900 K to 1100 K the slope of both signals possess a maximum. Therefore, the oxidation rate is largest in this temperature range. At 1100 K the maximum sample mass is reached and then slightly declining at higher temperatures. During this period, the H_2 release rate is at a constant low level, indicating that a steady-state is reached.

Above 1300 K, the H_2 release rate is again slightly increasing, while the sample mass is decreasing stronger at the same time. This is indicating that the oxide layer is losing its protective properties due to the volatilization of boron-containing gas species (see Figure 7.3). Consequently, the oxidation of the underlying material is proceeding stronger. However, the overall mass loss shows that the volatilization is outweighing the mass gain by oxidation. This is unlike the oxidation in oxygen-containing atmosphere were the sample mass is still increasing in this temperature range (see Figure 7.9b). Results from thermodynamic calculations explain this effect as depicted in Section 7.1, Figure 7.3: the generation of gaseous boron-containing species

is by several orders of magnitude higher in steam-containing atmosphere compared to oxygen-containing atmosphere.
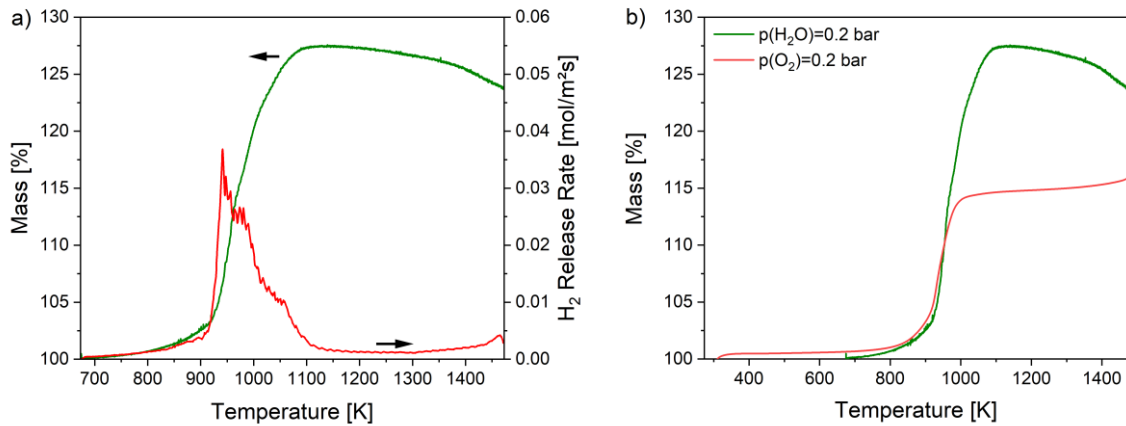
Figure 7.9: Measured H_2 release rate during heating of ZrB_2 with 5 K/min in H_2O/Ar-atmosphere (p_{H2O}=0.2 bar) and b) comparison of the observed mass gain with mass gain during oxidation of ZrB_2 in O_2/Ar (p_{O2}=0.2 bar).

The mass spectrum during heat-up of ZrB_2 in steam is depicted in Figure 7.10. Besides single ionized orthoboric acid $H_3BO_3^+$ and metaboric acid HBO_2^+ also molecules are detected which originate from fragmentation of these molecules ($H_2BO_3^+$, $H_2BO_2^+$, BO_2^+). Regarding the thermodynamic calculation (see Figure 7.3) also gaseous B_2O_3 and other B-O-H species could be present. However, these are likely to fragment into smaller molecules or condensate in the instrument or in the gas pipes before reaching the mass spectrometer.
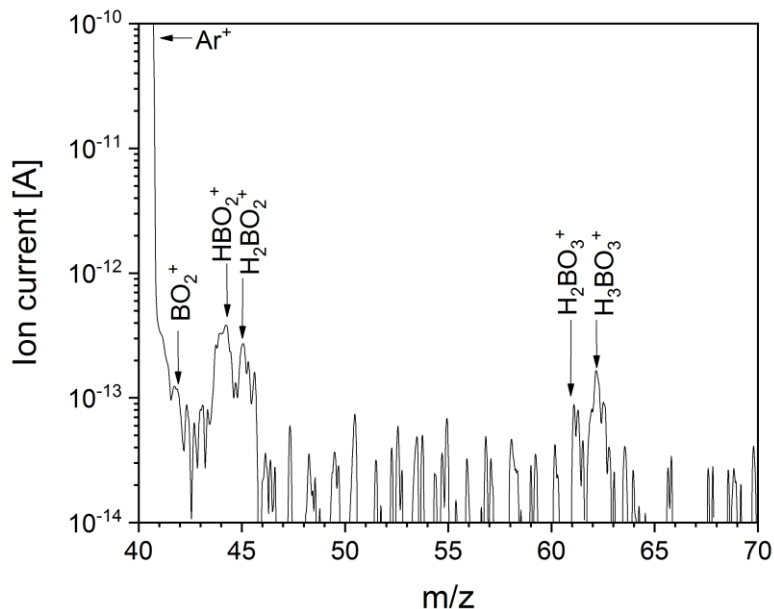
Figure 7.10: Mass spectrum measured during heating of ZrB_2 with 5 K/min in H_2O/Ar-atmosphere (p_{H2O}=0.2 bar).

The time dependent evolution of the ion current measured at mass to charge ratio (m/z) of 62, corresponding to H$_3$BO$_3$, is shown in Figure 7.11. During heat-up and equilibration at 673 K in Ar prior to the steam injection, no H$_3$BO$_3$ is present. At first by injection of the steam (indicated by vertical dashed line in Figure 7.11) the ion current at m/z=62 is increasing and reaching a maximum at about 1100 K. At higher temperatures, the ion current at m/z=62 is decreasing again. After stopping the steam flow at 1473 K, the ion current is immediately decreasing almost to the pre-test value. The maximum of the m/z=62 signal corresponds to the start of mass loss by direct evaporation of liquid B$_2$O$_3$ and by formation of gaseous hydroxides according to the following reactions:

$$B_2O_3(l) = B_2O_3(g) \tag{7.6}$$

$$B_2O_3 + H_2O = 2HBO_2 \tag{7.7}$$

$$B_2O_3 + 3H_2O = 2H_3BO_3 \tag{7.8}$$

Its noteworthy that the H$_2$-signal and the H$_3$BO$_3$-signal (m/z=62) are used to separate two individual effects acting at the same time on the mass change of the sample in steam. While the H$_2$-signal is indicative for the oxidation reaction (7.5) causing a mass gain, the H$_3$BO$_3$-signal (m/z=62) indicated the volatilization of the boron oxide causing a mass loss. Therefore the maximum in H$_2$-release at 1000 K corresponds to the maximum weight gain (Figure 7.9a) and the maximum in the m/z=62 signal at 1100 K to the onset of the samples weight loss. Note that no H$_2$ is released during the volatilization reactions.
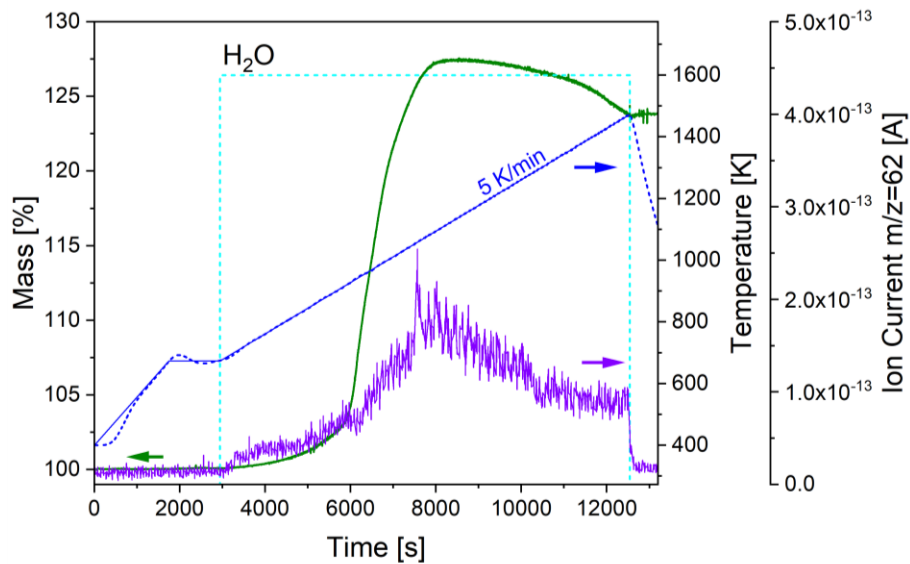
Figure 7.11: Ion current measured by mass spectrometry at m/z = 62 during heating of ZrB$_2$ with 5 K/min in H$_2$O/Ar-atmosphere (p$_{H2O}$=0.2 bar).

Isothermal tests

Isothermal oxidation tests of ZrB$_2$ in H$_2$O/Ar (p$_{H2O}$=0.2 bar) were conducted at 1073 K, 1273 K, 1473 K and 1673 K, respectively for 5 h. Experiments at 1073 K, 1273 K and 1473 K were conducted in the STA 409. Due to the higher temperature capability, the oxidation test at 1673 K was performed in the BOX furnace. For further experimental details see Section 3.2 and 3.3, respectively.

Figure 7.12 shows photographs of the compacted powder samples after the oxidation experiments. Oxidation at 1073 K resulted in a completely disintegration sample. However, the samples oxidized at 1273 K, 1473 K and 1673 K retained their structural integrity and formed a white oxide surface layer. The sample, which was oxidized at 1273 K showed crack formation at the edges. SEM investigations of the intact sample's surfaces (Figure 7.13) reveal a cauliflower-like morphology. The grain size is thereby increasing with the applied oxidation temperature. Small amounts of residual B$_2$O$_3$ on the surface are only observed after oxidation at 1273 K. Oxidation at 1473 K and 1673 K left only ZrO$_2$ at the samples surfaces.
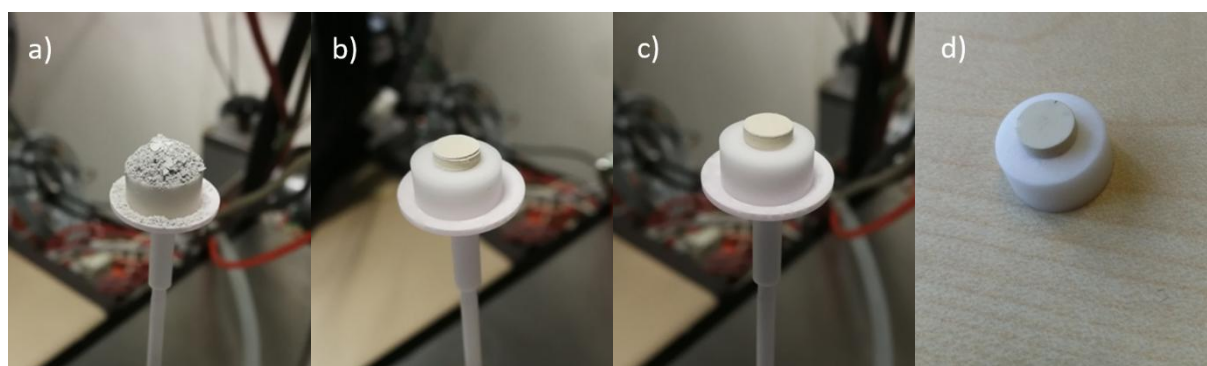
Figure 7.12: ZrB$_2$ samples after isothermal oxidation at a) 1073 K, b) 1273 K, c) 1473 K, and d) 1673 K in H$_2$O/Ar-atmosphere (p$_{H2O}$=0.2 bar) for 5 h. The sample diameter corresponds to 5 mm.

Figure 7.13: SEM micrographs of the ZrB$_2$ surface after isothermal oxidation at a) 1273 K, b) 1473 K and c) 1673 K in H$_2$O/Ar-atmosphere (p$_{H2O}$=0.2 bar) for 5 h. The scale bars correspond to 5 µm.

XRD investigation of the ZrB$_2$ samples after oxidation are shown in Figure 7.14. Oxidation at all investigated temperatures resulted in the formation of monoclinic ZrO$_2$ (PDF: 00-037-1484). No B$_2$O$_3$ or condensed H$_3$BO$_3$ was detected contrary to observations on B$_4$C oxidation in steam by Steinbrück et al. [72]. However, detection of B$_2$O$_3$ is difficult since the main XRD reflections are overlapping with reflections of m-ZrO$_2$. Furthermore, evaporation and volatilization of B$_2$O$_3$ and the remaining ZrO$_2$ crust on the surface might prevent a detection by XRD. The sample, which disintegrated during oxidation at 1073 K, does not show residual ZrB$_2$. This is clearly indicating that ZrB$_2$ was consumed completely by the oxidation reaction.

Figure 7.14: XRD pattern of ZrB$_2$ samples after isothermal oxidation in H$_2$O/Ar (p$_{H2O}$=0.2 bar) for 5 h.

Thermogravimetric results of the ZrB$_2$ oxidation in H$_2$O/Ar at 1073 K, 1273 K and 1473 K are shown in Figure 7.15. Oxidation at 1673 K was carried out in the BOX furnace. Therefore, no in-situ mass change was measured during this experiment. In first approximation, the mass change shows a parabolic behavior. The ZrB$_2$ sample, which was oxidized at 1073 K, shows the highest mass gain in accordance with the observed disintegration of the sample instead of formation of an intact outer oxide layer. In addition, the mass change exhibits a kink after about 1250 s at 1073 K. Below the kink, a lower slope compared to the samples oxidized at 1273 K and 1473 K indicates a lower mass change rate at 1073 K. However, after the kink the mass change rate is significantly accelerated. This is in accordance with a maximum in the H$_2$ release rate measured by mass spectrometry (see Figure 7.16). Therefore it is suggested, that at this time, the ZrB$_2$ sample is disintegrating and exposing new, unoxidized surface area and the real surface is bigger than the geometric surface. After about 5000 s, the mass increases nearly constant with time , indicating that a steady-state is achieved.

Figure 7.15: Measured mass change during isothermal oxidation of ZrB$_2$ in H$_2$O/Ar (p$_{H2O}$=0.2 bar) for 5 h at 1073K, 1273 K and 1473 K.

Figure 7.16 shows that the H$_2$ release rate during oxidation of ZrB$_2$ in H$_2$O/Ar (p$_{H2O}$=0.2 bar) is generally increasing with temperature. The time axis was moved to synchronize the beginning of steam injection. "Negative values" are referring to the heating and preconditioning phase in Ar. Oxidation at all temperatures resulted in a strong initial maximum of the H$_2$ release and hence of the oxidation rate. This effect is caused by the porosity of the compressed powder samples, resulting initially in a large surface area. However, after the initial maximum the H$_2$ release rate is decaying to an almost constant value of $1.5 \cdot 10^{-7}$ mol/s after 15000 s for all temperatures. Oxidation at 1073 K results in a second maximum after about 2000 s, which corresponds to the increase in mass gain after the observed kink (see Figure 7.15).
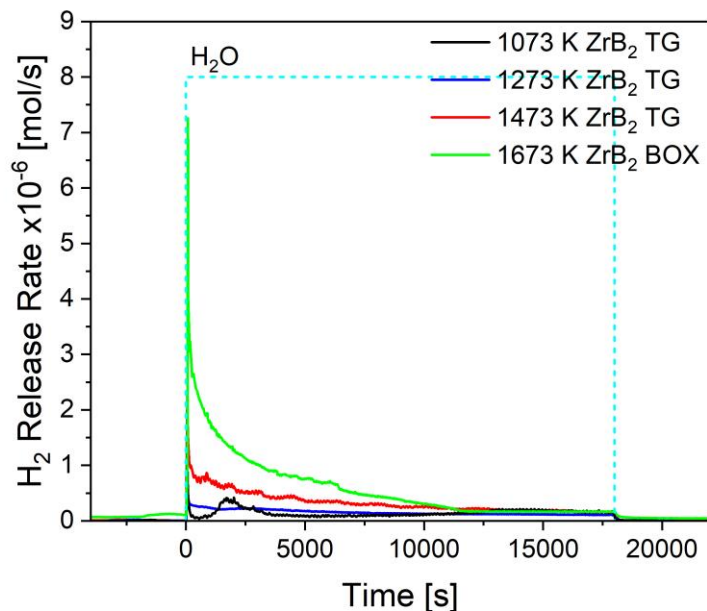
Figure 7.16: Measured H$_2$ release rate during isothermal oxidation of ZrB$_2$ in H$_2$O/Ar (p$_{H2O}$=0.2 bar) for 5 h at 1073K, 1273 K, 1473 K and 1673 K.

According to the oxidation reaction (7.5), a theoretical mass gain was derived from the measured H$_2$ release by integration. In contrast to the thermogravimetric measured mass change, the H$_2$-derived value does not include volatilization effects by formation of gaseous B-containing gas species. Therefore, the calculated H$_2$-derived mass change (Figure 7.17) is generally significantly higher compared to the thermogravimetric-derived value. For the oxidation at 1073 K, the mass change derived by thermogravimetry and mass spectroscopy is very similar, even including the kink after around 1250 s of oxidation. This shows that at the lowest investigated temperature of 1073 K, the influence of evaporation and volatilization of the B$_2$O$_3$ scale is only minor. With increasing temperature, the difference between the TG-derived and the H$_2$-derived value is increasing due to the increasing impact of evaporation and volatilization effects.

The H$_2$-derived mass change provides information on the oxidation reaction itself. The H$_2$-release provides information of the actual oxidation reaction. Note that no H$_2$ is released in the evaporation volatilization reactions (7.6)-(7.8).

The time dependence of the ion current at a mass to charge ratio (m/z) of 62, indicative for the orthorhombic acid H$_3$BO$_3$, is shown in Figure 7.18. With the onset of steam injection, the ion current at m/z = 62 is increasing. For the oxidation at 1073 K, the initial increase is steeper compared to experiments at 1273 K, 1473 K and 1673 K. However, the maximum ion current is similar for all oxidation temperatures. After stop of the steam injection, the ion current at m/z = 62 is going back to the pre-test value.
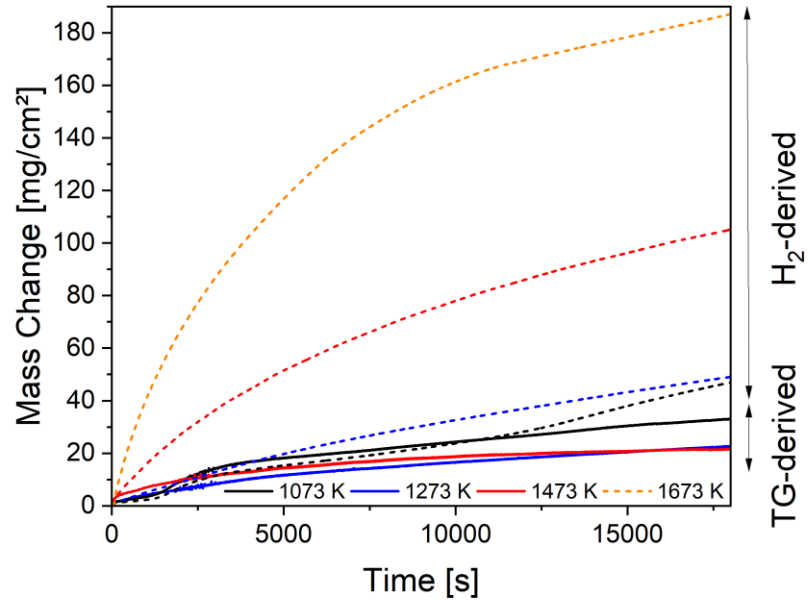
Figure 7.17: Comparison of the mass change of ZrB$_2$ derived from thermogravimetry (TG) and from the H$_2$-release measured by mass spectrometry.
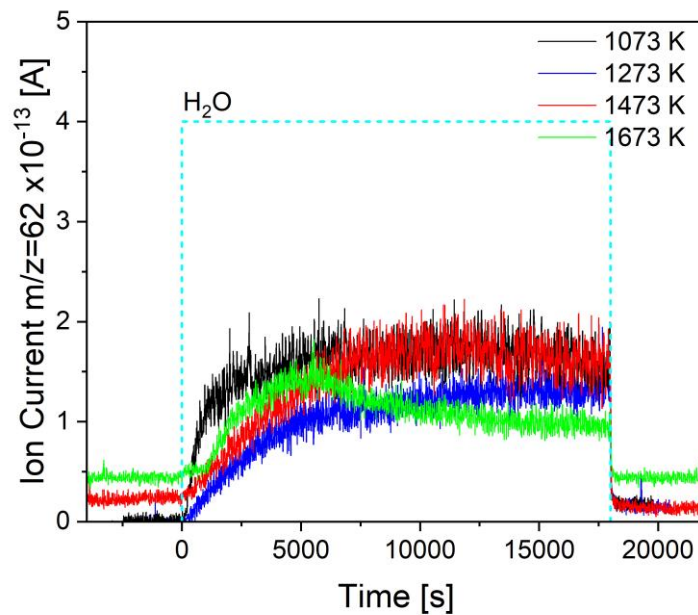
Figure 7.18: Measured ion current at m/z=62 during isothermal oxidation of ZrB$_2$ in H$_2$O/Ar-atmosphere (p$_{H2O}$=0.2 bar).

Figure 7.19 shows an Arrhenius plot of the total mass change during isothermal oxidation tests of ZrB$_2$ in H$_2$O/Ar (p$_{H2O}$=0.2 bar). Open and filled symbols represent the total weight change determined by a laboratory balance and by mass spectroscopic determination of the H$_2$-release, respectively.

The oxidation rate, determined with a laboratory balance (mass-derived, open symbols), is slightly decreasing with temperature. However, with an oxidation rate in the range of 3-6 mg/cm²h the temperature-dependence is very low.

Additionally, oxidation rates were determined from the associated H$_2$-release (equation (7.5)), measured by mass spectrometry. The oxidation rate shows an Arrhenius-type temperature dependence in the temperature range between 1273 K and 1673 K (solid line). The oxidation rate determined at 1073 K deviates from this trend with an oxidation rate similar to the 1273 K test. Differences between mass-derived and H$_2$-derived oxidation rates are based on the evaporation of B$_2$O$_3$ volatilization of boron-containing gas species (equation (7.6)-(7.8)) resulting generally in a lower mass gain. With increasing temperature (see also Figure 7.3), the partial pressures of the boron-containing gas species are increasing and therefore also the deviation between mass-derived and H$_2$-derived oxidation rates. This is also in accordance with micrographs and mass spectrometric investigation of H$_3$BO$_3$-release at m/z=62. However, differences between tests at different p$_{H2O}$ are negligibly small.
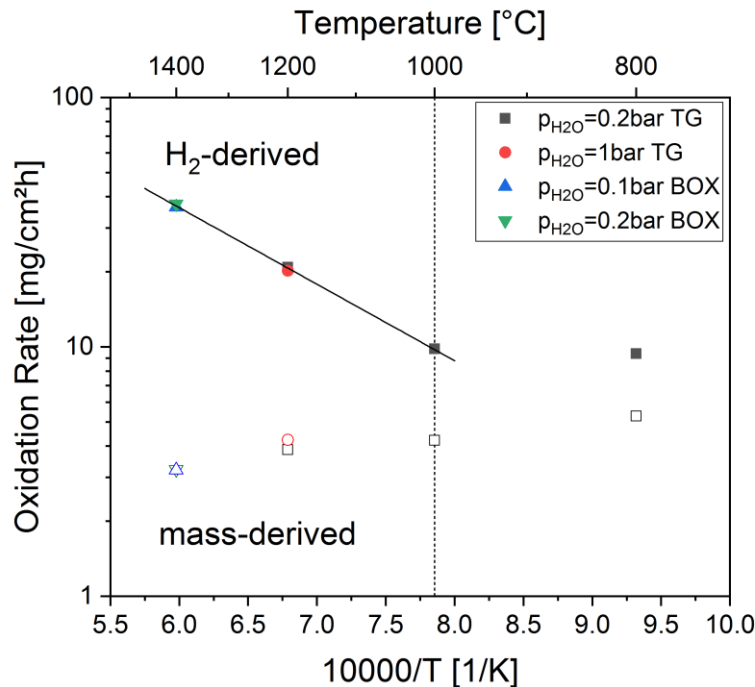
Figure 7.19: Arrhenius plot of the total mass change during isothermal oxidation of ZrB$_2$ in H$_2$O/Ar-atmosphere for 5 h. Open symbols: laboratory balance, filled symbols: calculated from H$_2$-release. The solid line is indicating the Arrhenius-type temperature dependence of the H$_2$-derived oxidation data in the range between 1273 K and 1673 K.

The time dependent mass change during isothermal oxidation of ZrB$_2$ in H$_2$O/Ar (p$_{H2O}$=0.2 bar) was fitted according to $\Delta w/A = k \cdot t^n$. The resulting rate constant k and exponent n are depicted in Figure 7.20a and Figure 7.20b, respectively. Additionally, k and n values are tabulated in the Appendix.

The rate constant is increasing with increasing temperature (Figure 7.20a). Considering the H$_2$-derived values, k shows a linear dependence on 1/T in the Arrhenius plot. The mass-derived k value shows a deviation from the H$_2$-derived value, which is increasing with decreasing temperature. At 1073 K, the mass-derived k value is two orders of magnitude higher than the H$_2$-derived value.

The exponent n, derived from the measurement of the H$_2$-release, shows a linear temperature dependence (Figure 7.20b). At the lowest investigated temperature of 1073 K, n shows almost linear oxidation kinetics. With increasing temperature, n is decreasing to sub-parabolic oxidation kinetics at the highest investigated temperature of 1673 K. The mass-derived n values show a large deviation from this behavior, indicating almost parabolic reaction order at 1073 K and 1273 K and almost cubic reaction kinetics at 1473 K, respectively. No temperature trend is recognizable.

Oxidation tests were conducted at p$_{H2O}$ = 0.1, 0.2 and 1 bar, respectively. However, the obtained k and n values are barely sensitive for the steam partial pressure, as long as enough steam is provided to avoid steam-starvation conditions.
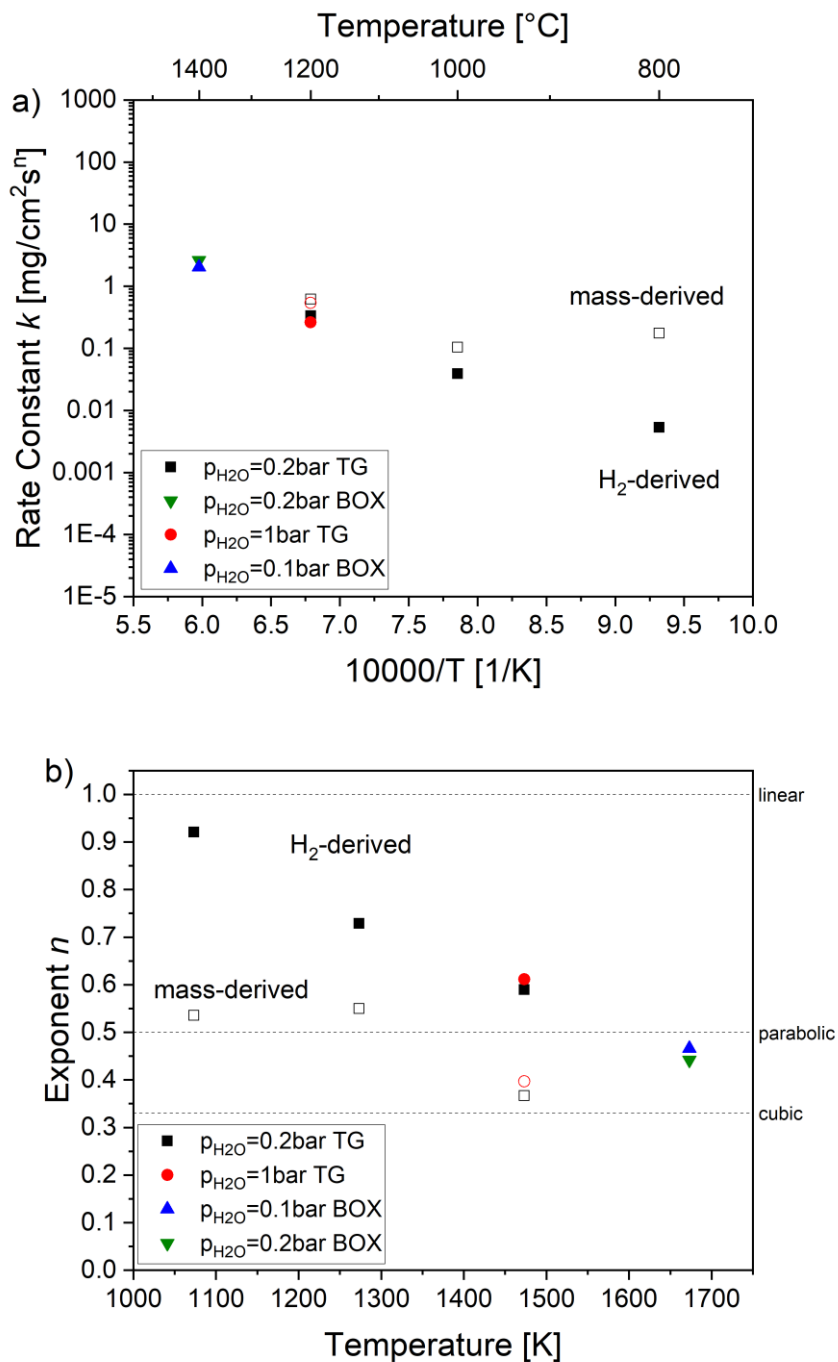
Figure 7.20: Derived a) rate constant k and b) exponent n for the oxidation of ZrB$_2$ in steam. Open symbols: derived by laboratory balance, filled symbols: calculated from H$_2$-release. Dotted lines indicate n values for linear, parabolic and cubic oxidation kinetics.

7.4. Discussion

Onset of oxidation

The conducted transient tests give insight into the onset of the oxidation reaction. In H_2O/Ar (p_{H2O}=0.2 bar), oxidation of ZrB_2 starts at about 700 K with the highest oxidation rate at about 950 K. The obtained results are very comparable to oxidation in O_2/Ar (p_{O2}=0.2 bar). Krauss et al. [163] found the onset of B_4C oxidation in oxygen and steam-containing atmosphere at the same temperature of 893 K. Figure 7.9b shows that oxidation in both atmospheres resulted in a nearly identical mass increase up to about 950 K. With further increasing temperature, oxidation in steam-containing atmosphere yields a higher mass gain to maximum 128 % at 1150 K compared to 115 % in oxygen-containing atmosphere at the same temperature.

Mass spectrometric measurements of the H_2-release upon oxidation of ZrB_2 in steam coincide with the thermogravimetric data (Figure 7.9a). From about 900 K to 1100 K both, the H_2-release and the mass change rate exhibit a maximum indicating the maximum oxidation rate. Temperature ranges below and above correspond to endothermic formation and evaporation of boron acid species, respectively. At temperatures between 1100 K and 1300 K, the H_2-release rate is at a constant low level, indicating that a steady-state is reached. Above 1300 K, the increasing H_2-release rate is indicating the acceleration of the oxidation reaction due to the evaporation and volatilization of the protective boria scale by formation of boron-containing gas species. However, the overall mass loss shows that the evaporation and volatilization of the boria scale is predominating over the mass gain by oxidation.

SEM investigations, depicted in Figure 7.13, revealed an open ZrO_2 network with a cauliflower-like microstructure. Therefore, the diffusion of oxidizing gas species (e.g. H_2O, O_2,...) through the condensed B_2O_3 (solid or liquid) is determining the oxidation of the underlying ZrB_2. After oxidation at the highest temperatures, the passivating B_2O_3 scale was consumed at the surface. As a result, the total mass even decreases during oxidation of ZrB_2 in steam-containing atmosphere at temperatures >1150 K, while the mass in oxygen-containing atmosphere further increases.

Volatilization of B_2O_3

Thermodynamic calculations performed in the present work, reveal the oxidation and volatilization characteristics of ZrB_2 in oxygen and steam. The partial pressures of the boron-containing gas species, which establish in equilibrium with condensed B_2O_3 in oxygen- and steam-containing atmosphere, are depicted in Figure 7.3. Due to the formation of gaseous boron hydroxide species, especially orthoboric acid H_3BO_3(g) and metaboric acid HBO_2(g), the partial pressures of volatile gas species are higher in steam- compared to oxygen-containing atmosphere. Because of the higher partial pressures in steam, the evaporation and volatilization of the B_2O_3 scale is much higher in steam compared to O_2-containing atmosphere (see Figure

7.3). This is consistent with thermodynamic calculations on the gas evolution in equilibrium with condensed B$_2$O$_3$ by Jacobson et al. [164]. In O$_2$-atmosphere of one bar pressure, BO$_2$(g) and B$_2$O$_3$(g) were formed. However, above 1300 K, addition of just 20 ppm H$_2$O resulted in the formation of HBO$_2$(g) with 1-3 orders of magnitude higher partial pressure compared to dry oxygen atmosphere. Jacobson et al. noted, that other H$_x$B$_y$O$_z$(g) species namely H$_3$BO$_3$(g) and H$_3$B$_3$O$_6$(g) became important at higher H$_2$O contents. According to Miyahara et al. [160] H$_3$B$_3$O$_6$(g) formation by polymerization of metaboric acid HBO$_2$(g) is very slow and H$_3$B$_3$O$_6$(g) is considered to be stable only at low temperatures. Previous studies on B-O-H-(C-F) gas chemistry [165][166][167] also concluded, that H$_3$B$_3$O$_6$(g) is not formed in significant amounts. Meschi et al. [168] found the H$_3$B$_3$O$_6$(g) amount to be less than 1% of the HBO$_2$(g) amount in equilibrium with B$_2$O$_3$(l) and water vapor at 1060-1450 K. In simulations of B$_4$C oxidation in steam, Steinbrück et al. [169] determined release rates of H$_3$B$_3$O$_6$(g) smaller than HBO$_2$(g) and H$_3$BO$_3$(g). However, SGTE data (see Section 4) resulted in unrealistic high partial pressure for H$_3$B$_3$O$_6$(g) in equilibrium with boria in steam. Therefore, H$_3$B$_3$O$_6$(g) was not considered in thermodynamic calculations (see Figure 7.3b) in this work.

Mass spectroscopic investigations (Figure 7.10) reveal the formation of HBO$_2$(g) and H$_3$BO$_3$(g) and their fragmentation products during oxidation of ZrB$_2$ in H$_2$O/Ar (p$_{H2O}$=0.2 bar). This is consistent with mass spectroscopic investigation of BN-oxidation in 2% H$_2$O/oxygen by Jacobson et al. [164] who observed H$_3$BO$_3$(g), HBO$_2$(g) and possibly BO$_2$(g). The evolution of the H$_3$BO$_3$$^+$-signal at m/z=62 during heat-up in H$_2$O/Ar (Figure 7.11) shows onset of volatilization from the very beginning of mass gain with steam injection at 673 K. With increasing temperature and mass gain, the H$_3$BO$_3$$^+$-signal reaches a maximum at 1100 K and is then slightly decreasing but remains at a high level. This is consistent with the calculated equilibrium partial pressure of H$_3$BO$_3$(g) above B$_2$O$_3$ (Figure 7.3b), which is high at low temperatures (2.4·10^{-3} bar at 673 K) and shows a relatively low decay with temperature. Therefore, the formation-rate of B$_2$O$_3$ must be rate determining for the H$_3$BO$_3$(g)-formation. At low temperatures, B$_2$O$_3$ formation is slow and at high temperatures, B$_2$O$_3$ is consumed as soon as it is formed by volatilization and direct evaporation. According to Steinbrück et al. [169], the release of gaseous boron-containing species switches from orthoboric acid H$_3$BO$_3$(g) at low temperatures to metaboric acid (HBO$_2$(g)) and B$_2$O$_3$(g) by direct evaporation of B$_2$O$_3$ at high temperatures.

In oxygen (p$_{O2}$=0.2 bar), evaporation of gaseous BO$_2$(g) and B$_2$O$_3$(g) is predominant at temperatures below and above 1766 K, respectively. The gas species B(g), BO(g) and B$_2$O$_2$(g) are only formed with very low partial pressures (Figure 7.3) or at extremely low oxygen partial pressures (Figure 7.2). Generally, partial pressures of gaseous species in equilibrium with condensed B$_2$O$_3$ are higher compared to equilibria with ZrO$_2$ or SiO$_2$. Formation of Zr-containing gas species and volatilization of ZrO$_2$ is negligible compared to B$_2$O$_3$. Therefore, oxidation of ZrB$_2$ is resulting in the observed remaining cauliflower-like open ZrO$_2$ network.

Oxidation kinetics

In oxygen, ZrB_2-oxidation proceeds according to reaction (7.1) under formation of zirconia and boria. Voitovich et al. [153] found oxidation of ZrB_2 in air beginning at 773-823 K. At higher temperatures (923-1053 K) oxidation proceeds with parabolic kinetics. Kuriakose et al. [170] found parabolic oxidation behavior even to higher temperatures of 1218-1529 K. In this stage, liquid boria fills the pores and prevents gas-phase diffusion of oxygen to the bare ZrB_2.

Evaporation and volatilization of boria was observed at temperatures above 1373 K (Opeka et al. [47]) up to 1473 K (Berkowitz-Mattuck [171]). Hence, oxidation kinetics change from parabolic to cubic (1053-1273 K) and above 1473 K to linear [153] behavior. However, Opeka et al. [47] found 10 wt% of B_2O_3 were retained even after 5h at 1673 K. Due to the much lower surface energy of boria (0.08 J/m²) compared to zirconia (1 J/m²) there is still a high driving force to cover ZrO_2 by B_2O_3 [47]. Tripp and Graham [172] separated oxidation and volatilization rates by isolated thermogravimetric determination of the samples and the condensed gas species mass, respectively. They conclude that below 1373 K vaporization is negligible. In this temperature range, oxidation is determined by diffusion of oxygen through the liquid B_2O_3 scale. At higher temperatures, vaporization became important resulting in overall paralinear oxidation kinetics. Parthasarathy et al. [173][174] developed a mechanistic model constructed from thermodynamic analysis. According to this, below 1673 K diffusion of dissolved oxygen through the liquid boria scale is rate limiting. Above 1673 K boria is lost by evaporation and Knudsen diffusion of molecular oxygen through the capillaries of the columnar oxide structure.

The preparation method of ZrB_2 samples significantly influences the resulting relative density [175]. Kuzenkova and Kislyi [156] showed that oxidation of ZrB_2 at 1273 K with a porosity of 8% and 12% resulted in a mass gain of 5 mg/cm² and 12 mg/cm², respectively, after 10 h. However, for oxidation of B_4C in steam, Steinbrück et al. [169] observed higher oxidation rates for porous samples only at the very beginning of the test. Once an oxide scale was formed, a constant reaction rate is established and obtained results are comparable with dense samples.

Besides evaporation and volatilization, active/passive-transition plays an important role in ZrB_2-oxidation. At low oxygen (or steam) partial pressures (see Figure 7.2), only gaseous oxidation products are formed, which is designated as active oxidation. At high oxygen partial pressures, condensed oxides ZrO_2 and B_2O_3 are formed. For ZrB_2, the active/passive-transition is at $\log(p_{O_2})$ = -20.53 bar at 1473 K according to Figure 7.2.

Isothermal tests were used to evaluate the oxidation kinetics of ZrB_2 in steam. Due to the high vapor pressure of B_2O_3, which is among the highest for oxides [158], thermogravimetric results represent a combination of the mass gain by oxidation (reaction (7.5)) and the mass loss by evaporation (reaction (7.6)) and volatilization ((7.7) and (7.8)) of the B_2O_3 scale. Therefore, additionally the H_2-release according to the oxidation reaction (7.5) was evaluated.

119

Figure 7.20 shows that oxidation kinetics of ZrB$_2$ in H$_2$O/Ar are complex. Generally, neither oxidation rate, nor k or n show a significant p_{H2O}-dependence. The rate constant k shows an Arrhenius-type temperature dependence (Figure 7.20a). However, n is decreasing with temperature from almost linear kinetics at 1073 K to sub-parabolic kinetics at 1673 K (Figure 7.20b). While other studies reported parabolic oxidation kinetics for ZrB$_2$ in oxygen-containing atmosphere, this was not reasonable in this work especially at and below 1273 K. Due to the temperature-dependent oxidation kinetics, a determination of the activation energy was omitted. No activation energies for ZrB$_2$ in steam-containing atmosphere are available in literature. However, data for the oxidation of ZrB$_2$ in oxygen-containing atmosphere are determined by Kuriakose and Margrave [170] and Berkowitz-Mattuck [171]. Kuriakose and Margrave [170] found an activation energy for the oxidation of ZrB$_2$ in oxygen of 82.8 ± 4 kJ/mol in the temperature range 1219-1529 K. Additionally, the parabolic rate constant was found to be direct proportional to the oxygen partial pressure. Berkowitz-Mattuck [171] confirmed the activation energy and p_{O2}-dependence as found by Kuriakose and Margrave at low temperatures. Additionally, Berkowitz-Mattuck [171] determined an activation energy of 322 ± 21 kJ/mol and a low p_{O2}-dependence above 1400 K, indicating a change in the oxidation mechanism around 1330 K. The activation energy at high temperatures is similar to the value for direct evaporation of B$_2$O$_3$ of 383 kJ/mol determined by Krauss et al. [163] for T > 1473 K. Therefore, at high temperatures the direct evaporation of B$_2$O$_3$ is rate determining for both, the oxidation of ZrB$_2$ in steam and in oxygen. However, gaseous B$_2$O$_3$(g) was not found in mass spectroscopic investigations because it probably reacts in the gas phase with steam to form H$_3$BO$_3$(g) and HBO$_2$(g) and probably also condenses to a certain amount in colder parts of the off-gas system. At low temperatures, the rate determining process is the formation and evaporation of gaseous boric acids [169] and their diffusion through the gaseous boundary layer [164], respectively. Steinbrück et al. [169] determined an activation energy of 21.6 kJ/mol at T < 1373 K for the formation and evaporation of gaseous boric acids during oxidation of B$_4$C in steam. Therefore, ZrB$_2$ in steam at T ≥ 1273 K probably already shows a superimposition of both, the evaporation and transport of gaseous boric acids and the direct evaporation of boria.

The oxidation rates obtained from the H$_2$-release (9.4-37.4 mg/cm²h) are therefore higher than by thermogravimetry (3-6 mg/cm²h). Oxidation rates are generally higher in steam-containing atmosphere. Brown [176] noted that the presence of moisture in the air resulted in a 44-59% higher mass gain compared to dry air at 922 K. Kaufman and Clougherty [177] observed similar oxidation rates for the oxidation of HfB$_2$ with and without H$_2$O in He-O$_2$ at 1760 K while a fivefold increase of the oxidation rate was found at 1206 K. This is consistent with the direct evaporation and volatilization of boria above 1770 K (see discussion above). Therefore, not the formation but the degradation of the boria scale is defining the oxidation characteristics in oxygen- and steam-containing atmosphere.

Although oxidation and volatilization rates are increasing with temperature, the H$_3$BO$_3$(g)-release at 1673 K was the smallest for all investigated temperatures. This is consistent with the calculated partial pressures of boron-containing gas species in steam (Figure 7.3b). With increasing temperature, the partial pressure of H$_3$BO$_3$(g) is decreasing, while HBO$_2$(g) is increasing. Above 1179 K, HBO$_2$(g) is the major volatilization product.

According to Nguyen et al. [178] the rate determining step for the oxidation of ZrB$_2$-containing ceramics is the diffusion of HBO$_2$(g) through the boundary layer. The authors furthermore note, that no significant difference in the oxidation rate was observed in low velocity water vapor compared to stagnant air [178].

Steinbrück et al. did thorough investigations on the oxidation of B$_4$C at high temperatures in steam [72][169][179]. Similar to oxidation of ZrB$_2$, a liquid B$_2$O$_3$ scale is formed, but other oxidation products are all gaseous CO(g) CO$_2$(g) and CH$_4$(g). Nevertheless, oxidation of B$_4$C is dominated by the formation, evaporation and volatilization of B$_2$O$_3$(l). Oxidation of B$_4$C follows paralinear reaction kinetics. The oxidation rate is determined by mass transport in the gas phase. As a result, the steam partial pressure near the reaction surface might be different from the bulk of the gas [169]. At low temperatures orthoboric acid is formed while at high temperatures metaboric acid forms accompanied by direct evaporation of B$_2$O$_3$ above 1770 K. In contrast to the oxidation of B$_4$C, additionally condensed ZrO$_2$ is formed during oxidation of ZrB$_2$. Therefore, not the whole surface is available for gas phase transport of oxidizing gas species and products. Diffusion paths through the porous ZrO$_2$ networks are comparatively longer and impede the exchange of gas species.

The oxidation of ZrN is exemplary for the oxidation without the formation of a passivating B$_2$O$_3$ layer. The equilibrium oxygen partial pressure for the oxidation of ZrN is thereby higher compared to pure Zr (see Figure 7.1a). Upon oxidation of ZrN, ZrO$_2$ is formed under release of N$_2$ resulting in complete oxidation and disintegration of the sample (see Figure 7.5). Harrison and Lee [180] reported stabilization of ZrO$_2$ by nitrogen at 1173-1273 K, resulting in lower oxidation rates than at 973-1073 K. At 1373 K, the ZrO$_2$ scale was no longer protective due to the increasing diffusivity of oxygen. Activation energies for oxidation of 241 ± 10 kJ/mol (748-923 K, Krusin-Elbaum and Wittmer [181]) and 229 kJ/mol (773-1123 K, Panjan et al. [182]), were determined for bulk and a 300 µm thin film ZrN, respectively. Oxinitrides (ZrN$_x$O$_y$), produced and reported in literature by mixing of ZrN and ZrO$_2$ powders, were not considered in the thermodynamic calculation due to the lack of thermodynamic data. However, the maximum mass of 119.5%, which is higher than 117% expected from reaction (7.4) alone, indicates the uptake of nitrogen into the oxidation product ZrO$_2$. Furthermore, with further increasing temperature the sample mass is decreasing under release of N$_2$. The observed disintegration of the sample is resulting from the increase in molar volume of 48% upon oxidation of ZrN. Steinbrück et al. have investigated the oxidation behavior of Zr-alloys in nitrogen-containing gas

mixtures [161][183]. The volume expansion upon oxidation of ZrN resulted in a spallation of the oxide scale and therefore in an escalation of the oxidation reaction. The observed onset of oxidation at 700 K is consistent with literature data for ZrN (748 K [181]) and ZrC (653-750 K [184]). Most authors observed parabolic oxidation kinetics for ZrN suggesting, that diffusion through the oxide scale is the rate controlling mechanism [180][181][182].

7.5.   Conclusion

Oxidation of compacted ZrB$_2$ powder samples was performed in flowing H$_2$O/Ar and O$_2$/Ar (p_{H2O}=p_{O2}=0.2 bar) up to maximum temperatures of 1673 K. The oxidation characteristics were determined by thermogravimetric and mass spectrometric analysis and post-test examinations.

The overall mass change during high-temperature oxidation of ZrB$_2$ is determined by superimposition of the mass gain by the actual oxidation reaction (7.3) and the evaporation and volatilization of the liquid boria scale by formation of boron-containing gas species. Quantitative mass spectrometric analysis of the H$_2$-release made it possible to separate oxidation effects from evaporation and volatilization effects and to reveal comprehensive insight into the high-temperature oxidation behavior of ZrB$_2$ in steam, which has been explored scarcely in literature. Oxidation in oxygen- and steam-containing atmosphere, respectively, yield about the same onset of oxidation. However, higher mass gain is observed upon oxidation in steam in accordance with literature data. Thermogravimetric investigation underestimated the actual oxidation rate considerably. An evaluation of the H$_2$-release revealed an Arrhenius-type temperature-dependence of the oxidation rates for T ≥ 1273 K. Oxidation kinetics of ZrB$_2$ in steam were complex and strongly temperature dependent. The exponent n was shifting from linear at 1073 K to sub-parabolic at 1673 K with a linear temperature-dependence. Passivation of the ZrB$_2$ sample, by formation of a dense oxide scale, occurred only for T≥1273 K in H$_2$O/Ar. At 1073 K, the ZrB$_2$ sample disintegrated and oxidized completely. The reason for this behavior is most likely found in the slow oxidation kinetics in conjunction with the high partial pressure of H$_3$BO$_3$(g) (4·10^{-4} bar) at 1073 K. Thermodynamic calculations provided insight into partial pressures of volatile boron-containing gas species formed in O$_2$- and H$_2$O-containing atmosphere in equilibrium with condensed B$_2$O$_3$. In dry O$_2$/Ar-atmosphere (p_{O2}=0.2 bar), BO$_2$(g) and B$_2$O$_3$(g) are the predominant gas species formed for temperatures below and above 1493 K, respectively. In contrast to that, partial pressures of boron-containing gas species are significantly higher in H$_2$O-containing atmosphere. For p_{H2O}=0.2 bar, orthoboric acid (H$_3$BO$_3$(g)) is formed with partial pressures higher than 3·10^{-4} bar. At temperatures higher than 1179 K, gaseous metaboric acid (HBO$_2$(g)) is the dominant gas species. The formation of gaseous B-O-H species, examined by mass spectroscopic analysis during oxidation of ZrB$_2$ in H$_2$O-containing atmosphere, was in very good agreement with thermodynamic calculations. Ionized species and their fragments (H$_3$BO$_3^+$, H$_2$BO$_3^+$, H$_2$BO$_2^+$, HBO$_2^+$ and BO$_2^+$ were identified. The release of H$_3$BO$_3$(g) (H$_3$BO$_3^+$ at m/z=62) was traced qualitatively during oxidation of ZrB$_2$ in H$_2$O/Ar in transient tests up to 1473 K and during isothermal oxidation at 1073 K, 1273 K, 1473 K and 1673 K, respectively. During heat-up of ZrB$_2$ in H$_2$O/Ar, release of H$_3$BO$_3$(g) starts already at 673 K and reaches a maximum at 1000 K corresponding to the maximum mass gain rate. With further increasing temperature, the H$_3$BO$_3^+$-signal is decreasing again. In isothermal tests, the H$_3$BO$_3^+$-signal reaches an approximately constant value after a rapid increase with the lowest value at the highest investigated temperature of 1673 K.

8. High-temperature oxidation of ZrB₂-containing SiC/Si-C-N CMC

In the present Section, the high-temperature oxidation behavior of ZrB_2-containing SiC/Si-C-N composites was investigated. To this end, a combination of CALPHAD-type equilibrium calculations and high-temperature oxidation tests were performed. Thermodynamic equilibrium calculations were performed to understand the fundamental interactions and reaction mechanisms of the ZrB_2-additive with the SiC-fibers and the precursor-derived Si-C-N matrix in oxidizing atmosphere. Phase stability diagrams, phase fractions and vapor pressure of gaseous oxidation and volatilization products were calculated.

In addition, oxidation tests were performed with ZrB_2-SiC/Si-C-N samples with a dimension of 3x10x10 mm^3. Samples were manufactured and provided by the German Aerospace Center (DLR e.V.) in the framework of the BMBF-project NewAccess [27]. The ZrB_2-additive was introduced into the CMC by using a mixture of Ceraset® PSZ 20 and ZrB_2-powder in a first laminating step of the SiC fiber-preform. All following PIP cycles were performed with pure Ceraset® PSZ 20. The neutron tomography image (see also Section 3.8) depicted in Figure 8.1 shows the ZrB_2-distribution in the obtained ZrB_2-SiC/Si-C-N CMC. Due to the significantly higher neutron cross section of B compared to Si, C and N, ZrB_2-rich regions in the CMC appear bright. The brighter the gray value the higher the boron content. The SiC-fiber bundles appears dark. Therefore, the ZrB_2-additve was distributed throughout the CMC in the precursor-derived Si-C-N ceramic matrix, even though locally the ZrB_2-content was not the same everywhere.

Oxidation tests were performed in transient tests and isothermally at temperatures between 1073 K and 1773 K in various flowing oxidizing O_2- and H_2O-containing atmospheres. The oxidation behavior was characterized with thermogravimetry, DTA, mass spectrometric analysis of gaseous oxidations and volatilization products and materialographic post-test examinations (see Section 3 for details).

A second batch of samples, consisting of ZrB_2-free SiC/Si-C-N CMC, was used to separate the influence of the ZrB_2-additive on the oxidation behavior of the ZrB_2-SiC/Si-C-N CMC. See also Section 3.1 for details. Figure 8.2 shows SEM micrographs of the ZrB_2-free CMC. SiC fibers are arranged in bundles in a 2D fabric with 0/90° orientation, embedded in a Si-C-N matrix.

Figure 8.1: Neutron tomography image of a ZrB_2-SiC/Si-C-N composite. The sample was prepared with an orientation of the SiC-fiber preform perpendicular (left) and parallel (right) to the image plane. The shorter dimension corresponds to an edge length of 1 mm. ZrB_2-rich Si-C-N matrix appears bright.
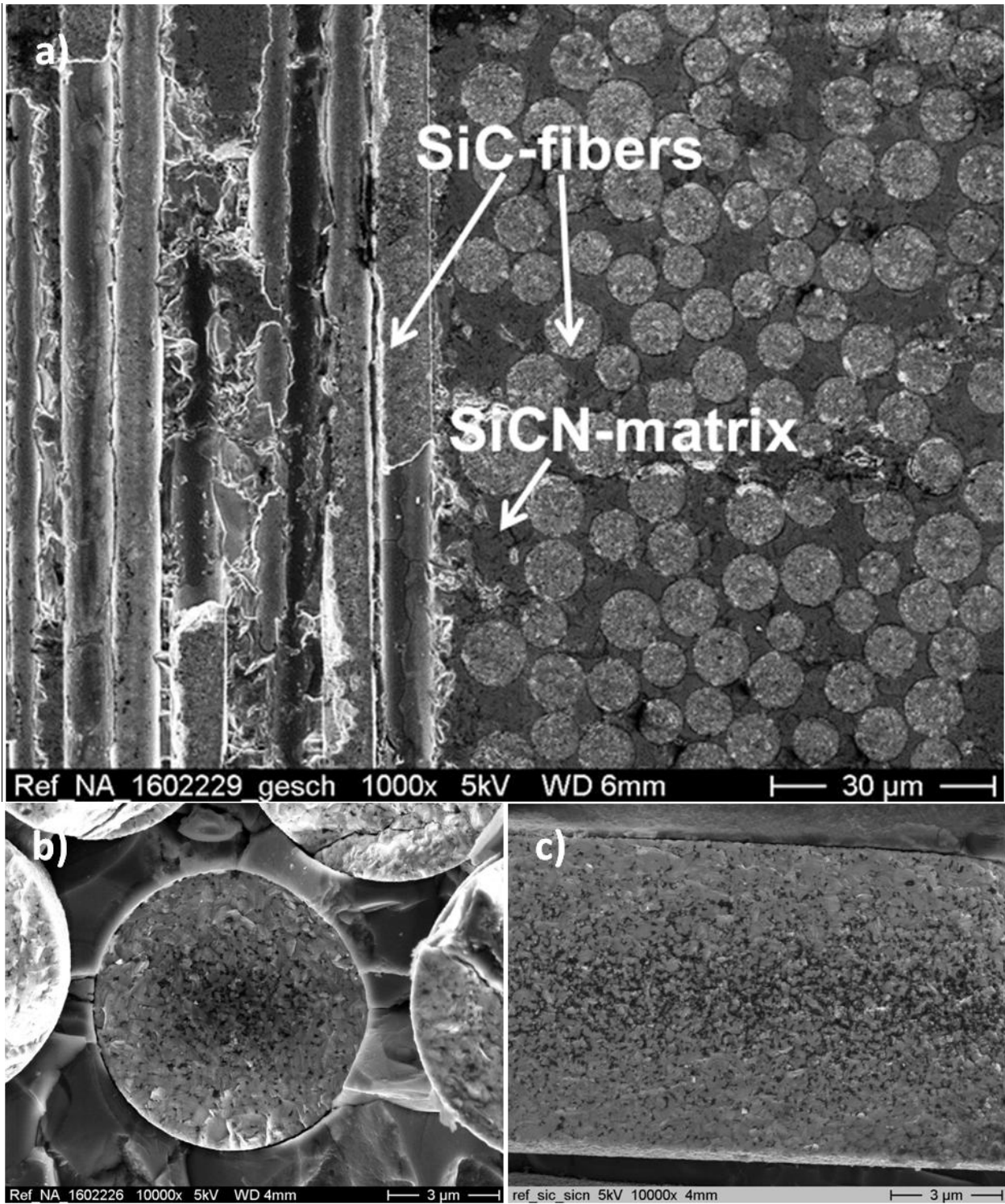
Figure 8.2: SEM micrographs of the cutting-edge of a SiC/Si-C-N composite in the status as-received; a) overview over the SiC-fibers in 2D fabric and the Si-C-N matrix, b) cross-section of the SiC-fiber and c) longitudinal section of a SiC-fiber.

8.1. Thermodynamic analysis of ZrB$_2$-SiC/Si-C-N oxidation

Thermodynamic calculations on the composition of ZrB$_2$-SiC/Si-C-N in oxidizing atmosphere were performed using the CALPHAD-method. The applied thermodynamic dataset in the system Zr-Si-B-C-N-O-H was compiled from literature data (see Section 4 for details). In addition, the liquid phase of the binary subsystems Zr-C and Zr-N was reoptimized to ensure compatibility in the multicomponent database.

The calculated phase stability diagrams in Figure 8.3 show, that silicon oxynitride (Si$_2$N$_2$O) is formed as intermediate oxidation product of Si-N-containing ceramics. Si$_2$N$_2$O has a limited stability range between the phases Si$_3$N$_4$ and SiO$_2$. The equilibrium partial pressures p_{O2} and p_{N2} for formation of Si$_2$N$_2$O are lower for the system Si-N-O compared to Si-C-N-O indicating a lower oxidation resistance.
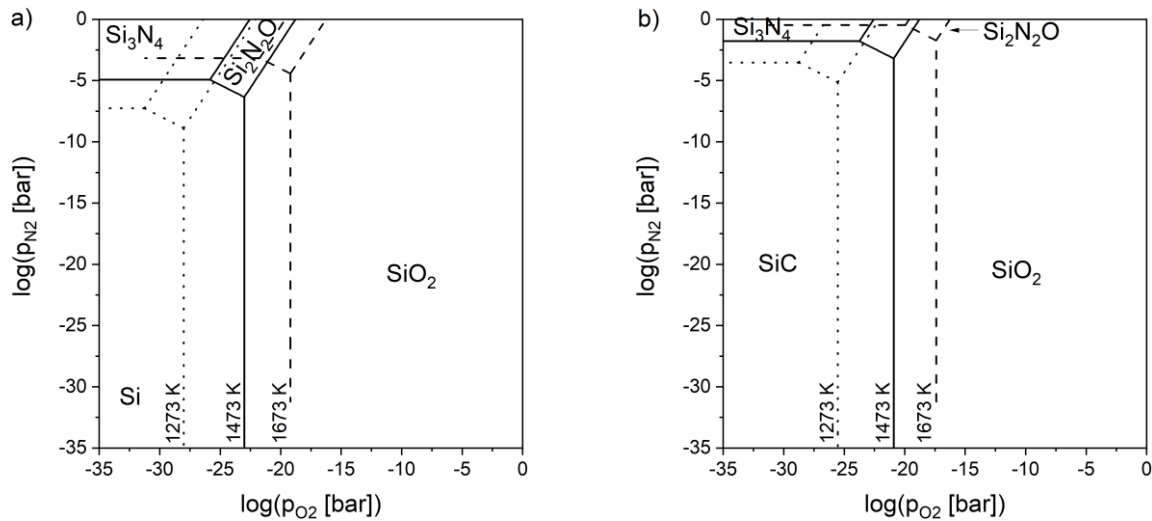
Figure 8.3: Calculated phase stability diagrams for the systems a) Si-N-O and b) Si-C-N-O at 1273 K, 1473 K and 1673 K.

Figure 8.4 shows the phase fraction diagram for the composition of the precursor-derived Si-C-N ceramic obtained from pyrolysis of Ceraset$^{®}$ PSZ 10 and PSZ 20 (see Section 5.1) as a function of the oxygen partial pressure p_{O2} calculated at 1473 K. Although the obtained Si-C-N ceramic is X-ray amorphous, the composition is located within the three-phase equilibrium SiC+Si$_3$N$_4$+C. Calculations were performed as a closed system consisting of a constant amount of substance (1 mol) at ambient pressure of $p = 1 \cdot 10^5$ Pa with a self-developing gas volume. Phase fraction diagrams were calculated with a small amount of Ar (x(Ar) = 0.01) to establish a stable gas phase under all conditions.

First, Si$_3$N$_4$ and SiC are oxydized under formation of Si$_2$N$_2$O and C:

$$SiC + Si_3N_4 + O_2 = 2Si_2N_2O + C \tag{8.1}$$

Second, the remaining carbon is oxidized to CO and CO$_2$ at higher p$_{O2}$.
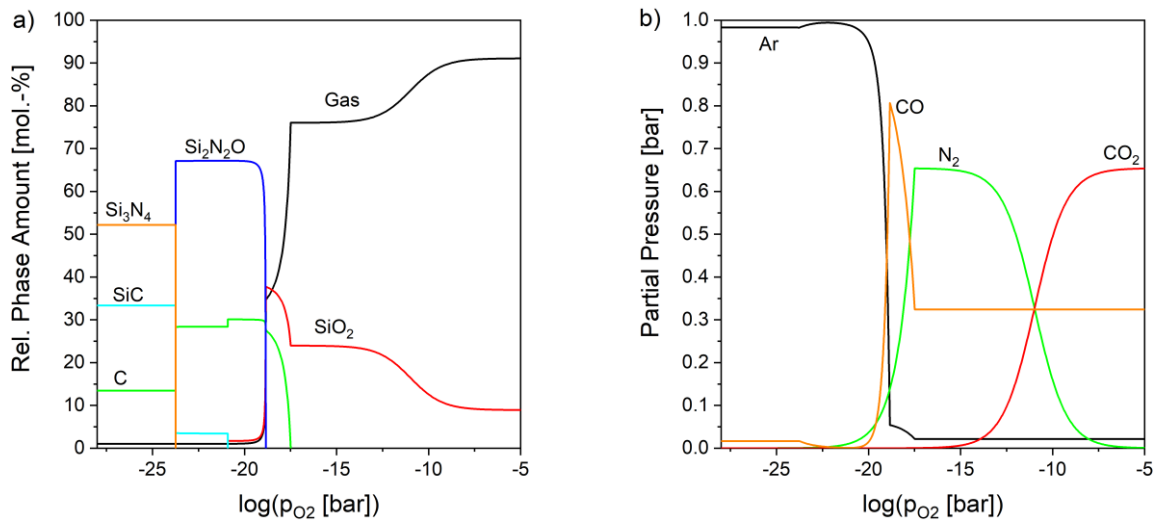
Figure 8.4: Calculated a) phase fraction diagram and b) composition of the gas phase for the precursor-derived Si-C-N ceramic obtained from Ceraset® PSZ 10 and PSZ 20 as a function of the oxygen partial pressures at 1473 K.

Figure 8.5 shows calculated partial pressures of the volatile SiO$_x$ species at 1473 K and the volatility diagrams calculated, after Lou and Heuer [159], at 1273 K, 1473 K and 1673 K as a function of p$_{O2}$. The equilibrium oxygen partial pressure for the oxidation reaction Si+O$_2$=SiO$_2$ at log p$_{O2}$ = -23.01 is marked with a dashed line. Below the dashed line, gaseous SiO$_x$ species are in equilibrium with solid Si, respectively. The majority gas species for log p$_{O2}$ < -23.01 are Si(g) and SiO(g), with increasing p$_{O2}$. For log p$_{O2}$ > -23.01, SiO(g) and SiO$_2$(g) are the majority gas species in equilibrium with the solid oxide SiO$_2$. Besides these majority gas species, which mainly contribute to the total partial pressure, also other minority gas species (Si$_2$(g), Si$_3$(g) and Si$_2$O$_2$(g)) are formed. With increasing temperature (see Figure 8.5b), the partial pressures of the individual gaseous SiO$_x$(g) species are increasing and the transition between the majority gas species is shifting to higher p$_{O2}$.

The formation of condensed oxide SiO$_2$ at p$_{O2}$ higher than indicated by the dashed line, has potentially a passivating effect on the oxidation behavior of the underlying material (See also active-passive transition in Section 1.1).
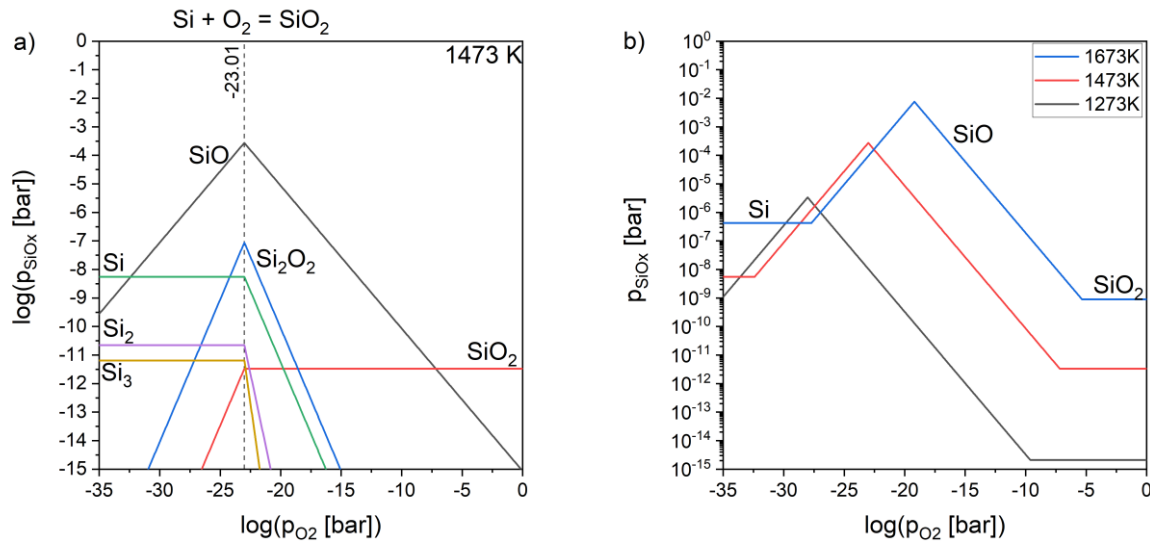
Figure 8.5: Calculated a) partial pressures of gas species in the Si-O system as a function of the oxygen partial pressure at 1473 K and b) associated volatility diagrams at 1273 K, 1473 K and 1673 K.

The composition of the self-developing gas phase for SiO_2 in a) oxygen and b) steam at p_{O2} = 0.2 bar and p_{H2O} = 0.2 bar, respectively, is depicted in Figure 8.6. The gas species O_2 and H_2O and their dissociation products are considered in the equilibrium calculations but not depicted. The same holds for the constant amount of Ar (x(Ar)=0.01) which was added as an inert gas to establish a stable gas phase at every temperature. In oxygen (Figure 8.6a), SiO_2(g) is formed with the highest partial pressure over the considered temperature range. Partial pressures of other gas species SiO(g), Si_2O_2(g) and Si(g) are at least one order of magnitude lower. In steam (Figure 8.6b), additionally the gaseous hydroxides are formed with partial pressures higher than those of gaseous oxides. $Si(OH)_4$(g) and $SiO(OH)_2$(g) are the main gas species formed below and above 1775 K, respectively. Due to the formation of gaseous hydroxides, partial pressures of gaseous Si-containing species are higher in steam compared to oxygen atmosphere.

In direct comparison, partial pressures of silicon-containing gas species formed in equilibrium with solid SiO_2 are several orders of magnitude lower than those of boron-containing gas species formed in equilibrium with condensed B_2O_3 under the same conditions (see Section 7.1, Figure 7.3).
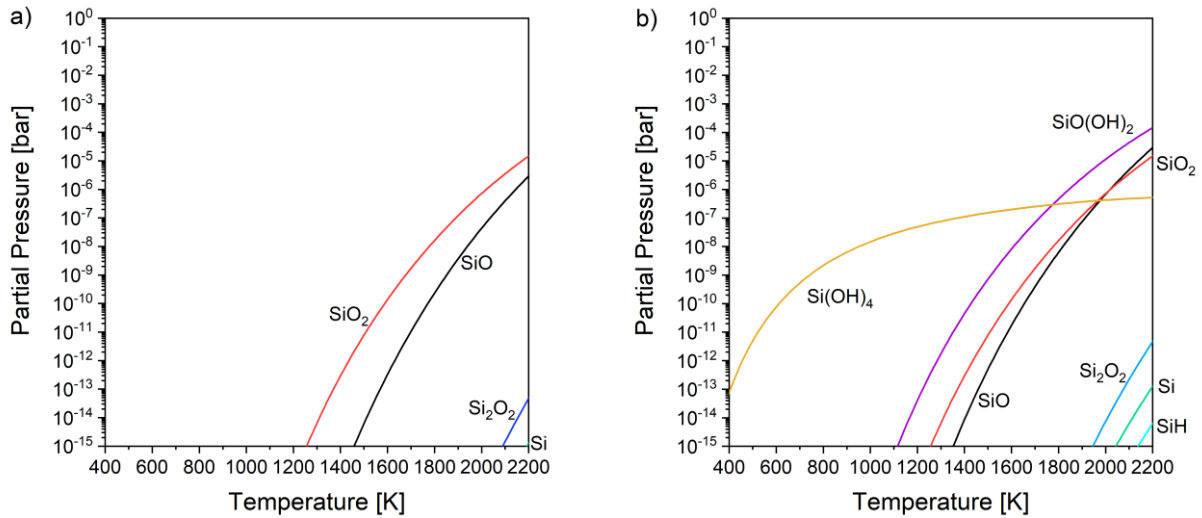
Figure 8.6: Calculated partial pressures of the silicon-containing gas species as a function of temperature for SiO$_2$ at a) p$_{O2}$ = 0.2 bar and b) p$_{H2O}$ = 0.2 bar.

Thermodynamic equilibrium calculations were performed to analyze the interaction of the ZrB$_2$-additive with the SiC-fiber and the Si-C-N matrix in oxidizing atmosphere. Reaction pairs of ZrB$_2$ with the thermodynamic equilibrium components of the ceramic fiber and matrix (C, SiC and Si$_3$N$_4$) were considered as mechanical powder mixtures. Figure 8.7 shows the corresponding calculated phase stability diagrams and the composition of the gas phase at 1473 K as a function of the oxygen partial pressure. Phase fractions of the reaction pair ZrB$_2$-C (see Figure 8.7a), are constant up to an oxygen partial pressure of 10$^{-20.5}$ bar, indicating that no reactions take place. At higher p$_{O2}$, ZrB$_2$ is oxidizing, forming ZrO$_2$ and B$_2$O$_3$, which is liquid at the considered temperature, according to reaction (7.1). At higher oxygen partial pressures, carbon is oxidizing under the formation of CO and CO$_2$ (see Figure 8.7b). Upon oxidation of ZrB$_2$ and SiC (see Figure 8.7c), ZrSiO$_4$ is formed at p$_{O2}$ = 10$^{-20.9}$ bar. With increasing p$_{O2}$, CO and CO$_2$ are formed from the oxidation of carbon. By the formation of CO and CO$_2$, the relative phase amounts of the gas phase is increasing. Due to the fixed constant amount of substance (1 mol), the relative phase amounts of ZrSiO$_4$ and B$_2$O$_3$(l) are decreasing. The overall oxidation reaction can be written as:

$$ZrB_2 + SiC + \frac{7+u}{2}O_2 = ZrSiO_4 + B_2O_3(l) + CO_u \; ; u = 0, 1, 2 \tag{8.2}$$
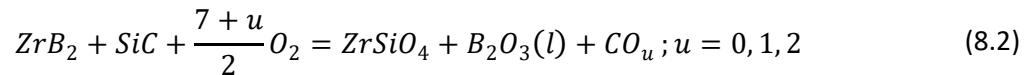
Phase equilibria of the reaction pair ZrB$_2$+Si$_3$N$_4$ in oxygen-containing atmosphere are more complex. At low p$_{O2}$ the siliconoxynitride Si$_2$N$_2$O is formed as intermediate oxidation product of Si$_3$N$_4$. Nitrogen released from the oxidation of Si$_3$N$_4$ leads to the formation of ZrN and BN from ZrB$_2$ (see also Section 6.2). With increasing p$_{O2}$, all nitrides (Si$_2$N$_2$O, ZrN and BN) are oxidized. ZrSiO$_4$ is formed and N$_2$ is released into the gas phase (see Figure 8.7f).
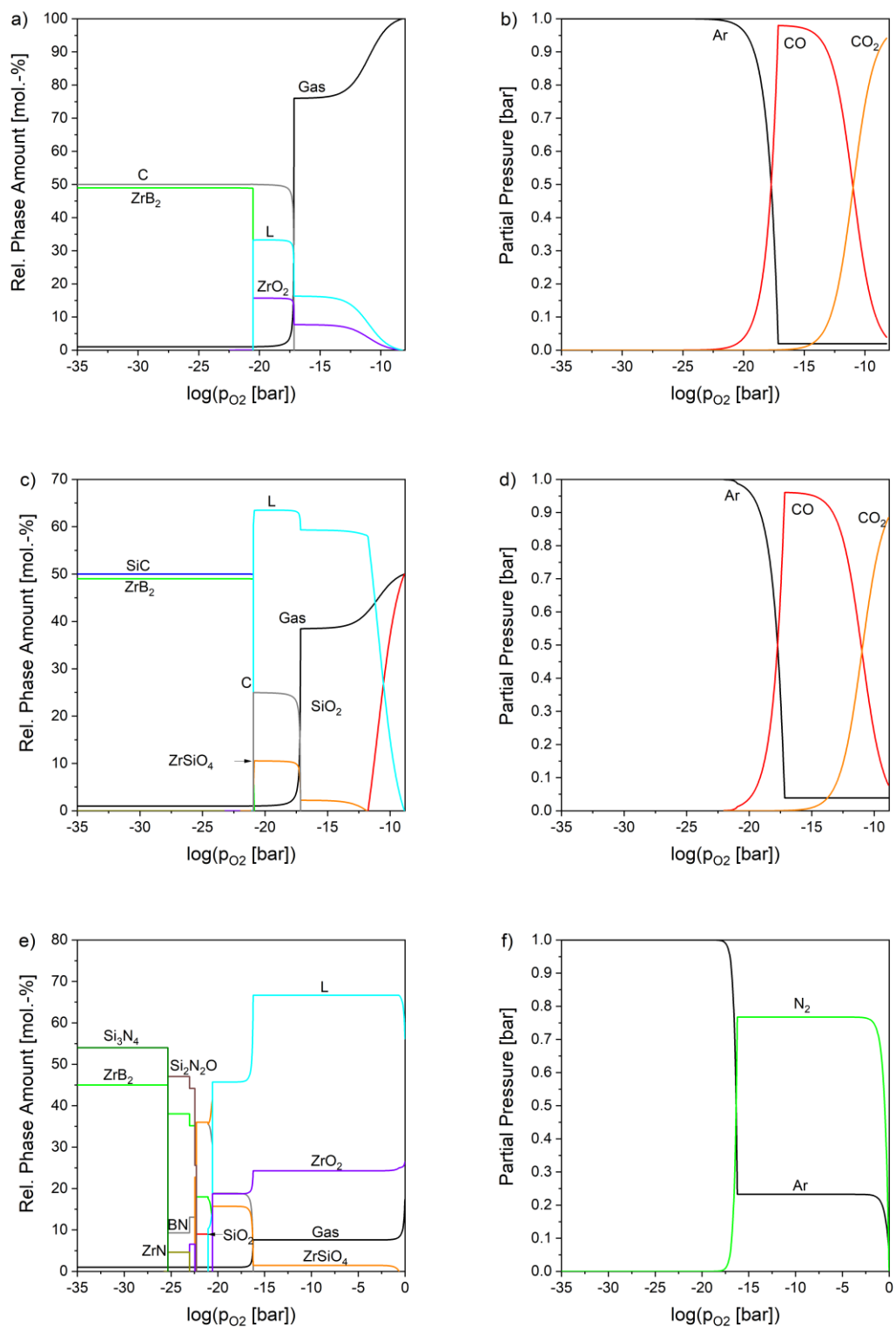
Figure 8.7: Phase fractions and related partial pressures of gas species for the initial couples a)-b) ZrB_2-C, c)-d) ZrB_2-SiC and e)-f) ZrB_2-Si_3N_4 as a function of the oxygen partial pressure (p_{O2}) at 1473 K.

8.2. High-temperature oxidation of SiC/Si-C-N CMC

High-temperature oxidation tests were performed with a SiC/Si-C-N composite. This CMC allows to separate the influence of the ZrB₂-additive on the oxidation behavior of the ZrB₂-SiC/Si-C-N composite described in Section 8.3. To this end, oxidation in O₂- and H₂O-containing atmospheres was investigated using thermogravimetry, materialographic post-test examinations and XRD.

Synthetic air (O₂/N₂/Ar) p$_{O2}$ = 0.14 bar

Figure 8.8 shows the measured mass change during isothermal oxidation of a SiC/Si-C-N CMC in synthetic air. A gas composition with $4 \cdot p_{O2} = p_{N2}$ was used. The necessity of using a protective gas, purging the balance case in this experimental in this setup (see Section 3.2), resulted in an effective gas composition of p_{O2} = 0.14 bar, p_{N2} =0.56 bar and p_{Ar} = 0.3 bar at the sample. The lowest investigated temperature of 1073 K results in an exponential mass loss with an overall mass loss of -1.81 mg/cm² after 100 h. With increasing temperature, an initial mass loss remains at 1273 K and 1373 K, which turns into a mass gain as oxidation progresses. The turning point shifts to an earlier time with increasing oxidation temperature. From 1473 K on, the initial mass change is positive and the mass change rate increases with increasing temperature. Upon oxidation at 1773 K, the mass decreases rapidly after an initial increase. The mass then increases gradually again, resulting in an overall mass change of 0.17 mg/cm².
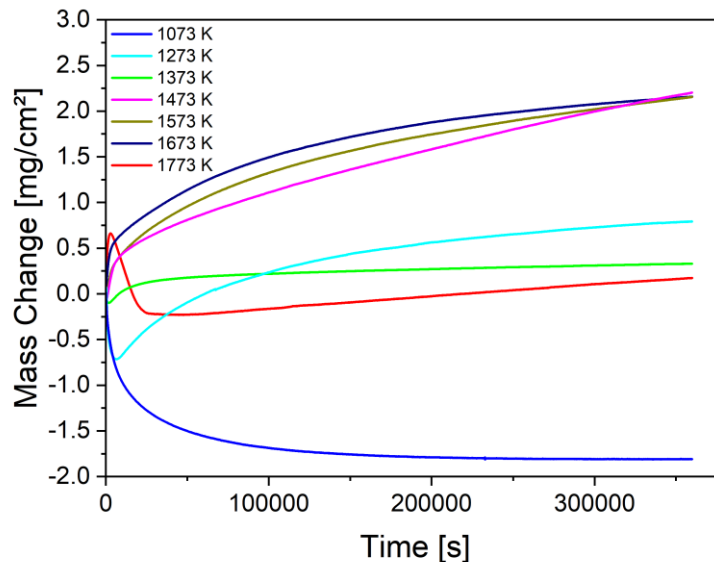
Figure 8.8: Measured mass change during oxidation of SiC/Si-C-N composites at 1073 K-1773 K in flowing synthetic air for 100 h.

Figure 8.9 shows cross-sections of SiC/Si-C-N CMC after 100 h oxidation in synthetic air. The arrangement of the SiC-fiber bundles in 0/90° geometry can be seen. The orientation of the SiC-fiber bundles is parallel and perpendicular to the image plane. The precursor-derived ceramic Si-

C-N matrix can be seen between the individual SiC-fabric layers and partly within the SiC-fiber bundles. The Si-C-N matrix shows cracks and channels due to shrinkage of the preceramic polymer during the pyrolysis process. On the flanks of these channels oxide has formed, which appears dark in the micrographs. With increasing oxidation temperature, the oxide becomes thicker and more pronounced. The corresponding XRD patterns of the oxidized SiC/Si-C-N composites (see Figure 8.10) show formation of β-Cristobalite. The intensity of the associated XRD reflections is increasing with the oxidation temperature. In its initial state, the composite shows only β-SiC XRD reflections of the fiber. In addition, spherical and presumably crystalline regions are present in the ceramic matrix from an oxidation temperature of 1473 K. However, no additional XRD reflexes are detected.
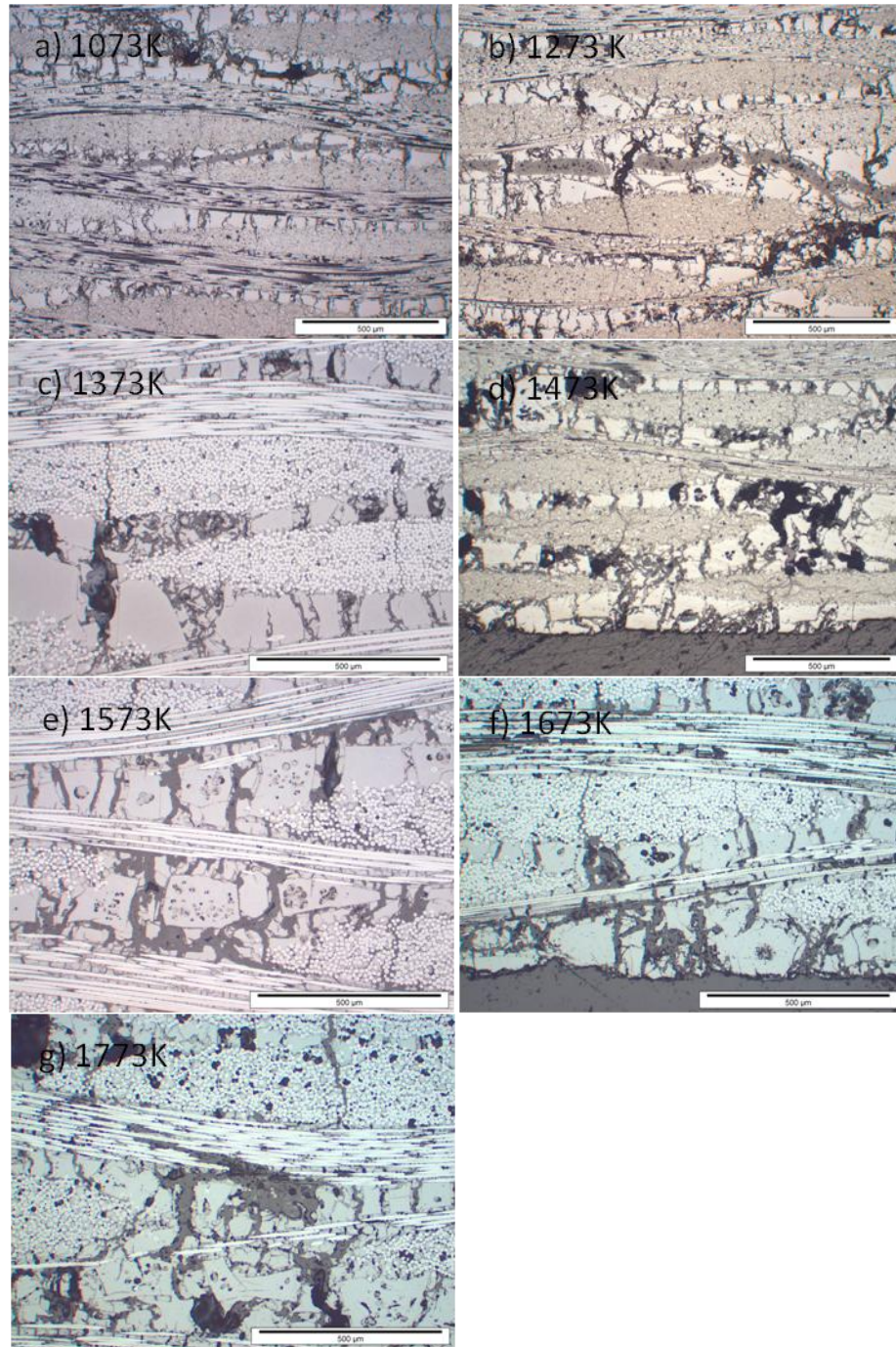
Figure 8.9: Micrographs of SiC/Si-C-N composites after oxidation at a) 1073 K, b) 1273 K, c) 1373 K, d) 1473 K, e) 1573 K, f) 1673 K and g) 1773 K in flowing synthetic air for 100 h The scale bar corresponds to 500 µm.
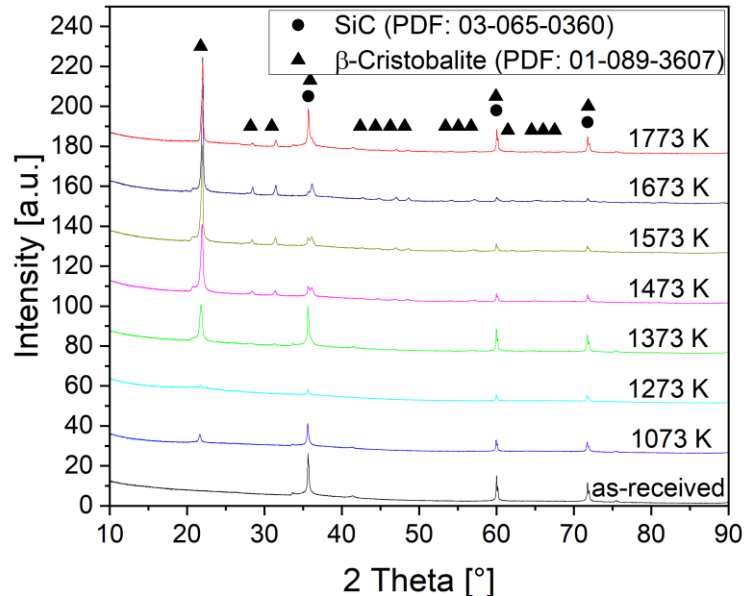
Figure 8.10: XRD pattern of SiC/Si-C-N composites after 100 h of oxidation in flowing synthetic air at 1073 K-1573 K.

H₂O/Ar p$_{H2O}$=0.2 bar

The mass change during oxidation of SiC/Si-C-N in steam/Ar-atmosphere (p_{H2O} = 0.2 bar) is shown in Figure 8.11. This composition was chosen analogously to the O_2/Ar- and H_2O/Ar-mixtures in Section 7. The highest mass increase is measured at the lowest oxidation temperature of 1073 K. With increasing oxidation temperature the mass gain decreases. At the highest oxidation temperature of 1473 K, the highest mass of 1.8 mg/cm^2 is reached after about 248000 s and then decreases again. In particular at 1073 K and 1273 K the mass increase in steam-containing atmosphere is significantly higher than in dry O_2-containing atmosphere.
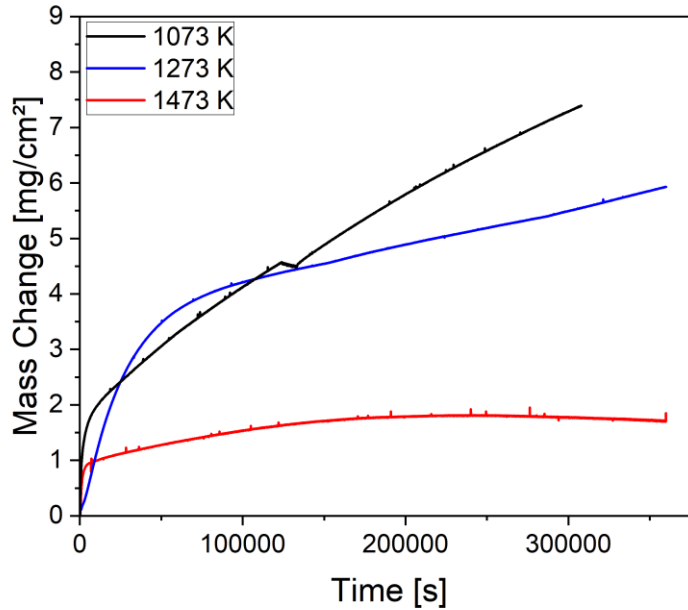
Figure 8.11: Measured mass change during oxidation of SiC/Si-C-N composites at 1073 K-1473 K in flowing steam/Ar-atmosphere p_{H2O}=0.2 bar for 100 h.

Prototypic combustion atmosphere p_{H2O}=0.05 bar, p_{O2}=0.13 bar, p_{CO2}=0.05 bar, p_{N2}=0.77 bar

The measured mass change during oxidation of SiC/Si-C-N composites in prototypic combustion atmosphere, as defined within NewAccess [27], is depicted in Figure 8.12. At the lowest investigated temperature of 1073 K, there is first a mass loss followed by a largely linear mass gain. At 1273 K and 1473 K there is an immediate increase in mass. The highest initial mass gain rate is observed at the highest temperature of 1473 K. However oxidation at 1273 K, results in the highest overall mass gain.
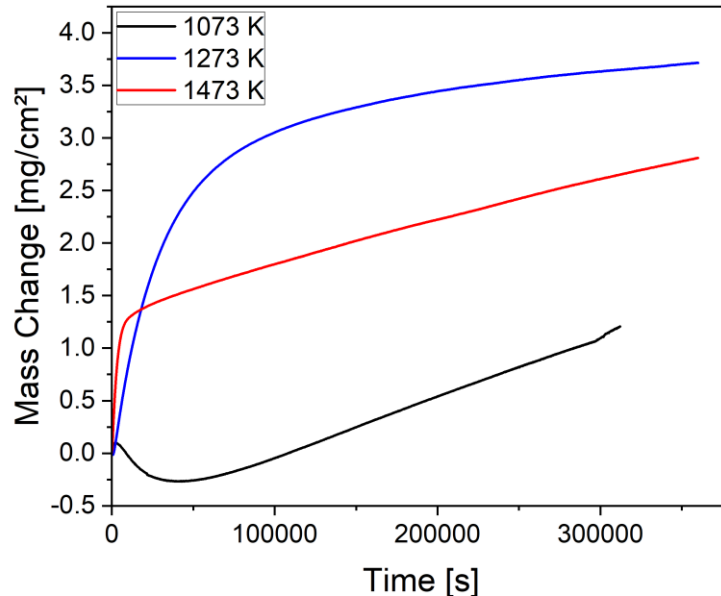
Figure 8.12: Measured mass change during oxidation of SiC/Si-C-N composites at 1073 K-1473 K in prototypic combustion atmosphere for 100 h.

An Arrhenius-type plot of the absolute mass change rates of SiC/Si-C-N composites in different O_2- and H_2O-containing atmospheres is depicted in Figure 8.13a. Data points were calculated from the total mass change after 100 h of isothermal oxidation. At lower temperatures H_2O-containing atmospheres result in higher overall mass change rates. Higher p_{H2O} in steam/Ar atmosphere ($p_{H2O} = 0.2$ bar) compared to prototypic combustion atmosphere ($p_{H2O} = 0.05$ bar and $p_{O2} = 0.13$ bar) lead to higher oxidation rates at 1073 K and 1273 K. Mass change rates in synthetic air ($p_{O2} = 0.14$ bar) are almost one order of magnitude lower at these temperatures. At 1473 K, the overall mass change rates are about the same in all three investigated atmospheres. For technical reasons, thermogravimetric tests above 1473 K were only possible in dry H_2O-free atmospheres (see Section 3.2). The overall mass change rates at 1473 K-1673 K in synthetic air do not differ significantly after 100 h. Only at 1773 K, above the carbothermal decomposition temperature of the ceramic Si-C-N matrix, the overall mass change rate decreases significantly.

A kinetic evaluation of these SiC/Si-C-N CMC oxidation experiments is generally difficult. There are a number of factors that influence the thermogravimetrically measured mass changes. The investigated SiC/Si-C-N CMC samples have an unfavorable open porosity, which allows the ingress of oxidizing atmosphere. Thus, the effective surface area of the samples is larger than the geometrically measured one. In addition, the size of the surface exposed to the oxidizing atmosphere probably changes during the experiments. This may become smaller or larger due to formation or volatilization of condensed oxides, respectively.

In addition, oxidation of different constituents of the CMC has a different effect on the measured mass change. While the formation of solid oxides leads to an increase in mass, the mass decreases due to oxidation of free carbon, for example from the Si-C-N matrix and by volatilization of condensed oxides. The carbothermal decomposition reaction of the Ceraset$^{®}$ PSZ 20-derived Si-C-N matrix above 1757 K also leads to a mass loss (see Section 5.1).

Since these effects could not be separated, even with more sophisticated models, the measured thermogravimetric data were fitted with a simple equation (1.1). The obtained rate constant k and exponent n are shown in Figure 8.13b and c, respectively. In particular, the obtained rate constant k has only an illustrative character due to the strong temperature-dependent reaction kinetics and the numerous overlapping effects (n is not constant!). Oxidation in H$_2$O-containing atmosphere gives the highest k-values. These increase with both p$_{H2O}$ and temperature. The determination of activation energies was therefore deliberately omitted.

However, the obtained exponent n Figure 8.13c allows a general conclusion on the nature of the effective oxidation kinetics. For all investigated atmospheres and temperatures the exponent n is in the order ≤ 0.5. This corresponds to parabolic or sub-parabolic reaction kinetics. For H$_2$O-containing atmospheres, n shifts significantly to smaller values with increasing temperature. In synthetic air this is also the case for temperatures above 1473 K. However, in synthetic air the exponent n also deviates to smaller values even at lower temperatures.
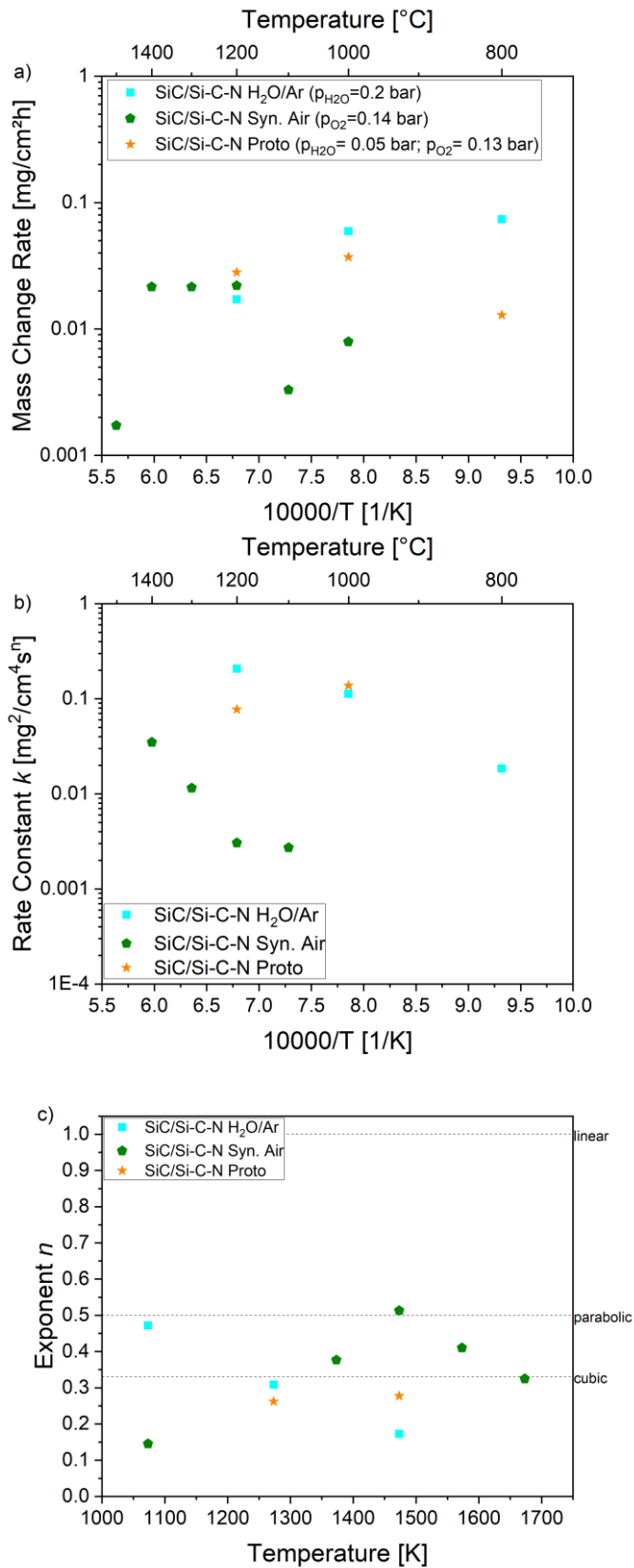
Figure 8.13: Obtained a) overall mass change rate, b) rate constant *k* and c) exponent *n* for the oxidation of SiC/Si-C-N composites in O_2- and H_2O-containing atmosphere, respectively.

8.3. High-temperature oxidation of ZrB_2-SiC/Si-C-N CMC

8.3.1. Mass spectrometric analysis

Samples of a ZrB_2-containing SiC/Si-C-N composite with a dimension of 10x10x3 mm³ were used for experimental investigation of the oxidation behavior. Both transient and isothermal oxidation tests were performed up to maximum temperatures of 1473 K and 1273 K in O_2- and H_2O-containing atmospheres, respectively.

Thermogravimetric measurements of the mass change during oxidation were performed using *Netzsch STA 449 F3 Jupiter* and *Netzsch STA 409* to reveal the oxidation behavior of the ZrB_2-SiC/Si-C-N composite.

Gaseous oxidation- and volatilization products were analyzed using the mass spectrometers *Netzsch QMS 403C Aëolos and Balzers GAM 300* coupled to the off-gas of the STAs.

Transient oxidation tests

Figure 8.14 shows thermogravimetric and mass spectrometric data for oxidation of a ZrB_2-SiC/Si-C-N composite in flowing O_2/Ar-atmosphere (p_{O2}=0.2 bar). The sample was heated from room temperature to 1473 K with 5 K/min. Up to about 600 K the mass of the sample is decreasing. Possibly due to the evaporation of adsorbed water or other volatile substances. Between 600 K and 800 K, the sample mass is approximately constant, followed by a minimum at 950 K. This minimum is accompanied by the release of CO and CO_2, indicating the oxidation of free carbon from the Si-C-N matrix. The release of CO is starting from 850 K while the release of CO_2 is shifted to higher temperatures of 950-1100 K. From temperatures of 950 K, the sample mass is increasing with temperature. At the same time, N_2 is released during the oxidation reaction of the Si-C-N matrix. Both is indicating the formation of a passivating solid oxide scale. With ongoing oxide growth, the mass increase rate and the release of gaseous oxidation products is decreasing.
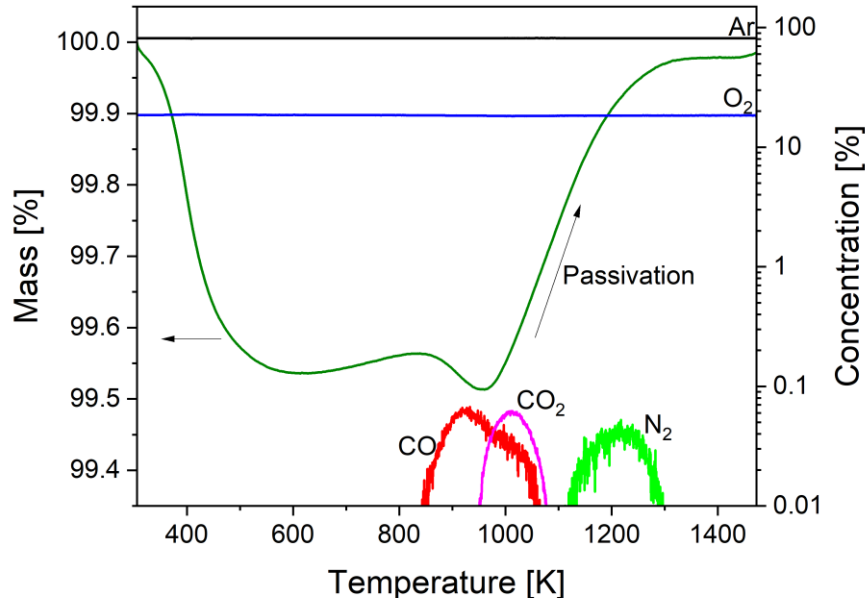
Figure 8.14: Mass change and off-gas composition measured by mass spectrometry during heat-up of ZrB$_2$-SiC/Si-C-N with 5 K/min in O$_2$/Ar-atmosphere (p$_{O2}$ = 0.2 bar).

Figure 8.15 shows thermogravimetric and mass spectrometric data for the oxidation of a ZrB$_2$-SiC/Si-C-N composite in H$_2$O/Ar-atmosphere (p$_{O2}$=0.2 bar). Heating up to 673 K and 10 min preconditioning was carried out in flowing Ar. Then, the sample was heated with 5 K/min to a maximum temperature of 1473 K in H$_2$O/Ar-atmosphere. Free cooling to room temperature was carried out in flowing Ar. During preconditioning in Ar, the sample mass is decreasing with temperature until a constant mass is reached. Mass spectrometric data show at the same time a release of CO$_2$, CH$_4$ and H$_2$ up to 0.01% of the off-gas composition. Residual water in the system is probably leading to a steam content of about 0.2% during this stage of the test. With the onset of steam injection during the heat-up stage, significant amounts of H$_2$, CO, CO$_2$ and CH$_4$ are produced. The steam content of the off-gas is at a constant value. However, the off-gas stream also contains the protective argon gas, which is preventing the ingress of steam into the balance but does not reach the sample. Therefore, the steam content in the off-gas is lower than at the sample position. Note that also in this test, CO and CO$_2$ are dominating at lower and higher temperatures, respectively. With increasing temperature, the content of CH$_4$ is decreasing. Upon free cooling in Ar, the signals of steam and gaseous oxidation products are rapidly decreasing while the sample mass is constant during this stage.
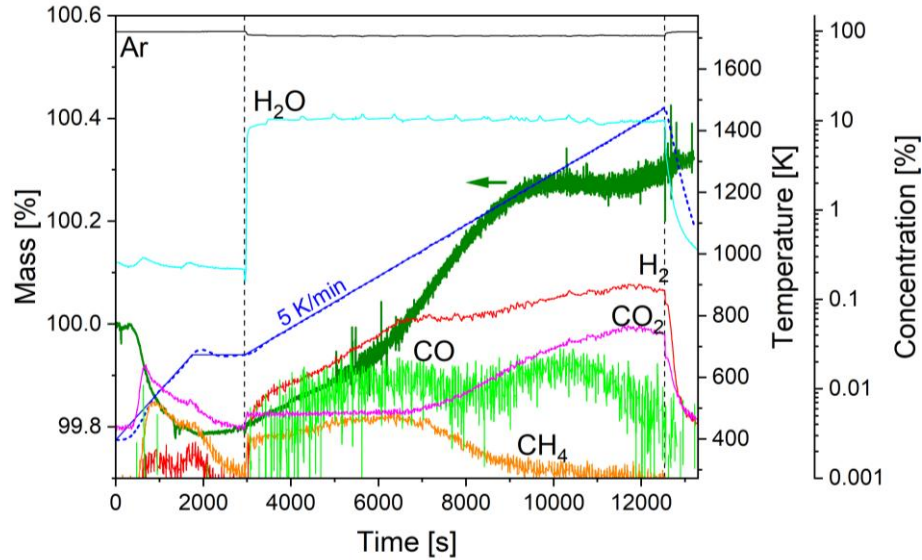
Figure 8.15: Thermogravimetric and mass spectrometric analysis of ZrB_2-SiC/Si-C-N oxidation in steam. After heat-up and equilibration in Ar, the sample was heated from 673 K to 1473 K with 5 K/min in H_2O/Ar-atmosphere (in between vertical dashed lines; p_{H2O}=0.2 bar). The set temperature program is indicated by a solid blue line.

Figure 8.16 shows the measured mass gain during heat-up in H_2O/Ar (p_{H2O}=0.2 bar) from 673 K to 1473 K. Additionally, the H_2-release rate determined by mass spectrometry is shown. The sample mass is increasing upon heat-up in steam-containing atmosphere. The maximum mass gain rate is reached in the temperature range 1000-1200K. From 1200 K to about 1350 K, the mass is approximately constant, increasing again at temperatures above 1350 K.

The H_2-release rate is increasing immediately with the onset of steam injection. Between 950 K and 1150 K a plateau is established. Maximum H_2 release rate is reached at about 1400 K.
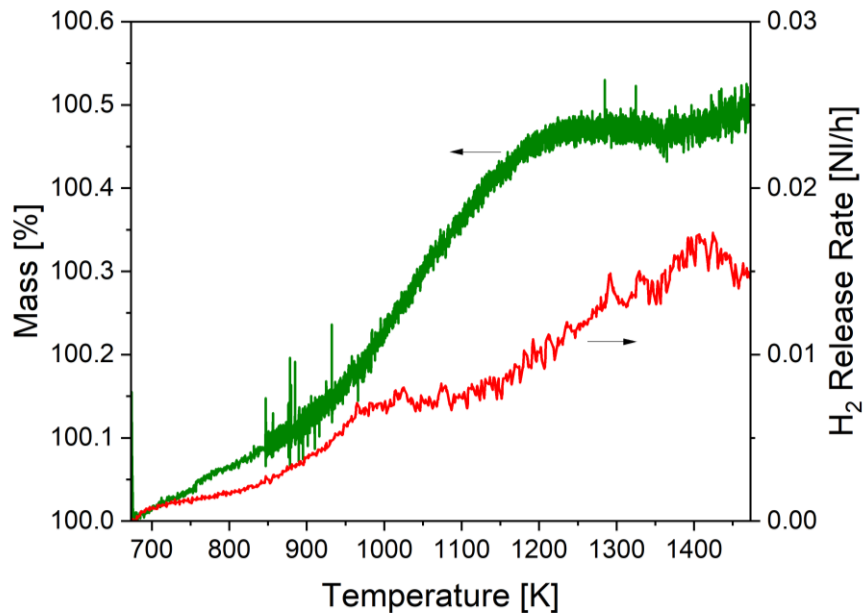
Figure 8.16: Measured H_2 release rate during heating of ZrB_2-SiC/Si-C-N with 5 K/min in H_2O/Ar-atmosphere (p_{H2O}=0.2 bar).

Due to the low ZrB_2 content of the ZrB_2-SiC/Si-C-N composite, the amount of gaseous boron-containing species in the off-gas is very low. Figure 8.17 shows, that with the onset of steam injection, the $H_3BO_3^+$-signal at m/z=62 is barely increasing. Note, that the scale of the ion current was chosen identical to the oxidation tests of pure ZrB_2 under the same conditions (see Section 7.3, Figure 7.11).
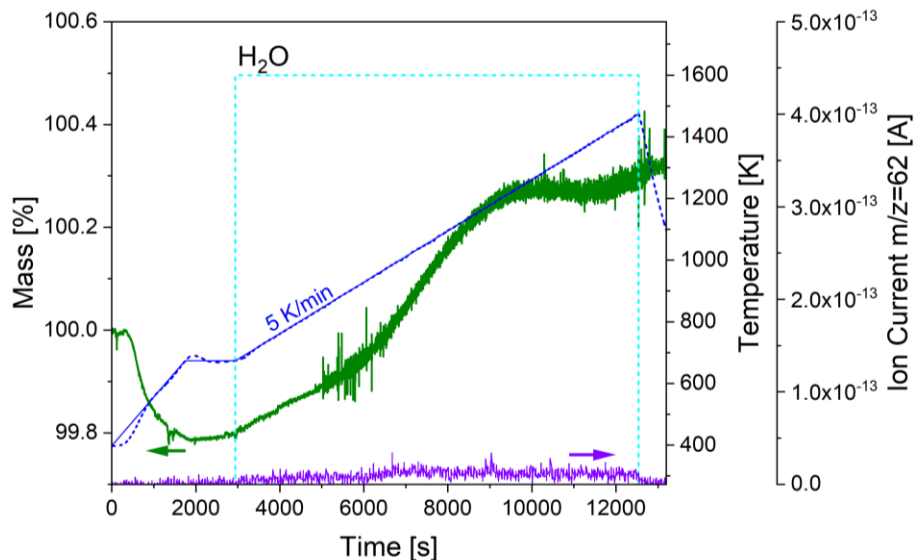
Figure 8.17: Ion current measured by mass spectrometry at m/z = 62 during heating of ZrB_2–SiC/Si-C-N with 5 K/min in H_2O/Ar-atmosphere (p_{H2O}=0.2 bar).

<u>Isothermal oxidation tests</u>

Samples were heated with 20 K/min up to the final test temperature in flowing Ar. After 10 min equilibration time, steam injection was started and samples were isothermally oxidized for 5 h in flowing H$_2$O/Ar (p$_{H2O}$=0.2 bar). Longer experiments were not performed because the H$_2$-release rate decreased considerably as the passivation of the samples proceeded.

Upon oxidation in steam, H$_2$ is released from various possible reactions of the components of the ZrB$_2$-SiC/Si-C-N composite:

$$ZrB_2 + 5H_2O = ZrO_2 + B_2O_3 + 5H_2 \tag{8.3}$$

$$SiC + 3H_2O = SiO_2 + CO + 3H_2 \tag{8.4}$$

$$SiC + 4H_2O = SiO_2 + CO_2 + 4H_2 \tag{8.5}$$

$$Si_3N_4 + 6H_2O = 3SiO_2 + 2N_2 + 6H_2 \tag{8.6}$$

$$C + H_2O = CO + H_2 \tag{8.7}$$

$$C + 2H_2O = CO_2 + 2H_2 \tag{8.8}$$
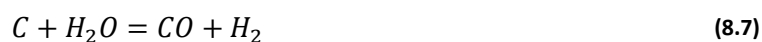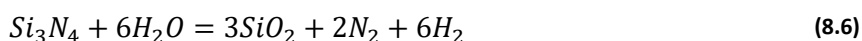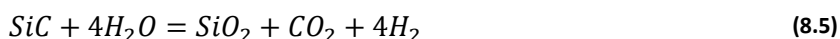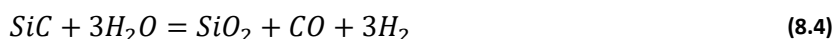
The H$_2$-release rates measured by mass spectrometry at 1073 K and 1473 K are depicted in Figure 8.18 on a common time scale. At t = 0 s, steam is injected. "Negative values" are referring to the heating and preconditioning phase in Ar. The detected H$_2$ signal in the preconditioning phase might result from the release of adsorbed H$_2$O from the system. With the onset of steam injection, the H$_2$-signal is increasing instantaneously. Oxidation at 1473 K resulted in a pronounced maximum of the H$_2$-release rate up to 0.065 Nl/s, while the maximum upon oxidation at 1073 K is less pronounced. After the initial maximum, the H$_2$-release rate is decreasing rapidly to a constant value of 0.002 Nl/s and 0.004 Nl/s at 1473 K and 1073 K, respectively. With the end of steam injection, the H$_2$-release rate is going back to a pre-test value.
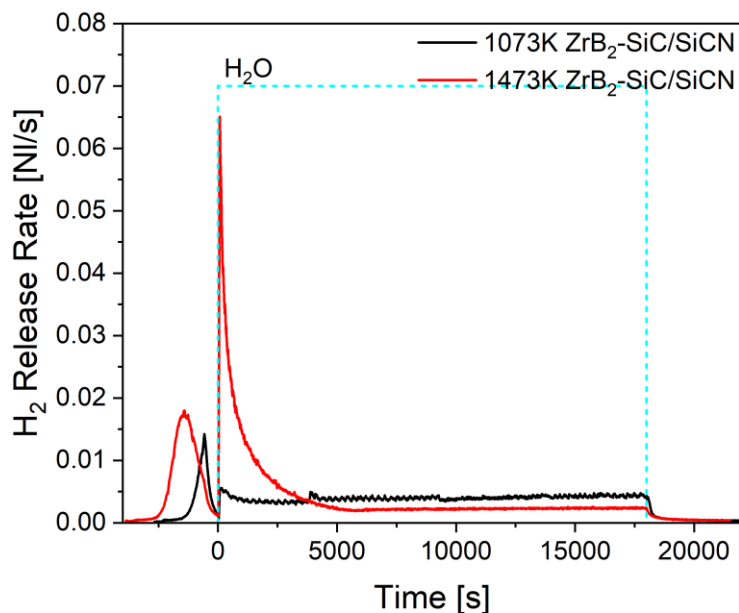
Figure 8.18: Measured H$_2$ release rate during isothermal oxidation of ZrB$_2$-SiC/Si-C-N in H$_2$O/Ar (p$_{H2O}$=0.2 bar) for 5 h at 1073 K, and 1473 K. The time axis was moved to indicate the beginning of steam injection. "Negative values" are referring to the heating and preconditioning phase in Ar.

Figure 8.19 shows the mass change during isothermal oxidation of ZrB$_2$-SiC/Si-C-N in H$_2$O/Ar (p$_{H2O}$=0.2 bar) at 1073 K and 1473 K. Data derived by thermogravimetry and mass spectrometric measurements of the H$_2$-release are compared. Oxidation at 1073 K shows linear mass gain (n = 0.951) after a short initial equilibration time (with parabolic kinetics). In contrast to that, parabolic oxidation kinetics (n = 0.626) are observed at 1473 K. This is resulting in a lower total mass gain after 5 h oxidation of 1.7 mg/cm² at 1473 K compared to 4.3 mg/cm² at 1073 K. The mass change calculated from the measured H$_2$-release rate (see Figure 8.18) according to reaction (8.3) shows very good agreement with the thermogravimetric data at 1073 K. Therefore, oxidation characteristics are dominated by ZrB$_2$ oxidation. Reactions producing volatile oxidation products resulting in a mass loss do not play an important role at this temperature. However, at 1473 K theoretical mass change calculated from the H$_2$-release is much higher compared to the measured mass gain. This is indicating that gaseous oxidation (CO(g), CO$_2$(g), N$_2$(g),...) and volatilization products (H$_3$BO$_3$(g), HBO$_2$(g), SiO(g),...) have a significant influence on the observed mass change during oxidation. Therefore, thermogravimetry is underestimating the oxidation kinetics. However, both thermogravimetry and mass spectrometry yield parabolic oxidation kinetics.
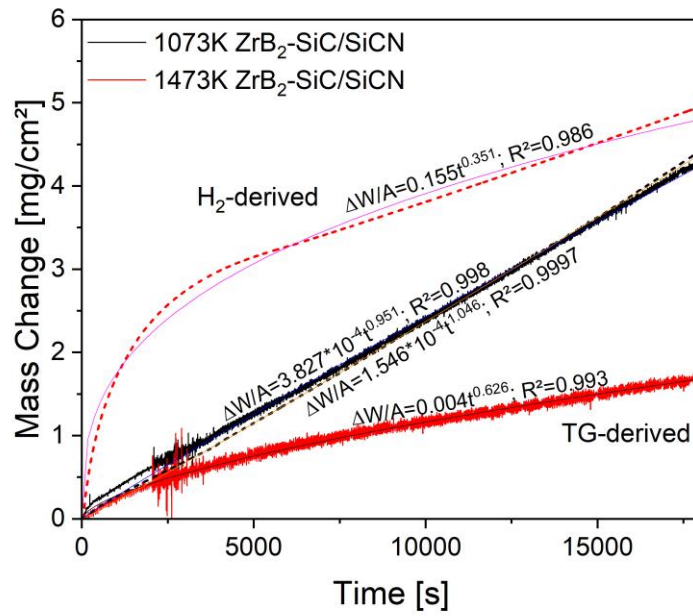
Figure 8.19: Comparison of the mass change of ZrB$_2$ derived from thermogravimetry (TG, solid lines) and from the H$_2$-release (dashed lines) measured by mass spectrometry. Obtained fit parameters are given additionally.

8.3.2. Thermogravimetric and microstructural analysis

In H₂O/Ar p_{H2O}=0.2 bar

Figure 8.20 shows ZrB₂-SiC/Si-C-N composites after isothermal oxidation at 1073 K, 1273 K and 1473 K in flowing H₂O/Ar for 100 h. Both samples sides are shown. With increasing oxidation temperature, the sample surface exhibits a white scale, which is more pronounced at one side of the sample. It must be noted, that samples were placed with one edge on a concave plate-like sample holder. Therefore, both sides of the samples experienced the same access to the oxidizing atmosphere. However, the ZrB₂-additive was introduced into the CMC in a first laminating step of the SiC fiber-preform using a mixture of Ceraset® PSZ 20 and ZrB₂-powder. Therefore, both sides of the obtained CMC exhibit a different ZrB₂-content. All subsequent PIP cycles were performed using pure Ceraset® PSZ 20.
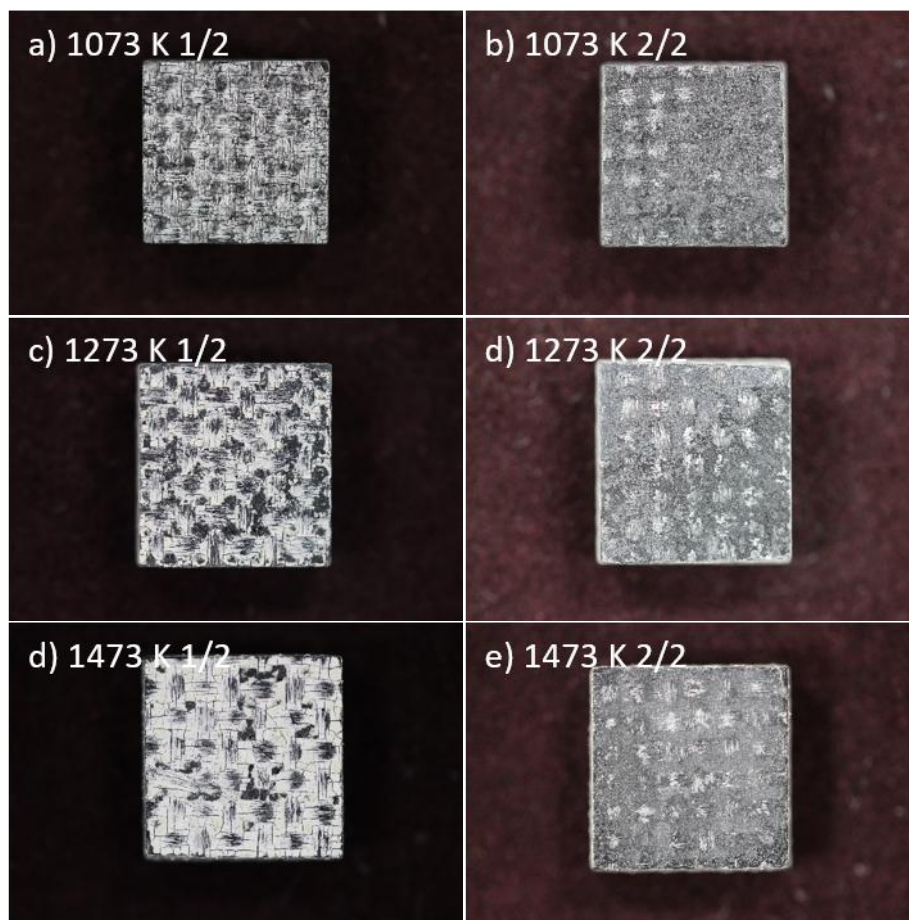
Figure 8.20: ZrB₂-SiC/Si-C-N composites after isothermal oxidation at a, b) 1073 K, c, d) 1273 K and e, f) 1473 K in flowing H₂O/Ar-atmosphere (p_{H2O} = 0.2 bar) for 100 h. Both samples sides are shown. The edge length of the samples corresponds to 10 mm.

XRD patterns of the ZrB₂-SiC/Si-C-N composite, oxidized at 1473 K (Figure 8.21a), reveal the composition of both sides of the sample. The darker side of the sample shows mainly reflections of β-Cristobalite. Only small reflections of monoclinic ZrO_2 and $ZrSiO_4$ are present. However, the white scaled side shows mainly $ZrSiO_4$ and less pronounced β-Cristobalite and monoclinic ZrO_2

reflections. With increasing temperature (see Figure 8.21b) the relative intensities, and therefore the amounts, of $ZrSiO_4$ and β-Cristobalite are increasing, while monoclinic ZrO_2 is decreasing.
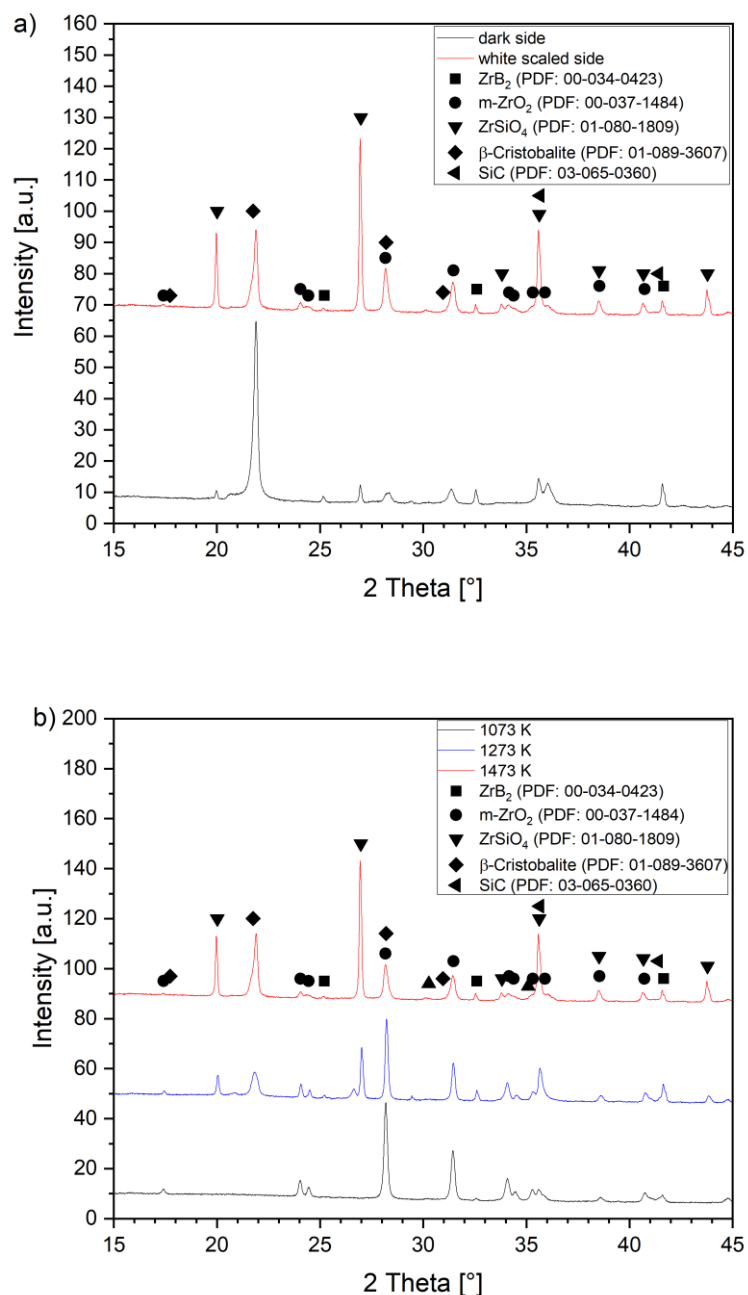
Figure 8.21: XRD patterns of ZrB₂-SiC/Si-C-N composites after isothermal oxidation in flowing H_2O/Ar (p_{H2O} = 0.2 bar) for 100 h. XRD patterns of a) both sides of a ZrB₂-SiC/Si-C-N composite after oxidation at 1473 K and b) the white scaled side after oxidation at 1073 K, 1273 K and 1473 K are compared.

Figure 8.22 shows SEM micrographs of a ZrB₂-SiC/Si-C-N composite after oxidation at 1473 K in H_2O/Ar for 100 h. In the cross-section, an oxide scale at the surface of the sample is visible in

Figure 8.22a, which is shown in detail in Figure 8.22b. In a ZrB$_2$-rich channel of the composite (Figure 8.22c and d), the ingress of the oxidizing atmosphere into the sample is visible. From the surface, ZrB$_2$ particles are oxidized as well as the surrounding Si-C-N matrix. The channel is filled with oxide and shows presumably open porosity. Further inside of the ZrB$_2$-rich channel, the ZrB$_2$ particles are unaffected. The oxidizing atmosphere did not reach this part of the sample marked with a dashed line.
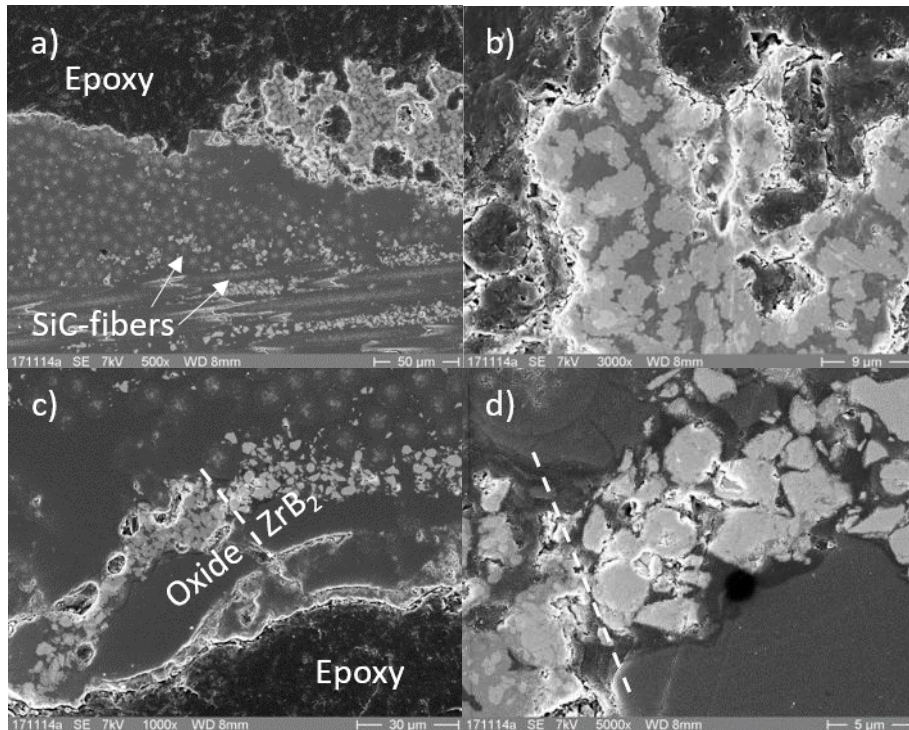
Figure 8.22: SEM micrographs showing a cross section of a ZrB$_2$-SiC/Si-C-N composite after oxidation at 1473 K in flowing H$_2$O/Ar-atmosphere (p$_{H2O}$ = 0.2 bar) for 100 h. The white oxide scale is shown in a) and details in b) with higher magnification. The dashed line indicates the ingress of the oxidizing atmosphere into a ZrB$_2$-rich region of the composite c) and details in d). Scale bars correspond to a) 50µm, b) 9 µm, c) 30 µm and d) 5µm.

EDX analysis depicted in Figure 8.23 reveals the composition of the oxidized region. ZrO$_2$ (white/1 and Figure 8.23c) as oxidation product of the ZrB$_2$ additive is surrounded by SiO$_2$ (dark/2 gray and Figure 8.23d) from the oxidation of the Si-C-N matrix. At the boundary in between, ZrSiO$_4$ (light grey/3 and Figure 8.23e) is formed from the reaction of ZrO$_2$ and SiO$_2$.

Thermodynamic calculations on the phase equilibria of ZrB$_2$ and the equilibrium constituents of the Si-C-N matrix (SiC, Si$_3$N$_4$ and C) in oxidizing atmosphere (see Section 8.1, Figure 8.7) predicted the formation of ZrSiO$_4$.
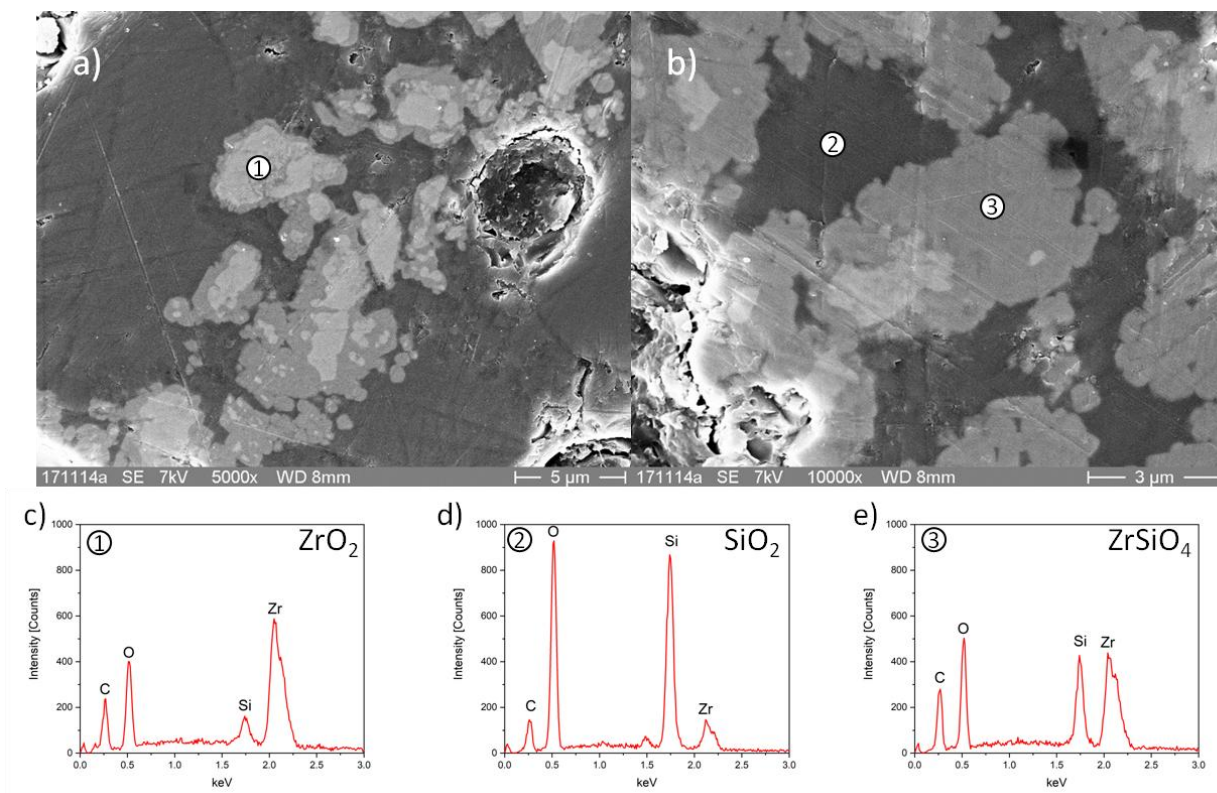
Figure 8.23 SEM/EDX-analysis of a ZrB$_2$-SiC/Si-C-N composite oxidized at 1473 K in flowing H$_2$O/Ar-atmosphere (p$_{H2O}$ = 0.2 bar) for 100 h. The scale bars correspond to a) 5μm and b) 3 μm, respectively.

Figure 8.24 shows SEM micrographs of a ZrB$_2$-SiC/Si-C-N composite after oxidation at 1073 K in H$_2$O/Ar for 1000 h.

On the surface of the composite, (Figure 8.24a and b) bubbles occur, which indicate the presence of a liquid phase at the oxidation temperature. Furthermore, the composite exhibits pores, which are apparently connected (Figure 8.24c and d). Cracks are observed parallel to the lamination plane (Figure 8.24e) associated with a significant swelling of the composite (Figure 8.24f).
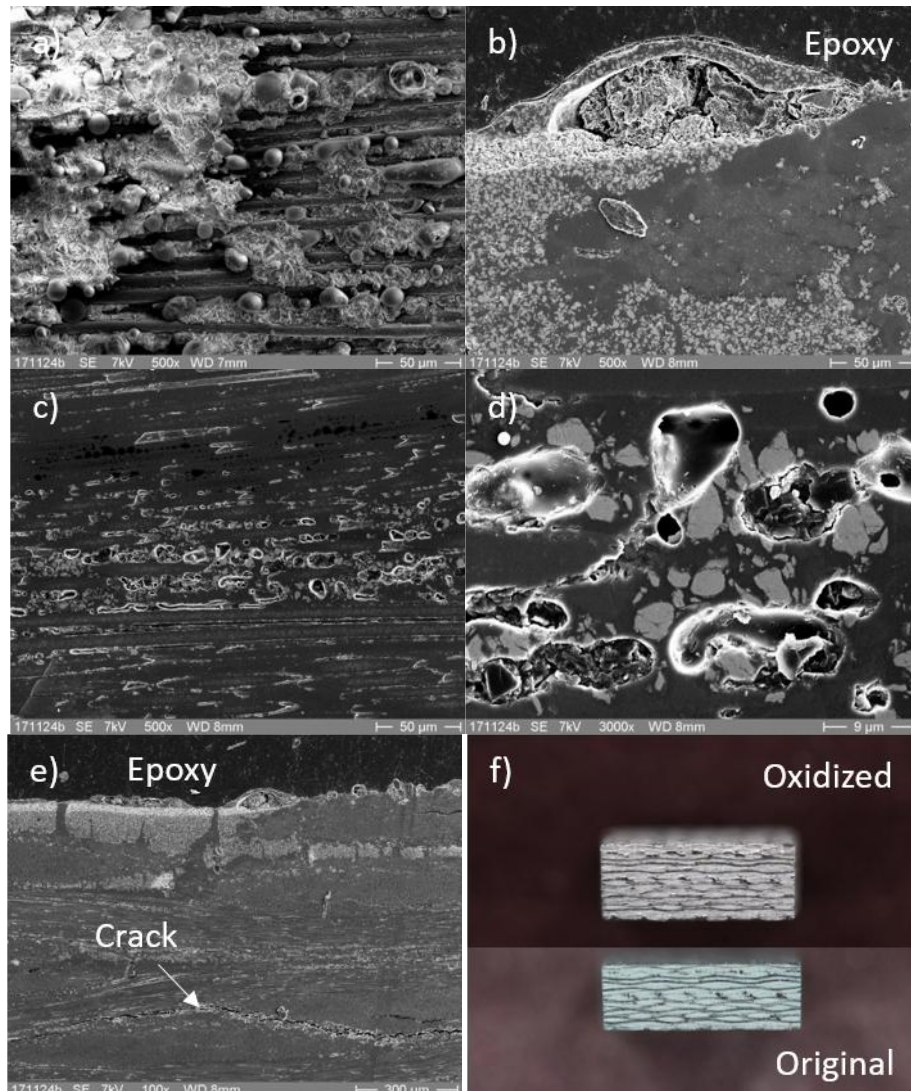
Figure 8.24: SEM micrographs of a ZrB₂-SiC/Si-C-N composite oxidized at 1073 K in flowing H_2O/Ar-atmosphere (p_{H2O} = 0.2 bar) for 100 h. Microstructural changes showing a) and b) bubbles at the surface, c) and d) pores, e) cracks. Photograph before and after oxidation f) indicates swelling of the composite. Scale bars correspond to a), b), c) 50 µm, d) 9 µm and e) 300 µm. The edge length of the sample before oxidation in f) is 3 mm x 10 mm.

The mass change during isothermal oxidation is depicted in Figure 8.25. After 100 h, at 1073 K, 1273 K and 1473 K the composite underwent a mass gain of 20.3 mg/cm², 8.3 mg/cm² and 3.3 mg/cm², respectively. Hence, the highest mass gain is observed during oxidation at 1073 K. With increasing temperature, the mass gain decreased. At 1073 K, the composite initially shows linear oxidation kinetics turning into rather subparabolic kinetics. At higher temperatures, oxidation kinetics shift to rather parabolic (1273 K) and subparabolic (1473 K) behavior.
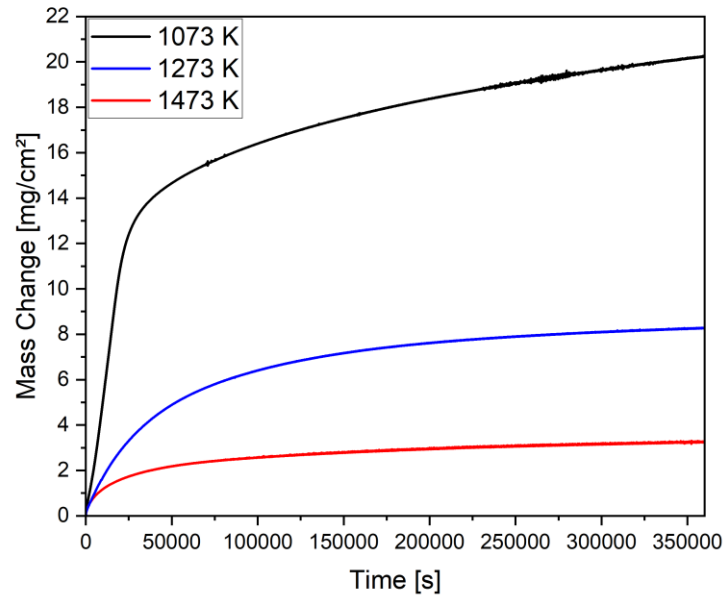
Figure 8.25: Measured mass change during oxidation of ZrB$_2$-SiC/Si-C-N composites at 1073 K, 1273 K and 1473 K in H$_2$O/Ar-atmosphere (p$_{H2O}$ = 0.2 bar) for 100 h.

In O₂/Ar p$_{O2}$ = 0.2 bar

Figure 8.26 shows photographs of ZrB₂-SiC/Si-C-N composites after isothermal oxidation in flowing O₂/Ar (p$_{O2}$ = 0.2 bar) for 100 h. With increasing oxidation temperature, the oxide scale is more pronounced. Similar to experiments in steam, characteristics of both sides of the samples are different due to different ZrB₂-distribution.

Figure 8.26: ZrB₂-SiC/Si-C-N composites after isothermal oxidation at a), b) 1073 K, c), d) 1273 K, e), f) 1473 K and g), h) 1673 K in O₂/Ar-atmosphere (p$_{O2}$ = 0.2 bar) for 100 h. Both sample sides are shown. The edge length of the samples corresponds to 10 mm.

Cross-sections of the ZrB₂-SiC/Si-C-N composite, oxidized at 1073 K (see Figure 8.27), show the oxidation behavior of the ZrB₂-additive. ZrB₂-rich areas of the composite are partly oxidized from the surface (see Figure 8.27a-b). ZrO₂, obtained by oxidation of ZrB₂ particles, is surrounded by SiO₂ (Figure 8.27c). A clear transition from oxidized to unoxidized ZrB₂ particles is

visible (Figure 8.27c). At the surface, accumulations of material and bubbles are present, which are connected to an open network of pores. Therefore, a certain amount of viscosity must be present at 1073 K, at least in an initial stage of oxidation.
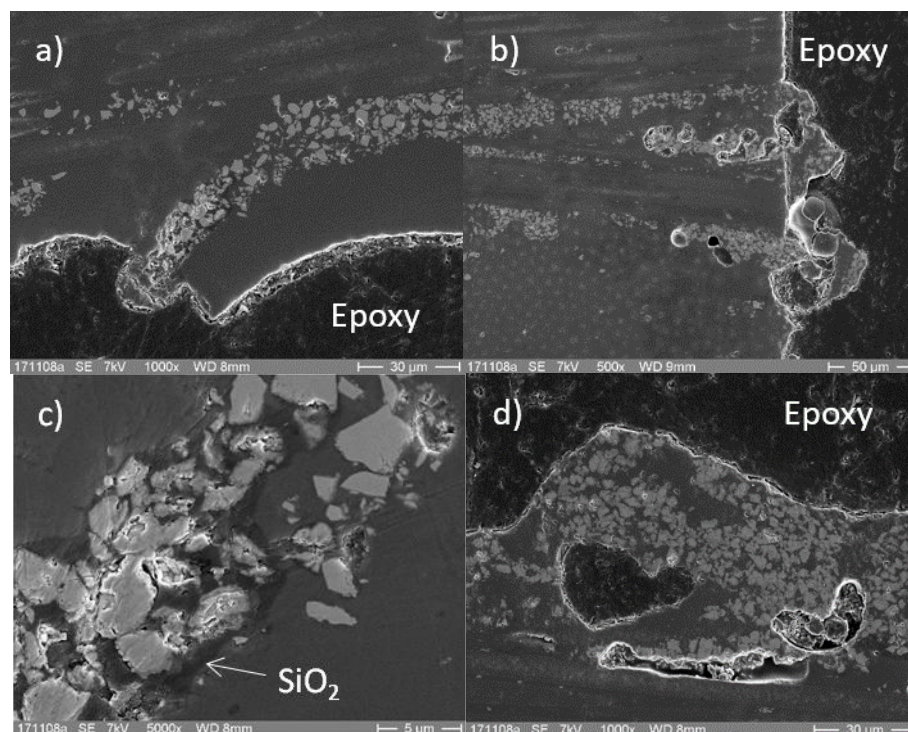
Figure 8.27: SEM micrographs showing cross-sections of a ZrB₂-SiC/Si-C-N composite after isothermal oxidation at 1073 K in flowing O₂/Ar-atmosphere (p_{O2} = 0.2 bar) for 100 h: a) and b) ZrB₂-rich channels with material accumulated at the surface; closer view of c) the transition are between oxidized and unoxidized region and d) ZrB₂-rich material and porosity at the surface. Scale bars correspond to a) 30 μm, b) 50μm, c) 5 μm and d) 30 μm.

Already after 1 h of oxidation in O₂/Ar, the formation of an oxide layer on the CMC is visible by a bluish discoloration (Figure 8.28a and b). SEM micrographs show that the oxide is present in the form of islands resembling a solidified melt (Figure 8.28c and d). However, no boron was detectable by EDX analysis in the oxide scale formed on the ZrB₂-SiC/Si-C-N composite (see Figure 8.28e and f). This is indicating, that boron is already lost in an early stage of oxidation by volatilization of boron-containing gas species.
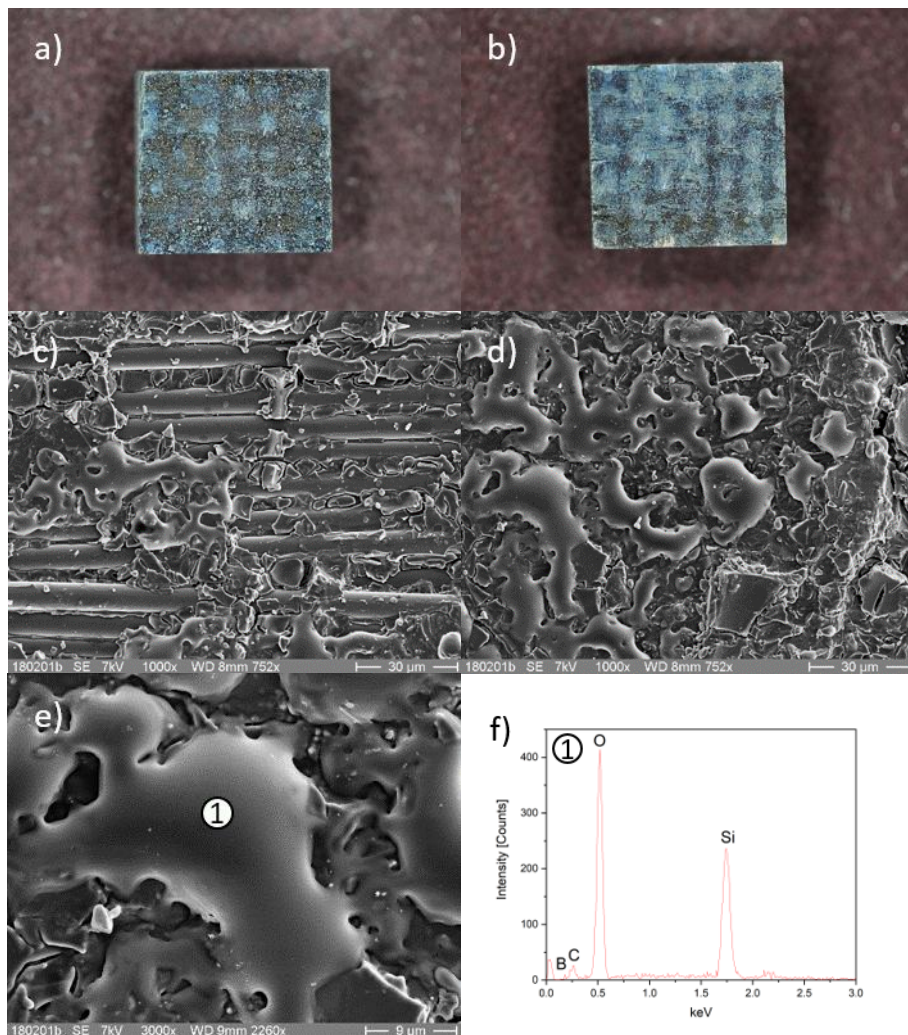
Figure 8.28: Both sides a) and b) of a ZrB₂-SiC/Si-C-N composite after oxidation at 1473 K in O_2/Ar-atmosphere (p_{O_2} =0.2 bar) for 1 h. SEM micrographs of the surface are visible in c)-e) and the EDX-analysis of (1) is given in f). The edge length of the sample in a) and b) is 10 mm. Scale bars correspond to c), d) 30 μm and e) 9 μm.

Thermogravimetric measurements reveal the mass change during oxidation (Figure 8.29). After 100 h of oxidation at 1073 K, the ZrB₂-SiC/Si-C-N composite exhibited a mass gain of 9.7 mg/cm². This is much higher compared to oxidation at higher temperatures. The mass gain is decreasing with increasing temperature up to 1473 K. Moreover, the mass gain during the initial hours of oxidation is lower at 1273 K and 1473 K. At 1673 K, the initial mass gain is even higher than at 1073 K. However, the mass is only slightly increasing during the proceeding test. The total mass gain after 100 h of oxidation at 1673 K is in between the tests at 1273 K and 1473 K.
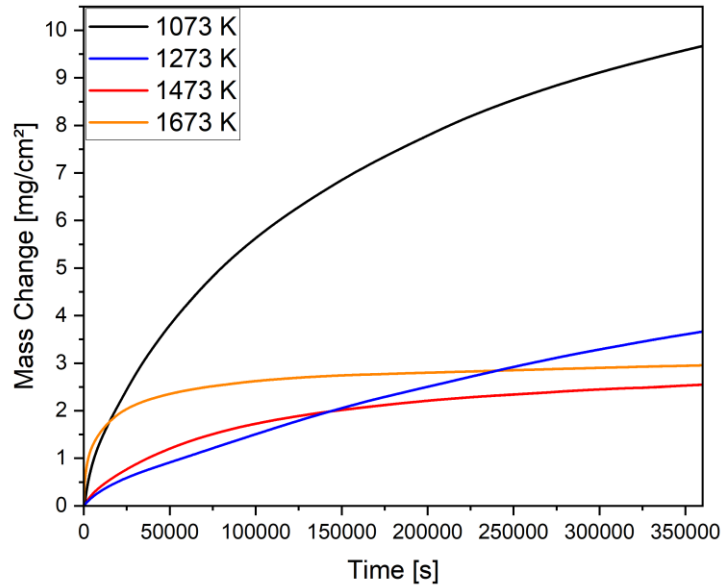
Figure 8.29: Measured mass change during oxidation of ZrB$_2$-SiC/Si-C-N composites at 1073 K, 1273 K, 1473 K and 1673 K in O$_2$/Ar-atmosphere (p$_{O2}$ = 0.2 bar) for 100 h.

O$_2$/N$_2$/Ar p$_{O2}$ = 0.14 bar

Figure 8.30 shows ZrB$_2$-SiC/Si-C-N composites after oxidation at 1073 K, 1273 K and 1473 K in synthetic air with a O$_2$/N$_2$-ratio of 20/80. The protective Ar gas, purging the balance case, resulted effectively in p$_{O2}$ = 0.14 bar and p$_{N2}$ = 0.56 bar at the sample.

Oxidation at 1073 K did not result in any visible change in the surface of the CMC (Figure 8.30a and b). After oxidation at 1273 K the sample surface turned slightly bluish (Figure 8.30c and d). Only oxidation at 1473 K resulted macroscopically in a pronounced oxide scale formation with white appearance (Figure 8.30 e and f).
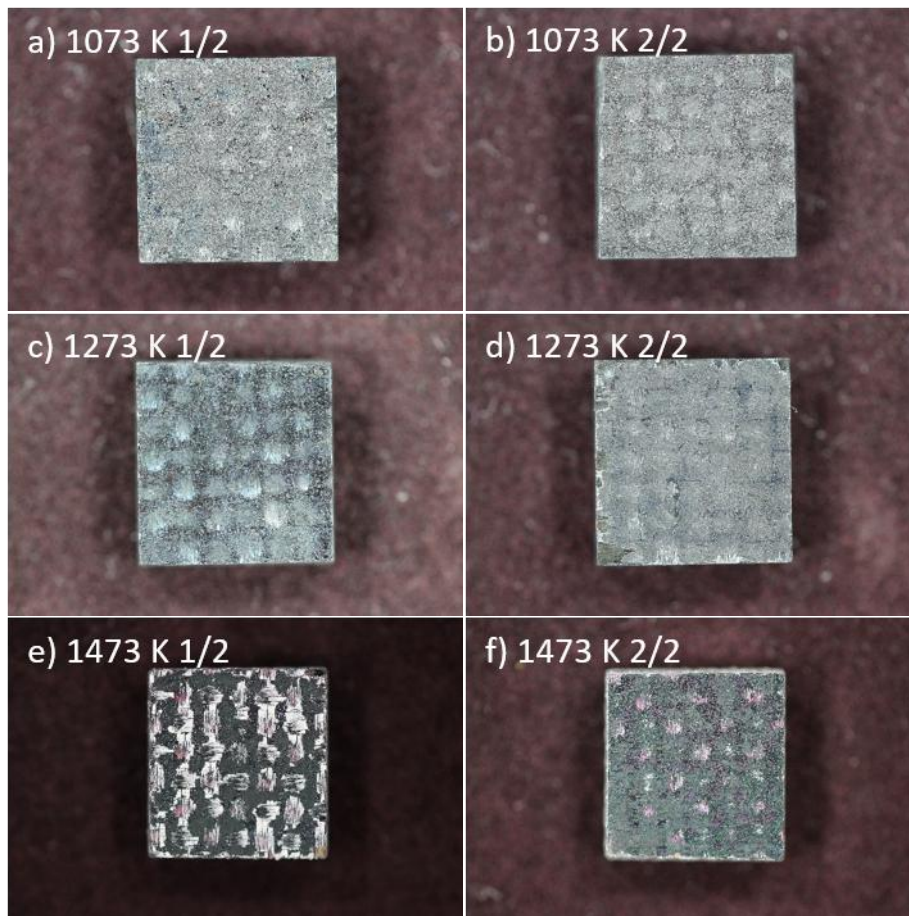
Figure 8.30: ZrB$_2$-SiC/Si-C-N composites after isothermal oxidation at a), b) 1073 K, c), d) 1273 K and e), f) 1473 K in O$_2$/N$_2$/Ar-atmosphere (p$_{O2}$ = 0.14 bar) for 100 h. Both sample sides are shown. The edge length of the samples corresponds to 10 mm.

The mass changes of the ZrB$_2$-SiC/Si-C-N composites during oxidation are depicted in Figure 8.31 (solid lines). Oxidation at 1073 K resulted in the highest mass gain of 9.0 mg/cm^2. Whereas a mass gain of 3.2 mg/cm^2 and 2.9 mg/cm^2 was detected after oxidation at 1273 K and 1473 K, respectively. Results for oxidation of ZrB$_2$-free SiC/Si-C-N composites (Section 8.2) under the same conditions are shown for comparison with dashed lines. Oxidation of the SiC/Si-C-N composite at 1473 K results in a mass gain of 2.2 mg/cm^2, which is lower compared to the ZrB$_2$-SiC/Si-C-N composite. At 1073 K, the ZrB$_2$-free composite shows even an overall mass loss of -1.8 mg/cm^2 whereas the ZrB$_2$-containing composite exhibited the highest mass gain.
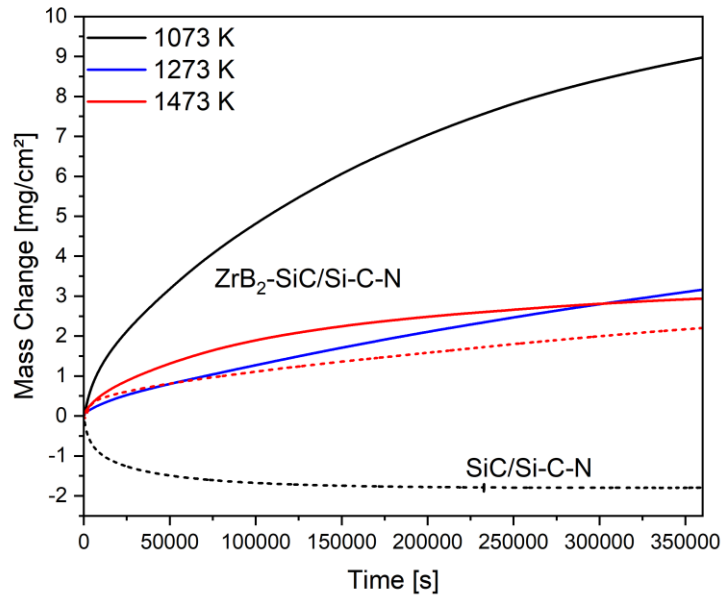
Figure 8.31: Measured mass change during oxidation of ZrB$_2$-SiC/Si-C-N composites at 1073 K, 1273 K and 1473 K in O$_2$/N$_2$/Ar-atmosphere (p$_{O2}$ = 0.14 bar) for 100 h. Data of SiC/Si-C-N composites (dashed lines, see Section 8.2) are shown for comparison.

Prototypic combustion atmosphere p$_{H2O}$=0.05 bar, p$_{O2}$=0.13 bar, p$_{CO2}$=0.05 bar, p$_{N2}$=0.77 bar

Oxidation tests with ZrB$_2$-SiC/Si-C-N composites were performed in prototypic combustion atmosphere. To this end a especially manufactured O$_2$/N$_2$/CO$_2$-gas mixture was mixed with steam prior to introducing it into the STA. (see details in Section 3.2).

Figure 8.32 depicts ZrB$_2$-SiC/Si-C-N composites after oxidation at 1073 K, 1273 K and 1473 K, respectively. With increasing temperature, the ZrB$_2$-SiC/Si-C-N composites exhibit a more pronounced oxide scale formation of whitish appearance. At the highest temperature of 1473 K, even detaching of small oxide flakes were observed. The more pronounced scale formation at one side of the sample was typical for the investigated ZrB$_2$-SiC/Si-C-N composite samples resulting from the preparation.
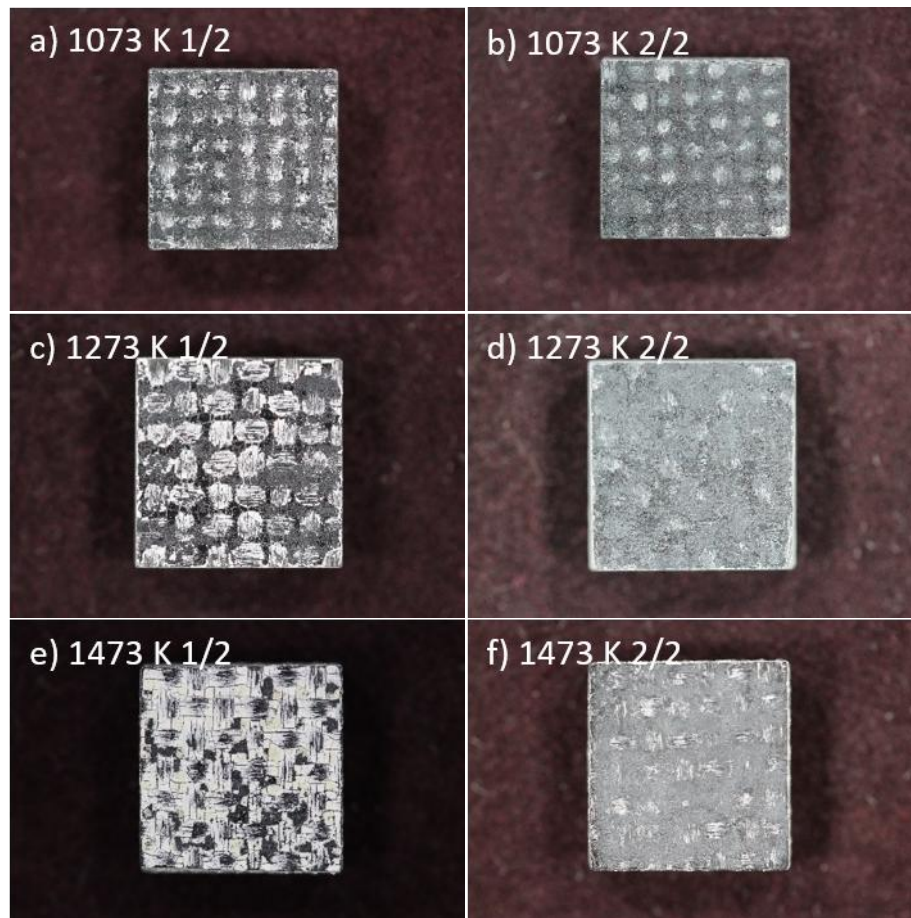
Figure 8.32: ZrB₂-SiC/Si-C-N composites after isothermal oxidation at a), b) 1073 K, c), d) 1273 K and e), f) 1473 K in prototypic combustion atmosphere for 100 h. Both sample sides are shown. The edge length of the samples corresponds to 10 mm.

Figure 8.33 shows the measured mass change of ZrB₂-SiC/Si-C-N composites during oxidation in prototypic combustion atmosphere. Results for the oxidation of ZrB₂-free SiC/Si-C-N composite (dashed lines, Section 8.2, Figure 8.12) are shown for comparison. Upon oxidation, the ZrB₂-SiC/Si-C-N composite exhibits the highest mass gain of 16.2 mg/cm² at a temperature of 1073 K. With increasing temperature, the total mass gain is decreasing to 5.5 mg/cm² and 3.3 mg/cm² at 1273 K and 1473 K, respectively. The ZrB₂-free SiC/Si-C-N composite shows a similar mass gain compared to the ZrB₂-SiC/Si-C-N composite upon oxidation at 1273 K and 1473 K. However, the oxidation behavior at 1073 K is very different. The ZrB₂-free SiC/Si-C-N composite shows even an initial mass loss and by far the lowest mass gain compared to oxidation at higher temperatures.
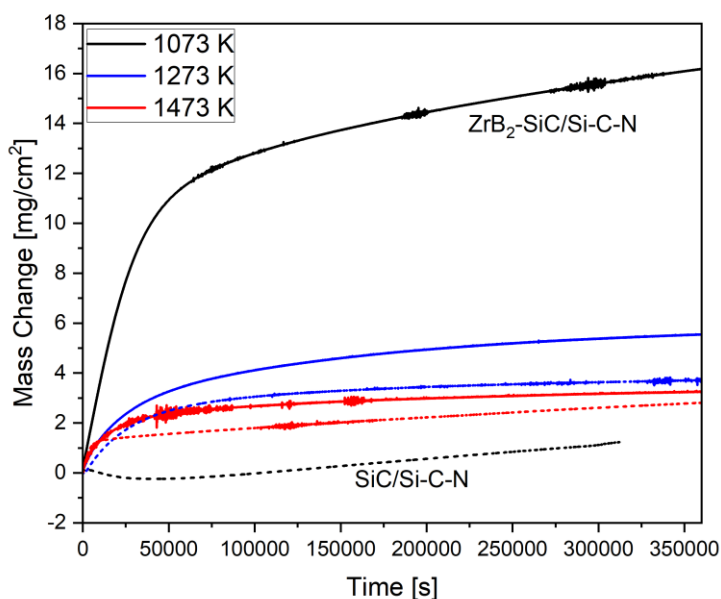
Figure 8.33: Measured mass change during oxidation of ZrB$_2$ZrB$_2$-SiC/Si-C-N composites at 1073 K, 1273 K and 1473 K in prototypic combustion atmosphere for 100 h. Data of SiC/Si-C-N composites (dashed lines, see Section 8.2) are shown for comparison.

Oxidation kinetics

Figure 8.34 shows an Arrhenius-type plot of mass change rates of the ZrB$_2$-SiC/Si-C-N composite in various atmospheres. Data points were calculated from the total mass change after 100 h of isothermal oxidation.

A number of effects superimpose the measured mass changes at the same time. Oxidation of different constituents of the CMC results in opposing effects on the overall mass change. Formation of condensed oxides (SiO$_2$, ZrO$_2$, ZrSiO$_4$) results in a mass gain. At the same time formation of gaseous CO or CO$_2$ by oxidation of free carbon, volatilization of silica or boria by formation silicon- or boron-containing gas species and direct evaporation yields a mass loss. In addition, at temperatures above 1757 K, carbothermal decomposition of the Ceraset$^®$ PSZ 20-derived ceramic Si-C-N matrix leads to a mass loss (see Section 5.1). Furthermore the investigated ZrB$_2$-SiC/Si-C-N CMC samples have an open porosity providing access for the oxidizing atmosphere. Therefore, the effective surface of the samples is larger than the geometrical surface. Upon proceeding exposure to the O$_2$- or H$_2$O-containing atmospheres, the size of the effective surface probably changes by blocking of pores with condensed oxidation products or volatilization. This makes a kinetic evaluation of the ZrB$_2$-SiC/Si-C-N oxidation difficult. The indicated mass change rate is therefore intended to visualize and summarize the results and may therefore differ for different stages of exposure.

The highest mass change rates were obtained in H_2O-containing atmospheres. Within the applied H_2O-containing atmospheres, the H_2O/Ar mixture (p_{H2O} = 0.2 bar) resulted in higher rates compared to the prototypic combustion atmosphere (p_{H2O} = 0.05 bar and p_{O2} = 0.13 bar). Atmospheres with O_2 as the major oxidant, O_2/Ar (p_{O2} = 0.2 bar) and O_2/N_2/Ar (p_{O2} = 0.14 bar), result in similar values. With increasing temperature, obtained mass change rates are decreasing.
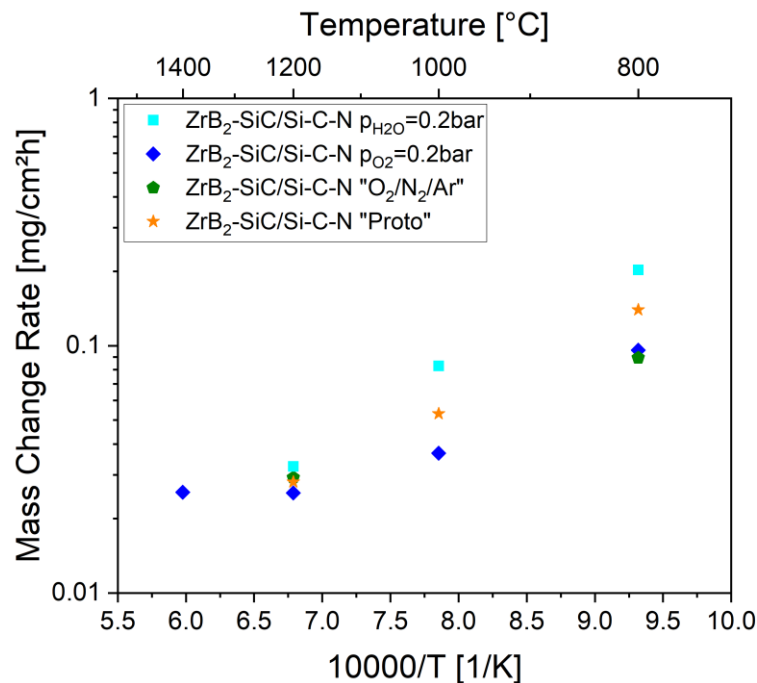
Figure 8.34: Arrhenius plot of the total mass change rate during isothermal oxidation of ZrB₂-SiC/Si-C-N composites in various O_2- and H_2O-containing atmospheres for 100 h.

Since the kinetics of the numerous superimposing effects cannot be separated, even with more sophisticated models, the measured thermogravimetric data were fitted according to the simple equation (1.1) ($\Delta w/A = k \cdot t^n$). The obtained rate constant k and exponent n are depicted in Figure 8.35a and b, respectively. The obtained rate constant k has only an illustrative character *since n* is not constant over the investigated temperature range. Therefore, no activation energies were determined. In H_2O-containing atmosphere the rate constant k is higher than in O_2-containing atmosphere and shows no pronounced temperature dependence. In O_2-containing atmosphere k-values increase with increasing temperature.

The obtained exponent n (see also Figure 8.13) is indicating the nature of the effective oxidation kinetics. For 100 h oxidation of ZrB₂-SiC/Si-C-N in H_2O-containing atmosphere n is in the subparabolic or cubic range and hardly temperature dependent. The very initial stage of oxidation shown in the 5 h experiments, on the other hand, shows linear kinetics at 1073 K shifting to parabolic (TG-derived) or cubic (MS-derived) kinetics at 1473 K. In particular n-values of ZrB₂-SiC/Si-C-N derived from the measured H_2-release correspond to oxidation of pure ZrB₂. This is indicating that in the initial stage ZrB₂-SiC/Si-C-N oxidation is given by the ZrB₂-additive. In

O$_2$-containing atmosphere, n shows a strong temperature dependence. At 1273 K, n indicates sublinear oxidation kinetics shifting to subparabolic and subcubic kinetics at 1473 K and 1673 K, respectively. At the lowest investigated temperature of 1073 K, however, n deviates from this trend indicating parabolic oxidation kinetics.
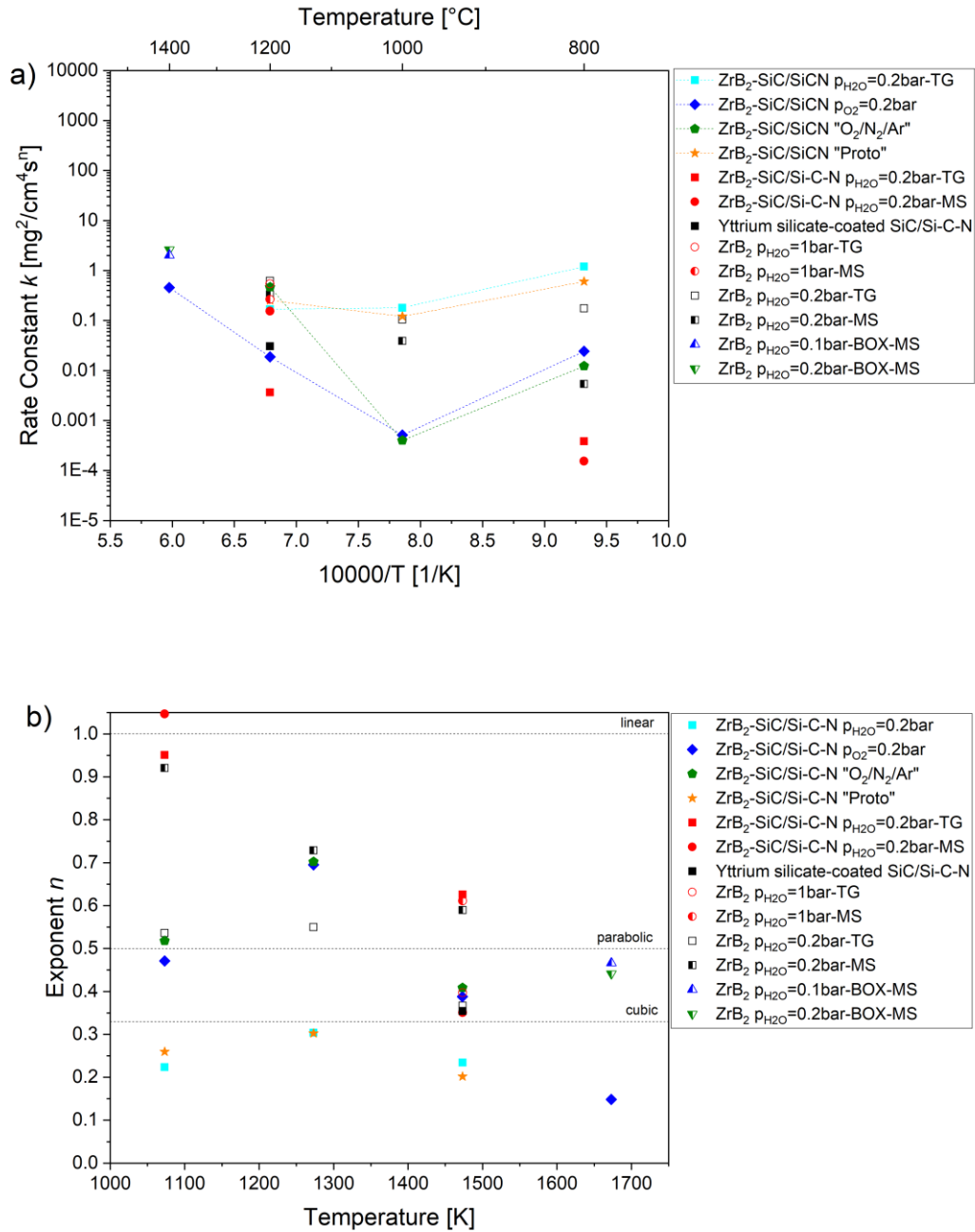
Figure 8.35: Derived a) rate constant and b) reaction order for the oxidation of a ZrB$_2$-SiC/Si-C-N composite in various O$_2$- and H$_2$O-containing atmospheres. Reaction orders for linear, parabolic and cubic oxidations kinetics are indicated. Results for oxidation of ZrB$_2$ (open symbols; see Section 7) are shown for comparison.

8.4.   Oxidation of SiC/Si-C-N under oxygen-starvation conditions

Figure 8.36a shows a SiC/Si-C-N composite which was exposed to 1773 K for 10 h in flowing Ar (100 ml/min). The composite has a matt white appearance. The end face of SiC-fibers, which are exposed at the cutting edges (Figure 8.36b) are partly hollow in the center. SiC-fibers, which are exposed at the topside of the composite, moreover show pitting (see Figure 8.36c and d). The surface of the composite (Figure 8.36e) exhibits an open porous structure, which is responsible for the matt white appearance. The EDX-analysis (Figure 8.36f) reveals, that the surface is mainly composed of silicon and carbon with only minor amounts of oxygen.

The oxygen and steam content in the Ar used (99.9999% purity) is specified as ≤ 0.5 ppm. However, due to connections in the gas supply up to the actual sample position, it could also be slightly higher. Holes in the SiC-fibers are resulting from active oxidation. At low oxygen partial pressures, only gaseous SiO_x species are formed instead of a protective SiO_2 scale. Therefore, the amount of oxygen on the surface of the SiC/Si-C-N composite, which is found in the EDX-analysis, is very small. The volatilization of the SiC-based composite is resulting in the observed material loss. The observed pitting by formation of holes in the fibers is most likely a local geometrical effect for instance initiated by pores (see Figure 8.2) or free carbon in the center of the Tyranno SA3 SiC-fiber. The hollow fiber end faces, depicted in Figure 8.36b, are therefore resulting from the higher surface of the porous fiber center. Active oxidation was also observed for the oxidation of SiC/SiC-composites under oxygen- or steam-starvation conditions at high temperatures were active oxidation of the material occurred [185]. According to Heuer and Lou [159] detectable weight loss occurs at $p_{SiO} > 10^{-8}$ bar. This corresponds to calculated partial pressures in Section 8.1, Figure 8.5.

Gaseous SiO_x species were condensating in colder parts of the furnace outsets in form of solid SiO_x fibers. These partially blocked the furnace outlet and led to a pressure increase and thus to a drift of the thermogravimetric signal. Therefore, the mass loss was not evaluated although this experiment was carried out in a STA. Furthermore, the mass loss by the carbothermic reaction of the matrix (see also Section 5.1.1, Figure 5.6) is superimposing the mass loss by active oxidation at the considered temperature of 1773 K. These effects cannot be separated.
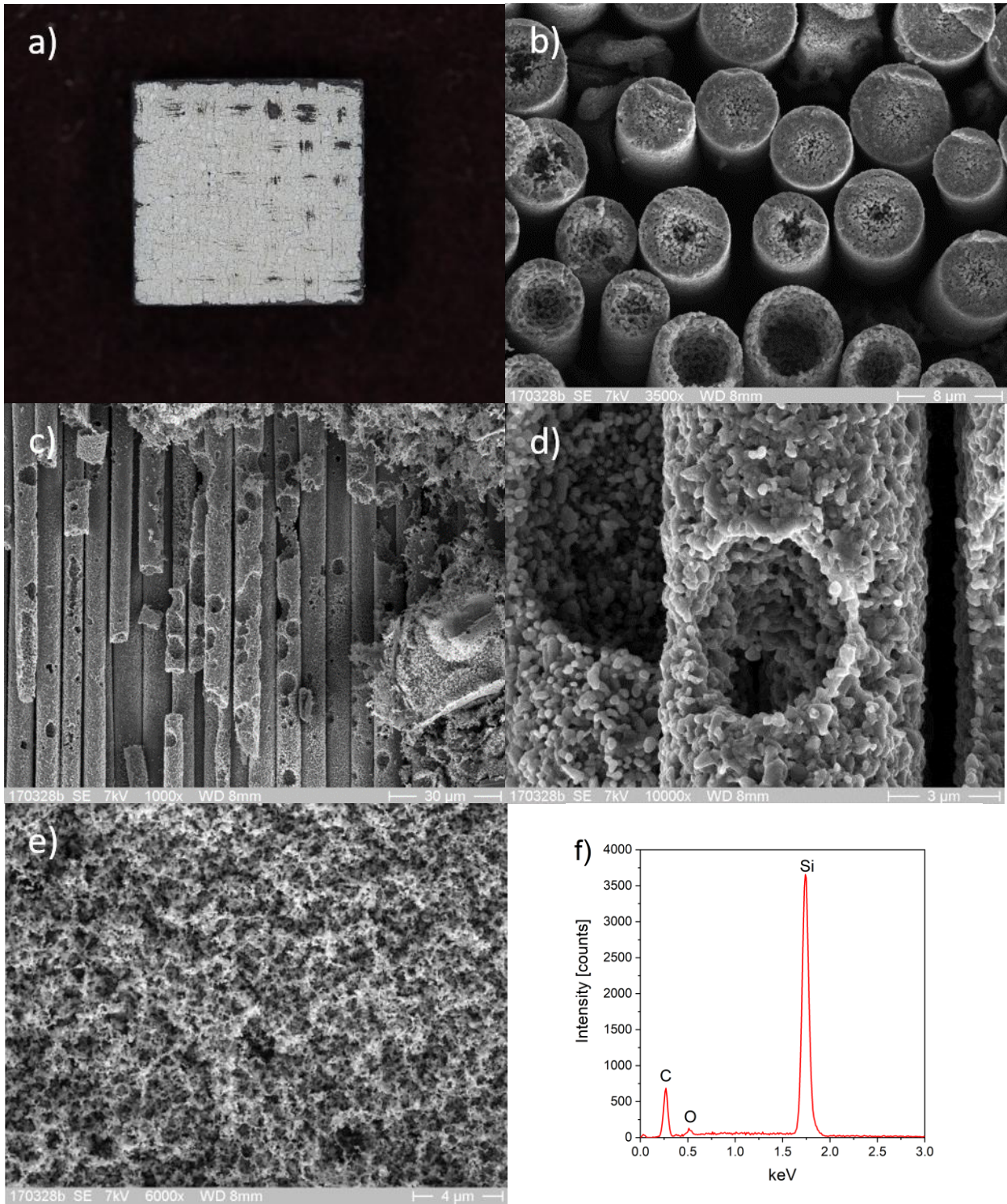
Figure 8.36: SiC/Si-C-N composite after exposure to flowing Ar for 10 h at 1773 K; a) overview (side length 10 mm); SEM micrographs of b) SiC-fibers at the cutting edge of the sample, c) SiC-fibers at the top-view of the sample, d) close-up of c), e) top-view of the SiC/SiCN sample and f) EDX analysis of e). Scale bars correspond to b) 8µm, c) 30 µm, d) 3 µm and e) 4 µm.

8.5.   Yttrium silicate-based environmental barrier coatings

A sample of the SiC/Si-C-N CMC was completely plasma spray coated with an yttrium silicate-based EBC at the German Aerospace Center. The composition of the yttrium silicate based coating is in the two-phase field $Y_2SiO_5+Y_2Si_2O_7$.

The mass change during oxidation of a yttrium silicate-coated SiC/Si-C-N CMC in prototypic combustion atmosphere is depicted in Figure 8.37 together with results of a bare SiC/Si-C-N and a ZrB₂-containing SiC/Si-C-N CMC. The coated CMC shows a slower mass increase during the initial phase of oxidation compared to the uncoated samples. Possibly because the oxidizing gas species must diffuse through the yttrium silicate coating. However, as oxidation proceeds, a steady state is reached and the coated and the bare CMC show the same mass increase. The ZrB₂-SiC/Si-C-N CMC exhibits the highest mass gain in prototypic combustion atmosphere as ZrB₂ is very prone to oxidation. As oxidation proceeds, the mass increase flattens out.

In order to effectively protect the underlying CMC, the EBC must be gas-tight. Yttrium silicate layers alone cannot provide this condition due to its porous microstructure and residual oxygen conductivity [186]. Full protection could be achieved by using a multilayer coating with for example SiC or Si as a bondcoating. A pure Si coating would limit the maximum application temperature to the melting point of 1687 K.
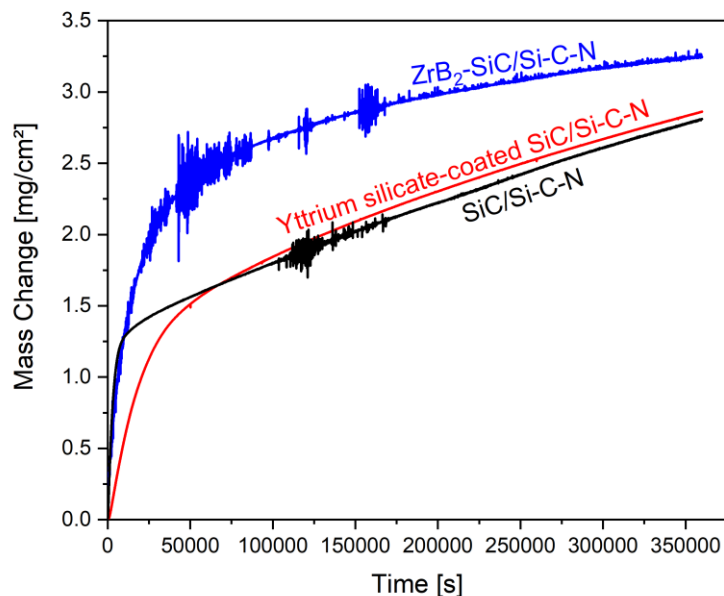
Figure 8.37: Measured mass change of SiC/Si-C-N, ZrB₂-SiC/Si-C-N and YMS/YDS-coated SiC/Si-C-N during isothermal oxidation at 1473 K in prototypic combustion atmosphere for 100 h.

8.6.   Discussion

ZrB$_2$ is considered as an ultra high temperature ceramic (UHTC) with potential application in extreme environments [155]. In addition, ZrB$_2$ is one of the most oxidation resistant transition metal diborides [154][153] (see also Section 7). An improved oxidation resistance is also reported for ZrB$_2$-SiC [46], ZrB$_2$-MeSi$_2$ (Me= Zr, Ta, Cr, Mo, W) [157][158] and boron-containing precursor-derived Si-B-C-N ceramics [20][187][188]. The use of a ZrB$_2$-additive is therefore supposed to improve the oxidation resistance of the SiC/Si-C-N CMC.

Thermodynamic calculations in the framework of this work (see Section 6) were used to investigate the interaction between the ZrB$_2$-additive and the equilibrium components (SiC, C, Si$_3$N$_4$) of the ceramic Si-C-N matrix. The first reaction to occur was found at 1870 K between ZrB$_2$ and Si$_3$N$_4$, under formation of a melt. However, this reaction takes place 113 K above the carbothermic reaction of the PSZ 20-derived Si-C-N matrix (see Section 5.1). Therefore, the use of the ZrB$_2$-additive does not further limit the maximum application temperature of the ZrB$_2$-SiC/Si-C-N-composite. In the present Section, additionally interactions between the ZrB$_2$-additive and constituents of the ceramic Si-C-N matrix (SiC, C, Si$_3$N$_4$) were considered under oxidizing conditions. There are partly complex and multi-stage reactions between the oxidation products of ZrB$_2$ (B$_2$O$_3$ and ZrO$_2$) and the Si-based CMC (Si$_2$N$_2$O, SiO$_2$). A very low eutectic temperature is known in the system SiO$_2$-B$_2$O$_3$ (T$_E$ = 713 K) [44]. The liquid B$_2$O$_3$ partly dissolves other elements (see also Section 6.2). Moreover, the formation of ZrSiO$_4$ from ZrO$_2$ and SiO$_2$ was confirmed by XRD and EDX analysis. Steinbrück et al. [72] found also crystalline B$_2$O$_3$ after oxidation of B$_4$C in steam by XRD. However, B$_2$O$_3$ is the only condensed oxidation product of B$_4$C. Moreover, the boron content of the ZrB$_2$-SiC/Si-C-N is low in comparison. In accordance with experimental literature data [188][189], the only condensed oxidation product found by XRD after oxidation of the ZrB$_2$-free SiC/Si-C-N CMC was β-cristobalite. Si$_2$N$_2$O was not detected as the very narrow calculated stability range (see Section 8.1, Figure 8.3) indicated. However, unlike the test under oxygen starvation conditions, all O$_2$- and H$_2$O-containing atmospheres and investigated temperatures resulted in formation of condensed oxides.

Transient tests of ZrB$_2$-SiC/Si-C-N oxidation in O$_2$-containing atmosphere (p$_{O2}$ = 0.2 bar) initially show the release of gaseous oxidation products (CO and CO$_2$) in conjunction with a mass loss at about 850 K. This indicated initially preferential oxidation of carbon from the composite. With increasing temperature, mass gain from about 950 K is indicating passivation by formation of condensed oxidation products. The simultaneous release of N$_2$ indicated the contribution of the nitrogen-containing ceramic Si-C-N matrix. Bahloul et al. observed beginning oxidation of Si-C-N in oxygen, with a weight loss by preferential combustion of free carbon, at a similar temperature of 923 K before degradation of siliconcarbonitride starting at higher temperatures [189].

Heating of ZrB$_2$-SiC/Si-C-N in H$_2$O-containing atmosphere (p$_{H2O}$ = 0.2 bar) resulted in oxidation from the start at 673 K. The oxidation reaction was indicated by both H$_2$-release and mass gain. The latter demonstrates passivation by formation of condensed oxidation products. This shows the higher oxidation potential of steam compared to oxygen. The maximum mass gain rate of ZrB$_2$-SiC/Si-C-N at 1000 K corresponds approximately to pure ZrB$_2$. Butchereit and Nickel [188] report the onset of oxidation for Si-B-C-N and Si-C-N in flowing dry oxygen at higher temperatures of 1173-1273 K and 1373 K, respectively. However, no heating rate was reported. Possibly our more sensitive test set-up combining TG and MS in combination with the open-pored samples yields lower start temperatures for oxidation.

Isothermal oxidation of ZrB$_2$-SiC/Si-C-N in both O$_2$- and H$_2$O-containing atmosphere shows the highest mass gain at the lowest investigated temperature of 1073 K. In H$_2$O/Ar atmosphere (p$_{H2O}$ = 0.2 bar) even a pronounced swelling of the CMC occurs perpendicular to the SiC-fabric planes. The overall mass gain is higher in H$_2$O-containing atmosphere for both the SiC/Si-C-N and the ZrB$_2$-SiC/Si-C-N composite. With increasing temperature, the total mass gain of the ZrB$_2$-SiC/Si-C-N CMC decreases. An exception is the oxidation at 1673 K in O$_2$/Ar (p$_{O2}$ = 0.2 bar). Here the mass gain is very high at the beginning of oxidation, but drops to the level at 1273 K or 1473 K. This is in accordance with literature. Butchereit and Nickel [188] found a two-fold increase in mass gain and oxide scale thickness for precursor-derived Si-C-N ceramics in moist (20 mol% H$_2$O) compared to dry oxygen atmosphere. However, precursor-derived Si-B-C-N ceramics did not differ significantly under both conditions, indicating a large influence of volatilization processes.

Oxidation of ZrB$_2$-free SiC/Si-C-N shows a different temperature-dependence. At the lowest investigated temperature of 1073 K, SiC/Si-C-N even shows an overall mass loss in both O$_2$- and H$_2$O-containing atmosphere. In O$_2$-containing atmosphere the initial mass change is even negative up to 1373 K. Mass spectroscopic detection of CO and CO$_2$ indicates that primarily carbon is oxidized at low temperatures resulting in a mass loss. At the same time formation kinetics of SiO$_2$ is too slow at these temperatures to form a passivating scale. With increasing temperature, the mass change predominantly increases. Even if this is not the case for the total mass change in individual cases, at least the initial mass change rate increases with temperature. For example, the test at 1773 K is above the carbothermic decomposition temperature of the ceramic Si-C-N matrix (see Section 5.1). Nevertheless, the initial mass gain seems to be a good indication of the oxidation itself. The later mass loss is then a result of the decomposition reaction of the ceramic matrix. The machined CMC samples exhibit open channels at the cutting edges. Additionally, the ceramic Si-C-N matrix has a residual open porosity resulting from the shrinkage of the preceramic polymer during pyrolysis. Both provides access for the oxidizing atmosphere. Only upon oxidation of the ZrB$_2$-free SiC/Si-C-N above 1273 K, these channels are effectively sealed by the formed oxide (see Figure 8.38).
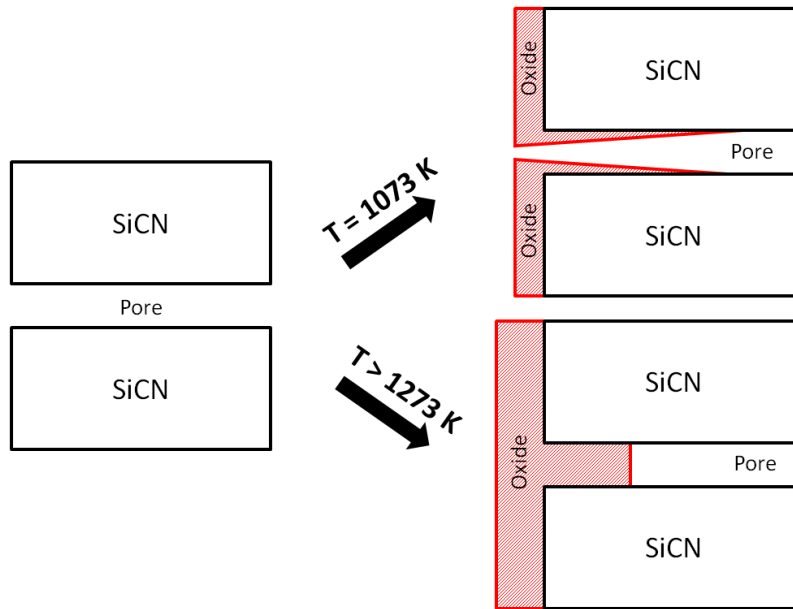
Figure 8.38: Schematic illustration of the oxide formation on porous SiC/Si-C-N CMC.

The mass change is always a superimposition of mass increase by passive oxidation and mass loss by volatilization of gas species, resulting in overall paralinear kinetics. Investigations based on thermogravimetry alone do not necessarily reflect the true oxidation behavior. Mass spectrometric investigations of the gas atmosphere provide deeper insight into the oxidation and volatilization reactions of ZrB$_2$-SiC/Si-C-N. Mass spectrometric analysis of pure ZrB$_2$-specimen revealed that boron-containing gas species are formed upon oxidation in steam (see Section 7.3). Due to the lower ZrB$_2$-content of ZrB$_2$-SiC/Si-C-N samples, the associated H$_3$BO$_3^+$-signal was very low under the same conditions and barely suited to follow the volatilization of boria. However, boria is highly volatile as thermodynamic calculations for pure ZrB$_2$ (see Section 7.1) have shown. As a result, boron was no longer detectable in the formed oxide scale by EDX even after only 1 h in O$_2$/Ar-atmosphere, although partial pressure of the boron-containing gas species and thus the volatilization rates are significantly lower in oxygen- than in steam-containing atmosphere. Thermodynamic calculations of the boron-containing gas species in Section 7.1 reveal partial pressures as high as ~10^{-4} bar for gaseous BO$_2$ and B$_2$O$_3$ under these conditions. Parthasarathy et al. [173] state that gaseous B$_2$O$_3$ exhibits even 1 atm partial pressure at 2223 K in p$_{O2}$ = 0.2 bar. Additions of niobium to pure ZrB$_2$ [190] and ZrB$_2$-SiC [191] were found to improve the stability of the liquid B$_2$O$_3$ layer against volatilization. For the latter, vanadium addition performed even better. However, bubbles formed on the surface of ZrB$_2$-SiC/Si-C-N samples demonstrated the presence of a liquid borosilicate scale at an initial stage of oxidation. The observation is consistent with the work of Butchereit and Nickel observing bubble formation upon oxidation of precursor-derived Si-B-C-N ceramics at temperatures from 1373 K [188]. In the present work, bubbles are even present after oxidation at 1073 K, well above the eutectic temperature in the SiO$_2$-B$_2$O$_3$ system (T$_E$ = 713 K) [44]. The observed melt-formation in accordance with the mass gain of the ZrB$_2$-SiC/Si-C-N CMC even at 1073 K is

contrary to the behavior of ZrB$_2$-free CMC. This demonstrates the passivation potential of the ZrB$_2$-additive even at low temperatures. In addition, the low surface free energy of boria (0.08 J/m²) compared to zirconia (1 J/m²) provides a driving force to cover the surface [47].

The transient tests demonstrated that the mass gain of ZrB$_2$-SiC/Si-C-N in steam-containing atmosphere is stagnating at temperatures higher than 1200 K, although the increasing H$_2$-release is indicating an acceleration of the oxidation reaction. This clearly indicates that volatilization reactions, generating a mass loss, are counteracting the mass gain by oxidation. Also the temperature corresponds well to the mass loss observed upon oxidation of ZrB$_2$ in steam-containing atmosphere (see Section 7.3, Figure 7.8). Due to a lower ZrB$_2$-content, the measured H$_3$BO$_3$-signal (m/z=62) indicating the volatilization of the boron oxide is significantly lower compared to oxidation of pure ZrB$_2$ samples under the same conditions (see Section 7.3).

Recession of Si-based materials by formation of volatile Si-OH species in steam-containing combustion atmosphere is known from literature [25][37][26][35]. Thermodynamic descriptions of the most important gas species Si(OH)$_4$ and SiO(OH)$_2$ were optimized by Avincola et al. [36]. Calculated partial pressures of Si-containing gas species (Figure 8.6) are several orders of magnitude lower compared to B-containing gas species (Figure 7.3) in O$_2$- as well as H$_2$O-containing atmosphere. Therefore, SiO$_2$-volatilization plays a negligible role compared to B$_2$O$_3$-volatilization under the conditions (time, temperature, flow rates and pressures) investigated in this work.

Quantitative analysis of H$_2$, as side product of the oxidation of ZrB$_2$-SiC/Si-C-N in steam, enables the separation of the oxidation- and volatilization reaction. This allows true insight into the oxidation kinetics. Figure 8.19 shows the mass change determined by thermogravimetry and calculated from the measured H$_2$-release, respectively. At 1073 K, the total mass change corresponds to the mass increase by the oxidation reaction alone. As a result ZrB$_2$-SiC/Si-C-N follows linear oxidation kinetics in both techniques. However at 1473 K, the mass change measured by thermogravimetry is significantly lower compared to the true oxidation reaction alone. The pronounced volatilization reaction at this temperature reduced the thermogravimetric measured mass change. Also oxidation kinetics determined from thermogravimetry appear parabolic. But H$_2$-release reveals actually cubic oxidation kinetics at 1473 K. The initial peak in the H$_2$-signal at beginning oxidation reaction is known for porous samples indicating a larger true surface of the sample [72][179]. As oxidation proceeds, pores are closed and the true oxidation behavior is exposed. The early H$_2$-signal during heating of the samples in pure Ar may indicate that adsorbed water has been released. The oxidation rate of ZrB$_2$-SiC/Si-C-N is up to four orders of magnitude lower than for pure ZrB$_2$ samples (Section 7.3). It is known from literature that the addition of a secondary silicon-containing phase improves the oxidation behavior of ZrB$_2$ [157], especially at higher temperatures where the stability and oxygen permeability of SiO$_2$ is lower compared to B$_2$O$_3$. However, McFarland et al. also found

that borosilicate glass can accelerate oxidation of SiC in oxygen at 1073 K and very high boria contents (>92 mol%) [192]. In ZrB$_2$-SiC/Si-C-N this effect should be small and limited to certain areas due to the small ZrB$_2$ fraction and consumption of the boron-resources by volatilization. Initial acceleration could even help to grow a protective silica scale at lower temperatures were silica formation kinetics are otherwise slow.

For complete oxidation protection during operation in combustion atmosphere an additional environmental coating (EBC) is required. The test with a yttriumsilicate-based EBC (see Section 8.5) shows that gas-tight coating is critical. Possible problems are cracking induced by thermal cycling or phase transitions or diffusion of oxidizing species along grain boundaries or coating defects. A multilayer coating with Si or SiC as bond coating, for example, could behave better in this respect. Here again chemical compatibility with the CMC and the EBC would be important. In this respect, the use of Si is uncritical. However, the maximum application temperature is limited by the melting point to $T_{m,Si} = 1687$ K. When using SiC, the application is limited by the formation of a CO partial pressure at the interface to the EBC [24] which can exceed atmospheric pressure at 1903 K [193].

8.7.   Conclusion

Oxidation tests of ZrB$_2$-containing and ZrB$_2$-free SiC/Si-C-N CMC were performed in O$_2$- and H$_2$O-containing atmospheres. Microstructure investigations have shown that oxidation of the exposed ZrB$_2$-additive together with the ceramic Si-C-N matrix is forming a borosilicate liquid phase. Thereby, exposed open cavities in the CMC are filled by the melt representing a self-healing effect.

At low temperatures, SiO$_2$ formation kinetics of the SiC/Si-C-N composite are too slow to form a passivating scale and free carbon is oxidized. For the ZrB$_2$-containing CMC the oxidation behavior is dominated by the ZrB$_2$-additive. At high temperatures, high partial pressures of boron-containing gas species in both O$_2$- and H$_2$O-containing atmospheres lead to volatilization of boron from the borosilicate melt. This means that boron would be consumed quickly at a damage site, but the solidifying melt leaves behind SiO$_2$. The possibility of separating oxidation and volatilization effects by combined use of thermogravimetry and mass spectrometry was demonstrated. It was shown that, especially at high temperatures, the sole consideration of the mass change provides false indications due to opposing effects.

In contrast to the intended use for closing cracks, for example caused by thermal cycling during operation, the ZrB$_2$-additive is exposed in the investigated CMC. The exposed ZrB$_2$-rich layers provide access for the oxidizing atmosphere. However, the present samples and experiments demonstrate the principle of improving the oxidation resistance of the CMC by formation of a melt. As a result inwards-diffusion of oxidizing gas species is stopped or slowed down. Therefore, the ZrB$_2$-additive is able to improve the oxidation resistance of the SiC/Si-C-N composite.

For ideal oxidation protection, the CMC would have to be as dense as possible, i.e. low and preferably closed residual porosity of the ceramic matrix to avoid exposed SiC-fibers and ZrB$_2$-additive. An applied environmental barrier coating must also be gas-tight to be able to protect the underlying CMC from the combustion atmosphere.

9. Zusammenfassung (Extended Abstract in German)

Durch das Einbetten von keramischen Fasern in eine ebenfalls keramische Matrix wird ein, im Gegensatz zu monolithischen Keramiken, quasi-plastisches nicht-sprödes Versagensverhalten erreicht. Zudem verfügen nicht-oxidische Si-basierte keramische Faserverbundwerkstoffe (Ceramic Matrix Composites, CMC) über eine hervorragende Hochtemperaturbeständigkeit und Zugfestigkeit. CMC finden daher zunehmend technischen Einzug in die Raumfahrt sowie in die Entwicklung von Turbinen für die Luftfahrt und zur stationären Energieerzeugung. Ihr Einsatz in Turbinen erlaubt daher eine Erhöhung der Verbrennungstemperatur und damit eine Verbesserung der Energieeffizienz gegenüber konventionellen metallischen Werkstoffen. Zudem ist die potentielle Gewichtsersparnis durch eine, im Vergleich zu konventionellen Nickel-Basislegierungen, um zwei Drittel niedrigere Dichte attraktiv für die Luftfahrt. Die extremen Bedingungen im Heißgaspfad, wie hohe Temperaturen und die oxidierende und korrosive Heißgasatmosphäre, stellen jedoch hohe Anforderungen an das CMC. Neben der individuellen Hochtemperaturstabilität der Komponenten (Faser, Faserbeschichtung, Matrix, Additive) können Wechselwirkungen untereinander die maximale Einsatztemperatur des CMC limitieren. Zudem erfordert die oxidierende und korrosive Heißgasatmosphäre einen umfassenden Oxidationsschutz des CMC.

In der vorliegenden Arbeit wurden CMC für den Einsatz als Strukturmaterial im Heißgaspfad von Gas- oder Flugturbinen untersucht. Dazu wurden thermodynamische Gleichgewichtsrechnungen mit Materialtests bei hohen Temperaturen und unter prototypischen Einsatzbedingungen kombiniert. Die CALPHAD-Methode (CALculation of PHAse Diagrams) erlaubte die thermodynamische Berechnung von Gleichgewichtszuständen wie Phasengleichgewichten sowie deren Zusammensetzung. Dies ermöglichte die Aufklärung von Reaktionen, die während der Pyrolyse von präkeramischen Polymeren ablaufen oder die Langzeitstabilität der erhaltenen Si-(B-)C-N Keramik limitieren, die zwischen Komponenten des CMC stattfinden oder deren Oxidations- und Volatilisationsverhaltens unter prototypischen Heißgasbedingungen begrenzen. Simultane Thermoanalyse (STA) bestehend aus Thermogravimetrie (TG) und Differenz-Thermoanalyse (DTA), in Kombination mit einer massenspektrometrischen Analyse der gasförmigen Pyrolyse-, Reaktions- und Oxidationsprodukte, erlaubten die experimentelle Validierung der thermodynamischen Berechnungen bei gezielt eingestellter Zusammensetzung der Atmosphäre.

Phasengleichgewichte in Si-(B-)C-N Keramiken aus Präkursor-Polymeren
(Phase equilibria in precursor-derived Si-(B-)C-N ceramics)

Durch Pyrolyse der präkeramischen Polysilazane Ceraset$^®$ PSZ 10 und PSZ 20 sowie eines Polyborosilazans wurden Si-C-N und Si-B-C-N Keramiken hergestellt. Dazu wurden die präkeramischen Polymere, in fließender Ar- oder Ar/N$_2$-Atmosphäre, zunächst durch schrittweises Aufheizen auf 573 K vernetzt und anschließend bei Temperaturen von 1273 K bis 1773 K pyrolysiert. Durch eine Kombination aus STA, Massenspektroskopie (MS), Röntgendiffraktometrie (XRD) und Rasterelektronenmikroskopie (REM) wurden Pyrolyseverhalten, Hochtemperaturbeständigkeit, Zersetzungsreaktionen und Kristallisationsverhalten der Si-(B-)C-N Keramik sowie der Einfluss von Temperatur und Stickstoffpartialdruck untersucht. Außerdem wurde die CALPHAD Methode verwendet, um die Bildung gasförmiger Pyrolyse- und Zersetzungsprodukte vorauszusagen sowie Phasenstabilitäten als Funktion von Temperatur und Stickstoffpartialdruck zu berechnen.

Auf Basis der Zusammensetzung der flüssigen Polymere wurde deren Umwandlung in eine feste amorphe Keramik als geschlossenes System modelliert. Wasserstoff, der in der Polymerkette als Bestandteil der funktionellen Gruppen vorkommt, wurde in Form wasserstoffhaltiger Gasmoleküle freigesetzt. Die Art der Moleküle ist dabei abhängig vom Verhältnis der im Polymer vorkommenden Elemente Si:B:C:N:H. Für Ceraset$^®$ PSZ 10 und PSZ 20 ergaben sich daraus H$_2$ und CH$_4$ als Hauptbestandteil der Gasphase. Der Partialdruck anderer Gasspezies war sehr gering. Die Freisetzung dieser gasförmigen Pyrolyseprodukte wurde experimentell durch massenspektrometrische Analyse bestätigt. Zusammen mit STA-Untersuchungen wurde gezeigt, dass es sich bei der Pyrolyse um einen zweistufigen endothermen Prozess handelt. Die Zusammensetzung der Gasphase hat einen direkten Einfluss auf die Zusammensetzung der verbleibenden festen Keramik. Die Rechnungen wurden als geschlossenes System durchgeführt, bei dem die Gasphase im thermodynamischen Gleichgewicht mit der festen Phase bleibt. Bei der experimentell durchgeführten Pyrolyse wurden die gebildeten Gasspezies (H$_2$, CH$_4$) aber mit der fließenden Atmosphäre abgeführt, was zu einem etwas niedrigeren Kohlenstoffgehalt der erhaltenen Si-C-N Keramik führte. Dennoch stimmte die berechnete und die tatsächliche Zusammensetzung der erhaltenen Keramik gut überein. Diese befindet sich, für Temperaturen kleiner 1757 K, im thermodynamischen Gleichgewicht im Dreiphasengebiet SiC+C+Si$_3$N$_4$. Als niedermolekulare Fraktion des Ceraset$^®$ Polysilazans zeigte PSZ 10 während des anfänglichen Vernetzungsschrittes einen höheren Masseverlust als Ceraset$^®$ PSZ 20 durch Abdampfen von Oligomeren. Jedoch unterschieden sich die erhaltenen Keramiken nicht in ihrer Zusammensetzung.

Die Zusammensetzung der erhaltenen Si-C-N Keramik bestimmt ebenfalls deren Hochtemperaturstabilität. Die Kombination aus CALPHAD-Modellierung und Hochtemperatur-Experimenten ermöglichte die maximale Anwendungstemperatur und die zugrundeliegenden

Mechanismen für die aus Ceraset$^{®}$ PSZ 10 bzw. PSZ 20 hergestellten Si-C-N Keramiken zu bestimmen. Berechnete Phasenstabilitätsdiagramme zeigten, dass bei 1757 K die Reaktion von Kohlenstoff C mit Si_3N_4 unter Bildung von SiC und Freisetzung von N_2 stattfindet. Dies wurde durch kombinierte massenspektrometrische und thermogravimetrische Untersuchungen qualitativ und quantitativ bestätigt. Die Umwandlungstemperatur sinkt dabei mit fallendem Stickstoffpartialdruck. Sie wurde experimentell in Ar/N_2 (p_{N2}=0.5 bar) bei 1773 K und in reinem Ar bereits bei 1673 K gefunden. Dabei kristallisierte die ansonsten homogene und Röntgen-amorphe Si-C-N Matrix und wurde porös.

Es wurden ebenfalls thermodynamische Rechnungen und experimentelle Untersuchungen an Polyborosilazanen und daraus erhaltenen (borhaltigen) Si-B-C-N Keramiken durchgeführt. Aus der Literatur ist die Beständigkeit von Si-B-C-N Keramiken gegen die carbothermische Reaktion bis zu 2273 K bekannt. Aufgrund der Einkapselung der SiC und Si_3N_4 Körner durch eine sogenannte turbostratische BNC$_x$-Struktur kommt es zu einer erhöhten Widerstandsfähigkeit gegen Kristallisation und Degradation. In dieser Arbeit wurde die Pyrolyse eines Polyborosilazans mit der Zusammensetzung eines "*Si-B-C-N_2* präkeramischen Polymers" thermodynamisch modelliert. Außerdem wurde die Pyrolyse und die Hochtemperaturstabilität eines "*Si-B-C-N_1* Polyborosilazans" experimentell untersucht. Anhand der unterschiedlichen Zusammensetzung der *Si-B-C-N_2* und *Si-B-C-N_1* Keramiken wurden deren Hochtemperaturstabilität und die zugrundeliegenden Reaktionen thermodynamisch modelliert und diskutiert.

Thermodynamische Gleichgewichtsrechnungen auf Basis der Zusammensetzung des *Si-B-C-N_2* Polyborosilazans (SiBC$_3$N$_3$H$_{10}$)$_n$ ergaben, dass bei Temperaturen bis 1500 K die festen Phasen Si_3N_4, C und BN im Gleichgewicht mit der Gasphase vorliegen. Diese bestand, wie bei Ceraset$^{®}$ PSZ 10 und PSZ 20 hauptsächlich aus H_2 und CH_4. Zusätzlich vorkommendes N_2 (p_{N2}=0,06-0,12 bar) und NH_3 (p_{NH3}<4·10^{-4} bar) deuteten auf einen Stickstoffüberschuss des Polymers hin. Si- und B-haltige Gasspezies hatten lediglich einen sehr niedrigen Partialdruck (<10^{-8} bar). Bei der Pyrolyse des Polymers zur festen Si-B-C-N Keramik sank dadurch der C- und N-Gehalt während das Si:B-Verhältnis konstant blieb ((SiBC$_3$N$_3$H$_{10}$)$_n$→SiBC$_{1.4}$N$_{2.3}$). Im Gegensatz zu thermodynamischen Gleichgewichtsrechnung auf Basis der Zusammensetzung des Polymers (Si$_3$N$_4$+BN+C+SiC), enthielt das berechnete Phasengleichgewicht auf Basis der Zusammensetzung der Keramik kein SiC (Gas+Si$_3$N$_4$+BN+C). Die Zusammensetzung der *Si-B-C-N_2* Keramik (x(N) = 0,4035) befand sich sehr nah an der Phasengrenze zwischen Si$_3$N$_4$+C+SiC+BN (0,23 < x(N) < 0,41) und Si$_3$N$_4$+Gas+C+BN (x(N) > 0,41). Dadurch kann eine kleine Schwankung des Stickstoffgehalts des Präkursor-Polymers in einem der beiden Phasengleichgewichte resultieren.

Experimentelle STA- und MS-Untersuchungen wurden an einem *Si-B-C-N_1* Polyborosilazan Präkursor-Polymer durchgeführt. Der Masseverlust während des anfänglichen

Vernetzungsschrittes des *Si-B-C-N_1* Polyborosilazans war, trotz gleicher Temperaturführung, deutlich höher als bei Ceraset® PSZ 10 und PSZ 20 und verbunden mit einer ausgeprägten Freisetzung von H_2. Die dadurch gebildeten Bläschen waren auch noch in der erhaltenen Si-B-C-N Keramik enthalten. Dadurch war die keramische Ausbeute des *Si-B-C-N_1* Polyborosilazans mit etwa 50 wt.% kleiner als die der Ceraset® PSZ 10 (60 wt.%) und PSZ 20 (67 wt.%) Si-C-N Präkursor-Polymere. Bei der eigentlichen Pyrolyse handelte es sich dann um einen mehrstufigen endothermen Prozess unter Freisetzung von H_2 und CH_4.

Die Hochtemperaturstabilität und die zugrundeliegenden Hochtemperatur-Reaktionen wurden mit thermodynamischen Rechnungen auf Basis der Zusammensetzung der *Si-B-C-N_2* ($Si_1B_1C_{1.4}N_{2.3}$) und *Si-B-C-N_1* ($Si_6B_1C_5N_7$) Keramiken untersucht. Die Zusammensetzung beider Si-B-C-N Keramiken befand sich bei Temperaturen bis 1757 K im Phasengleichgewicht $Si_3N_4+SiC+BN+C$. Allerdings unterschieden sich die Phasenanteile stark. Der Bor-Gehalt entsprach dabei 17,54 at.% (*Si-B-C-N_2*) bzw. 5,25 at.% (*Si-B-C-N_1*). Die Einsatztemperatur-limitierende Reaktion war für beide untersuchten Si-B-C-N Keramiken, wie bei Ceraset® PSZ 10 und PSZ 20, die carbothermische Reaktion von Si_3N_4 und C unter Bildung von SiC und Freisetzung von N_2 bei 1757 K. Aufgrund unterschiedlicher Si:B:C-Verhältnisse wird bei der *Si-B-C-N_2* Keramik das Si_3N_4 komplett aufgebraucht und bei der *Si-B-C-N_1* Keramik der komplette freie Kohlenstoff. Dadurch befinden sich die Zusammensetzungen der resultierenden Si-B-C-N Keramik im thermodynamischen Gleichgewicht in den Phasengebieten Gas+C+BN+SiC (*Si-B-C-N_2*) bzw. Gas+Si_3N_4+SiC+BN (*Si-B-C-N_1*). Die *Si-B-C-N_1* Keramik zeigt dadurch bei 2114 K zusätzlich die thermische Zersetzung des verbliebenen Si_3N_4. Der ideale Stickstoffgehalt für eine maximale Hochtemperaturstabilität wurde für das jeweilige Si:B:C-Verhältnis aus den thermodynamischen Rechnungen ermittelt. Dies sind Zusammensetzungen, bei denen keine flüssigen oder gasförmigen Reaktionsprodukte gebildet werden. Für die *Si-B-C-N_2* Keramik ergaben sich für x(N) < 0,41 bzw. < 0,23 maximale Einsatztemperaturen von 1757 K und 2568 K. Die *Si-B-C-N_1* Keramik hatte die höchste Einsatztemperatur von 1757 K für 0,16 < x(N) < 0,43.

Experimentell zeigte sich die überlegene Hochtemperaturbeständigkeit der Si-B-C-N Keramik gegenüber den Ceraset® PSZ 10 und PSZ 20 Si-C-N Keramiken. Selbst oberhalb der carbothermischen Reaktionstemperatur zeigte die *Si-B-C-N_1* Keramik einen deutlich niedrigeren Masseverlust, keinen freiwerdenden Stickstoff und keine Veränderung der Mikrostruktur (bei 1673 K). Die erhaltenen Si-B-C-N Keramiken waren bei Temperaturen von 1473 K-1773 K in Ar/N_2 bzw. 1473 K-1673 K in Ar XRD-amorph. Nur Wärmebehandlung bei 1773 K in fließendem Ar führte zur Kristallisation von β-SiC als Folge der carbothermischen Reaktion und Si durch thermische Zersetzung von Si_3N_4 unter Nickstoff-Mangel Bedingungen. Obwohl Si_3N_4 eine Gleichgewichtsphase der *Si-B-C-N_1* Keramik ist, wurde, anders als bei Si-C-N Keramiken aus Ceraset® PSZ 10- und PSZ 20, keine Kristallisation von α-/β-Si_3N_4 beobachtet.

Phasengleichgewichte und Konstitution in ZrB$_2$-haltigen SiC/Si-C-N CMC

(Phase equilibria and constitution in ZrB$_2$-containing SiC/Si-C-N CMC)

Ein ZrB$_2$/Si-C-N Komposit wurde durch Pyrolyse einer Mischung aus ZrB$_2$-Pulver und dem Polysilazan Ceraset$^{®}$ PSZ 20 hergestellt. Zusätzlich wurden Reaktionen zwischen dem ZrB$_2$-Additiv und den Bestandteilen der keramischen Si-C-N Matrix (Si$_3$N$_4$, SiC und C), welche die Hochtemperaturbeständigkeit limitieren, mit der CALPHAD-Methode identifiziert. Die erste auftretende Reaktion (ZrB$_2$+Si$_3$N$_4$=ZrN+2BN+L(Si,Zr,B,N)) tritt bei 1870 K auf. Dies ist 113 K oberhalb der Einsatztemperatur-limitierenden carbothermischen Zersetzungsreaktion der Si-C-N Matrix (Si$_3$N$_4$+3C=3SiC+2N$_2$). Dadurch gibt es im ZrB$_2$/Si-C-N Komposit keine weitere Reaktion, welche die maximale Einsatztemperatur gegenüber der reinen Si-C-N Keramik reduziert.

Der Bildungsmechanismus von ZrC$_x$N$_y$ wurde durch eine Kombination von CALPHAD-Modellierung mit Schlüsselexperimenten identifiziert. Daraus wurde ein Bildungsmechanismus für ZrC$_x$N$_y$ vorgeschlagen: Eine direkte Reaktion des ZrB$_2$-Additivs mit den Bestandteilen der Si-C-N Matrix konnte durch CALPHAD-Modellierung bei den untersuchten Temperaturen (T < 1773 K) ausgeschlossen werden. Stattdessen deuteten eine ausgeprägtere ZrC$_x$N$_y$-Bildung bei Pyrolyse des ZrB$_2$/PSZ 20-Gemisches in Ar/N$_2$-Atmosphäre (p$_{N2}$=0.5 bar) verglichen mit reinem Ar sowie Nitrierexperimente mit ZrB$_2$-Pulver auf eine primäre Gas/Feststoff-Reaktion hin. Dabei wird zunächst ZrN aus der Reaktion von ZrB$_2$ mit der Ar/N$_2$-Atmosphäre gebildet (ZrB$_2$+3/2N$_2$=ZrN+2BN). Das berechnete Phasenstabilitätsdiagramm zeigte, dass ZrB$_2$ nur bei hohen Temperaturen und niedrigen Stickstoff-Partialdrücken stabil ist. Bei niedrigeren Temperaturen und hohem p$_{N2}$ sind ZrN und BN die stabilen Gleichgewichtsphasen. Mit steigendem p$_{N2}$ verschiebt sich die entsprechende Umwandlungsreaktion zu niedrigeren Temperaturen. Sobald ZrN gebildet ist, löst sich Kohlenstoff aus der Si-C-N Matrix und es entsteht ein ZrC$_x$N$_y$-Mischkristall. Aufgrund der gleichen Kristallstruktur und ähnlichem Gitterparameter existiert im System ZrC-ZrN eine vollständige Löslichkeit. Röntgendiffraktometrische Untersuchungen des gebildeten ZrC$_x$N$_y$-Mischkristalls ergaben einen Kohlenstoffanteil von C/(C+N) = 0.56. Daher kann die Bildung von ZrC$_x$N$_y$ durch geeignete Pyrolysebedingungen während der Herstellung des ZrB$_2$/Si-C-N Komposits innerhalb des Stabilitätsbereichs von ZrB$_2$ verhindert werden. Dies ist bei kleinem Stickstoffpartialdruck und moderaten Temperaturen unterhalb von 1673 K der Fall.

Das Hochtemperatur Oxidationsverhalten von ZrB$_2$
(High-temperature oxidation behavior of ZrB$_2$)

Das Hochtemperatur-Oxidationsverhalten von ZrB$_2$ Pulverpresslingen in fließender H$_2$O /Ar- und O$_2$/Ar-Atmosphäre (p$_{H2O}$=p$_{O2}$=0,2 bar) wurde bei Temperaturen von bis zu 1673 K untersucht. Die Oxidation setzte in sauerstoff- bzw. wasserdampfhaltiger Atmosphäre bei etwa der selben Temperatur ein. Allerdings wurde in Wasserdampf eine stärkere Massezunahme beobachtet. Die Gesamt-Masseänderung während der Hochtemperatur-Oxidation von ZrB$_2$ resultierte aus der Überlagerung zweier Effekte: Der Massezunahme durch die eigentliche Oxidationsreaktion und die Volatilisation des gebildeten flüssigen B$_2$O$_3$ in Form von Bor-haltigen Gasspezies. Daher unterschätzten reine thermogravimetrische Untersuchungen stark die tatsächliche Oxidationsrate des ZrB$_2$. Durch quantitative massenspektrometrische Analyse der H$_2$-Freisetzung war es möglich, die Oxidationsreaktion von Verdampfung und Volatilisation zu trennen. Dadurch war die Untersuchung des Hochtemperatur-Oxidationsverhaltens von ZrB$_2$ in Wasserdampf zugänglich, was in der Literatur selten zu finden ist. Die Oxidationskinetik von ZrB$_2$ ist komplex und stark temperaturabhängig. Die Oxidationskinetik zeigte eine lineare Temperaturabhängigkeit. Diese ändert sich mit steigender Temperatur von einem linearen (T=1073 K) zu einem sub-parabolischen (T=1673 K) Oxidationsverhalten. Eine Passivierung des ZrB$_2$ durch Bildung einer dichten Oxidschicht erfolgte in H$_2$O/Ar nur für Temperaturen ab 1273 K. Bei 1073 K zerfiel der ZrB$_2$-Pressling und oxidierte vollständig, da bei dieser Temperatur die Oxidationskinetik langsam und der Partialdruck von H$_3$BO$_3$(g) mit 4·10^{-4} bar hoch ist. Thermodynamische Gleichgewichtsberechnungen ergaben die Partialdrücke der Bor-haltigen Gasspezies, die aus B$_2$O$_3$ in O$_2$- und H$_2$O-haltiger Atmosphäre gebildet werden. In O$_2$-haltiger Atmosphäre (p$_{O2}$=0,2 bar) sind BO$_2$(g) (T<1493 K) und B$_2$O$_3$(g) (T>1493 K) die vorherrschenden Gasspezies. Im Gegensatz dazu sind die Partialdrücke der Bor-haltigen Gasspezies in H$_2$O-haltiger Atmosphäre deutlich höher. Bei p$_{H2O}$=0,2 bar wird Orthoborsäure (H$_3$BO$_3$(g)) mit Partialdrücken oberhalb von 3·10^{-4} bar gebildet. Bei Temperaturen oberhalb von 1179 K ist Metaborsäure (HBO$_2$(g)) die vorherrschende Gasspezies. Die massenspektrometrische Analyse der in H$_2$O-haltiger Atmosphäre gebildeten, gasförmigen B-O-H Spezies bestätigte die thermodynamischen Rechnungen. Ionisierte Gasmoleküle und deren Fragmente (H$_3$BO$_3^+$, H$_2$BO$_3^+$, H$_2$BO$_2^+$, HBO$_2^+$ und BO$_2^+$) wurden identifiziert. Die Freisetzung von H$_3$BO$_3$(g) (H$_3$BO$_3^+$ bei m/z=62) wurde während der Oxidation von ZrB$_2$ in H$_2$O/Ar in transienten (bis 1473 K) und isothermen Tests (1073 K, 1273 K, 1473 K und 1673 K) qualitativ verfolgt. Während des Aufheizens von ZrB$_2$ in H$_2$O/Ar begann die Freisetzung von H$_3$BO$_3$(g) bereits bei 673 K und erreichte bei 1000 K ein Maximum. Dies stimmte mit der maximalen Massezunahme überein. Mit weiter steigender Temperatur fiel das H$_3$BO$_3^+$-Signal wieder ab. Bei isothermen Tests erreichte das H$_3$BO$_3^+$-Signal, nach einem starken anfänglichen Anstieg, einen etwa konstanten Wert, der bei der höchsten untersuchten Temperatur von 1673 K am kleinsten war.

Das Hochtemperatur Oxidationsverhalten ZrB$_2$-haltiger SiC/Si-C-N CMC
(High-temperature oxidation behavior of ZrB$_2$-containing SiC/Si-C-N CMC)

Das Oxidationsverhalten eines ZrB$_2$-haltigen SiC/Si-C-N CMC wurde in fließenden O$_2$- und H$_2$O haltigen Atmosphären bei Temperaturen bis 1673 K untersucht. Das ZrB$_2$ war als funktionales Additiv fein in der keramischen Si-C-N Matrix verteilt, mit dem Ziel die Oxidationsbeständigkeit des CMC zu verbessern. Zusätzlich wurde ein ZrB$_2$-freies SiC/Si-C-N CMC untersucht, um den Einfluss des Additivs zu untersuchen.

Thermodynamische Rechnungen wurden genutzt, um die Wechselwirkungen zwischen dem ZrB$_2$-Additiv und den Gleichgewichtsbestandteilen der keramischen Si-C-N Matrix (SiC, C, Si$_3$N$_4$; siehe auch Kapitel 5.1) unter oxidierenden Bedingungen zu identifizieren. Die Oxidationsprodukte des ZrB$_2$-Additivs (B$_2$O$_3$ und ZrO$_2$) und des SiC/Si-C-N CMC (Si$_2$N$_2$O, SiO$_2$) zeigten neben einem niedrig schmelzenden Eutektikum im System SiO$_2$-B$_2$O$_3$ (T$_E$ = 713 K) auch die Bildung von ZrSiO$_4$. Dies wurde mittels XRD und EDX-Analyse betätigt. Nach Oxidation des ZrB$_2$-freien CMC wurde als einziges kristallines Oxidationsprodukt β-Cristobalit gefunden. Wie thermodynamische Rechnungen zeigten, weist Si$_2$N$_2$O lediglich einen sehr kleinen Stabilitätsbereich auf.

Während des Aufheizens in O$_2$-haltiger Atmosphäre zeigte das ZrB$_2$-SiC/Si-C-N CMC bei etwa 850 K durch bevorzugte Oxidation von freiem Kohlenstoff zunächst einen Masseverlust unter Freisetzung von CO und CO$_2$. Mit steigender Temperatur nahm die Masse ab etwa 950 K durch Oxidation der keramischen Si-C-N Matrix unter Bildung fester Oxidationsprodukte zu. Oxidation in H$_2$O-haltiger Atmosphäre führte sowohl für das ZrB$_2$-freie (SiC/Si-C-N), als auch für das ZrB$_2$-haltige (ZrB$_2$-SiC/Si-C-N) CMC zu einer höheren Gesamtmasseänderung als in O$_2$-haltiger Atmosphäre. Bereits ab der niedrigsten untersuchten Temperatur von 673 K wurden feste Oxidationsprodukte gebildet. Unter isothermen Bedingungen zeigte das ZrB$_2$-SiC/Si-C-N sowohl in O$_2$- wie in H$_2$O-haltiger Atmosphäre die höchste Massezunahme bei der niedrigsten untersuchten Oxidationstemperatur von 1073 K. Mit steigender Temperatur nahm die Masseänderung des ZrB$_2$-SiC/Si-C-N CMC ab. Das ZrB$_2$-freie SiC/Si-C-N CMC zeigte eine andere Temperaturabhängigkeit des Oxidationsverhaltens. Bei der niedrigsten untersuchten Temperatur von 1073 K zeigte SiC/Si-C-N sowohl in O$_2$- als auch H$_2$O-haltiger Atmosphäre einen Masseverlust. In O$_2$-haltiger Atmosphäre war die Masseänderung zu Beginn der Oxidation sogar bis zu 1373 K negativ. Der massenspektrometrische Nachweis von CO und CO$_2$ belegte, dass bei niedrigen Temperaturen zunächst freier Kohlenstoff oxidiert und zu einem Masseverlust führt. Bei diesen Temperaturen war die Bildungskinetik von SiO$_2$ zu langsam, um eine passivierende Oxidschicht zu bilden. Mit steigender Oxidationstemperatur nahm die Probenmasse, insbesondere zu Beginn der Oxidation, zu. Die Gesamtmasse hingegen sank beispielsweise bei Temperaturen oberhalb der carbothermischen Zersetzungsreaktion der keramischen Si-C-N Matrix (Si$_3$N$_4$+3C=3SiC+2N$_2$ bei 1757 K).

Gleichzeitige Massezunahme durch Oxidation und Masseverlust durch Volatilisation überlagern die Gesamtmasseänderung des ZrB_2-SiC/Si-C-N CMC. Während des Aufheizens in H_2O-haltiger Atmosphäre hoben sich beide Effekte bei Temperaturen oberhalb von etwa 1200 K auf, obwohl die zunehmende H_2-Freisetzung auf eine Beschleunigung der Oxidationsreaktion hindeutete. Thermodynamische Rechnungen zeigten, dass borhaltige Gasspezies für die Volatilisation hauptverantwortlich sind. Sowohl in O_2- als auch in H_2O-haltiger Atmosphäre waren die Partialdrücke der borhaltigen Gasspezies mehrere Größenordnungen höher als die der siliziumhaltigen Gasspezies. Durch den niedrigeren ZrB_2-Gehalt des CMC, war das massenspektrometrisch gemessene H_3BO_3-Signal (m/z=62), welches auf die Volatilisation des Boroxids hinweist, allerdings wesentlich kleiner als bei der Oxidation von reinem ZrB_2 unter denselben Bedingungen. Nach einer Stunde bei 1473 K in O_2/Ar-Atmosphäre konnte kein Bor mehr in der Oxidschicht nachgewiesen werden. Thermodynamische Rechnungen zeigten, dass der Partialdruck der borhaltigen Gasspezies BO_2 und B_2O_3 unter diesen Bedingungen ~10^{-4} bar beträgt. Bläschen auf der Oberfläche des ZrB_2-SiC/Si-C-N Komposits belegten das Vorhandensein eines flüssigen Borosilikats in einem frühen Stadium der Oxidation. Die quantitative massenspektrometrische Analyse von H_2 als Nebenprodukt der Oxidationsreaktion von ZrB_2-SiC/Si-C-N in Wasserdampf erlaubte die Messung der eigentlichen Oxidationskinetik und damit die Trennung der Oxidationsreaktion von Volatilisationseffekten. Bei Temperaturen von 1073 K war die Oxidationsreaktion alleine für die thermogravimetrisch gemessene Masseänderung verantwortlich. Dadurch zeigte das ZrB_2-SiC/Si-C-N sowohl in thermogravimetrischen als auch in massenspektrometrischen Messungen eine lineare Oxidationskinetik. Bei 1473 K hingegen reduzierten Volatilisationsreaktionen die thermogravimetrisch gemessene Masseänderung deutlich. Thermogravimetrie ergab hier scheinbar parabolische Oxidationskinetik. Der freigesetzte Wasserstoff offenbarte bei dieser Temperatur hingegen kubische Oxidationskinetik. Die Oxidationsrate von ZrB_2-SiC/Si-C-N war bis zu vier Größenordnungen niedriger als die der reinen ZrB_2 Proben. Besonders bei hohen Temperaturen ist die Stabilität und Sauerstoffdurchlässigkeit von SiO_2 kleiner als die von B_2O_3.

Freiliegende Lagen der gesägten CMC Proben boten Zugang für die oxidierende Atmosphäre. Zusätzlich wies die keramische Si-C-N Matrix durch Schrumpfen des präkeramischen Polymers während der Pyrolyse eine offene Porosität auf. Für einen optimalen Oxidationsschutz muss das CMC möglichst dicht sein, sodass das ZrB_2-Additiv nur lokal an entstehenden Rissen durch Bildung einer Schmelze aktiv wird und diese verschließt. Das ZrB_2-SiC/Si-C-N CMC zeigte die gewünschte Bildung einer Schmelze. Außerdem zeigten Mikrostrukturuntersuchungen, dass die Oxidation in ZrB_2-reichen Kavitäten stoppte. Dadurch ließ sich zeigen, dass das ZrB_2-Additiv in der Lage sein könnte, Risse durch Bildung einer Schmelze zu verschließen. Die Diffusion oxidierender Gasspezies in das CMC würde dadurch gestoppt oder stark verlangsamt werden. Das ZrB_2-Additiv ist daher geeignet die Oxidationsbeständigkeit des SiC/Si-C-N zu verbessern. Der Test eines Yttriumsilikat-beschichteten (Y_2SiO_5+$Y_2Si_2O_7$) SiC/Si-C-N CMC in prototypischer

Verbrennungsatmosphäre zeigte lediglich anfänglich eine Verlangsamung der Oxidation. Möglicherweise wäre ein mehrlagiges EBC mit Si oder SiC als Haftvermittlerschicht besser geeignet, dauerhaft einen gasdichten Schutz des darunter liegende CMC zu gewährleisten.

Insgesamt bot die Kombination von CALPHAD-Methode und Hochtemperatur-Experimenten in allen Teilgebieten eine hervorragende und sich ergänzende Herangehensweise zur Aufklärung der ablaufenden Mechanismen. Zudem bestätigten die thermodynamischen Rechnungen die experimentellen Ergebnisse qualitativ und sehr oft auch quantitativ.

A. Appendix

A.1 Curriculum vitae

Professional career

12/2019 – Today **Development Engineer**
Berliner Glas GmbH, Product Development EUV

PhD Studies

01/2015 – 11/2019 **PhD student**
Institute for Applied Materials – Applied Materials Physics (IAM-AWP), Karlsruhe Institute of Technology

Education

03/2013 – 05/2014 **Working Student**
Robert Bosch GmbH in Schwieberdingen
Power electronics

04/2012 – 05/2014 **Master of Science in Material Science** (in English-language)
Universität Stuttgart
Master thesis: Microstructure and stress evolution during epitaxial metal film growth

10/2008 – 12/2011 **Bachelor of Science in Materialwissenschaft**
Universität Stuttgart
Bachelor thesis: Nitriding of a binary Ni-Ti alloy

09/1998 – 06/2007 **Abitur**
Mörike Gymnasium Ludwigsburg

A.2   Publications

Publications

I.J. Markel, J. Glaser, M. Steinbrück, H.J Seifert, *High-temperature reactions and phase evolution in precursor-derived ZrB₂/Si-C-N composites*, Journal of the European Ceramic Society 39, 2585-2593, 2019

M. Steinbrück, V. Angelici Avincola, I.J. Markel, U. Stegmaier, U. Gerhards, H.J. Seifert, *Oxidation of SiC$_f$-SiC CMC cladding tubes for GFR application in impure helium atmosphere and materials interactions with tantalum liner at high temperatures up to 1600°C*, Journal of Nuclear Materials 517 (15), 337-348, 2019

I.J. Markel, J. Glaser, M. Steinbrück, H.J. Seifert, *Experimental and computational analysis of PSZ 10- and PSZ 20-derived Si-C-N ceramics*, Journal of the European Ceramic Society 39, 195-204, 2019

M.K. Große, T. Van Duijnhoven, M. Steinbrück, C. Tang, S. Ahmad, U. Gerhards, I.J. Markel, H.J. Seifert, *High temperature interaction of SiC and Zry-4*, Proceedings of the 2018 ICAPP, 590-597, 2018

Presentations and Posters

I.J. Markel, J. Glaser, M. Steinbrück, H.J. Seifert, *Thermodynamic modelling and experimental investigation of a self-healing SiC$_f$/SiCN CMC*, MSE 2018 Darmstadt, Germany (oral presentation)

I.J. Markel, D.M. Cupid, H.J. Seifert, *Computational Thermodynamics in the Y-Si-C-H-O System*, TMS 2018 Phoenix, USA (oral presentation)

I.J. Markel, M. Steinbrück, D.M. Cupid, H.J. Seifert, *Integrated Computational/Experimental Design of Self-healing CMCs*, MS&T 2017 Pittsburgh, USA (oral presentation)

I.J. Markel, V. Angelici Avincola, D.M. Cupid, H.J. Seifert, *Thermodynamic modelling of high-temperature oxidation of SiC CMC materials*, QUENCH Workshop 2016 Karlsruhe, Germany (oral presentation)

I.J. Markel, D.M. Cupid, M. Steinbrück, H.J. Seifert, *Thermodynamic Calculations in the Y-Si-C-O-H System: Phase stability and corrosion resistance of Yttrium-Silicate EBCs on SiC in moist atmosphere*, MSE 2016 Darmstadt, Germany (poster presentation)

I.J. Markel, D.M. Cupid, M. Steinbrück, H.J. Seifert, *Thermodynamic calculations in the Y-Si-C-O-H system for yttrium silicate based EBCs*, HTCMC 2016 Toronto, Canada (oral presentation)

A.3   Additional data

Table A.1: Derived rate constant k and exponent n for the oxidation of ZrB_2 in steam shown in Figure 7.20.

Material	T [K]	p_{H2O} [bar]	H$_2$-derived			mass-derived		
			k [mg/cm²s^n]	n	R^2	k [mg/cm²s^n]	n	R^2
ZrB_2	1073	0.2	0.01	0.92	0.982	0.18	0.54	0.982
ZrB_2	1273	0.2	0.04	0.73	0.999	0.10	0.55	0.998
ZrB_2	1473	0.2	0.33	0.59	0.996	0.62	0.37	0.990
ZrB_2	1473	1.0	0.26	0.61	0.993	0.54	0.40	0.992
ZrB_2	1673	0.1	2.03	0.47	0.985	-	-	-
ZrB_2	1673	0.2	2.63	0.44	0.971	-	-	-

List of Symbols

$a_0, a_1, a_2,...$ coefficients of the analytical description of the Gibbs free energy

A, B, C...   elements

α coefficient of thermal expansion

$A_j^{v_j-}$ Anion with charge v_j

B_k^0 neutral species in ionic two-sublattice liquid model

$C_i^{v_i+}$ Cation with charge v_i

C_p heat capacity

c_{H2} concentration of H_2

C_l coefficient

ΔC_l correction term for C_l

d^{hkl} lattice plane spacing

$\emptyset$ diameter

E_a activation energy

E_i error

f fugacity

F_i functions

G Gibbs free energy

H enthalpy

k kinetic rate constant

k_l linear reaction constant

L liquid phase / melt

L_i measured value

$^v L_{ij}$ Redlich-Kister parameter

λ wave length

List of Symbols

m/z	mass to charge ratio
μ	chemical potential
n	exponent
n^{Φ}	amount of phase Φ
Ω	interaction parameter
p	pressure
p_0	total pressure
p_i	partial pressure of component *i*
P and Q	stoichiometric numbers describing the number of sites on the particular lattice
R	ideal gas constant
S	entrophy
σ_{total}	total microscopic neutron cross section
t	time
T	temperature
T_c	critical temperature
T_m	melting temperature
Θ^{hkl}	diffraction angle
Va^{-Q}	Vacancy with hypothetical induced change Q
$\dot{V}$	flow rate
W_i	values
$\Delta w/A$	mass change per unit area
x(Ar)	(mole) fraction of phase, element or (gas) species
y_i	fraction of constituent *i* in gas or melt

List of Figures

List of Tables

References

[1]   A. Rüdiger and W. Pritzkow, "Die Entwicklung oxidkeramischer Faserverbundwerkstoffe am Fraunhofer ISA / Zentrum HTL in Zusammenarbeit mit W.E.C. Pritzkow Spezialkeramik," *Keramische Zeitschrift 03,* pp. 166-169, 2013.

[2]   D. M. Wilson and L. R. Visser, "High performance oxide fibers for metal and ceramic composites," *Composites: Part A 32,* pp. 1143-1153, 2001.

[3]   W. Glaubitt, D. Sporn and R. Jahn, "Ceramic fibers from sol-gel precursors," *Proceedings of 5. international conference on ceramic processing science and technology, Friedrichshafen (Germany),* pp. 745-749, 1995.

[4]   W. Krenkel, "Carbon Fiber Reinforced CMC for High-Performance Structures," *International Journal of Applied Ceramic Technology 1 (2),* pp. 188-200, 2004.

[5]   W. Krenkel, "Cost Effective Processing of CMC Composites by Melt Infiltration (Lsi-Process)," *Ceramic Engineering and Science Proceedings 22(3),* pp. 443-454, 2001.

[6]   Y. Katoh, K. Ozawa, C. Shih, T. Nozawa, R. J. Shinavski, A. Hasegawa and L. L. Snead, "Continuous SiC fiber, CVI SiC matrix composites for nuclear applications: Properties and irradiation effects," *Journal of Nuclear Materials 448,* pp. 448-476, 2014.

[7]   B. Mainzer, M. Frieß, R. Jemmali and D. Koch, "Development of polyvinylsilazane-derived ceramic matrix composites based on Tyranno SA3 fibers," *Journal of the Ceramic Society of Japan 124 (10),* pp. 1035-1041, 2016.

[8]   S. Bernard, M. Weinmann, P. Gerstel, P. Miele and F. Aldinger, "Boron-modified polysilazane as a novel single-source precursor for SiBCN ceramic fibers: synthesis, melt-spinning, curing and ceramic conversion," *Journal of Materials Chemistry 15,* pp. 289-299, 2005.

[9]   B. Clauß and D. Schawaller, "Modern Aspects of Ceramic Fiber Development," *Advances in Science and Technology 50,* pp. 1-8, 2006.

[10]   J. Wang, Z. Yang, X. Duan, D. Jia and Y. Zhou, "Microstructure and mechanical properties of SiC/SiBCN ceramic matrix composites," *Journal of Advanced Ceramics 4 (1),* pp. 31-38, 2015.

[11]   H. Salmang, H. Scholze and R. Telle, Keramik, Berlin Heidelberg: Springer-Verlag, 2006.

[12]   W. Krenkel, Ceramic Matrix Composites: Fiber Reinforced Ceramics and their Applications, Weinheim: Wiley-VCH, 2008.

[13]   N. P. Bansal and J. Lamon, Ceramic Matrix Composites Materials, Modelling and Technology, Hoboken, New Jersey: John Wiley & Sons, 2015.

[14]   B. Clauß, "Fasern und Preformtechniken zur Herstellung keramischer Verbundwerkstoffe," *Keramische Zeitschrift 53 (10),* pp. 916-923, 2001.

[15]   H. J. Seifert, J. Peng, H. L. Lukas and F. Aldinger, "Phase equilibria and thermal analysis of Si-C-N ceramics," *Journal of Alloys and Compounds 320,* pp. 251-261, 2001.

[16]   J. Bill, T. W. Kamphowe, A. Müller, T. Wichmann, A. Zern, A. Jalowieki, J. Mayer, M. Weinmann, J. Schuhmacher, K. Müller, J. Peng, H. J. Seifert and F. Aldinger, "Precursor-derived Si-(B-)C-N ceramics: thermolysis, amorphous state and crystallization," *Applied Organometallic Chemistry 15,* pp. 777-793, 2001.

[17]   Y. Iwamoto, K. Kikuta and S. Hirano, "Synthesis of poly-titanosilazanes and conversion into Si3N4-TiN ceramics," *Journal of the Ceramic Society of Japan 108 (4),* pp. 350-356, 2000.

[18]   H. Wang, B. Gao, X. Chen, J. Wang, S. Chen and Y. Gou, "Synthesis and pyrolysis of a novel preceramic polymer PZMS from PMS to fabricate hightemperature-resistant ZrC/SiC ceramic composite," *Applied Organometallic Chemistry 27,* pp. 166-173, 2013.

[19]   J. Yuan, S. Hapis, H. Breitzke, Y. Xu, C. Fasel, H. J. Kleebe, G. Buntkowsky, R. Riedel and E. Ionescu, "Single-Source-Precursor Synthesis of Hafnium-Containing Ultrahigh-Temperature Ceramic Nanocomposites (UHTC-NCs)," *Inorganic Chemistry 53,* pp. 10443-10455, 2014.

[20]   F. Liu, J. Kong, C. Luo, F. Ye, X. Luan, N. Tian, Y. Liu, H. Zhang, J. Gu and Y. Tang, "High temperature self-healing SiBCN ceramics derived from hyperbranched polyborosilazanes," *Advanced Composites and Hybrid Materials 1,* pp. 506-517, 2018.

[21]   P. Greil, "Near Net Shape Manufacturing of Polymer Derived Ceramics," *Journal of the European Ceramic Society 18,* pp. 1905-1914, 1998.

[22]   P. Greil, "Active-Filler-Controlled Pyrolysis of Preceramic Polymers," *Journal of the American Ceramic Society 78,* pp. 835-848, 1995.

References

[23]   G. Stantschev, M. Frieß, R. Kochendörfer and W. Krenkel, "Long fibre reinforced ceramics with active fillers and a modified intra-matrix bond based on the LPI process," *Journal of the European Ceramic Society 25,* pp. 205-209, 2005.

[24]   D. M. Cupid and H. J. Seifert, "Thermodynamic Calculations and Phase Stabilities in the Y-Si-C-O System," *Journal of Phase Equilibria and Diffusion 28,* pp. 90-100, 2007.

[25]   R. C. Robinson and J. L. Smialek, "SiC Recession Caused by SiO2 Scale Volatility under Combustion Conditions: I, Experimental Results and Empirical Model," *Journal of the American Ceramic Society 82 (7),* pp. 1817-1825, 1999.

[26]   E. J. Opila, J. L. Smialek, R. C. Robinson, D. S. Fox and N. S. Jacobson, "SiC Recession Caused by SiO2 Scale Volatility under Combustion Conditions: II, Thermodynamics and Gaseous-Diffusion Model," *Journal of the American Ceramic Society 82 (7),* pp. 1826-1834, 1999.

[27]   "NEW Advanced Ceramic Composites for Energy Saving gas turbineS - NewAccess," 25 May 2020. [Online]. Available: https://www.fona.de/de/massnahmen/foerdermassnahmen/foerderinitiative-materialforschung-fuer-die-energiewende/newaccess.php. [Accessed 4 January 2021].

[28]   "Ceramic Components for Industrial Gas Turbines (CERCO)," CORDIS Forschungsergebnisse der EU, 3 December 2003. [Online]. Available: https://cordis.europa.eu/article/id/84711-new-testing-methods-for-new-ceramic-parts/de. [Accessed 4 January 2021].

[29]   H. Wadley, "High Temperature Coatings," 24 April 2013. [Online]. Available: https://www2.virginia.edu/ms/research/wadley/high-temp.html. [Accessed 4 January 2021].

[30]   F. W. Zok, "Ceramic-matrix composites enable revolutionary gains in turbine engine efficiency," *American Ceramic Society Bulletin 95 (5),* pp. 22-28, 2016.

[31]   R. Kennedy, "Ceramic Matrix Composite Technology is GE's Centerpiece Jet Propulsion Strategy for the 21st Century," GE Aviation The Blog, 22 April 2019. [Online]. Available: https://blog.geaviation.com/technology/42869/#:~:text=As%20CMCs%20further%20populate%20the,to%20private%20industry%20for%20decades. [Accessed 4 January 2021].

[32]   S. Francis, "CompositesWorld: GE Aviation delivers 25,000th CMC component," 18 August 2018. [Online]. Available: https://www.compositesworld.com/news/ge-aviation-

delivers-25000th-cmc-component. [Accessed 4 January 2021].

[33]   T. Kellner, "Space Age Ceramics Are Aviation's New Cup Of Tea," 13 July 2016. [Online]. Available: https://www.ge.com/news/reports/space-age-cmcs-aviations-new-cup-of-tea. [Accessed 4 January 2021].

[34]   N. S. Jacobson, "Corrosion of Silicon-Based Ceramics in Combustion Environments," *Journal of the American Ceramic Society 76 (1),* pp. 5-28, 1993.

[35]   E. J. Opila, "Oxidation and Volatilization of Silica Formers in Water Vapor," *Journal of the American Ceramic Society, 86 (8),* pp. 1238-1248, 2003.

[36]   V. A. Avincola, D. Cupid and H. J. Seifert, "Thermodynamic modeling of the silica volatilization in steam related to silicon carbide oxidation," *Journal of the European Ceramic Society 35,* pp. 3809-3818, 2015.

[37]   E. J. Opila and R. E. Hann, "Paralinear Oxidation of CVD SiC in Water Vapor," *Journal of the American Ceramic Society 80 (1),* pp. 197-205, 1997.

[38]   K. Hack, The SGTE Casebook: Thermodynamics at Work, 2nd Edition, Cambridge, England: Woodhead Publishing Limited, 2008.

[39]   M. Fritsch, H. Klemm, M. Herrmann and B. Schenk, "Corrosion of selected ceramic materials in hot gas environment," *Journal of the European Ceramic Society 26,* pp. 3557-3565, 2006.

[40]   H. Klemm, M. Fritsch and B. Schenk, "Corrosion of Ceramic Materials in Hot Gas Environment," *Proceedings of the 28th International Conference on Advanced Ceramics and Composites 25(4),* pp. 463-468, 2004.

[41]   K. N. Lee, D. S. Fox and N. P. Bansal, "Rare earth silicate environmental barrier coatings for SiC/SiC composites and Si3N4 ceramics," *Journal of the European Ceramic Society 25,* pp. 1705-1715, 2005.

[42]   N. S. Jacobson, "Silica Activity Measurements in the Y2O3–SiO2 System and Applications to Modeling of Coating Volatility," *Journal of the American Ceramic Society 97 (6),* pp. 1959-1965, 2014.

[43]   G. Costa and N. S. Jacobson, "Mass spectrometric measurements of the silica activity in the Yb2O3–SiO2 system and implications to assess the degradation of silicate-based coatings in combustion environments," *Journal of the European Ceramic Society 35 (15),*

pp. 4259-4267, 2015.

[44]   B. Kasper, Phasengleichgewichte im System B-C-N-Si, Dissertation Universität Stuttgart, 1996.

[45]   N. S. Jacobson, G. N. Morscher, D. R. Bryant and R. E. Tressler, "High-Temperature Oxidation of Boron Nitride: II, Boron Nitride Layers in Composites," *Journal of the American Ceramic Society 82 (6),* pp. 1473-1482, 1999.

[46]   W. G. Fahrenholtz and G. E. Hilmas, "Oxidation of ultra-high temperature transition metal diboride ceramics," *International Materials Reviews 57,* pp. 61-72, 2012.

[47]   M. M. Opeka, I. G. Talmy, E. J. Wuchina, J. A. Zaykoski and S. J. Causey, "Mechanical, thermal and oxidation properties of refractory hafnium and zirconium compounds," *Journal of the American Ceramic Society 19,* pp. 2405-2414, 1999.

[48]   A. Müller, P. Gerstel, M. Weinmann, J. Bill and F. Aldinger, "Si-B-C-N Ceramic Precursors Derived from Dichlorodivinylsilane and Chlorotrivinylsilane. 1. Precursor Synthesis," *Chemistry of Materials 14 (8),* pp. 3398-3405, 2002.

[49]   A. Müller, J. Peng, H. J. Seifert, J. Bill and F. Aldinger, "Si-B-C-N Ceramic Precursors Derived from Dichlorodivinylsilane and Chlorotrivinylsilane. 2. Ceramization of Polymers and High-Temperature Behavior of Ceramic Materials," *Chemistry of Materials 14 (8),* pp. 3406-2412, 2002.

[50]   J. J. van Laar, "Die Schmelz- oder Erstarrungskurven bei binären Systemen, wenn die feste Phase ein Gemisch der beiden Komponenten ist, und eine Verbindung auftritt.," *Zeitschrift für Physikalische Chemie 53, 64, 66,* pp. 216, 257, 197-237, 1908.

[51]   C. H. Johansson, "Thermodynamisch begründete Deutung der Vorgänge bei der Austenit-Martensit-Umwandlung," *Archiv für das Eisenhüttenwesen 11 (5),* pp. 241-251, 1937.

[52]   G. J. Schmitz and U. Prahl, Handbook of Software Solutions for ICME, Weinheim, Germany: Wiley-VCH, 2017.

[53]   L. Kaufman and M. Cohen, "The martensitic transformation in the iron-nickel system," *The Journal of Metals 8 (10),* pp. 1393-1401, 1956.

[54]   J. L. Meijering, "Calculation of the nickel-chromium-copper phase diagram from binary data," *Acta Metallurgica 5 (5),* pp. 257-264, 1957.

[55] L. Kaufman and H. Bernstein, Computer Calculation of Phase Diagrams: With Special Reference to refractory Metals, New York and London: Academic Press Inc., 1970.

[56] J. O. Anderson, T. Helander, L. Höglund, P. F. Shi and B. Sundman, "Thermo-Calc and DICTRA, Computational tools for materials science," *Calphad 26,* pp. 273-312, 2002.

[57] H. J. Seifert and F. Aldinger, "Applied Phase Studies," *Zeitschrift für Metallkunde 87(11),* pp. 841-853, 1996.

[58] O. Redlich and A. T. Kister, "Algebraic Representation of Thermodynamic Properties and the Classification of Solutions," *Industrial & Engineering Chemistry 40 (2),* pp. 345-348, 1948.

[59] F. D. Murnaghan, "The Compressibility of Media under Extreme Pressures," *Proceedings of the National Acadamy of Sciences (USA) 30,* pp. 244-247, 1944.

[60] A. F. Guillermet, P. Gustafson and M. Hillert, "The representation of thermodynamic properties at high pressures," *Journal of Physics and Chemistry of Solids 46 (12),* pp. 1427-1429, 1985.

[61] X. G. Lu, M. Selleby and B. Sundman, "Implementation of a new model for pressure dependence of condensed," *Computer Coupling of Phase Diagrams and Thermochemistry 29,* pp. 49-55, 2005.

[62] E. Brosh, G. Makov and R. Z. Shneck, "Application of CALPHAD to high pressures," *Computer Coupling of Phase Diagrams and Thermochemistry 31,* pp. 173-185, 2007.

[63] H. L. Lukas, S. G. Fries and B. Sundman, Computational Thermodynamics - The CALPHAD Method, Cambridge: Cambridge University Press, 2007.

[64] A. S. Jordan, "A Theory of Regular Associated Solutions Applied to the Liquidus Curves of the Zn-Te and Cd-Te Systems," *Metallurgical and Materials Transactions B 1(1),* pp. 239-249, 1970.

[65] M. Temkin, "Mixtures of fused salts as ionic solutions," *Acta Physicochimica URSS 20,* pp. 411-420, 1945.

[66] M. Hillert and L. I. Staffansson, "The Regular Solution Model for Stoichiometric Phases and Ionic Melts," *Acta Chemica Scandinavica 24(10),* pp. 3618-3626, 1970.

[67] M. Hillert and L. I. Staffansson, "An analysis of the phase equilibria in the Fe-FeS system,"

Metallurgical and Materials Transactions B 6, pp. 37-41, 1975.

[68] M. Hillert, B. Jansson, B. Sundman and J. Agren, "A Two-Sublattice Model for Molten Solutions with Different Tendency for Ionization," *Metallurgical Transactions A 16,* pp. 261-266, 1985.

[69] H. L. Lukas, E. T. Henig and B. Zimmermann, "Optimization of phase diagrams by a least squares method using simultaneously different types of data," *Calphad 1,* pp. 225-236, 1977.

[70] A. D. Pelton and H. Schmalzried, "On the Geometrical Representation of Phase Equilibria," *Metallurgical Transactions 4,* pp. 1395-1404, 1973.

[71] NETZSCH-Gerätebau GmbH, "Simultaneous Thermal Analyzer – STA 449 F3 Jupiter®," Selb, Germany.

[72] M. Steinbrück, A. Meier, U. Stegmaier and L. Steinbock, Experiments on the Oxidation of Boron Carbide at High Temperatures, Karlsruhe: Forschungszentrum Karlsruhe in der Helmholtz-Gemeinschaft, Wissenschaftliche Berichte FZKA 6979, 2004.

[73] E. J. Mittemeijer and U. Welzel, Modern Diffraction Methods, Weinheim, Germany: Wiley-VCH, 2012.

[74] U. Stuhr, M. Grosse and W. Wagner, "The TOF-strain scanner POLDI with multiple frame overlap—concept and performance," *Materials Science and Engineering A: Structural Materials: Properties, Microstructure and Processing 437 (1),* pp. 134-138, 2006.

[75] V. F. Sears, "Neutron scattering lengths and cross sections," *Neutron News 3 (3),* pp. 26-37, 1992.

[76] Scientific Group Thermodata Europe (SGTE), Grenoble Campus, 1001 Avenue Centrale, BP66, F-38402 Saint Martin d'Heres, France, http://www.sgte.org.

[77] J. Gröbner, H. L. Lukas and F. Aldinger, "Thermodynamic Calculation of the Ternary System Al-Si-C," *Calphad 20 (2),* pp. 247-254, 1996.

[78] R. W. Oleshinski and G. J. Abbaschian, "The C-Si (Carbon-Silicon) system," *Bulletin of Alloy Phase Diagrams 5,* pp. 486-489, 1984.

[79] H. M. Chen, F. Zheng, H. S. Liu, L. B. Liu and Z. P. Jin, "Thermodynamic assessment of B-Zr and Si-Zr binary systems," *Journal of Alloys and Compounds 468,* pp. 209-216, 2009.

[80]   H. M. Chen, Y. Xiang, S. Wang, F. Zheng, L. B. Liu and Z. P. Jin, "Thermodynamic assessment of the C-Si-Zr system," *Journal of Alloys and Compounds 474,* pp. 76-80, 2009.

[81]   H. Duschanek, P. Rogl and MSIT, "B-C-Zr Ternary Phase Diagram Evaluation," MSI Materials Science International Services GmbH, Stuttgart, Germany, 1998.

[82]   A. F. Guillermet, "Analysis of thermochemical properties and phase stability in the zirconium-carbon system," *Journal of Alloys and Compounds 217,* pp. 69-89, 1995.

[83]   X. Ma, C. Li, K. Bai, P. Wu and W. Zhang, "Thermodynamic assessment of the Zr-N system," *Journal of Alloys and Compounds 373,* pp. 194-201, 2004.

[84]   C. Wang, M. Zinkevich and F. Aldinger, "On the thermodynamic modelling of the Zr-O system," *Computer Coupling of Phase Diagrams and Thermochemistry 28,* pp. 281-292, 2004.

[85]   H. Mao, M. Selleby and O. Fabrichnaya, "Thermodynamic reassessment of the Y2O3-Al2O3-SiO2 system and its subsystems," *Computer Coupling of Phase Diagrams and Thermochemistry 32,* pp. 399-412, 2008.

[86]   N. A. Toropov and F. Y. Galakhov, "Liquation in the system ZrO2-SiO2," *Bulletin of the Academy of Sciences of the USSR, Division of chemical science volume 5,* pp. 153-156, 1956.

[87]   W. C. Butterman and W. R. Foster, "Zircon Stability and the Zirconium Oxide -- Silica Phase Diagram," *American Mineralogist 52 (5-6),* pp. 880-885, 1967.

[88]   W. C. Butterman, Equilibrium Phase Relations among Oxides in the Systems GeO2, GeO2-B2O3, HfO2-B2O3, ZrO2-SiO2-B2O3, and ZrO2-SiO2, Ohio State University, Columbus, OH: PhD Disseration, 1965.

[89]   R. Telle, F. Greffrath and Prieter, "Direct observation of the liquid miscibility gap in the zirconia-silica system," *Journal of the European Ceramic Society 35,* pp. 3995-4004, 2015.

[90]   P. Franke, "ZrO2-SiO2," *unpublished work,* 2011.

[91]   A. Kaiser, M. Lobert and R. Telle, "Thermal stability of zircon (ZrSiO4)," *Journal of the European Ceramic Society 28,* pp. 2199-2211, 2008.

[92]   S. N. Karlsdottir and J. W. Halloran, "Zirconia Transport by Liquid Convection during Oxidation of Zirconium Diboride–Silicon Carbide," *Journal of the American Ceramic*

Society 91 (1), pp. 272-277, 2008.

[93]   W. C. Beard, W. C. Butterman, D. E. Koopman, H. E. Wenden and W. R. Foster, "Research on Phase Equilibria between Boron Oxides and Refractory Oxides, Including Silicon and Aluminum Oxides," *Quarterly Progress Report No. 9, October 1, 1961-December 31, 1961, Technical Report, Ohio State University Research Foundation, Columbus, OH,* 1962.

[94]   N. Dupin, I. Ansara, C. Servant, C. Toffolon, C. Lemaignan and J. C. Brachet, "A thermodynamic database for zirconium alloys," *Journal of Nuclear Materials 275 ,* pp. 287-295, 1999.

[95]   M. Steinbrück, "Hydrogen absorption by zirconium alloys at high temperatures," *Journal of Nuclear Materials 334,* p. 58–64, 2004.

[96]   Y. Zhong and D. D. Macdonald, "Thermodynamics of the Zr–H binary system related to nuclear fuel sheathing and pressure tube hydriding," *Journal of Nuclear Materials 423,* pp. 87-92, 2012.

[97]   H. J. Seifert, H. L. Lukas and F. Aldinger, "Development of Si-B-C-N Ceramics Supported by Phase Diagrams and Thermochemistry," *Berichte der Bunsengesellschaft für Physikalische Chemie 102,* pp. 1309-1313, 1998.

[98]   H. J. Seifert and F. Aldinger, "Thermodynamic Calculations in the Si-B-C-N-O System," in *J. Bill, F. Wakai, F. Aldinger (Eds.), Precursor-Derived Ceramics: Synthesis, Structures and High Temperature Mechanical Properties*, Weinheim, New York, Wiley-VCH, 1999, pp. 165-174.

[99]   H. J. Seifert and F. Aldinger, "Phase Equilibria in the Si-B-C-N System," in *M. Jansen (ed.) High Performance Non-Oxide Ceramics I, Structure and Bonding, Vol. 101*, Heidelberg, Springer-Verlag, 2002, pp. 1-58.

[100]   I. J. Markel, J. Glaser, M. Steinbrück and H. J. Seifert, "Experimental and computational analysis of PSZ 10- and PSZ 20-derived Si-C-N ceramics," *Journal of the European Ceramic Society 39,* p. 195–204, 2019.

[101]   J. Bill, J. Schuhmacher, K. Müller, S. Schempp, J. Seitz, J. Dürr, H. P. Lampertner, J. Golczewski, J. Peng, H. J. Seifert and F. Aldinger, "Investigations into the structural evolution of amorphous Si-C-N ceramics from precursors," *Zeitschrift für Metallkunde 91,* pp. 335-351, 2000.

[102] J. Bill, J. Seitz, G. Thurn, J. Dürr, J. Canel, B. Z. Janos, A. Janowiecki, D. Sauter, S. Schempp, H. P. Lamparter, J. Mayer and F. Aldinger, "Structure Analysis and Properties of Si-C-N Ceramics Derived from Polysilazanes," *Physica Status Solidi A 166,* pp. 269-296, 1998.

[103] J. Dürr, P. Schempp, P. Lamparter, J. Bill, S. Steeb and F. Aldinger, "X-ray and neutron small angle scattering with Si-C-N ceramics using isotopic substitution," *Solid State Ionics 101-103,* pp. 1041-1047, 1997.

[104] H. J. Seifert, J. Peng, J. Golczewski and F. Aldinger, "Phase equilibria of precursor-derived Si-(B-)C-N ceramics," *Applied Organometallic Chemistry 15 (10),* pp. 794-808, 2001.

[105] C. Garcia-Garrido, P. E. Sanchez-Jimenez, L. A. Perez-Maqueda, A. Perejon and J. M. Criado, "Combined TGA-MS kinetic analysis of multistep processes. Thermal decomposition and ceramification of polysilazane and polysiloxane preceramic polymers," *Physical Chemistry Chemical Physics 18,* pp. 29348-29360, 2016.

[106] R. Riedel, G. Passing, H. Schönfelder and R. J. Brook, "Synthesis of dense silicon-based ceramics at low temperatures," *Nature 355,* pp. 714-716, 1992.

[107] N. Janakiraman, M. Weinmann, J. Schuhmacher, K. Müller, J. Bill and F. Aldinger, "Thermal Stability, Phase Evolution, and Crystallization in Si-B-C-N Ceramics Derived from a Polyborosilazane Precursor," *Journal of the American Ceramic Society 85,* pp. 1807-1814, 2002.

[108] J. A. Golczewski, "New paradigm of a metastable phase diagram presenting structural transformations induced by annealing of Si–C–N amorphous ceramics derived from polymer precursors," *International Journal of Materials Research 100,* pp. 203-207, 2009.

[109] J. A. Golczewski and F. Aldinger, "Thermodynamic modeling of amorphous Si–C–N ceramics derived from polymer precursors," *Journal of Non-Crystalline Solids 347,* pp. 204-210, 2004.

[110] J. Wilfert, Innovative Verarbeitungsverfahren und neue Polymersysteme für amorphe SiBNC-Netzwerke, Stuttgart: Dissertation Universität Stuttgart, 2011.

[111] U. Müller, M. Weinmann and M. Jansen, "Cl2MeSi–NH–BCl2 and ClMe2Si–NH–BCl2: novel processable single source precursors of amorphous Si/C/B/N ceramics," *Journal of Materials Chemistry 18,* pp. 3671-3679, 2008.

[112]   J. Wilfert and M. Jansen, "Curing preceramic SiBNC polymers infusible by radical polymerization," *Journal of Materials Chemistry 21,* pp. 13422-13428, 2011.

[113]   R. Riedel, A. Kienzle, W. Dressler, L. Ruwisch, J. Bill and Aldinger, "A silicoboron carbonitride ceramic stable to 2000 °C," *Nature 382,* pp. 796-798, 1996.

[114]   A. Jalowiecki, J. Bill, F. Aldinger and J. Mayer, "Interface characterization of nanosized B-doped Si3N4/SiC ceramics," *Composites Part A 27,* pp. 717-721, 1996.

[115]   J. Peng, Thermochemistry and Constitution of Precursor-Derived Si-(B-)C-N Ceramics, Dissertation: Universität Stuttgart, 2002.

[116]   M. Weinmann, J. Schuhmacher, H. Kummer, S. Prinz, J. Peng, H. J. Seifert, K. Müller, J. Bill and F. Aldinger, "Synthesis and Thermal Behavior of Novel Si-B-C-N Ceramic Precursors," *Chemistry of Materials 12,* pp. 623-632, 2000.

[117]   J. Peng, H. J. Seifert and F. Aldinger, "Thermal stability of Precursor-Derived Si-(B-)C-N Ceramics," in *Innovative Processing and Synthesis of Ceramics, Glasses, and Composites IV, Ceramic Transactions, volume 115*, Westerville, Ohio, The American Ceramic Society, 2000, pp. 251-262.

[118]   A. Müller, P. Gerstel, M. Weinmann, J. Bill and F. Aldinger, "Correlation of boron content and high temperature stability in Si-B-C-N ceramics," *Journal of the European Ceramic Society 20,* pp. 2655-2659, 2000.

[119]   A. Müller, P. Gerstel, M. Weinmann, J. Bill and F. Aldinger, "Correlation of boron content and high temperature stability in Si-B-C-N ceramics II," *Journal of the European Ceramic Society 21,* pp. 2171-2177, 2001.

[120]   A. H. Tavakoli, P. Gerstel, J. A. Golczewski and J. Bill, "Kinetic effect of boron on the crystallization of Si3N4 in Si–B–C–N polymer-derived ceramics," *Journal of Materials Research 26 (4),* pp. 600-608, 2011.

[121]   A. H. Tavakoli, P. Gerstel, J. A. Golczewski and J. Bill, "Quantitative X-ray Diffraction Analysis and Modeling of the Crystallization Process in Amorphous Si–B–C–N Polymer-Derived Ceramics," *Journal of the American Ceramic Society 93 (5),* pp. 1470-1478, 2010.

[122]   Y. Gao, S. J. Widgeon, T. B. Tran, A. H. Tavakoli, G. Mera, S. Sen, R. Riedel and A. Navrotsky, "Effect of demixing and coarsening on the energetics of poly(boro)silazane-derived amorphous Si-(B-)C-N ceramics," *Scripta Materialia 69,* pp. 347-350, 2013.

[123] A. H. Tavaloki, J. A. Golczewski, J. Bill and A. Navrotsky, "Effect of boron on the thermodynamic stability of amorphous polymer-derived Si-(B-)C-N ceramics," *Acta Materialia 60,* pp. 4514-4522, 2012.

[124] A. H. Tavakoli, P. Gerstel, J. A. Golczewski and J. Bill, "Effect of boron on the crystallization of amorphous Si–(B–)C–N polymer-derived ceramics," *Journal of Non-Crystalline Solids 355,* pp. 2381-2389, 2009.

[125] J. She and D. Jiang, "An attractive way to heal surface defects of some carbide and boride ceramics," *Materials Letters 26,* pp. 313-317, 1996.

[126] I. J. Markel, J. Glaser, S. Steinbrück and H. J. Seifert, "High-temperature reactions and phase evolution in precursor-derived ZrB2/Si-C-N composites," *Journal of the European Ceramic Society 39,* p. 2585–2593, 2019.

[127] S. Wagner, "Thermodynamics of the Interface Reactions of Selected Oxidation and Erosion Protective Layers for Carbon-fibre Reinforced Composites," *Dissertation Universität Stuttgart,* 2003.

[128] W. A. Johnson and R. F. Mehl, "Reaction kinetics in processes of nucleation and growth," *Transactions of the American Institute of Mining, Metallurgical, and Petroleum Engineers 135,* pp. 416-458, 1939.

[129] M. Avrami, "Granulation, Phase Change, and Microstructure Kinetics of Phase Change. III," *The Journal of Chemical Physics 9 (2),* pp. 177-184, 1941.

[130] A. Kolmogoroff, "Zur Statistik der Kristallisationsvorgänge in Metallen," *Izvestija Akademii Nauk SSSR Serija Matematicheskaja 1 (3),* pp. 355-359, 1937.

[131] L. Kaufman, "Calculation of Multicomponent Refractory Composite Phase Diagrams," *ManLabs, Inc., Cambridge Massachusetts,* 1986.

[132] Z. Nasiri, M. Mashhadi and A. Abdollahi, "Effect of short carbon fiber addition on pressureless densification and mechanical properties of ZrB2–SiC–Csf nanocomposite," *International Journal of Refractory Metals and Hard Materials 51,* pp. 216-223, 2015.

[133] W. M. Guo, S. X. Gu, Y. You, Q. G. Jiang, S. H. Wu and H. T. Lin, "Densification and Thermal Stability of Hot-Pressed Si3N4–ZrB2 Ceramics," *Journal of the American Ceramic Society 98 (12),* pp. 3651-3654, 2015.

[134] W. M. Guo, L. X. Wu, T. Ma, S. X. Gu, Y. You, H. T. Lin, S. H. Wu and G. J. Zhang, "Chemical

References

reactivity of hot-pressed Si3N4–ZrB2 ceramics at 1500–1700°C," *Journal of the European Ceramic Society 35,* pp. 2973-2979, 2015.

[135] L. Brewer and H. Haraldsen, "The Thermodynamic Stability of Refractory Borides," *Journal of the Electrochemical Society 102 (7),* pp. 399-406, 1955.

[136] R. Kiessling and Y. H. Liu, "Thermal Stability of The Chromium, Iron, and Tungsten Borides In Streaming Ammonia And The Existence of a New Tungsten Nitride," *Journal of Metals 3,* pp. 639-642, 1951.

[137] S. W. Yin, L. Wang, L. G. Tong, F. M. Yang and Y. H. Li, "Kinetic study on the direct nitridation of silicon powders diluted with α-Si3N4 at normal pressure," *International Journal of Minerals, Metallurgy and Materials 20 (5),* pp. 493-498, 2013.

[138] H. Rode and V. Hlavacek, "Detailed Kinetics of Titanium Nitride Synthesis," *AIChE Journal 41 (2),* pp. 377-388, 1995.

[139] J. Roger, L. Maillé and M. A. Dourges, "Isothermal nitridation kinetics of TiSi2 powders," *Journal of Solid State Chemistry 212,* pp. 134-140, 2014.

[140] C. Agte and K. Moers, "Methoden zur Reindarstellung hochschmelzender Carbide, Nitride und Boride und Beschreibung einiger ihrer Eigenschaften," *Zeitschrift für anorganische und allgemeine Chemie 198,* pp. 233-275, 1931.

[141] H. Bittner, H. Goretzki, F. Benesovsky and H. Nowotny, "Über einige Monocarbid-Mononitrid-Systeme und deren magnetische Eigenschaften," *Monatshefte für Chemie 94,* pp. 518-526, 1963.

[142] R. Kieffer, P. Ettmayer, H. Nowotny and G. Dufek, "New investigations concerning miscibility of transition-metal nitrides and carbides," *Metall 26 (7),* pp. 701-708, 1972.

[143] S. Binder, W. Lengauer, P. Ettmayer, J. Bauer, J. Debuigne and M. Bohn, "Phase equilibria in the systems Ti-C-N, Zr-C-N and Hf-C-N," *Journal of Alloys and Compounds 217,* pp. 128-136, 1995.

[144] K. Constant, R. Kieffer and P. Ettmayer, "Über das pseudoternäre System ZrO-ZrN-ZrC," *Monatshefte für Chemie 106,* pp. 823-832, 1975.

[145] W. Lengauer, S. Binder, K. Aigner, P. Ettmayer, A. Guillou, J. Debuigne and G. Groboth, "Solid state properties of group IVb carbonitrides," *Journal of Alloys and Compounds 217,* pp. 137-147, 1995.

[146] H. Holleck, Binäre und ternäre Carbid- und Nitridsysteme der Übergangsmetalle, Berlin-Stuttgart: Gebrüder Borntraeger, 1984.

[147] Y. Sun, Y. Li, D. Su, S. Wang and Y. Xu, "Preparation and charakterization of high temperature SiCN/ZrB2 ceramic composite," *Ceramics International 41,* pp. 3947-3951, 2015.

[148] N. L. Okamoto, M. Kusakari, K. Tanaka, H. Inui and S. Otani, "Temperature dependence of thermal expansion and elastic constants of single crystals of ZrB2 and the suitability of ZrB2 as a substrate for GaN film," *Journal of Applied Physics 93 (1),* pp. 88-93, 2003.

[149] J. W. Zimmermann, G. E. Hilmas and W. G. Fahrenholtz, "Thermophysical Properties of ZrB2 and ZrB2-SiC Ceramics," *Journal of the American Ceramic Society 91 (5),* pp. 1405-1411, 2008.

[150] J. Peng, H. J. Seifert and F. Aldinger, "Thermal Expansion Behavior of Precursor-Derived Amorphous Si-C-N and Si-B-C-N Ceramics," *Journal of Materials Science & Technology 18 (2),* pp. 139-142, 2002.

[151] K. Aigner, W. Lengauer, D. Rafaja and P. Ettmayer, "Lattice parameters and thermal expansion of Ti(CxN1-x), Zr(CxN1-x), Hf(CxN1-x) and TiN1-x from 298 to 1473 K as investigated by high-temperature X-ray diffraction," *Journal of Alloys and Compounds 215,* pp. 121-126, 1994.

[152] B. Yates, M. J. Overy and O. Pirgon, "The anisotropic thermal expansion of boron nitride," *Philosophical Magazine 32 (4),* pp. 847-857, 1975.

[153] R. F. Voitovich, É. A. Pugach and L. A. Men'shikova, "High-temperature oxidation of zirconium diboride," *Soviet Powder Metallurgy and Metal Ceramics 6 (6),* pp. 462-465, 1967.

[154] L. Kaufman and E. Cloughterty, "Technical Report RTD-TDR-63-4096, Part 1," *Air Force Materials Laboratory, Wright-Patterson AFB, OH,* 1963.

[155] W. G. Fahrenholtz and G. E. Hilmas, "Ultra-high temperature ceramics: Materials for extreme environments," *Scripta Materialia 129,* pp. 94-99, 2017.

[156] M. A. Kuzenkova and P. S. Kisly, "Investigation of the oxidation resistance of zirconium boride-molybdenum disilicide alloys," *Poroshkovaya metallurgiya 10,* pp. 75-79, 1965.

[157] R. Inoue, Y. Arai, Y. Kubota, Y. Kogo and K. Goto, "Oxidation of ZrB2 and its composites: a

review," *Journal of Materials Science 53,* pp. 14885-14906, 2018.

[158] M. M. Opeka, I. G. Talmy and J. A. Zaykoski, "Oxidation-based materials selection for 2000°C+ hypersonic aerosurfaces: Theoretical considerations and historical experience," *Journal of Materials Science 39,* pp. 5887-5904, 2004.

[159] A. H. Heuer and V. L. K. Lou, "Volatility Diagrams for Silica, Silicon Nitride, and Silicon Carbide and Their Application to High-Temperature Decomposition and Oxidation," *Journal of the American Ceramic Society 73 (10),* pp. 2789-2803, 1990.

[160] N. Miyahara, S. Miwa, N. Horiguchi, I. Sato and O. Masahiko, "Chemical reaction kinetics dataset of Cs-I-B-Mo-O-H system for evaluation of fission product chemistry under LWR severe accident conditions," *Journal of Nuclear Science and Technology 56 (2),* pp. 228-240, 2019.

[161] M. Steinbrück and S. Schaffer, "High-Temperature Oxidation of Zircaloy-4 in Oxygen–Nitrogen Mixtures," *Oxidation of Metals 85,* pp. 245-262, 2016.

[162] A. Ermoline, M. Schoenitz and E. Dreizin, "High-temperature phase equilibria in the system Zr–O–N," *Journal of Materials Research 21,* pp. 320-328, 2006.

[163] W. Krauss, G. Schanz and H. Steiner, TG-Rig Tests (Thermal Balance) on the Oxidation of B4C. Basic experiments, modelling and evaluation approach, Forschungszentrum Karlsruhe: SAM-COLOSS-P027, FZKA 6883, 2003.

[164] N. Jacobson, S. Farmer, A. Moore and H. Sayir, "High-Temperature Oxidaion of Boron Nitride: I, Monolithic Boron Nitride," *Journal of the American Ceramic Society 82 (2),* pp. 393-398, 1999.

[165] R. A. Yetter, H. Rabitz and F. L. Dryer, "Kinetics of high-temperature B/O/H/C Chemistry," *Combustion and Flame 83,* pp. 43-62, 1991.

[166] L. Pasternack, "Gas-phase modeling of homogeneous boron/oxygen/hydrogen/carbon combustion," *Combustion and Flame 90,* pp. 259-268, 1992.

[167] R. C. Brown, C. E. Kolb and R. A. Yetter, "Gas phase kinetic modeling and sensitivity analysis of B/H/O/C/F combustion systems," *US Office of Naval, Research Report No. ARI-RR-964,* 1993.

[168] D. J. Meschi, W. A. Chupka and J. Berkowitz, "Heterogeneous Reactions Studied by Mass Spectrometry. I. Reactions of B2O3(s) with H2O(g)," *The Journal of Chemical Physics 33*

(2), pp. 530-533, 1960.

[169]   M. Steinbrück, M. S. Veshchunov, A. V. Boldyrev and V. E. Shestak, "Oxidation of B4C by steam at high temperatures: New experiments and modelling," *Nuclear Engineering and Design 237,* pp. 161-181, 2007.

[170]   A. K. Kuriakose and J. L. Margrave, "The Oxidation Kinetics of Zirconium Diboride and Zirconium Carbide at High Temperatures," *Journal of the Electrochemical Society 111 (7),* pp. 827-831, 1964.

[171]   J. B. Berkowitz-Mattuck, "High-Temperature Oxidation III. Zirconium and Hafnium Diborides," *Journal of the Electrochemical Society 113,* pp. 908-914, 1966.

[172]   W. C. Tripp and H. C. Graham, "Thermogravimetric Study of the Oxidation of ZrB in the Temperature Range of 800°C to 1500°C," *Journal of the Electrochemical Society 118 (7),* pp. 1195-1199, 1971.

[173]   T. A. Parthasarathy, R. Rapp, M. Opeka and R. J. Kerans, "A model for the oxidation of ZrB2, HfB2 and TiB2," *Acta Materialia 55,* pp. 5999-6010, 2007.

[174]   T. A. Parthasarathy, R. A. Rapp, M. Opeka and R. J. Kerans, "Effects of Phase Change and Oxygen Permeability in Oxide Scales on Oxidation Kinetics of ZrB2 and HfB2," *Journal of the American Ceramic Society 92 (5),* pp. 1079-1086, 2009.

[175]   S.-Q. Guo, "Densification of ZrB2-based composites and their mechanicaland physical properties: A review," *Journal of the European Ceramic Society 29,* pp. 995-1011, 2009.

[176]   F. H. Brown, "Stability of Titanium Diboride and Zirconium Diboride in Air, Oxygen, and Nitrogen," *California Inst. of Tech., Pasadena Jet Propulsion Lab, No.JPL-PR-20-252,* 1955.

[177]   L. Kaufman and E. Cloughterty, "Technical Report RTD-TDR-63-4096, Part 2," *Air Force Materials Laboratory, Wright-Patterson AFB, OH,* 1965.

[178]   Q. N. Nguyen, E. J. Opila and R. C. Robinson, "Oxidation of Ultrahigh Temperature Ceramics in Water Vapor," *Journal of The Electrochemical Society 151 (10),* pp. B558-B562, 2004.

[179]   M. Steinbrück, "Oxidation of boron carbide at high temperatures," *Journal of Nuclear Materials 336,* p. 185–193, 2005.

References

[180] R. W. Harrison and W. E. Lee, "Mechanism and Kinetics of Oxidation of ZrN Ceramics," *Journal of the American Ceramic Society 98 (7),* pp. 2205-2213, 2015.

[181] L. Krusin-Elbaum and M. Wittmer, "Oxidation Kinetics of ZrN Thin Films," *Thin Solid Films 107 (1),* pp. 111-116, 1983.

[182] P. Panjan, B. Navinsek, A. Cvelbar, A. Zalar and I. Milosev, "Oxidation of TiN, ZrN, TiZrN, CrN, TiCrN and TiN/CrN Multilayer Hard Coatings Reactively Sputtered at Low Temperature," *Thin Solid Films 281-282 (1),* p. 298–301, 1996.

[183] M. Steinbrück, F. O. da Silva and M. Grosse, "Oxidation of Zircaloy-4 in steam-nitrogen mixtures at 600-1200 °C," *Journal of Nuclear Materials 490,* pp. 226-237, 2017.

[184] Y. Katoh, G. Vasudevamurthy, T. Nozawa and L. L. Snead, "Properties of Zirconium Carbide for Nuclear Fuel Applications," *Journal of Nuclear Materials 441 (1-3),* pp. 718-742, 2013.

[185] M. Steinbrück, V. Angelici Avincola, I. J. Markel, U. Stegmaier, U. Gerhards and H. J. Seifert, "Oxidation of SiCf-SiC CMC cladding tubes for GFR application in impure helium atmosphere and materials interactions with tantalum liner at high temperatures up to 1600°C," *Journal of Nuclear Materials 517,* pp. 337-348, 2019.

[186] R. Golden and E. J. Opila, "Oxygen Tracer Diffusion in Yttrium Silicates," *41st ICACC, Daytona Beach, Florida,* 2017.

[187] F. Aldinger, M. Weinmann and J. Bill, "Precursor-derived Si-B-C-N ceramics," *Pure and Applied Chemistry 70 (2),* pp. 439-448, 1998.

[188] E. Butchereit and K. G. Nickel, "Oxidation behaviour of Precursor Derived Ceramics in the System Si-(B)-C-N," *Key Engineering Materials 175-176,* pp. 69-78, 2000.

[189] D. Bahloul, M. Pereira and P. Goursat, "Silicon carbonitride derived from an organimetallic precursor - influence of the microstructure on the oxidation behavior," *Ceramics International 18 (1),* pp. 1-9, 1992.

[190] M. Kazemzadeh Dehdashti, W. G. Fahrenholtz and G. E. Hilmas, "Oxidation of zirconium diboride with niobium additions," *Journal of the European Ceramic Society 33,* p. 1591–1598, 2013.

[191] D. A. Krivoshein, M. A. Maurakh, V. S. Dergunova, Y. N. Petrov and Y. N. Lebedev, "Method of manufacture and oxidation resistance of a graphite material with zirconium

diboride, silicon, and vanadium additions," *Soviet Powder Metallurgy and Metal Ceramics volume 17,* pp. 460-463, 1978.

[192] B. McFarland, V. A. Avincola, M. Morales and E. Opila, "Identification of a new oxidation/ dissolution mechanism for boria-accelerated SiC oxidation," *Journal of the American Ceramic Society 103(5),* pp. 5214-5231, 2020.

[193] H. Seifert, S. Wagner, O. Fabrichnaya, H. Lukas, F. Aldinger, T. Ullmann, M. Schmücker and H. Schneider, "Yttrium Silicate Coatings on Chemical Vapor Deposition-SiC-Precoated C/C-SiC:Thermodynamic Assessment and High-Temperature Investigation," *Journal of the American Ceramic Society 88 (2),* pp. 424-430, 2005.